The Effects of Chemical Weathering on Thermal-Infrared Spectral Data and Models: Implications for Aqueous Processes on the Martian Surface

by

Elizabeth Barger Rampe

A Dissertation Presented in Partial Fulfillment
of the Requirements for the Degree
Doctor of Philosophy

Approved May 2011 by the
Graduate Supervisory Committee:

Thomas Sharp, Chair
Philip Christensen
Richard Hervig
Everett Shock
Lynda Williams

ARIZONA STATE UNIVERSITY

August 2011

ABSTRACT

Chemical and mineralogical data from Mars shows that the surface has been chemically weathered on local to regional scales. Chemical trends and the types of chemical weathering products present on the surface and their abundances can elucidate information about past aqueous processes. Thermal-infrared (TIR) data and their respective models are essential for interpreting Martian mineralogy and geologic history. However, previous studies have shown that chemical weathering and the precipitation of fine-grained secondary silicates can adversely affect the accuracy of TIR spectral models. Furthermore, spectral libraries used to identify minerals on the Martian surface lack some important weathering products, including poorly-crystalline aluminosilicates like allophane, thus eliminating their identification in TIR spectral models. It is essential to accurately interpret TIR spectral data from chemically weathered surfaces to understand the evolution of aqueous processes on Mars.

Laboratory experiments were performed to improve interpretations of TIR data from weathered surfaces. To test the accuracy of deriving chemistry of weathered rocks from TIR spectroscopy, chemistry was derived from TIR models of weathered basalts from Baynton, Australia and compared to actual weathering rind chemistry. To determine how specific secondary silicates affect the TIR spectroscopy of weathered basalts, mixtures of basaltic minerals and small amounts of secondary silicates were modeled. Poorly-crystalline aluminosilicates were synthesized and their TIR spectra were added to spectral libraries. Regional Thermal Emission Spectrometer (TES) data were modeled using libraries containing these poorly-crystalline aluminosilicates to test for their presence on the Mars.

Chemistry derived from models of weathered Baynton basalts is not accurate, but broad chemical weathering trends can be interpreted from the data. TIR models of mineral mixtures show that small amounts of crystalline and amorphous silicate

weathering products (2.5-5 wt.%) can be detected in TIR models and can adversely affect modeled plagioclase abundances. Poorly-crystalline aluminosilicates are identified in Northern Acidalia, Solis Planum, and Meridiani. Previous studies have suggested that acid sulfate weathering was the dominant surface alteration process for the past 3.5 billion years; however, the identification of allophane indicates that alteration at near-neutral pH occurred on regional scales and that acid sulfate weathering is not the only weathering process on Mars.

DEDICATION

To my mother, Mary, who always encouraged and nurtured my love of science and has been the perfect combination of role model, teacher, and friend.

ACKNOWLEDGMENTS

I have had the privilege of knowing so many wonderful people who made my time at ASU one that I will reflect on fondly. My sincerest thanks goes out to the following people:

My advisor, Tom Sharp, was always enthusiastic about my research. He deserves a special thanks for the countless hours he devoted to cultivating my scientific writing skills.

Mike Kraft, who so generously gave up his time to discuss ideas, develop projects, and help me study for my comprehensive exams.

My committee members, Phil Christensen, Rick Hervig, Everett Shock, and Lynda Williams for proposing new avenues of research that were interesting and fruitful.

My tremendous support group of friends, including (but not limited to) Chelsea Allison, Wendy Bohon, Brittany Brand, Chris Edwards, Danny Foley, Jen Glass, Jenna Green, Natalie Hinkel, Katie Kaleida, Sue Lederer, Christine Lee, Emily McLinden, Lillian Ostrach, Miriam Riner, Allie Rutledge, Carl Segerblom, Jean-Francois Smekens, Lev Spivak-Birdorf, and Alka Tripathy. A few people are especially dear to me. Nina Lanza has been a tremendous friend, colleague, housemate, office mate, road trip partner, etc., etc. Her positive energy is contagious and her support and friendship have given me confidence in my own abilities. Kelsey Young is so much like me, it's crazy, and I can't wait to spend more time with her in Houston. Katie Alexander is simply a wonderful person whose company I enjoy immensely. Zach Wallace has the biggest heart of anyone I know and his friendship has helped me in so many ways.

My colleagues and people who have helped me with my projects along the way, without whom, I could not have performed the research presented here. Janice Bishop, Chris Edwards, Tim Glotch, Takahiro Hiroi, Penny King, Cheryl Replogle, Deanne Rogers, Steve Ruff, and Emmanuel Soignard. My colleagues at Johnson Space Center

were especially helpful in developing Chapters 4 and 5. Doug Ming taught me the importance of allophane and encouraged me to synthesize it. DC Golden devoted so much of his time teaching me how to make allophane. Julie Quinn, Brad Sutter, and Cheri Achilles were helpful in the lab and made me feel like part of the research group. They all made research so exciting and fun that I am starting a post-doc with the same research group this summer.

My family, Mom, Dad, Fred, and Alicia for all of their love and support. I am so lucky to have them.

This work was supported by the NASA Graduate Student Researchers Program Fellowship, a grant from the Mars Data Analysis Program, and the Arizona State University Graduate College Dissertation Fellowship.

TABLE OF CONTENTS

Page

CHAPTER Page

CHAPTER Page

CHAPTER Page

CHAPTER Page

CHAPTER Page

CHAPTER Page

LIST OF TABLES

LIST OF FIGURES

1 Introduction

Chemical and mineralogical data of the Martian surface indicates that it has experienced a variety of aqueous alteration and chemical weathering processes over time. Thermal-infrared (TIR) spectroscopy has been essential in developing our understanding of petrologic and aqueous alteration processes on Mars. Mineral abundances are derived from TIR data by linear deconvolution, a linear least squares algorithm that uses a library of mineral spectra to fit a measured spectrum [*Ramsey and Christensen*, 1998]. Linear deconvolution assumes that the measured spectrum is a linear combination of the spectra of the minerals that comprise the surface, proportional to the minerals' areal abundance. Accurate modeled mineral abundances can be returned if the correct phases are present in the end-member spectral library and if the surface is relatively coarse-grained, with grain diameters >60 microns [*Ramsey and Christensen*, 1998; *Feely and Christensen*, 1999; *Wyatt et al.*, 2001]. Mineral models can, in turn, be used to derive the chemistry of a planetary surface if the exact chemistry of each mineral end member is known [*Wyatt et al.*, 2001]. Chemical weathering can cause inaccurate spectral models for two reasons: 1) poorly-crystalline and amorphous weathering products are generally not present in spectral libraries, making it difficult to characterize the structure and composition of weathering products on a planetary surface, and 2) fine-grained materials and coatings cause non-linear spectral mixing in the TIR region [*Moersch and Christensen*, 1995; *Ramsey and Christensen*, 1998; *Kraft*, 2003], making it difficult to quantify primary and secondary mineral abundances on a planetary surface.

Thermal-IR spectral models of the Martian surface from the Thermal Emission Spectrometer (TES) on Mars Global Surveyor suggest that the surface is primarily composed of basalt [*Bandfield et al.*, 2000; *Christensen et al.*, 2000]. TES models provide evidence for aqueous alteration products; however, the identity of these products and the extent of alteration have been subjects of debate. High-silica phases are

identified in spectral models globally but are present in higher concentrations at mid-to-high latitudes [*Bandfield et al.*, 2000; *Wyatt and McSween*, 2002; *Rogers and Christensen*, 2007; *Minitti and Hamilton*, 2010]. Initially, these phases were interpreted as primary volcanic glass, suggesting that low latitude surfaces were basaltic and mid-to-high latitude surfaces were andesitic [*Bandfield et al.*, 2000]. Subsequent interpretations suggested these high-silica phases are weathering products, such as clay minerals, amorphous silica, and poorly-crystalline aluminosilicates, indicating that mid-to-high latitude surfaces were chemically weathered [*Wyatt and McSween*, 2002; *Kraft et al.*, 2003; *Michalski et al.*, 2005; *Michalski et al.*, 2006a; *Minitti et al.*, 2007; *Rogers and Christensen*, 2007].

In contrast, orbital near-infrared (NIR) spectral data from the Observatoire pour la Minéralogie, l'Eau, les Glaces et l'Activité (OMEGA) and the Compact Reconnaissance Imaging Spectrometer for Mars (CRISM) do not support the presence of secondary silicates in these terrains [*Bibring et al.*, 2005; *Rogers and Christensen*, 2007]. These datasets show evidence for phyllosilicates, zeolites, and opaline silica in specific locations in the oldest terrains on Mars, suggesting that aqueous alteration under near-neutral to alkaline pH and high water-to-rock ratios was prevalent during the Noachian Period (~4.5-3.7 Ga) [*Bibring et al.*, 2005; 2006; *Poulet et al.*, 2005; *Bishop et al.*, 2008; *Ehlmann et al.*, 2008; 2009; *Mustard et al.*, 2008]. Conversely, spectral models of TES data from these older regions generally do not identify these alteration minerals in significant abundances [*Michalski and Noe Dobrea*, 2007]. It has been suggested that TES models do not detect alteration minerals in these regions because 1) NIR spectroscopy is more sensitive to the detection of hydrated alteration minerals than TIR spectroscopy; 2) the spatial resolution of CRISM and OMEGA are better than TES and these alteration minerals are too localized to be detected by TES; and 3) the physical properties of surfaces that contain alteration minerals are more conducive to their

detection by NIR than by TIR spectroscopy [*Michalski and Fergason*, 2009]. This discrepancy between TIR models and NIR data of the Martian surface and the identity of the high-silica phases in TIR spectral models are important issues that must be resolved in order to better understand chemical weathering environments on Mars.

The geochemistry of Martian rocks and soils has been analyzed from orbit by the Gamma Ray Spectrometer (GRS), from the surface by the Alpha Particle X-ray Spectrometers (APXS) on the two Viking landers and the Pathfinder and MER rovers, and from Martian meteorites collected on Earth. The chemistries from all of these datasets are broadly consistent with a basaltic lithology; however, surface geochemistry inferred from TES spectral models shows enrichment in SiO_2 and alkalis relative to the other datasets, suggesting that the chemistry derived from TES models is inaccurate [*McSween et al.*, 2009]. *McSween et al.* [2009] proposed that chemical weathering may cause inaccurate TIR model-derived chemistry, but specific reasons for the enrichment in SiO_2 and alkalis have not been explained.

1.1 Purpose and Goals

TIR spectral models are a primary means by which igneous minerals and alteration products are characterized on the Martian surface. Evidence for chemical weathering and aqueous alteration on Mars demonstrates the importance of understanding how chemical weathering affects the TIR model-derived mineralogy. The types of weathering products present on a surface reveal information about past aqueous environments. A primary goal of NASA's Mars Exploration Program is to determine if life ever arose on Mars [*MEPAG*, 2010]. The identification of specific weathering products and their abundances on the Martian surface allow us to determine the evolution of the Martian hydrosphere and help identify areas that may have been habitable. An incomplete representation of weathering products in TIR spectral libraries limits our interpretations of weathering environments on Mars.

The purpose of this research is to improve our interpretations of TIR spectral models of chemically weathered surfaces and to develop a more complete understanding of chemical weathering environments on the Martian surface. The goals of this work are 1) to characterize the effects that crystalline and amorphous silicate weathering products have on TIR spectral models of igneous minerals; 2) test the accuracy of deriving chemistry from weathered rock surfaces; and 3) add TIR spectra of common poorly-crystalline weathering products on Earth to Martian spectral libraries and test for their presence on the Martian surface.

1.2 Background

1.2.1 Chemical Weathering on Earth

Chemical weathering involves the aqueous dissolution of primary igneous phases, the transportation of elements in solution, and the precipitation of secondary phases. In a rock, chemical weathering is most intense near the surface, where there is the most exposure to fluids. Fluids percolate into the rock through fine fractures, dissolve primary phases, and precipitate weathering products within these fractures. The fractures become planes of weakness and, over time, with physical weathering, the portion of the rock between the fracture and the surface breaks off and becomes part of the surrounding soil [*Taylor and Eggleton*, 2001]. The zone of chemical weathering near the surface of a rock, known as a weathering rind, is visibly separate from the unweathered interior, where the interior is usually dark and the weathered zone is brown or red in color [*Colman*, 1982]. The weathering rind is primarily composed of igneous phases and volumetrically small amounts of weathering products [*Kraft*, 2009]. Since basalt is the most common rock type on Mars, this discussion of chemical weathering will focus on chemical weathering processes in basalts.

Studies of weathered basalts from Baynton, Australia show that the susceptibility of basaltic minerals to aqueous alteration is olivine > volcanic glass > plagioclase >

clinopyroxene > Fe-Ti-oxide [*Nesbitt and Wilson*, 1992]. Other studies suggest slightly different sequences of alteration and list glass as the most susceptible phase [*Colman*, 1982; *Eggleton et al.*, 1987] and pyroxene as more susceptible to dissolution than plagioclase [*Colman*, 1982]. Clinopyroxene dissolves at a faster rate than plagioclase so that while plagioclase may begin to alter before pyroxene, plagioclase may remain in the rock after all pyroxene has been altered [*Eggleton et al.*, 1987]. The order of igneous mineral susceptibility to aqueous alteration is similar for different climate regimes; however, climate affects the rate of weathering, where basalts in wetter climates alter more quickly than basalts in arid climates [*Eggleton et al.*, 1987].

The types of chemical weathering products that form in a weathering rind or soil are dependent on the parent materials being altered, the amount of fluid present, the fluid pH, and the amount of time that the rocks and soils are weathered under these conditions [*Taylor and Eggleton*, 2001]. Therefore, the types of chemical weathering products can tell us about past aqueous processes and the environments in which they formed. There are a variety of weathering products with wide ranges of compositions and degrees of crystallinity. Iron-oxides and hydroxides are very common in weathered rocks and soils because Fe^{2+} present in igneous phases like olivine, glass, and pyroxene is soluble and readily oxidizes to insoluble Fe^{3+} in the presence of water. Common Fe-oxides in weathered surfaces include hematite (Fe_2O_3, common in arid environments), goethite (FeO(OH), common in wetter environments), and ferrihydrite (a poorly-crystalline, hydrated Fe-oxide that is commonly the first Fe-bearing weathering product to form). Sulfate minerals are products of acid-sulfate weathering, so they are indicative of aqueous environments with low pH. Common sulfates include gypsum, anhydrite, and jarosite. Carbonate minerals are products of alteration in alkaline aqueous environments and common carbonates include calcite, dolomite, and magnesite. While these phases are important for understanding the conditions of chemical weathering environments, this

discussion will focus on silicate weathering products because the studies presented here were designed to constrain the identities and abundances of secondary silicates on Mars as these phases are difficult to differentiate using thermal infrared spectroscopy.

Silicate weathering products can be crystalline (meaning they have long-range atomic order), amorphous (no regular atomic order), or poorly-crystalline (short-range atomic order). Studies of chemically weathered surfaces generally focus on clay minerals, which are hydrous, crystalline, sheet silicates (or phyllosilicates) that are <2 microns in size. Clay minerals form under acidic to alkaline pH and high water-to-rock ratios. The building blocks of clay minerals are octahedral and tetrahedral sheets. The octahedral (O) sheet is a plane of cations in 6-fold coordination bonded to either oxygen or hydroxides. The tetrahedral (T) sheet is made up of a plane of Si cations in 4-fold coordination with oxygen. These O and T sheets are combined in either TO or TOT layers. Aluminum commonly exchanges for Si in the tetrahedral sheet because the Al^{3+} cation is similar in size to the Si^{4+} cation. Clay minerals are grouped based on the configuration of their sheets, their chemistry, and their ability to absorb water. Clays with TO structures are 1:1 layer silicates and these include kaolin group minerals, where Al is in the octahedral sheet, and serpentine group minerals, where Mg is in the octahedral sheet. Clays with TOT structures are 2:1 layer silicates. Many of these minerals have cations between the TOT layers and have the ability to absorb H_2O when they have layer charges of -0.2 to -0.6, from the substitution of Al for Si in the tetrahedral sheet. Illite has Al in the octahedral sheet and K between the 2:1 layers but cannot accept interlayer H_2O because the layer charge is too high. Smectites have a variety of cations in the octahedral sheet; montmorillonite has Al^{3+}, nontronite has Fe^{2+} and Fe^{3+}, and saponite has Mg^{2+}. Smectites can have a variety of cations between the 2:1 layers, including Ca^{2+}, K^{+}, Mg^{2+}, and Na^{+} and readily take on water in these interlayer sites.

Chlorites are 2:1 layer silicates with an additional octahedral sheet between the 2:1 layers [*Moore and Reynolds*, 1989; *Taylor and Eggleton*, 2001].

Zeolites are framework silicate minerals that form from weathering or aqueous alteration under alkaline pH and high water-to-rock ratios. They can form in a variety of environments, including surficial weathering, diagenesis of volcanic ash in saline lakes or marine environments, percolating groundwater, hydrothermal alteration, and contact and burial metamorphism. The types of zeolites that form are dependent on the parent material and aqueous environment. For example, clinoptilolite, chabazite, mordenite, erionite, and phillipsite form by the alteration of volcanic ash in hydrothermal, percolating groundwater, or contact metamorphic environments. Heulandite, chabazite, natrolite, and stilbite form within vugs in volcanic rocks from groundwater percolation. Heulandite, analcime, and laumontite form in low-grade metamorphic environments [*Nesse*, 2000].

Poorly-crystalline and amorphous silicate weathering products have not been characterized as well as sheet silicates and zeolites because they are generally present in volumetrically small amounts in weathering rinds, they are difficult to separate from other weathering products, and they lack long-range atomic order, which makes them difficult to study by diffraction-based techniques. However, these phases are important because they are some of the first phases to precipitate during chemical weathering. Studies of weathered basalt in terrestrial environments show that weathering rinds generally lack crystalline clays and the bulk of the weathered material is poorly-crystalline [*Colman*, 1982]. Allophane and imogolite are poorly-crystalline, hydrated aluminosilicates that are low-temperature weathering products of volcanic glass. They are common in basaltic weathering rinds and soils derived from volcanic ash on Earth [*Wada et al.*, 1972; *Colman*, 1982; *Wada*, 1989]. Allophane is composed of roughly spherical, hollow particles 3-5 nm in diameter. The walls of these particles are made up

of curved Si-rich tetrahedral and Al-octahedral layers, similar to 1:1 layer clays. Allophane, which forms at neutral to mildly acidic pH (~5-7), has molar Si/Al ratios from 0.5 to 1, where Al-rich allophanes form at lower pH [*Childs et al.*, 1990]. Imogolite has a molar Si/Al ratio of 0.5 and is composed of curved Si-tetrahedral and Al-octahedral layers that form tubes 100s of nm long. Imogolite forms in slightly more acidic fluids than allophane [*Wada*, 1989]. Allophane and imogolite can form as gel films (i.e. a network of particles) on rock surfaces [*Wada et al.*, 1972; *Farmer et al.*, 1985]. Further weathering of allophane and imogolite results in the precipitation of halloysite or gibbsite. Hisingerite is the Fe analog of allophane; however, its structure and chemistry have not been well characterized [*Wada*, 1989]. Poorly-crystalline aluminosilicates whose compositions fall outside of the allophane and imogolite range are generally referred to as "gels," which are homogenous semisolids made up of a network of fine particles [*Neuendorf et al.*, 2005].

The major rock-forming elements include Si, Al, Fe, Mg, Ca, Na, K, and Ti. The relative abundances of these elements can be used to assess the conditions and extent of weathering that a surface has experienced. Their concentrations and mobility relative to one another are dependent on the primary phases from which they are released and the secondary phases in which they are present. Basalt weathering rind studies show that, in general, incipient weathering causes rapid loss of K, Mg, Ca, and Na from the weathering profile [*Colman*, 1982; *Eggleton et al.*, 1987; *Nesbitt and Wilson*, 1992]. Potassium is released from volcanic glass through selective leaching, and Mg is lost from the dissolution of olivine. Calcium and Na are lost at a lower rate than Mg because they reside mostly in plagioclase and pyroxene. K, Mg, Ca, and Na are removed from the weathering profile because they are absent from many secondary phases that form early in weathering, such as allophane and Fe-oxides. Si is more slowly and uniformly removed and is primarily released from dissolution of olivine. Al, Fe, and Ti are

relatively immobile because Al is retained in poorly-crystalline aluminosilicates and is least soluble at near-neutral pH, Fe is retained in Fe-oxides and hydroxides, and Ti is largely present in insoluble minerals like ilmenite [*Colman*, 1982; *Drever*, 1992; *Eggleton et al.*, 1987; *Nesbitt and Wilson*, 1992].

The chemical trends that accompany weathering are displayed on various ternary diagrams. The most common ternary diagram projects through Si and displays Al_2O_3, $CaO+Na_2O+K_2O$, and $Fe_{total}+MgO$ at the apices. As weathering progresses, the composition moves away from the $CaO+Na_2O+K_2O$ apex because of the rapid loss of these elements during incipient chemical weathering. With more intense weathering, the composition moves towards the Al_2O_3 apex because of the precipitation of kaolinite and gibbsite. This trend is common for basaltic rocks in many different environments and is a characteristic of basalt weathering under near-neutral pH conditions on Earth [*Nesbitt and Wilson*, 1992; *Hurowitz and McLennan*, 2007].

1.2.2 Tools for Interpreting Chemical Weathering Environments on Mars

Past chemical weathering and aqueous alteration environments on Mars are inferred from in situ chemical measurements and from the types of weathering products present on the surface. The distribution of weathering products on the surface is generally characterized by spectroscopic measurements. There are two main wavelength ranges used to identify alteration products: the near-infrared (NIR), from ~1-5 microns, and the thermal-infrared (TIR), from ~5-50 microns (2000-200 cm^{-1}). Absorptions in - both of these spectral ranges are primarily from lattice vibrations in minerals. The NIR region samples the upper few microns of a surface, and NIR spectroscopy can be used to identify hydrated phases because absorptions from stretching and bending vibrations within hydroxyl groups, H_2O, and metal cation-OH bonds occur in this wavelength region. Thus, NIR spectroscopy is a useful tool for identifying hydrated and/or hydroxylated secondary silicates, like clay minerals, opaline silica, allophanes, and

hydrated aluminosilicate gels. Absorptions from OH groups and H_2O generally occur at 1.4 and 1.9 microns for most hydrated phases and are not diagnostic absorptions. The absorptions from cation-OH vibrations are distinct for different minerals and are used to identify hydrated secondary phases present on the Martian surface. For example, Al-OH bonds in the octahedral layer in montmorillonite absorb near 2.2 microns, while Fe-OH bonds in the octahedral layer in nontronite absorb near 2.3 microns. The two primary NIR spectrometers orbiting Mars are OMEGA on Mars Express and CRISM on the Mars Reconnaissance Orbiter. OMEGA has a spectral range of 0.35-5.1 microns with a spatial resolution of ~0.5-5 km [*Bibring et al.*, 2006], while that of CRISM is 0.362-3.92 microns with a spatial resolution of ~20 m [*Murchie et al.*, 2007].

Thermal-IR spectroscopy samples the upper few 10s of microns of a surface and detects various stretching and bending vibrations within silicates, carbonates, sulfates, and oxides, making it a useful tool for identifying a wide range of minerals. Each mineral has a distinct TIR spectrum that is dependent on its structure and chemical composition. Within silicates, Si-O stretching absorptions occur at ~8-12 microns (or 1200-800 cm^{-1}) and Si-O bending absorptions occur at ~15-25 microns (or 600-400 cm^{-1}) [*Hunt*, 1980]. The position of the absorption represents the resonant frequency of an optical phonon. When the frequency of the oscillating electric field matches the harmonic frequency of the phonon, the energy of the electric field is converted to kinetic energy, causing the crystal lattice to vibrate. The frequency is lower for heavier atoms and weaker bond strengths. For silicate minerals, a greater extent of polymerization of silica tetrahedra increases the frequency of Si-O stretching modes. Modes within framework silicates, like quartz and feldspar, require the most energy and the energy progressively decreases for chain silicates (pyroxenes), sheet silicates (clays), and nesosilicates (olivine).

Emission spectrometers measure the energy emitted from a surface. This energy is in the form of radiance and has an overall shape of a Planck curve corresponding to the temperature of the surface. The measured radiance spectrum is converted to an emissivity spectrum by dividing the radiance spectrum by the Planck curve corresponding to the temperature of the surface [*Christensen and Harrison*, 1993; *Ruff et al.*, 1997].

The TIR spectrum of a geologic surface is a linear combination of the spectra of each mineral within the surface, scaled to the areal abundance of each mineral [*Thomson and Salisbury*, 1993]. Linear mixing is expected in the TIR wavelength region because the absorption coefficients of the minerals are high and photons only interact with one grain [*Thomson and Salisbury*, 1993; *Ramsey and Christensen*, 1998]. Mineral abundances can be deduced from the TIR spectrum of a surface using linear deconvolution, a linear least squares fitting routine that uses a library of mineral spectra to calculate a spectrum to fit the measured spectrum [*Ramsey and Christensen*, 1998]. To explain the mathematics behind linear deconvolution, take an example of estimating the composition of a three-band emission spectrum of a rock surface using a spectral library with three end members. The emissivity values of the measured spectrum at the three spectral bands are known (E1, E2, and E3); the emissivity values of the three end members at band 1 are known (e_{11}, e_{21}, and e_{31}); the emissivity values of the three end members at band 2 are known (e_{12}, e_{22}, and e_{32}); and the emissivity values of the three end members at band 3 are known (e_{13}, e_{23}, and e_{33}). We want to solve for the fraction of each of the three end members from the measured spectrum (f_1, f_2, and f_3). We can do so with the following set of equations:

$$E1 = e_{11}f_1+e_{21}f_2+e_{31}f_3$$

$$E2 = e_{12}f_1+e_{22}f_2+e_{32}f_3$$

$$E3 = e_{13}f_1+e_{23}f_2+e_{33}f_3$$

Since there are three equations and three unknowns (f_1, f_2, and f_3), we can find a unique solution and solve for the areal percentages of each end member. The system is overdetermined if the number of end members in the library exceeds the number of spectral bands.

There are two primary problems with linear deconvolution: 1) the modeled mineralogy is dependent on the spectral library, so if a mineral present on a geologic surface is not in the spectral library, the modeled mineralogy will not be consistent with the actual mineralogy; and 2) coatings and fine-grained phases, with diameters smaller than the wavelength, cause non-linear spectral mixing. Non-linear mixing occurs in fine-grained materials because photons interact with more than one grain. These interactions change the morphology and intensity of the main absorption features (i.e. Reststrahlen bands) and the regions between the absorptions (i.e. the "intraband" regions) [*Salisbury and Wald*, 1992; *Moersh and Christensen*, 1995]. Absorptions in TIR spectra occur where the absorption coefficient of the material is high, meaning the material is strongly self-absorbing and little energy can reach the detector. When grain diameters are similar to the wavelength, photons interact with multiple grain surfaces before exiting the material, and each interaction adds reflected and emitted energy. Thus, more energy is reaching the detector, causing lower spectral contrast within Reststrahlen bands [*Moersch and Christensen*, 1995]. In the intraband regions, the material has low absorption coefficients and a refractive index (n) greater than 1. At large grain sizes, energy can escape the surface of a grain and be detected because of the low absorption coefficient. When grain diameters are similar to the wavelength, photons are transmitted through multiple grains and since $n > 1$, the ray path for the photons is increased and less energy reaches the detector. Thus, intraband regions for fine-grained materials display lower emissivity [*Moersch and Christensen*, 1995].

For coated rocks, the emissivity spectrum can be described as a combination of the energy emitted from the coating and the energy emitted from the underlying rock, transmitted through the coating. *Christensen and Harrison* [1993] described the emitted energy from a coated rock using the following equation:

$$E_{coated\ rock} = E_{substrate} * e^{-kx} + E_{coating} * (1 - e^{-kx})$$

where k is the absorption coefficient and x is the thickness of the coating. Silica-rich coatings are common on basalts weathered in semi-arid environments [*Curtiss et al.*, 1985; *Crisp et al.*, 1990; *Minitti et al.*, 2007; *Chemtob et al.*, 2010]. Silica coatings have high k from 1200-1040 cm^{-1} and 540-380 cm^{-1} from Si-O stretching and bending absorptions, respectively, so the rock spectrum underlying a silica coating will not be detected over these wavelength ranges [*Kraft*, 2009]. A study of silica coated basalts by Kraft [2009] showed that the position of maximum n and k values in the Si-O stretching regions are offset, where the peak n value occurs at 1050 cm^{-1} and the peak k value occurs at 1115 cm^{-1}. This offset creates a shoulder near 1050 cm^{-1} on the Si-O stretching absorption because the high n values at this wavelength causes more energy from the underlying basalt to be refracted away from the detector. The refraction of the emitted energy from the underlying basalt causes non-linear spectral mixing between the coating and underlying basalt so that the spectral models are inaccurate.

Linear deconvolution can return accurate modeled mineral abundances within 5-10 vol.% for unaltered igneous and metamorphic rocks [*Feely and Christensen*, 1999; *Wyatt et al.*, 2001] and coarse-grained mineral mixtures when grain diameters are >60 microns [*Ramsey and Christensen*, 1998]. Errors and detection limits have been calculated from spectral models of mineral mixtures with known mineral abundances and from estimating igneous and metamorphic mineral abundances by petrography. Detection limits are ~10 vol.% [*Ramsey and Christensen*, 1998; *Feely and Christensen*, 1999]; however, errors and detection limits are dependent on the composition of a

surface. For example, carbonate minerals have a lower detection limit than silicate minerals in a silicate rock because silicate mineral absorptions overlap one another while absorptions from carbonates are at shorter wavelengths and have fewer interferences from other mineral groups.

Chemical weathering produces coatings and fine-grained particles that cause non-linear spectral mixing. TIR spectra of basalts with synthetic silica coatings only a few microns thick cannot be modeled as linear mixtures of silica and basalt spectra [*Kraft et al.*, 2003]. Models of weathering rinds on Columbia River Basalts (CRB) underestimate plagioclase-to-pyroxene ratios, indicating that non-linear mixing from weathering compromises the igneous mineralogy derived from TIR spectral models [*Kraft*, 2009]. In addition to non-linear mixing, spectral models of weathered surfaces can be inaccurate because of a lack of poorly-crystalline weathering products in spectral libraries. Weathered CRB surfaces and altered tephras from Hawaii are comprised of poorly-crystalline aluminosilicates instead of crystalline phyllosilicates, but TIR models of these surfaces falsely identify significant abundances of phyllosilicates [*Michalski et al.*, 2006b; *Hamilton et al.*, 2008].

1.2.3 Chemical Evidence for Aqueous Alteration on Mars

In situ chemical measurements of rocks and soils on the Martian surface from rover and lander missions suggest element mobility from aqueous fluids. Alpha Particle X-ray Spectrometer data of Viking 1 and 2 soils and Pathfinder rocks and soils show elevated levels of S and Cl, which could be a result of aqueous leaching processes [*Clark et al.*, 1982; *Golombek et al.*, 1997; *Rieder et al.*, 1997]. Rocks and soils measured by the APXS in Gusev crater display high S abundances, indicating that acid-sulfate weathering has been an important alteration process [*Ming et al.*, 2006]. Rock classes Wishstone and Watchtower in Gusev are enriched in Al and Ti compared to the unaltered Adirondack class basalts, and the mineralogy of these rocks derived from APXS chemistry, Mini-TES

spectral models, and Mossbauer spectra show that they contain significant amounts of poorly-crystalline aluminosilicates, like allophane [*Ming et al.*, 2006]. Rocks and soils enriched in Si and Ti near Home Plate in Gusev are indicative of acid sulfate leaching environments [*Ming et al.*, 2008] or hydrothermal alteration at near-neutral pH [*Ruff et al.*, 2011]. APXS measurements of outcrops at Endurance, Fram, and Eagle crater in Meridiani Planum suggest S mobility upwards and Cl mobility downwards, consistent with the transportation and precipitation of salts through evaporation of acidic groundwater [*Clark et al.*, 2005]. Mass balance calculations from the chemical data also suggest the presence of significant amounts of secondary silica and aluminosilicates [*Clark et al.*, 2005]. Comparisons of all in situ chemical measurements across the Martian surface from APXS data from the two Viking landers, Pathfinder, and the two Mars Exploration Rovers show that the greatest amount of variation lies in Fe+Mg abundances [*Hurowitz and McLennan*, 2007]. This trend has been interpreted to result from preferential dissolution of olivine by global-scale acid sulfate alteration during the Hesperian Period (~3.7-3 Ga) [*Hurowitz et al.*, 2006; *Hurowitz and McLennan*, 2007].

1.2.4 Spectroscopic Evidence for Aqueous Alteration on Mars

NIR and TIR spectroscopy indicate that different aqueous alteration processes have defined each Martian time period. NIR spectral data from OMEGA and CRISM suggest there is a variety of phyllosilicate compositions in multiple Noachian-aged terrains (~4.5-3.7 Ga), including Mawrth Vallis, Nili Fossae, Gale crater, and the putative deltas in Eberswalde and Holden craters [*Poulet et al.*, 2005; *Ehlmann et al.*, 2008; *Mustard et al.*, 2008; *Wray et al.*, 2008; *Ehlmann et al.*, 2009; *Milliken et al.*, 2009]. CRISM data from Nili Fossae and Mini-TES spectra from Gusev crater have identified carbonate minerals in Noachian-aged materials [*Ehlmann et al.*, 2009; *Morris et al.*, 2010]. The presence of phyllosilicates and carbonates in the oldest Martian terrains suggests that there was widespread alkaline alteration at high water-to-rock ratios. The

identification of zeolite, prehnite, and serpentine in Nili Fossae further supports hydrothermal alteration or low-grade metamorphism early in Mars' history [*Ehlmann et al.*, 2009]. NIR spectroscopy of Hesperian-aged surfaces (~3.7-3 Ga) shows evidence for sulfates and opaline silica, suggesting alteration in acidic fluids and lower water-to-rock ratios than in the Noachian [*Bibring et al.*, 2005; 2006; *Milliken et al.*, 2008]. This is consistent with chemical and mineralogical data from Meridiani and Gusev that show evidence for S-enrichments and sulfate minerals [*Clark et al.*, 2005; *Ming et al.*, 2006; 2008; *Wang et al.*, 2006]. However, soils from the Phoenix lander have 3-5 wt.% $CaCO_3$, which may have precipitated from thin films of alkaline fluids in periods of high obliquity during the recent past [*Boynton et al.*, 2009].

TES models identify elevated abundances of high-silica phases at mid-to-high latitudes, suggesting regional chemical weathering processes have affected these surfaces; however, the nature of these high-silica phases and their abundances remain disputed. Low albedo Martian surfaces have been divided into two separate TES spectral types, Surface Type 1 (ST1) and Surface Type 2 (ST2) by *Bandfield et al.* [2000]. ST1 is located in older, low latitude surfaces, and models primarily identify feldspar and clinopyroxene, indicating these surfaces are unweathered basalt. ST2 is located in younger, mid-to-high latitude surfaces, and models identify greater amounts of high-silica phases and higher plagioclase-to-pyroxene ratios than ST1. The high-silica phases were originally identified as K-rich volcanic glass (i.e. obsidian), so ST2 was interpreted as unweathered andesite [*Bandfield et al.*, 2000]. Subsequent studies have suggested that the high-silica phases identified in ST2 models could be phyllosilicates, opaline silica, or poorly-crystalline aluminosilicates like allophane, formed by chemical weathering [*Bandfield*, 2002; *Wyatt and McSween*, 2002; *Kraft et al.*, 2003; *Wyatt et al.*, 2004; *Michalski et al.*, 2005]. The inference of poorly-crystalline aluminosilicates on the Martian surface is supported by the identification of allophane in Meridiani and Gusev

from mass balance models of APXS data [*Clark et al.*, 2005; *Ming et al.*, 2006]. Orbital chemistry from the Gamma Ray Spectrometer on Mars Odyssey shows increased levels of hydrogen at mid-to-high Martian latitudes, indicating these regions have buried surface H_2O ice [*Boynton et al.*, 2002]. The presence of water ice at these latitudes and morphological evidence for active permafrost processes [*Kreslavsky et al.*, 2008] suggests that weathering could have occurred in the recent past at low-temperatures and low water-to-rock ratios and caused the precipitation of poorly-crystalline aluminosilicates [*Wyatt et al.*, 2004; *Kraft*, 2009]. Further investigations of low-albedo, regional TES signatures show that there are 11 distinct surface types [*Rogers et al.*, 2007]. Models of each of these surface types identify significant high-silica phase abundances (>10 vol.%); however, models of Solis-type and Northern Acidalia-type spectra identify the most with >30 vol.% [*Rogers and Christensen*, 2007; *Minitti and Hamilton*, 2010]. The high-silica phases in Northern Acidalia were inferred to be secondary because of the availability of H_2O at mid-to-high latitudes, while the high-silica phases in Solis were inferred to be primary because Solis is at lower latitudes and H_2O would not be available [*Rogers and Christensen*, 2007]. Conversely, models of the TES spectral types from *Rogers et al.* [2007] with five additional mafic and intermediate glasses show that glasses are not identified and, thus, are likely not important regional phases [*Minitti and Hamilton*, 2010].

1.3 Importance of this Study

Previous studies have shown that chemical weathering adversely affects TIR spectral models, and the extensive orbital and in situ evidence for a variety of chemical weathering environments on the Martian surface show that it is critical that we understand how to interpret spectral models of weathered Martian surfaces. A series of unresolved issues remain that must be addressed to better understand chemical weathering environments on Mars:

1) The identity of the high-silica phases in TES spectral models is a topic of debate. These phases have been inferred to be poorly-crystalline aluminosilicates based on the position of TES absorption minima but the presence of poorly-crystalline aluminosilicates on Mars has yet to be tested by TES modeling.

2) NIR spectra identify phyllosilicates in Noachian terrains but TES models of the same surfaces rarely identify phyllosilicates over the detection limit (10 vol.%). It is important to reconcile the differences between NIR and TIR data to be able to estimate phyllosilicate abundances and their spatial extent to help us constrain the aqueous processes that formed them.

3) TIR models of terrestrial weathered basalts overestimate high-silica phases and falsely identify phyllosilicates. It is essential to understand how different silicate weathering products affect modeled high-silica phases to better interpret TIR spectral models of weathered Martian surfaces.

4) Surface chemistry and geochemical processes have been inferred from TES models. Model-derived chemistry differs significantly from chemistry measured with other techniques. It has been suggested that chemical weathering causes the differences between TES-derived and measured surface chemistry; however, the accuracy of TIR-derived chemistry from weathered basalts has not been evaluated.

The work presented here addresses these issues by:

1) Assessing the accuracy of chemistry derived from TIR spectral models of weathered basalts from Baynton, Australia, whose chemistry and chemical weathering trends have been studied previously.

2) Determining the detection limits of crystalline and amorphous secondary silicates in linear deconvolution models by modeling TIR spectra of physical mixtures of basaltic igneous minerals with known amounts of phyllosilicate and amorphous silica. Taking

these detection limits into account, TES data from clay-bearing surfaces in Mawrth Vallis are modeled to estimate clay mineral abundances.

3) Characterizing the effects of crystalline and amorphous secondary silicates on TIR modeled high-silica phases by modeling TIR spectra of physical mixtures of igneous minerals with known amounts of phyllosilicate and amorphous silica.

4) Testing for the presence of poorly-crystalline aluminosilicates on the Martian surface by adding allophane and aluminosilicate gel spectra to TES spectral libraries.

The Mars Science Laboratory (MSL) is scheduled to launch in fall 2011 and will visit a location that has evidence for phyllosilicates. The landing site has been narrowed down to four prospective sites. This research has important implications for assessing the alteration mineralogy of the potential landing sites and helping the Martian science community decide on a site that would meet the mission goal of assessing the habitability of a region that has a history of aqueous processes [*Mahaffy*, 2007].

This dissertation is organized into four body chapters, followed by a conclusions chapter. The first body chapter (Chapter 2) covers TIR spectral models of weathered terrestrial basalts from Baynton, Australia. TIR models are used to derive surface chemistry. The derived chemistry is compared to the measured surface chemistry to determine the accuracy of deriving chemical data from TIR spectral models of weathered surfaces. Chapter 3 reports on TIR spectral models of physical mixtures of igneous minerals with small to moderate amounts of clay or amorphous silica. This experiment was designed to determine the detection limits of crystalline and amorphous chemical weathering products and how they affect the identification of igneous minerals and high-silica phases. Chapter 4 describes the synthesis procedures for allophanes and aluminosilicate gels and their characterization by TIR emission spectroscopy, NIR reflectance spectroscopy, X-ray diffraction, atomic absorption spectroscopy, transmission FTIR spectroscopy, and transmission electron microscopy. In Chapter 5, the TIR

emission spectra of select allophanes and an aluminosilicate gel described in Chapter 4 are added to TES spectral libraries to test for the presence of poorly-crystalline aluminosilicates on the Martian surface using the regional TES spectra identified by *Rogers et al.* [2007], TES spectra from the four candidate landing sites for MSL, and Mini-TES spectra of chemically altered rocks from Gusev. Chapter 6 summarizes how this research has resolved issues regarding the interpretations of TIR spectral models of weathered surfaces and presents an updated view on chemical weathering processes on Mars.

2 Deriving Chemistry from Thermal-Infrared Spectra of Weathered Basalt: Implications for Remotely Determining Chemical Trends on Mars

2.1 Introduction

Interpretations of thermal-infrared (TIR) data from the Thermal Emission Spectrometer (TES) on Mars Global Surveyor, Mini-TES on the Mars Exploration Rovers, and the Thermal Emission Imaging System (THEMIS) on Mars Odyssey have been essential for understanding the composition of the Martian surface. Remote and in-situ spectral and chemical data indicate that the Martian surface is dominantly basalt [*Christensen et al.*, 2000a; *Bandfield et al.*, 2000; *Christensen et al.*, 2003; *Christensen et al.*, 2004a,b; *Rogers and Christensen*, 2007] and has been chemically weathered under a variety of aqueous conditions [*Christensen et al.*, 2004b; *Bibring et al.*, 2005,2006; *Ming et al.*, 2006; *Wang et al.*, 2006; *Mustard et al.*, 2008; *Ehlmann et al.*, 2009]. Chemically weathered basalts on Earth display a sequence of mineralogical and chemical changes or trends with increasing alteration that are specific to the weathering environment and the extent of alteration [*Eggleton et al.*, 1987; *Nesbitt and Wilson*, 1992]. Mineral abundances can be derived from TIR data with linear unmixing models using a library of end-member mineral spectra [*Ramsey and Christensen*, 1998]. Rock chemistry and classification of fresh igneous rocks can be accurately derived from TIR spectral models [*Hamilton and Christensen*, 2000; *Wyatt et al.*, 2001]; however, the effects of chemical weathering on TIR spectral model-derived chemistry are poorly constrained. Because the Martian surface is chemically altered to varying degrees, it is important to determine whether TIR spectral models of chemically weathered basalts can be used to accurately derive chemistries and chemical trends. If this technique is accurate, it could be used to better understand both modern and ancient chemical weathering environments on Mars and, thus, the record of aqueous processes over time.

In this chapter, TIR spectra and spectral models of weathered basalt samples from Baynton, Australia are presented. The bulk chemistry and chemical trends are derived from spectral models of interiors and weathered basalt surfaces. The modeled chemical trends are compared to those determined by X-ray fluorescence and by previous authors [*Eggleton et al.*, 1987; *Nesbitt and Wilson*, 1992]. Finally, the accuracy of deriving chemistry and chemical trends from TIR spectral models is assessed and implications for remotely interpreting chemical trends on Mars are discussed.

2.2 Background

2.2.1 Chemical Weathering on Mars

Chemical and mineralogical data measured at the various landing sites on Mars indicate that the surface has been altered by aqueous processes. The instrument suites on the Mars Exploration Rovers (MER) have identified sulfates and high levels of sulfur at Meridiani Planum and Gusev crater, indicating that sulfuric acid interacted with the rocks and sediments at these sites and that acid-sulfate weathering is an important aqueous process [*Squyres et al.*, 2004a; *Ming et al.*, 2006; *Wang et al.*, 2006]. The identification of hematite spherules and other diagenetic features in Meridiani by the MER instrument suite demonstrate a complex aqueous alteration history [*Squyres et al.*, 2004a]. Alpha Particle X-ray Spectrometer (APXS) analyses in Gusev crater display chemical trends that suggest aqueous alteration, including high Fe^{3+}/Fe_{total} ratios and increased S+Cl+Br abundances [*Ming et al.*, 2006]. Normative mineralogic models from APXS data suggest the precipitation of sulfates and poorly-crystalline aluminosilicates, like allophane, in select rocks [*Ming et al.*, 2006]. Mini-TES spectral models of the potential allophane-bearing rocks indicate the presence of a basaltic glass-like product [*Ruff et al.*, 2006], which has been also interpreted as a poorly-crystalline aluminosilicate [*Ming et al.*, 2006]. *Hurowitz et al.* [2007] and *Hurowitz and McLennan* [2007] analyzed chemical weathering environments on Mars by plotting chemical trends derived for rock and soil

samples from Chryse Planitia (Viking 1 landing site), Ares Vallis (Pathfinder landing site), Gusev, and Meridiani on the same ternary diagrams that were used by *Nesbitt and Wilson* [1992] to understand terrestrial weathering trends. The Martian trends are distinctly different from those described in terrestrial near-neutral weathering environments and only show variation in Fe and Mg concentrations, rather than depletion in alkalis. The trend seen in Martian data has been used to infer widespread acidic alteration under low water-to-rock ratios, resulting in selective dissolution of olivine [*Hurowitz and McLennan*, 2007; *Bandfield et al.*, 2010].

The positive identification of weathering products through near-infrared (NIR) spectroscopic observations of Mars indicate that chemical weathering is an influential surface process and that alteration conditions have changed through time. NIR data from the Observatoire pour la Minéralogie, l'Eau, les Glaces et l'Activité (OMEGA) and the Compact Reconnaissance Imaging Spectrometer for Mars (CRISM) indicate the presence of phyllosilicates and other hydrated silicates and carbonates in the most ancient terrains, suggesting that alteration under high water-to-rock ratios and near-neutral to alkaline pH occurred during the Noachian era [*Bibring et al.*, 2006; *Ehlmann et al.*, 2008; *Mustard et al.*, 2008; *Ehlmann et al.*, 2009]. There are many different secondary silicates in these terrains, including Fe/Mg-and Al-smectites, kaolinite, chlorite, illite and/or muscovite, zeolites, serpentine, and opaline silica, which indicate spatial and temporal variations in aqueous environments [*Bibring et al.*, 2005; *Poulet et al.*, 2005; *Bishop et al.*, 2008; *Ehlmann et al.*, 2008; *Mustard et al.*, 2008; *Ehlmann et al.*, 2009]. Orbital NIR data show the presence of widespread sulfate minerals in Hesperian surfaces and localized opaline silica deposits, suggesting these surfaces were altered under acidic conditions with lower water-to-rock ratios [*Bibring et al.*, 2005; *Gendrin et al.*, 2005; *Bibring et al.*, 2006; *Milliken et al.*, 2008].

Spectral models of TES data are indicative of limited chemical weathering of the Martian surface, but the types of weathering products on the surface are a topic of debate. TES models identify significant abundances of high-silica phases (phyllosilicates, zeolites, volcanic glass, and opal) in most Martian regions [*Rogers and Christensen*, 2007]. However, silicate weathering products and volcanic glasses are spectrally similar in the TIR and may substitute for one another in spectral models [*Wyatt and McSween*, 2002; *Michalski et al.*, 2006; *Kraft*, 2009], making it difficult to identify secondary silicates with certainty. Additionally, current spectral libraries lack poorly-crystalline alteration products that are common in terrestrial environments [*Colman*, 1982; *Wada*, 1989], and these products may be mistakenly modeled as crystalline secondary silicates [*Hamilton et al.*, 2008]. TES spectral models of mid- and high-latitude low-albedo (i.e. non-dusty) surfaces suggest widespread precipitation of silicate alteration products, which may include phyllosilicates or poorly-crystalline silicates like allophane or opaline silica [*Wyatt and McSween*, 2002; *Kraft et al.*, 2003; *Wyatt et al.*, 2004; *Michalski et al.*, 2005; *Kraft*, 2009]. Modeling the mineralogy of weathered surfaces can be problematic because chemical weathering and the precipitation of secondary phases in a coating geometry results in non-linear mixing of spectral components [*Rampe et al.*, 2007; *Kraft*, 2009]. It is important to determine if and how accurately rock chemistry can be derived from TIR spectral models of weathered surfaces to assess this technique for characterizing the surface chemistry of Mars.

2.2.2 Chemical Trends with Weathering

Geochemical and mineralogical trends with chemical alteration of terrestrial basalt at near-neutral pH have been studied in detail. In general, these studies show that the sequence of weathering of basaltic components is glass ~ olivine > plagioclase > pyroxene > oxides [*Colman*, 1981; *Colman*, 1982; *Eggleton et al.*, 1987; *Nesbitt and Wilson*, 1992; *Moore*, 1996]. As aqueous alteration proceeds, the chemical variations

include early removal of alkali and alkaline earth elements, progressive removal of silica, and oxidation of iron from Fe^{2+} to Fe^{3+}. These chemical trends are similar for different localities and are traditionally displayed on ternary diagrams with combinations of Al_2O_3, CaO, Na_2O, K_2O, total FeO, and MgO as components. Variations in chemistry can be used to define chemical trends caused by aqueous alteration.

The order of element mobility varies slightly between different weathering regimes. For early stages of weathering (i.e. in weathering rinds), the order has been calculated as Ca $\geq$ Na > Mg > Si > Al $\geq$ K > Fe > Ti [*Colman*, 1982]. For more advanced stages of weathering (i.e. profiles from basalt weathered to saprolite), the order has been calculated as Ca > Na > Mg > K = Mn > Si > Fe = Ti > Al [*Eggleton et al.*, 1987]. The variation in relative mobility of Si, Al, and Fe are a result of the types of secondary phases that precipitate in different environments. Mature soil profiles contain Al- and Fe-oxides and oxyhydroxides, while weathering rinds are dominated by poorly-crystalline aluminosilicates, such as allophane, and Fe-oxides and oxyhydroxides [*Colman*, 1982]. It is important to note that crystalline clay minerals are generally not present in weathering rinds [*Colman*, 1982; *Michalski et al.*, 2006], and the mineralogy of weathering rinds is difficult to determine because of the poorly-crystalline nature of the weathering products and the volumetrically small amounts of weathering products in the rind. The mineralogical compositions of basalt weathering rinds have been well characterized by *Colman* [1982] and a similar quantitative characterization of Baynton basalt weathering rinds is beyond the scope of this chapter.

2.2.3 Deriving Mineralogy and Chemistry from TIR Spectra

Linear deconvolution is the primary method by which mineralogical composition is interpreted from a TIR spectrum of a mineral mixture, such as a rock. This method uses a linear least squares algorithm and a library of mineral spectra to fit a TIR spectrum and model the mineral abundances present in a surface. This technique assumes that the

energy emitted from a surface is a linear combination of the energy emitted from each phase at the surface, proportional to the areal abundances of those phases [*Ramsey and Christensen*, 1998]. Linear mixing is a good assumption for relatively coarse-grained fresh rock surfaces in the TIR wavelength region (~5-50 microns) because minerals have high absorption coefficients in this spectral range and photons only interact with one mineral [*Thomson and Salisbury*, 1993; *Ramsey and Christensen*, 1998]. Linear deconvolution returns accurate mineral abundances with a 5-10 vol.% error for fresh igneous and metamorphic rock surfaces and particulate mineral mixtures with grain sizes >60 μm [*Ramsey and Christensen*, 1998; *Feely and Christensen*, 1999; *Hamilton and Christensen*, 2000; *Wyatt et al.*, 2001]. Furthermore, TIR spectral models of fresh igneous surfaces have been used to accurately derive rock chemistry and IUGS rock classifications for terrestrial samples [*Wyatt et al.*, 2001]. Rock chemistry can be derived from TIR models by first converting the vol.% mineral abundances to wt.% by multiplying the vol.% abundances by the specific gravity of each mineral and normalizing to 100%. Then, wt.% mineral abundances are multiplied by the wt.% oxides of each end member and added together to determine surface chemistry [*Rogers and Aharonson*, 2008].

Rock chemistry derived from TES models of Martian low-albedo surfaces has been used to infer rock types and to identify chemical trends [*McSween et al.*, 2003; *Hurowitz et al.*, 2007]. Low-albedo surfaces are examined because they are less dusty and, thus, TIR spectra of these surfaces have less particle scattering so that linear deconvolution models are more accurate. Early interpretations of chemistry derived from TES models showed mid-to-high-latitude surfaces are enriched in SiO_2 and alkalis. This implies that either these rocks were formed by hydrous melting of the Martian mantle or that the excess silica was a product of chemical weathering [*McSween et al.*, 2003]. *McSween et al.* [2009] compared orbital chemistry derived from TES models to orbital

chemistry measured by the Gamma Ray Spectrometer (GRS) and in-situ measurements from the MER and Pathfinder landing sites. They found that silica-rich rocks on Mars, produced by partial melting and/or fractional crystallization, are uncommon or absent and concluded that chemical weathering inhibits the ability to derive accurate chemistry and interpret petrology from TES models. However, the specific reasons why weathering causes differences between TES-derived chemistry and chemistry measured by other datasets have not been addressed.

The purpose of this investigation is to determine the accuracy of TIR-derived chemical abundances for weathered basaltic rocks. This study addresses the following questions: 1) How does the precipitation of poorly-crystalline phases in weathering rinds affect model-derived chemistry and model-derived chemical trends? 2) How does spectral library composition affect the model-derived chemistry and chemical weathering trends? 3) How does chemical weathering specifically affect the interpretation of the petrologic classification from TIR model-derived chemistry? 4) Can we use TIR model-derived chemistry to determine chemical trends and, thus, better understand aqueous alteration environments on Mars?

2.3 Methods

2.3.1 Baynton Basalt Collection and Sample Preparation

Basalt samples were collected in September 2006 in four different exposures near the town of Baynton, Australia, located 85 km northwest of Melbourne. Weathered basalt corestones were removed from soil (Figure 2.1), and excess soil loosely attached to surfaces was removed with compressed air. Mineralogy, chemistry, and provenance of the Baynton basalt are described in detail by *Eggleton et al.* [1987] and *Nesbitt and Wilson* [1992]. The basalt is tholeiitic, comprised of olivine, clinopyroxene,

Figure 2.1. Baynton basalt sample, in place. Samples were removed from soil.

orthopyroxene, plagioclase, and glass and is late Tertiary in age. The samples have experienced relatively different degrees of weathering, based on the color and thickness of the weathering rinds.

Seven hand samples were prepared for TIR spectroscopy. Samples were cut with a rock saw perpendicular to their weathered surfaces. TIR spectra of the interior surface and one to three weathered surfaces for each sample were measured (Table 2.1). Polished thin sections were prepared for petrography and electron microprobe analyses. Bulk material from six sample interiors and weathered material from one surface of each of these samples were powdered to analyze their mineralogy and chemistry by X-ray diffraction (XRD) and X-ray fluorescence (XRF), respectively (Table 2.1). Weathered material was collected by scraping the upper few millimeters of the weathered surface.

2.3.2 Instrumentation

XRD was performed on a Panalytical X-Pert Pro with Cu-Kα radiation at the LeRoy Eyring Center for Solid State Sciences at ASU. Patterns were collected from 5-65° 2θ in 0.05° steps. The X-Pert High Score Plus program was used to identify minerals present in the XRD patterns. Bulk powders of surfaces and interiors were sent to Washington University for XRF major-element rock analyses. The methods of these analyses are detailed by *Couture* [1989, 1993].

Plane-polarized and cross-polarized transmitted light and reflected light petrography was performed with a Leica DMRX petrographic microscope at the Lunar and Planetary Institute. Spot analyses, line scans, and element maps were performed on a Cameca SX100 electron microprobe at NASA Johnson Space Center, using a 40 nA incident beam current and 15 kV accelerating potential. Analyses used calibration standards of olivine (for Fe), diopside (for Si, Ca, Mg), feldspar (orthoclase for K, oligoclase for Na and Al), rutile (for Ti), rhodonite (for Mn), and apatite (for P).

Table 2.1. Experimental analyses performed on each sample.

Sample	TIR	XRF	XRD	EMP	Petrography
01-A-int[a]	X	X	X		X
01-A-S1[b]	X				
01-A-S2	X	X	X		
01-B-int	X	X	X		X
01-B-S1	X				
01-B-S2	X				
01-B-S3	X	X	X		
01-C-int	X	X	X		X
01-C-S1	X	X	X		
01-C-S2	X				
02-A-1-int	X	X	X		X
02-A-1-S1	X	X	X		
02-A-1-S2	X				
02-B-int	X	X	X		
02-B-S1	X	X	X		
02-B-S2	X				
03-A-2-int	X	X	X		X
03-A-2-S1	X				
03-A-2-S2	X	X	X		
04-B-3-int	X			X	X
04-B-3-S1	X				
04-B-3-S2	X				

[a] "Int" denotes interior

[b] "S" denotes surfaces

TIR spectra of weathered surfaces and interiors were collected at the Mars Space Flight Facility at Arizona State University (ASU), using a Nicolet Nexus 670 spectrometer configured to measure emitted energy [*Christensen and Harrison*, 1993; *Ruff et al.*, 1997]. Samples were heated to 80 °C to increase the signal-to-noise ratio. Spectra were collected 140 times over the course of ~3 minutes, from 200-2000 cm^{-1} with 2 cm^{-1} spectral resolution. We measured 70 °C and 100 °C blackbodies to calibrate raw data to radiance [*Christensen and Harrison*, 1993]. Radiance spectra were transformed to emissivity spectra by normalizing to the Planck curve corresponding to the derived sample temperature [*Ruff et al.*, 1997].

2.3.3 Linear Deconvolution and Derived Chemistry

Two libraries of mineral TIR emissivity spectra were assembled for use in modeling Baynton TIR spectra. Library 1 contained spectra of minerals found in the Baynton basalt and the Baynton soil profile by previous studies [*Eggleton et al.*, 1987; *Nesbitt and Wilson*, 1992], including plagioclase solid solutions, orthopyroxenes, clinopyroxenes, olivine, phyllosilicates, volcanic glass, and accessory minerals (Table 2.2). Library 2 was the same spectral library used by *Rogers and Christensen* [2007] to model TES spectra but lacked the Martian surface dust end member (Table 2.2). The main differences between Library 1 and 2 were that Library 1 had more clay minerals, including kaolinite, halloysite, and nontronite, and that Library 2 contained shocked plagioclase, pigeonite, opal, amphibole, and zeolite end members, all of which were not in Library 1.

Linear deconvolution modeling of TIR Baynton emissivity spectra was performed using both spectral libraries following the methods of [*Ramsey and Christensen*, 1998]. Models included a blackbody spectrum correction to account for differences in spectral contrast between the library and basalt spectra. Modeled phase abundances were renormalized after excluding the blackbody end member. Linear

Table 2.2.TIR spectral library

Mineral Group	Spectral End-Member	Composition and Source for Oxide Abundances
Quartz	Quartz BUR-4120*†	SiO_2 [a]
Feldspar	Albite WAR-0244*†	$(K_{0.04}Na_{0.87}Ca_{0.02})(Al_{0.95}Si_{3.05})O_8$ [a]
	Andesine BUR-240*†	$(K_{0.01}Na_{0.53}Ca_{0.48})(Al_{1.53}Si_{2.48})O_8$ [a]
	Anorthite BUR-340†	$(Na_{0.08}Ca_{0.89})(Fe_{0.02}Mg_{0.03})(Al_{1.98}Si_{2.03})O_8$ [a]
	Bytownite WAR-1384*†	$K_{0.02}(Na_{0.32}Ca_{0.57})(Fe_{0.01}Mg_{0.03})(Al_{1.63}Si_{2.30})O_8$ [a]
	Labradorite WAR-4524*†	$K_{0.01}(Na_{0.53}Ca_{0.49})(Al_{1.58}Si_{2.44})O_8$ [a]
	Microcline BUR-3460*†	$(K_{0.72}Na_{0.25})(Al_{1.06}Si_{2.96})O_8$ [b]
	Oligoclase WAR-5804*†	$(K_{0.03}Na_{0.78}Ca_{0.23})(Al_{1.26}Si_{2.75})O_8$ [a]
	Orthoclase WAR-RGSAN01†	$(K_{0.65}Na_{0.18}Ca_{0.03}Fe_{0.15})(Al_{1.07}Si_3)O_8$ [d]
	Shocked An 22.6 GPa†	90% An75, 10% pyroxene [h]
	Shocked An 56.3 GPa†	90% An75, 10% pyroxene [h]
Orthopyroxene	Bronzite BUR-1920†	$(Ca_{0.03}Mg_{1.51}Fe_{0.42})(Al_{0.02}Si_{1.98})O_6$ [a]
	Bronzite NMNH-93527†	$(Ca_{0.06}Mg_{1.43}Fe^{2+}_{0.36}Fe^{3+}_{0.05}Al_{0.08})(Al_{0.14}Si_{1.86})O_6$ [a]
	Enstatite HS-9.4B*†	$(Ca_{0.02}Mg_{1.77}Fe_{0.20})Si_2O_6$ [a]
Clinopyroxene	Augite HS-119.4B*	$(Ca,Mg,Fe^{2+},Fe^{3+},Ti,Al)_2(Si,Al)_2O_6$ [d]
	Augite NMNH-119197*†	$(Ca,Mg,Fe^{2+},Fe^{3+},Ti,Al)_2(Si,Al)_2O_6$ [d]
	Augite NMNH-9780†	$(Ca,Mg,Fe^{2+},Fe^{3+},Ti,Al)_2(Si,Al)_2O_6$ [d]
	Augite NMNH-122302†	$(Ca,Mg,Fe^{2+},Fe^{3+},Ti,Al)_2(Si,Al)_2O_6$ [d]
	Diopside WAR-6474*†	$(Ca_{0.86}Mg_{0.56}Fe^{2+}_{0.20}Fe^{3+}_{0.20}Na_{0.15}Al_{0.02})(Al_{0.08}Si_{1.92})O_6$ [a]
	Hedenbergite (Manganoan) HS-10.4B*	$(Ca_{0.95}Mg_{0.16}Fe^{2+}_{0.61}Fe^{3+}_{0.09}Mn_{0.15}Na_{0.03}Al_{0.03})Si_{1.99}O_6$ [a]
	Hedenbergite (Manganoan) DSM-HED01†	$(Ca_{0.98}Mg_{0.26}Fe_{0.47}Mn_{0.27})Si_2O_6$ [a]
	Pigeonite†	$(Ca_{0.2}Mg_{0.72}Fe_{1.08})Si_2O_6$ [g]
	Hypersthene NMNH-B18247*	$(Ca_{0.09}Mg_{1.22}Fe^{2+}_{0.56}Fe^{3+}_{0.03}Al_{0.05})(Al_{0.11}Si_{1.89})O_6$ [b]
Olivine	Fayalite WAR-FAY01*†	Fo1.2 [e]
	Forsterite BUR-3720A*†	Fo91 [e]
	KI3115 Fo68*†	Fo68 [e]
	KI3362 Fo60*†	Fo60.4 [e]
	KI3373 Fo35*†	Fo34.9 [e]
	KI3008 Fo10*†	Fo9.7 [e]
Zeolite	Crystalline heulandite†	$(Ca,Na)_{2\text{-}3}Al_3(Al,Si)_2Si_{13}O_{36}\cdot 12(H_2O)$ [c]
	Crystalline stilbite†	$NaMgCa_4[Al_8Si_{28}O_{72}]\cdot 28\text{-}32(H_2O)$ [c]
Sheet silicates	Antigorite NMNH-47108†	$Mg_3SiO_5(OH)_4$ [c]
	Biotite BUR-840*†	$Fe3+_{1.75}Mg_{3.25}Fe_{2.32}Al_{2.07}Ti_{0.51}Si_{6.09}(OH,F)_{0.72}$ [d]
	Chlorite WAR-1924*	$(Mg,Fe^{2+},Fe^{3+},Mn,Al)_{12}[(Si,Al)_8O_{20}](OH)_{16}$ [a]
	Halloysite WAR-5102*	$Al_4Si_4O_{10}(OH)_8$ [c]
	Illite IMt-2*	$(K_{1.35},Na_{0.02})Al_{3.41}[Si_{7.26}(Fe_{0.67},Mg_{0.55})O_{20}](OH)_4$ [d]

	Illite IMt-1 <0.2 microns†	$(K_{1.35},Na_{0.02})Al_{3.41}[Si_{7.26}(Fe_{0.67},Mg_{0.55})O_{20}](OH)_4$ [a]
	Kaolinite KGa-1b*	$Al_4Si_{3.9}O_{10}(OH)_8$ [d]
	Montmorillonite (Ca) STx-1*	$(Ca_{0.1},Na_{0.03})(Al_{1.13}Mg_{0.33})Si_{4.18}O_{10}(OH)_2$ [d]
	Ca-montmorillonite STx-1 <0.2 microns†	$(Ca_{0.1},Na_{0.03})(Al_{1.13}Mg_{0.33})Si_{4.18}O_{10}(OH)_2$ [a]
	Muscovite WAR-5474*†	$K_2Al_4[Si_6Al_2O_{20}](OH,F)_4$ [a]
	Nontronite WAR-5108*	$(Al_{0.15}Fe_{1.84}Mg_{0.02})(Al_{0.51}Si_{3.49})O_{10}(OH)_2$ [i]
	Saponite (Saponite)*	$(Li_{0.09}Mg_{2.72}Fe^{3+}_{0.03}Al_{0.07})(Al_{0.04}Si_{3.96})O_{10}(OH)_2$ [j]
	Saponite <0.2 microns†	$(Li_{0.09}Mg_{2.72}Fe^{3+}_{0.03}Al_{0.07})(Al_{0.04}Si_{3.96})O_{10}(OH)_2$ [j]
	Serpentine HS-8.4B*†	$Mg_{2.36}[Si_{1.72}O_5](OH)_4$ [a]
Am. Silica	Al-opal†	78.7 wt.% SiO_2, 8.2% Al_2O_3, 1.5 wt.% FeO [f]
	K-rich glass*†	77.9 wt% SiO_2, 5.67 wt% K_2O [g]
	Opal-A (02-011)†	$SiO_2 \bullet nH_2O$ [c]
	SiO_2 Glass†	SiO_2 [g]
Amphibole	Magnesiohastingsite HS-115.4B†	$(Na_{0.45}K_{0.15})(Ca_{1.85}Na_{0.15})(Mg_{3.60}Fe_{0.84}Al_{0.13}Ti_{0.03})(Al_{1.71}Si_{6.29})O_{22}(OH)_2$ [a]
	Actinolite HS-116.4B†	$(Ca_{1.82}Na_{0.13})(Mg_{4.39}Fe_{0.55})(Si_{7.60}Al_{0.04})O_{22}(OH)_2$ [a]
.	Magnesiohornblende WAR-0354†	$(Ca_{1.71}Na_{0.09})(Mg_{4.20}Fe_{0.64})(Si_{7.31}Al_{0.21})O_{22}(OH)_2$ [a]
Sulfates	Anhydrite S9*†	$CaSO_4$ [c]
	Gypsum (Satin spar) S8*	$CaSO_4 \bullet 2H_2O$ [c]
	Gypsum ML-S6†	$CaSO_4 \bullet 2H_2O$ [c]
	Kieserite C5492-1*	$MgSO_4 \bullet H_2O$ [c]
Carbonates	Calcite C2*	$CaCO_3$ [a]
	Calcite C40†	$CaCO_3$ [a]
	Dolomite C20*†	$Ca_{104}Mg_{96}(CO_3)_2$ [a]
Fe-oxide	Hematite BUR-2600 50*†	Fe_2O_3 [c]
Blackbody	Blackbody*†	

* End members in Library 1

† End members in Library 2

[a] Oxide compositions from microprobe data from *Christensen et al.* [2000b]

[b] Oxide compositions from bulk XRF data from *Christensen et al.* [2000b]

[c] Oxide compositions estimated from stoichiometric compositions in *Nesse* [2000]

[d] Oxide compositions from microprobe from *Hamilton and Christensen* [2000]

[e] Oxide compositions from *Koeppen and Hamilton* [2008]

[f] Oxide compositions from *Gallup* [1997]

[g] Oxide compositions from *Wyatt et al.* [2001]

[h] Oxide compositions from *Haskin and Salpas* [1992]

[i] Oxide composition of sample NAu-1 *Michalski et al.* [2005]

[j] Oxide compositions from *Michalski et al.* [2005]

deconvolution was performed over the wavelength range 305-1360 cm^{-1}. Modeled abundances were converted from volume percent (vol.%) to weight percent (wt. %) using the specific gravities of the mineral end members listed in *Nesse* [2000]. The median specific gravity was used when a range was provided for an end member. Modeled mineral abundances were converted to chemical composition using oxide abundances for end members reported in the TES spectral library (Table 2.2) [*Christensen et al.*, 2000b]. Generalized chemical formulae from *Nesse* [2000] were used to derive chemical compositions of the two zeolites, halloysite, oxides, carbonates, and sulfates because oxide abundances were not reported in the TES spectral library. Chemical compositions of zeolites can be Ca-, Na-, and K-rich. We used the Ca-rich end members in our calculations because we plot the combined $CaO+Na_2O+K_2O$ values, so differentiating between the chemical end members will not affect these values. Furthermore, the abundances of CaO, Na_2O, and K_2O in zeolites are on the order of a few wt.%, so the identification of 10 wt.% Na-stilbite vs. Ca-stilbite in a model would have a small effect on model-derived alkali abundances. We calculated chemical compositions according to the methods of *Wyatt et al.* [2001]. Iron abundances are reported in terms of total iron (FeO_T), a combination of FeO and Fe_2O_3.

2.4 Results

2.4.1 Measured Mineralogy and Chemistry of Baynton Basalts

Qualitative mineralogic analyses of interiors and weathered surfaces show that our samples are similar to those studied by *Eggleton et al.* [1987] and *Nesbitt and Wilson* [1992]. XRD analyses of bulk interior materials identify primarily plagioclase feldspars and clinopyroxenes. XRD patterns of interior material show evidence for lesser amounts of olivine, ilmentite, magnetite, zeolite (analcime), and a 10 Å phase that could be a zeolite or phyllosilicate, such as illite, indicating the interiors have been altered. XRD patterns of powder scraped from weathered surfaces have low count rates and high

backgrounds, suggesting that most of the material that makes up the weathering rinds is amorphous or poorly-crystalline, as was reported for weathering rinds of basalts and andesites from the Pacific Northwest [*Colman*, 1982]. Some crystalline material is present in the weathering rinds, and most peaks in XRD patterns correspond to plagioclase feldspars and clinopyroxenes. Small, broad peaks near 7 Å and 10 Å suggest the presence of minor amounts of secondary silicates, such as kaolinite and illite, respectively, which could be from residual soil on the surfaces. The breadth of these peaks suggests these materials could be poorly-crystalline.

Electron microprobe analyses indicate that the pyroxenes range from augite to diopside in composition ($En_{42}Fs_{18}Wo_{40}$ to $En_{40}Fs_{10}Wo_{50}$) and plagioclase compositions range from oligoclase to labradorite (An_{28} to An_{60}). Olivine crystals are chemically zoned from Fo_{82} cores to Fo_{43} rims. Electron microprobe analyses indicate minor amounts of ilmenite, magnetite, K- and Na-rich volcanic glass with an andesitic composition, and apatite. Backscattered electron (BSE) imagery and optical petrography from all samples show olivine phenocrysts are altered, as exemplified by brown alteration products and pitted interiors (Figure 2.2).

XRF analyses of interiors and weathered surfaces of our samples generally show a decrease in relative SiO_2, CaO, Na_2O, and MgO abundances with chemical weathering and an increase in relative Al_2O_3 and FeO_T abundances (Table 2.3). These chemical weathering trends are displayed on an Al_2O_3-(Na_2O+K_2O+CaO)-(MgO+FeO_T) ternary diagram and compared to bulk weathering trends determined by *Nesbitt and Wilson* [1992] (Figure 2.3). Weathering trends and oxide abundances for interiors and weathered surfaces are similar to those reported by *Nesbitt and Wilson* [1992], although *Nesbitt and Wilson* [1992] report a greater relative enrichment in Al_2O_3 and we observe a greater relative enrichment in FeO_T. These relative chemical differences reflect differences in

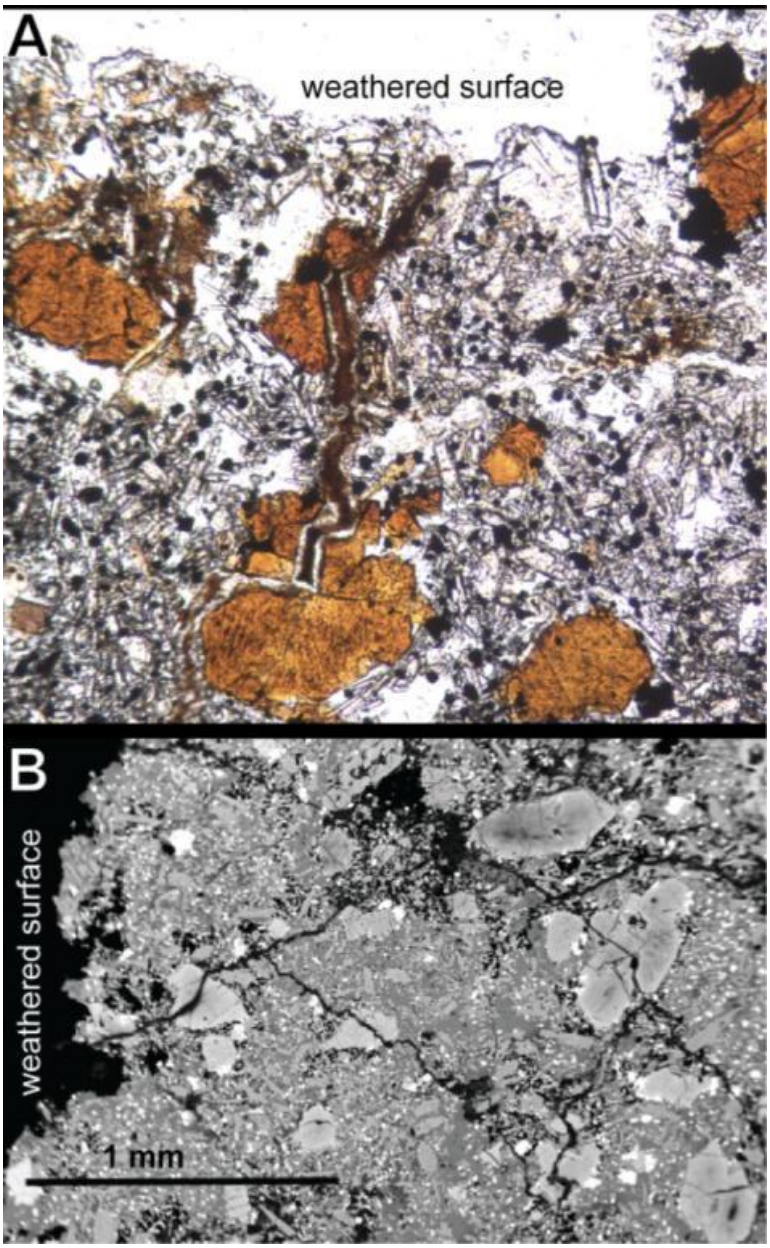

Figure 2.2. A) Petrographic image of sample BAY-06-02-C1 in plane light (50 x magnification). Olivine phenocrysts are weathered throughout and are brown in color. B) Backscattered electron image of a cross-section through a weathered surface of sample 02C1, showing pervasive fractures near the surface and relatively unaltered phenocrysts. Note that the minerals closest to the weathered surface are primary to the rock and are the same as the minerals in the rock interior.

the methods used to sample materials for XRF analyses. *Nesbitt and Wilson* [1992] collected samples from the interiors of 1-2 kg corestones and sampled outward through degraded rock layers and soil up to a few meters from the corestones to examine the bulk weathering trend. Weathering products in the soil are very different from the weathering products in our weathering rinds because materials in the soils have been weathered for longer amounts of time and may experience different weathering conditions than weathering rinds [*Colman*, 1982]. Thus, soils are enriched in crystalline clay minerals, causing weathering trends to display greater enrichments in Al_2O_3. Weathering rinds are dominated by Fe-oxides and small amounts of poorly-crystalline aluminosilicates, leading to greater enrichments in FeO_T.

Relative element mobilities in the Baynton weathering environment were calculated from XRF data by assuming that a reference constituent remains constant with weathering [*Colman*, 1982]. TiO_2 was assumed constant between the interiors and weathered surfaces. This is generally a good assumption because TiO_2 is immobile except at pH < 2.5 and most of the Ti is present in Fe-oxides, which are stable in weathering rinds [*Colman*, 1982]. TiO_2 abundances in XRF data appear higher in weathered surfaces than fresh surfaces because other elemental oxides are lost so that the relative abundance of TiO_2 increases. The wt.% abundance of each elemental oxide is multiplied by the ratio of wt.% TiO_2 in the interior to wt.% TiO_2 in the weathered surface. The relative element mobility in these samples is Na $\geq$ Ca > K > Mg > Si > Mn > Al > Ti > Fe. This is consistent with other weathering rinds [*Colman*, 1982], except Baynton samples show greater K mobility. It is difficult to assess K mobility in weathered basalts because it is only present in small amounts in glass in the interiors [*Colman*, 1982].

Table 2.3. Measured chemistry from XRF, H_2O-free, wt.%

	01-A-int	01-B-int	01-C-int	02-A-1-int	02-B-int	03-A-2-int
SiO_2	52.9	53.6	53.7	46.6	46.3	52.1
Al_2O_3	15.7	15.1	15.0	12.1	11.8	16.4
FeO_T	10.8	10.7	10.6	12.5	12.4	10.1
MgO	6.6	6.9	6.9	8.0	8.6	3.2
CaO	7.9	7.5	7.5	11.2	11.0	7.4
Na_2O	3.0	2.9	3.0	3.5	3.6	3.8
MnO	0.1	0.1	0.1	0.2	0.2	0.1
K_2O	0.7	0.8	0.8	1.3	1.3	2.4
TiO_2	2.0	2.0	1.9	3.7	3.6	3.2
P_2O_5	0.3	0.3	0.3	1.0	1.0	1.2
LOI, unnormalized	0.9	1.0	0.8	1.7	1.4	0.6
	01-A-S2	01-B-S3	01-C-S1	02-A-1-S1	02-B-S1	03-A-2-S2
SiO_2	40.9	40.8	51.4	54.9	43.4	49.8
Al_2O_3	21.0	17.1	19.4	14.6	17.3	17.1
FeO_T	23.5	34.2	12.3	10.2	18.0	15.1
MgO	3.9	2.5	5.8	6.2	5.1	2.9
CaO	4.5	1.6	5.9	7.5	7.2	4.6
Na_2O	1.6	0.8	1.9	3.1	1.2	2.8
MnO	0.1	0.2	0.1	0.1	0.3	1.4
K_2O	0.3	0.2	0.4	1.0	1.5	2.2
TiO_2	3.7	2.2	2.4	1.9	4.9	3.0
P_2O_5	0.4	0.3	0.3	0.3	1.1	1.2
LOI, unnormalized	13.4	11.0	5.9	0.5	8.2	4.1

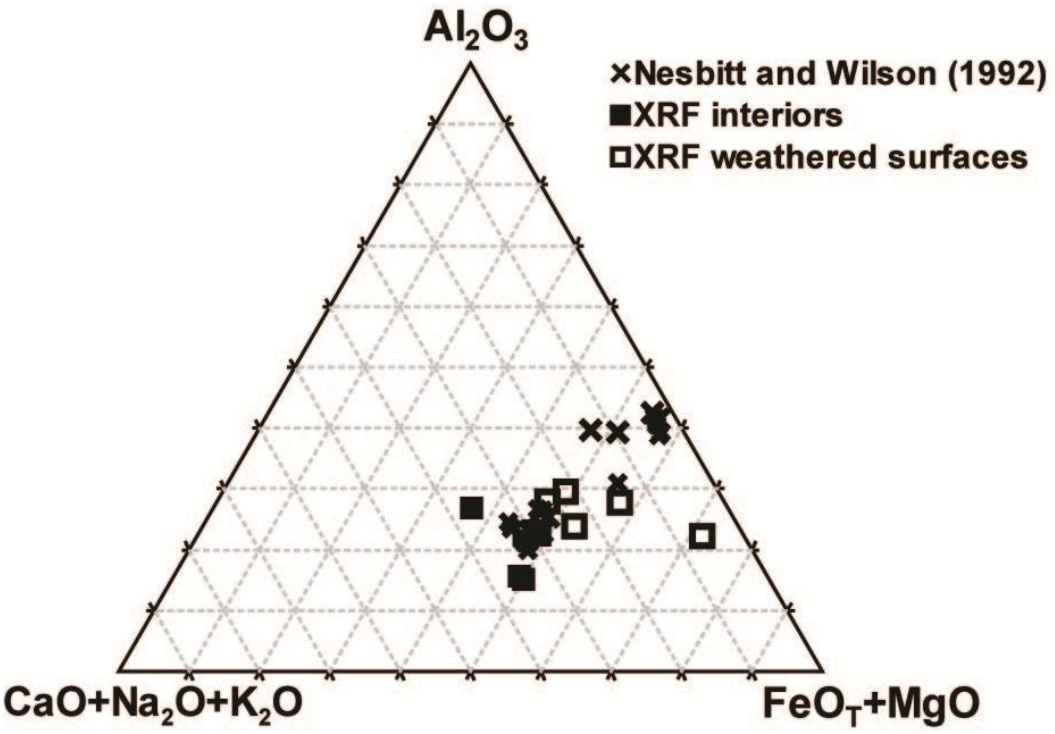

Figure 2.3. Ternary diagram of mol.% values from XRF results in this study (square symbols, where black squares are interiors and open squares are weathered surfaces) and from *Nesbitt and Wilson* [1992] (X symbols). Both data show a loss of alkalis with increased weathering, but data from this study show a greater relative enrichment in $FeO_{T+}MgO$ with increased weathering, while data from Nesbitt and Wilson [1992] show a greater relative enrichment in Al_2O_3 with increased weathering. This difference is from sampling techniques, where we sampled weathering rinds and *Nesbitt and Wilson* [1992] sampled through the soil. Soils are dominated by crystalline clay minerals, causing a greater relative increase in Al_2O_3. FeO_T = total Fe.

2.4.2 TIR Emission Spectra of Basalt Interiors and Weathered Surfaces

TIR emission spectra of the Baynton basalt interiors are typical of basalts and show overlapping absorptions in four main regions: 1) 1250-800 cm^{-1} (broad, U-shaped), 2) 500-400 cm^{-1}, 3) 650-500 cm^{-1}, and 4) 400-300 (Figure 2.4). These absorptions correspond to 1) Si(Al)-O stretching bond vibrations, 2) Si(Al)-O bending vibrations, 3) Si(Al)-O deformation bond vibrations, and 4) octahedrally coordinated metal cation-oxygen (M^{VI}-O) vibrations [*Michalski et al.*, 2006]. TIR emission spectra of weathered basalt surfaces show absorptions in three main regions: 1) 1250-1000 cm^{-1} (sharp, V-shaped), 2) 500-400 cm^{-1}, and 3) 650-500 cm^{-1} from the same types of bond vibrations as listed for basalt interiors (Figure 2.4). The Si(Al)-O stretching absorption has an emissivity minimum at slightly shorter wavelengths than the interior spectrum (~9.5 microns vs. 10 microns, respectively), indicating a greater abundance of SiO_2-rich phases in weathered surfaces [*Michalski et al.*, 2006].

2.4.3 Spectral Models of Basalt Interiors and Weathered Surfaces

Spectral models of basalt interiors using either library generally identify significant amounts (>10 vol.%) of basaltic igneous phases and minor amounts (<10 vol.%) of alteration products. Spectral models using Library 1 identify significant amounts of plagioclase (mostly bytownite and/or oligoclase), olivine, pyroxene (augite, bronzite, and enstatite), K-rich volcanic glass, smectite (montmorillonite and nontronite), and minor amounts of hematite, illite, kaolinite, K-feldspar (microcline), and carbonate (dolomite) (Figure 2.5). Spectral models using Library 2 identify significant amounts of pyroxene (mostly diopside), plagioclase (mostly bytownite and oligoclase), olivine, hematite, and zeolite (mostly stilbite), and identify minor amounts of K-feldspar, phyllosilicates (illite and smectite), carbonate (dolomite), sulfate (anhydrite), and

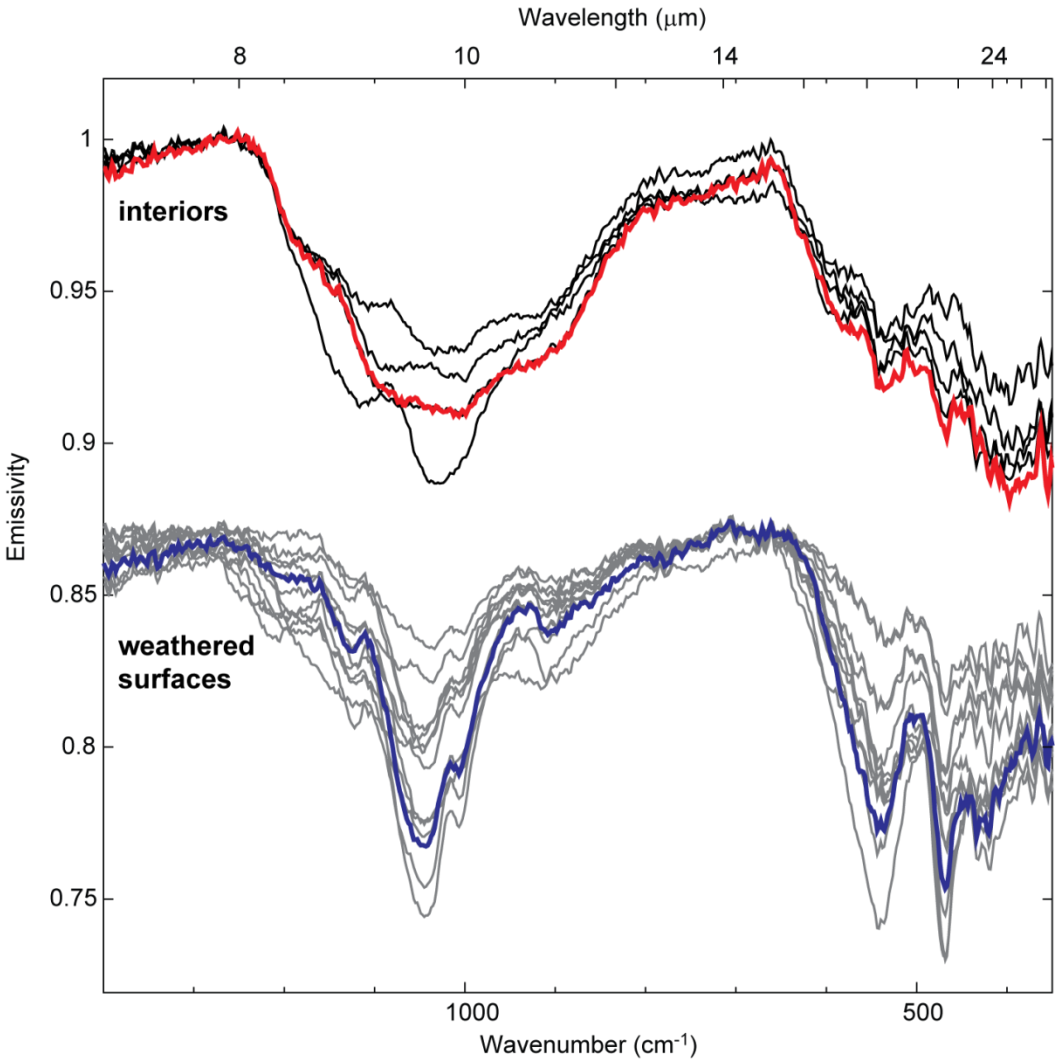

Figure 2.4. TIR emission spectra of all interiors and weathered surfaces of Baynton samples. Samples with characteristic interior and weathered surface spectral shapes are highlighted in red and blue, respectively. Note the sharp, V-shaped absorption in the weathered surface has a minimum at shorter wavelengths than the interior (1050 vs. 1000 cm^{-1}, respectively), indicating the presence of SiO_2-rich phases in the weathered surface.

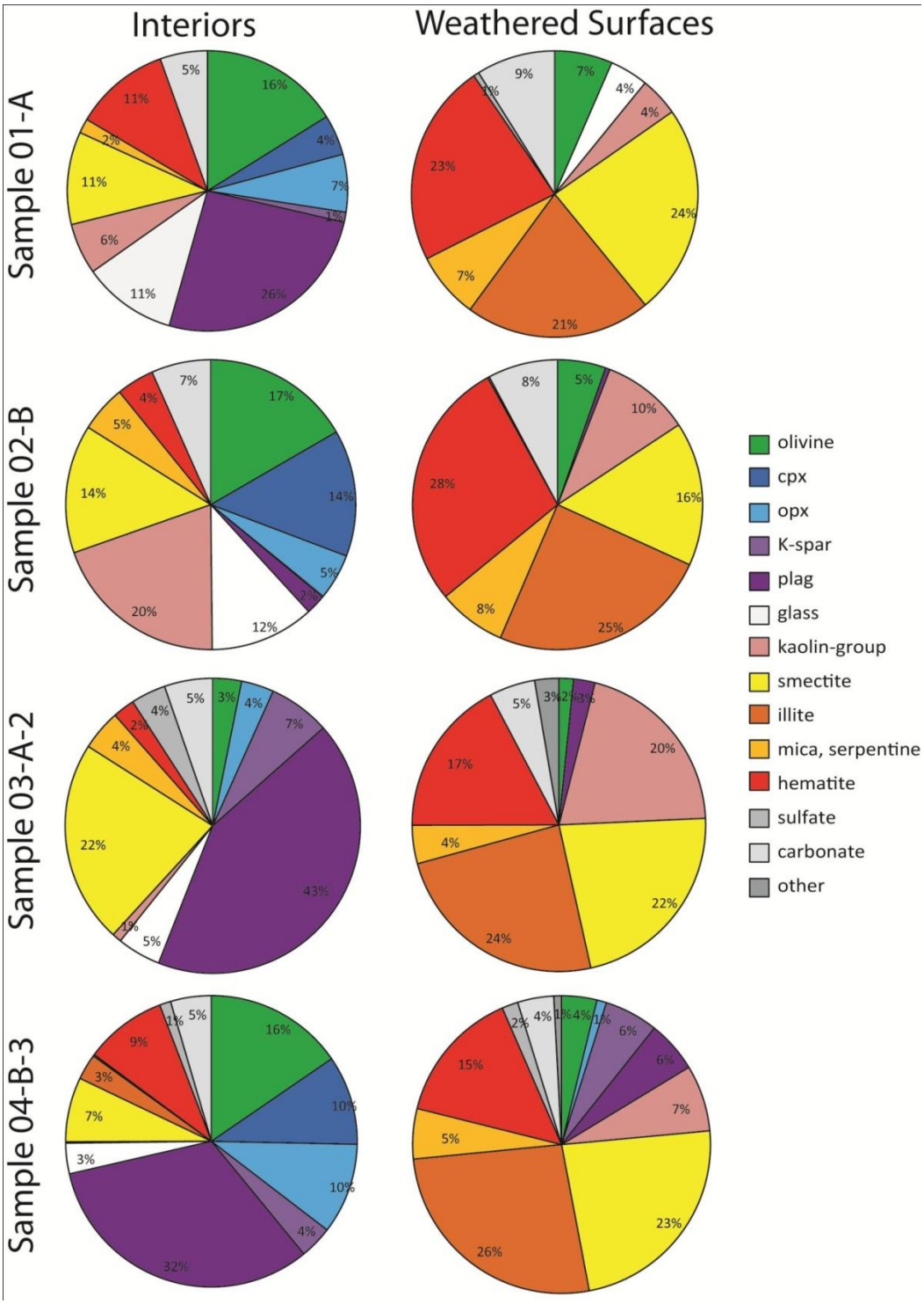

Figure 2.5. TIR-model derived mineral abundances using Library 1 from interior and weathered surfaces of four samples (one from each sampling location). Interiors are dominated by igneous minerals, while weathered surfaces generally lack igneous minerals and are dominated by crystalline clay minerals and hematite.

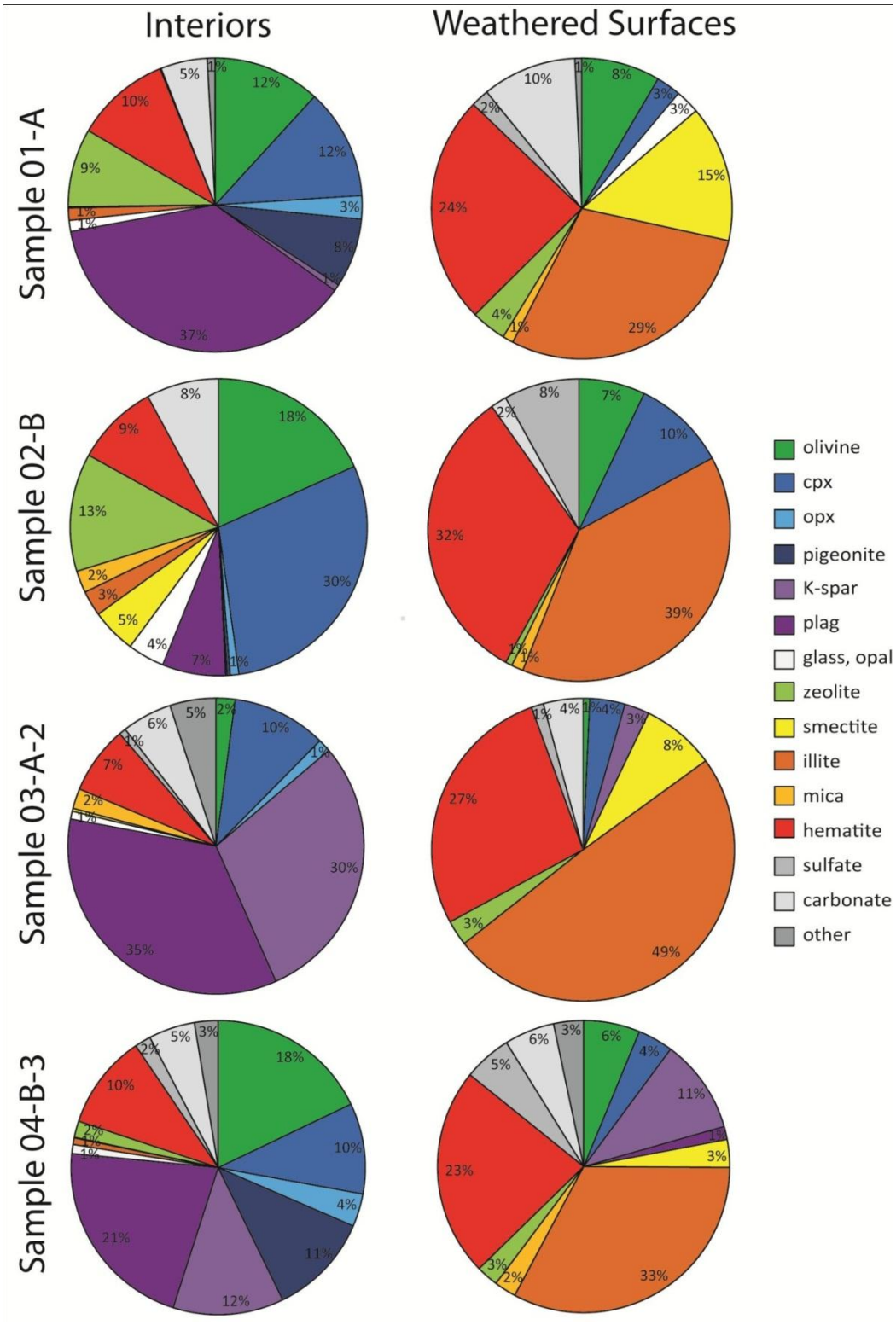

Figure 2.6. TIR-model derived mineral abundances using Library 2 from interior and weathered surfaces of four samples (one from each sampling location). Interiors are dominated by igneous minerals, while weathered surfaces generally lack igneous minerals and are dominated by crystalline clay minerals and hematite. Note that more illite and K-spar is used in models with Library 2, compared to models with Library 1.

amorphous silica (Figure 2.6). Spectral models using Library 2 identify more clinopyroxene and less glass than models using Library 1. Spectral models using Library 2 also identify more zeolite, which was not included in Library 1.

Spectral models of weathered basalt surfaces using either library generally identify significant amounts (i.e. >10 vol.%) of chemical weathering products and minor amounts of basaltic igneous minerals. Library 1 models identify significant amounts of illite, hematite, kaolinite, and smectite (montmorillonite and nontronite), and minor amounts of olivine, pyroxene, plagioclase, carbonate (dolomite), and other phyllosilicates (muscovite, biotite, and serpentine) (Figure 2.5). Library 2 models identify significant amounts of illite and hematite, and minor amounts of zeolite (stilbite), pyroxene, plagioclase, smectite, carbonate (dolomite), and sulfate (anhydrite) (Figure 2.6). Spectral models using Library 2 identify more illite and hematite and less smectite than models using Library 1. Spectral models using Library 1 identify more kaolinite in weathered surfaces, which was not included in Library 2.

2.5 Discussion

2.5.1 Measured Chemistry and Chemical Trends

XRF measurements of the samples in this study show similar bulk compositions to *Nesbitt and Wilson* [1992] and similar chemical weathering trends to those of *Eggleton et al.* [1987] and *Nesbitt and Wilson* [1992], with loss of Ca, Mg, K, Na, and Si and relative enrichment in Al, Fe^{3+}, and Ti. However, *Nesbitt and Wilson* [1992] report greater relative enrichment in Al_2O_3 than this study and this study generally shows greater relative enrichment in FeO_T with weathering (Figure 2.2). These discrepancies are likely due to differences in sampling procedures. The basalt interiors measured for this study yielded bulk chemical measurements that plot comparably to the *Nesbitt and Wilson* [1992] data. The method for collecting weathered material in this study sampled the outer few millimeters of weathered rock surfaces because this represents the material

that would be observed in remote sensing measurements of rocky material. These outer rinds do not represent the bulk chemical losses in the system. Rather, these rock surfaces are zones of active precipitation of secondary minerals and mineraloids, including Fe-oxides and oxyhydroxides and poorly-crystalline aluminosilicates. The method in this study preferentially sampled accumulated Fe_2O_3, driving the compositions toward the FeO_T axis in ternary plots and producing the disparity between chemical data presented here and those of *Nesbitt and Wilson* [1992] (Figure 2.3). Note that the measured SiO_2 and Al_2O_3 abundances from weathered surfaces of samples 01-C and 02-A-1 are greater than other samples (Table 2.3). This might be a case where these surfaces contained greater amounts of primary secondary aluminosilicates.

The observations of preferential weathering of olivine in this study are consistent with the order of mineral susceptibility in previous studies of Baynton basalts that report olivine > plagioclase > pyroxene > Fe-Ti-oxides [*Eggleton et al.*, 1987; *Nesbitt and Wilson*, 1992]. Calculations of relative element mobility (Na $\geq$ Ca > K > Mg > Si > Mn > Al > Ti > Fe) are consistent with those calculated for basalt and andesite weathering rinds from the Pacific Northwest (Ca $\geq$ Na > Mg > Si > Al $\geq$ K > Fe > Ti) [*Colman*, 1982]. Conversely, *Eggleton et al.* [1987] report that Al is less mobile than Fe. This difference in element mobility reflects the differences between the aqueous conditions and extent of weathering experienced by weathering rinds and soils. Soils have experienced more intense weathering and have greater abundances of crystalline aluminosilicate clays and aluminum hydroxides (gibbsite), while weathering rinds have experienced limited aqueous alteration, so they lack crystalline clays and are composed of Fe-oxides and oxyhydroxides and poorly-crystalline aluminosilicates.

2.5.2 Model-Derived Chemistry and Chemical Trends

The model-derived chemistry of basalt interiors is broadly similar to the chemistry measured by XRF (Tables 2.3, 2.4), but FeO_T is overestimated by TIR models

because they falsely identify hematite. The identification of hematite in spectral models may be due to chemical alteration of the interiors, as exemplified by alteration of olivine phenocrysts (Figure 2.2). Alteration of olivine results in the precipitation of small amounts of Fe-oxides and oxyhydroxides [*Eggleton*, 1984]. The TIR models identify hematite for two reasons. Because hematite is the only Fe-oxide in the library, hematite is used to model other Fe-oxides, such as magnetite, ilmenite, and other various secondary Fe-oxides and oxyhydroxides. Additionally, iron oxides are commonly overestimated because of graybody effects [*Wyatt et al.*, 2001]; hematite is spectrally flat in the Si-O stretching region of TIR spectra so hematite can be selected by the modeling routine instead of a blackbody end member to adjust spectral contrast. The identification of hematite shifts the modeled composition towards the FeO_T+MgO apex in ternary diagrams (Figures 2.7 and 2.8).

The model-derived chemistry of weathered surfaces shows less SiO_2 and Na_2O and more FeO_T and K_2O than the chemistry measured by XRF, but this effect is more pronounced than for the interiors. The overestimation of hematite in spectral models can account for the differences between measured and modeled FeO_T. Although the weathered surfaces are relatively enriched in iron-oxides, the models exaggerate this enrichment because of the graybody effect described above. Furthermore, the coating geometry of secondary phases causes the overestimation of alteration products [*Michalski et al.*, 2006b]. In addition to overestimating hematite, models overestimate zeolite and phyllosilicate abundances, particularly illite. Weathering rinds are typically composed of poorly-crystalline aluminosilicates, such as allophane, rather than crystalline clay minerals [*Colman*, 1982]; however, spectral libraries lack poorly-crystalline phases as they are difficult to isolate for TIR spectroscopy. Instead, models identify structurally and compositionally similar materials, including phyllosilicates, zeolites, and

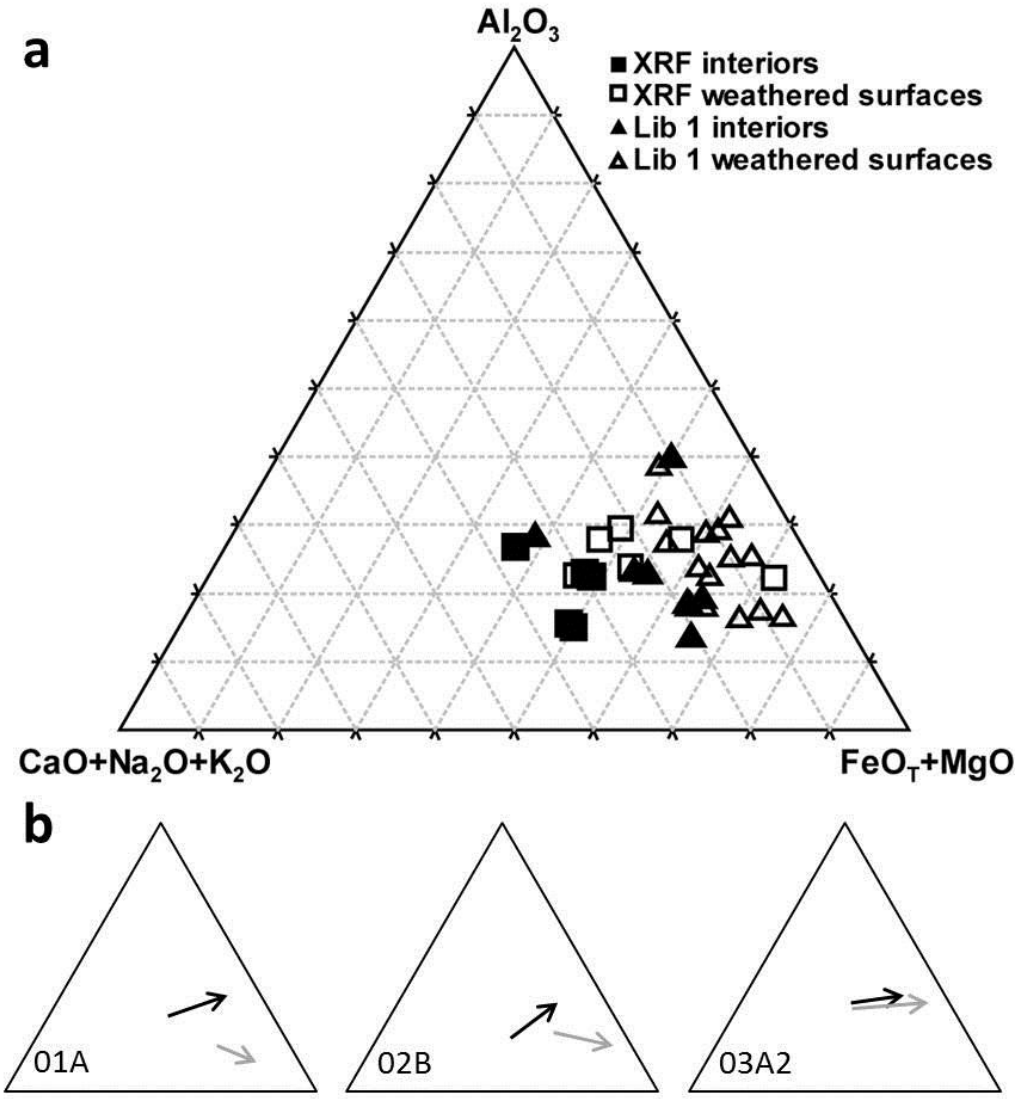

Figure 2.7. a) Ternary diagram showing measured XRF chemistry of interiors (black squares) and weathered surfaces (open squares) and model-derived chemistry using Library 1 of interiors (black triangles) and weathered surfaces (open triangles). In general, with increased weathering, there is a relative decrease in alkalis and relative enrichment in FeO_T+MgO for measured and modeled chemistries. b) Investigations of measured and modeled trends of three individual samples show that measured trends can vary between samples. Measured and modeled trends (black and gray arrows, respectively) are similar, but modeled trends show greater increase in FeO_T+MgO because of significant modeled hematite abundances.

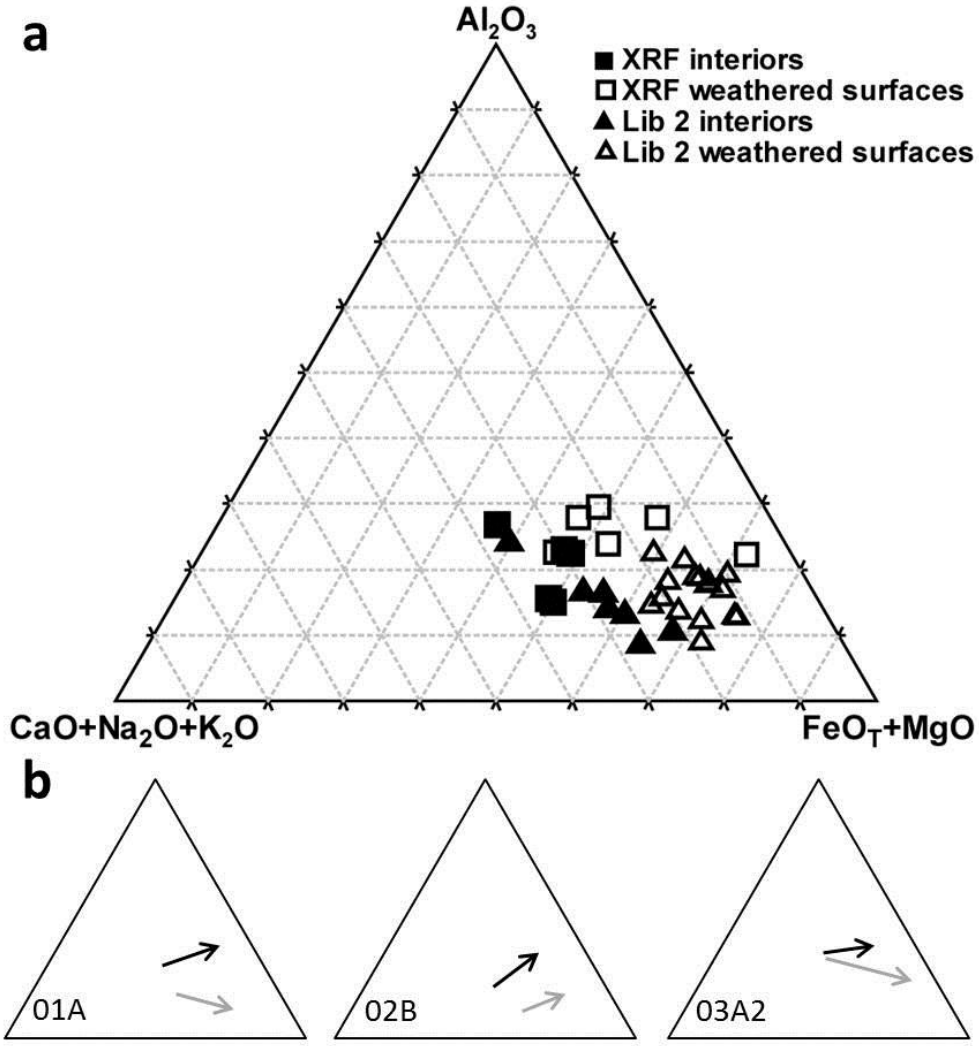

Figure 2.8. a) Ternary diagram showing measured XRF chemistry of interiors (black squares) and weathered surfaces (open squares) and model-derived chemistry using Library 2 of interiors (black triangles) and weathered surfaces (open triangles). With increased weathering, there is a relative decrease in alkalis and relative enrichment in FeO_T+MgO for measured and modeled chemistries. b) Investigations of measured and modeled trends of three individual samples show that measured trends can vary between samples. Measured and modeled trends (black and gray arrows, respectively) are similar, but modeled trends show greater increase in FeO_T+MgO because of significant modeled hematite abundances.

glasses. While many phyllosilicates and zeolites are similar in composition to poorly-crystalline aluminosilicates and their detection would not greatly affect model-derived chemistry, the identification of significant illite abundances in spectral models of weathered Baynton surfaces causes the overestimation of K_2O.

There are significant differences between measured chemistry and TIR-derived chemistry for weathered surfaces, particularly in terms of SiO_2, Al_2O_3, and FeO_T abundances. For example, the measured chemistry of sample 01-B-S3 shows 40.8 wt.% SiO_2, 17.1 wt.% Al_2O_3 and 34.2 wt.% FeO_T (Table 2.3), while the model using Library 1 reports 54 wt.% SiO_2, 22 wt.% Al_2O_3 and 10 wt.% FeO_T (Table 2.4). Weathering rinds are mineralogically heterogeneous on the scale of TIR observations. The range of measured values for each oxide between the five different weathered surfaces is similar to the range of values for each oxide derived from TIR spectral models. This suggests that chemistry derived from TIR spectroscopy may be more accurate when averaged for multiple surfaces, as occurs when remotely measuring a planetary surface.

The preferential sampling of rock coatings by TIR spectroscopy and subsequent non-linear mixing with an incomplete spectral library, as discussed above, explains the discrepancies between measured and model-derived trends. The derived chemical trends generally show a decrease in SiO_2, MgO, CaO, and Na_2O and an increase in FeO_T and K_2O with weathering. Significant modeled hematite abundances in weathered surfaces causes the apparent decrease in SiO_2 and increase in FeO_T with weathering, and the identification of illite causes the apparent increase in K_2O which is not accurate. The modeled decrease in MgO, CaO, and Na_2O with weathering occurs because fewer igneous minerals are identified in models of weathered surfaces (i.e. plagioclase, pyroxene, and olivine), as a result of non-linear mixing between primary minerals and secondary phases in a coating geometry [*Rampe et al.*, 2007; *Kraft et al.*, 2009].

A closer look at modeled weathering trends of individual rocks shows variation between samples (Figures 2.7b and 2.8b). Each rock surface has a unique history of aqueous alteration, causing mineralogical heterogeneities between and within the weathering rinds. Thermal-infrared spectra and models derived from them are very sensitive to coating composition and thickness [*Kraft et al.*, 2003]. Minor compositional differences result in large spectral differences, causing greater variation in the model- derived chemical trends than the measured trends for individual samples. One additional cause of the differences between measured and modeled chemical trends is the sampling procedures. TIR samples the upper few 10s of microns of a surface, while the upper few millimeters of the weathering rind were scraped off for XRF measurements, likely adding much more igneous material and homogenizing the measured trends between samples. While there are differences between measured and model-derived chemical trends, they are generally similar, showing a depletion of alkalis and enrichment in FeO_T. Model-derived chemical trends show greater enrichment in FeO_T than measured trends, but model-derived trends could still be interpreted as chemical weathering trends if derived from a planetary surface. Using TIR models to infer chemistry and chemical trends from weathered surfaces is more accurate when weathered surfaces are averaged to account for the small-scale heterogeneities in weathering rinds.

2.5.3 Effect of Spectral Library on Model-Derived Chemistry

Modeled-derived chemistries for weathered surfaces are improved when the spectral library includes phases that are present in the weathered surface. Library 1 was designed to contain end members identified in the rocks by *Eggleton et al.* [1987] and *Nesbitt and Wilson* [1992], resulting in more accurately derived chemistry (Figures 2.5a and 2.6a). The model-derived chemistry using Library 2 (Table 2.5) is generally further from the measured chemistry and has lower SiO_2, TiO_2, and Al_2O_3 and greater FeO_T and CaO values than models with Library 1.

Table 2.4. TIR-model-derived mineralogical and chemical compositions, Library 1

Derived Abundances, vol.%	01-A-int	01-A-S1	01-A-S2	01-B-int	01-B-S1	01-B-S2
Quartz	0 ± 0	1 ± 0	0 ± 0	0 ± 0	0 ± 0	0 ± 0
K-Feldspar	1 ± 1	0 ± 0	0 ± 0	3 ± 1	0 ± 0	0 ± 0
Plagioclase	29 ± 2	0 ± 0	0 ± 0	27 ± 2	1 ± 1	2 ± 1
OPX	6 ± 1	0 ± 0	0 ± 0	6 ± 1	0 ± 0	0 ± 0
High-Ca Px	4 ± 2	0 ± 0	0 ± 0	8 ± 2	0 ± 0	0 ± 0
Olivine	12 ± 1	0 ± 0	5 ± 1	10 ± 1	0 ± 0	5 ± 1
Sheet-Silicates	20 ± 4	79 ± 5	58 ± 7	22 ± 4	73 ± 5	62 ± 4
Mica	2 ± 1	5 ± 1	7 ± 1	1 ± 1	6 ± 1	6 ± 1
Serpentine	0 ± 0	2 ± 1	0 ± 0	0 ± 0	0 ± 0	0 ± 0
Glass	13 ± 1	0 ± 0	5 ± 2	15 ± 1	0 ± 0	0 ± 0
Amphibole	0 ± 0	0 ± 0	0 ± 0	0 ± 0	3 ± 1	5 ± 1
Hematite	6 ± 1	5 ± 1	13 ± 1	3 ± 1	11 ± 1	14 ± 1
Sulfate	0 ± 0	2 ± 0	1 ± 1	0 ± 0	0 ± 1	0 ± 0
Carbonate	6 ± 0	5 ± 0	10 ± 1	5 ± 0	6 ± 0	6 ± 0
	01-B-S3	01-C-int	01-C-S1	01-C-S2	02-A-1-int	02-A-1-S1
Quartz	0 ± 0	0 ± 0	2 ± 0	3 ± 1	0 ± 0	0 ± 0
K-Feldspar	0 ± 0	0 ± 1	0 ± 0	0 ± 1	0 ± 0	0 ± 0
Plagioclase	1 ± 1	30 ± 2	0 ± 0	8 ± 2	0 ± 0	0 ± 0
OPX	0 ± 0	7 ± 1	0 ± 0	2 ± 1	3 ± 1	0 ± 0
High-Ca Px	0 ± 0	7 ± 1	0 ± 0	3 ± 2	7 ± 1	0 ± 0
Olivine	0 ± 0	9 ± 1	1 ± 1	4 ± 1	8 ± 1	4 ± 1
Sheet-Silicates	85 ± 4	23 ± 4	72 ± 5	49 ± 5	67 ± 3	57 ± 6
Mica	2 ± 0	0 ± 0	5 ± 1	3 ± 0	0 ± 0	8 ± 1
Serpentine	2 ± 1	0 ± 0	0 ± 0	0 ± 0	1 ± 1	0 ± 0
Glass	0 ± 0	15 ± 1	3 ± 1	10 ± 2	9 ± 1	0 ± 0
Amphibole	0 ± 1	0 ± 0	0 ± 0	0 ± 1	0 ± 0	2 ± 1
Hematite	4 ± 1	4 ± 1	9 ± 1	10 ± 1	1 ± 1	20 ± 1
Sulfate	4 ± 1	0 ± 0	3 ± 0	5 ± 1	0 ± 0	0 ± 0
Carbonate	3 ± 0	6 ± 0	6 ± 0	4 ± 0	3 ± 0	8 ± 1
	02-A-1-S2	02-B-int	02-B-S1	02-B-S2	03-A-2-int	03-A-2-S1
Quartz	0 ± 0	0 ± 0	0 ± 0	0 ± 0	0 ± 0	0 ± 1
K-Feldspar	0 ± 0	0 ± 1	0 ± 0	0 ± 0	7 ± 1	0 ± 0
Plagioclase	0 ± 0	2 ± 2	1 ± 1	0 ± 0	42 ± 2	5 ± 1
OPX	0 ± 0	4 ± 2	0 ± 0	0 ± 0	3 ± 1	0 ± 0
High-Ca Px	0 ± 0	13 ± 2	0 ± 0	0 ± 0	0 ± 0	3 ± 2
Olivine	5 ± 1	12 ± 1	4 ± 1	1 ± 1	2 ± 1	7 ± 1
Sheet-Silicates	60 ± 3	40 ± 5	61 ± 5	67 ± 4	25 ± 2	45 ± 6
Mica	8 ± 1	3 ± 1	8 ± 1	8 ± 1	2 ± 1	4 ± 1
Serpentine	0 ± 0	2 ± 1	0 ± 0	0 ± 0	2 ± 1	0 ± 0
Glass	0 ± 0	14 ± 1	0 ± 0	0 ± 0	5 ± 1	17 ± 2
Amphibole	6 ± 1	0 ± 0	0 ± 0	2 ± 1	0 ± 0	0 ± 0
Hematite	12 ± 1	2 ± 1	17 ± 1	14 ± 1	1 ± 1	8 ± 1
Sulfate	0 ± 0	0 ± 0	0 ± 1	0 ± 0	4 ± 0	2 ± 1
Carbonate	9 ± 1	7 ± 0	9 ± 0	8 ± 0	5 ± 0	8 ± 0

	03-A-2-S2	04-B-3-int	04-B-3-S1	04-B-3-S2		
Quartz	0 ± 0	0 ± 0	0 ± 0	2 ± 0		
K-Feldspar	0 ± 0	4 ± 1	7 ± 1	10 ± 1		
Plagioclase	3 ± 1	37 ± 2	6 ± 2	11 ± 3		
OPX	0 ± 0	9 ± 1	1 ± 1	10 ± 3		
High-Ca Px	0 ± 0	9 ± 2	0 ± 0	3 ± 2		
Olivine	1 ± 1	13 ± 1	3 ± 1	10 ± 1		
Sheet-Silicates	75 ± 4	12 ± 5	63 ± 4	30 ± 5		
Mica	4 ± 0	0 ± 0	5 ± 0	4 ± 1		
Serpentine	0 ± 0	0 ± 0	1 ± 1	0 ± 0		
Glass	0 ± 0	4 ± 1	0 ± 0	0 ± 0		
Amphibole	2 ± 1	0 ± 0	1 ± 1	0 ± 0		
Hematite	10 ± 1	5 ± 1	8 ± 1	9 ± 1		
Sulfate	0 ± 0	2 ± 1	2 ± 0	6 ± 2		
Carbonate	5 ± 0	5 ± 0	4 ± 0	5 ± 0		
Derived Abundances, wt.%	01-A-int	01-A-S1	01-A-S2	01-B-int	01-B-S1	01-B-S2
Quartz	0 ± 0	1 ± 0	0 ± 0	0 ± 0	0 ± 0	0 ± 0
K-Feldspar	1 -1/+0	0 ± 0	0 ± 0	3 ± 0	0 ± 0	0 ± 0
Plagioclase	26 -4/+2	0 ± 0	0 ± 0	25 -4/+2	0 ± 1	1 ± 0
OPX	7 -2/+1	0 ± 0	0 ± 0	7 -3/+1	0 ± 0	0 ± 0
High-Ca Px	5 ± 0	0 ± 0	0 ± 0	9 -4/+4	0 ± 0	0 ± 0
Olivine	16 -3/+1	0 ± 0	7 -2/+1	13 -2/+3	0 ± 0	6 ± 1
Sheet-Silicates	17 -1/+0	74 ± 1	49 -6/+3	19 -1/+0	65 -1/+0	52 ± 2
Mica	2 ± 0	5 ± 0	7 -1/+2	1 -1/+0	6 ± 0	6 ± 0
Serpentine	0 ± 0	2 ± 1	0 ± 0	0 ± 0	0 ± 0	0 ± 0
Glass	11 -2/+4	0 ± 0	4 -1/+0	13 -3/+5	0 ± 0	0 ± 0
Amphibole	0 ± 0	0 ± 0	0 ± 0	0 ± 0	3 -1/+0	5 ± 0
Hematite	11 -2/+4	10 ± 0	23 -3/+6	6 ± 1	20 -1/+2	24 -2/+3
Sulfate	0 ± 0	2 ± 0	1 -1/+0	0 ± 0	0 ± 0	0 ± 0
Carbonate	5 -1/+2	5 ± 0	9 -1/+2	5 -1/+2	6 -0/+1	6 -0/+1
	01-B-S3	01-C-int	01-C-S1	01-C-S2	02-A-1-int	02-A-1-S1
Quartz	0 ± 0	0 ± 0	2 ± 0	2 ± 0	0 ± 0	0 ± 0
K-Feldspar	0 ± 0	0 -0/+1	0 ± 0	0 -0/+1	0 ± 0	0 ± 0
Plagioclase	1 -1/+0	27 -6/+3	0 ± 0	7 ± 2	0 ± 0	0 ± 0
OPX	0 ± 0	8 -2/+1	0 ± 0	2 ± 1	4 -3/+2	0 ± 0
High-Ca Px	0 ± 0	8 -0/+1	0 ± 0	3 -2/+1	8 -5/+4	0 ± 0
Olivine	0 ± 0	12 -1/+2	1 ± 0	5 ± 1	12 -2/+1	6 -2/+1
Sheet-Silicates	82 -3/+4	20 ± 0	65 ± 0	44 -2/+3	62 -7/+10	46 -6/+3
Mica	2 ± 0	0 ± 0	5 ± 0	3 ± 0	0 ± 0	8 ± 1
Serpentine	2 -1/+0	0 ± 0	0 ± 0	0 ± 0	1 ± 0	0 ± 0
Glass	0 ± 0	13 -2/+4	2 ± 1	9 ± 1	8 ± 1	0 ± 0
Amphibole	0 -0/+1	0 ± 0	0 ± 0	0 -0/+1	0 ± 0	2 ± 1
Hematite	7 ± 0	7 ± 1	16 ± 1	17 -2/+3	2 -1/+0	32 -4/+6
Sulfate	3 ± 1	0 -0/+1	3 ± 0	4 ± 1	0 ± 0	0 ± 0
Carbonate	3 ± 0	5 ± 1	6 ± 0	4 ± 0	3 -0/+1	7 ± 1
	02-A-1-	02-B-int	02-B-S1	02-B-S2	03-A-2-	03-A-2-

	S2				int	S1
Quartz	0 ± 0	0 ± 0	0 ± 0	0 ± 0	0 ± 0	0 ± 0
K-Feldspar	0 ± 0	0 -0/+1	0 ± 0	0 ± 0	7 ± 0	0 ± 0
Plagioclase	0 ± 0	2 -2/+1	1 ± 1	0 ± 0	43 -1/+2	4 ± 0
OPX	0 ± 0	5 -1/+3	0 ± 0	0 ± 0	4 -1/+0	0 ± 0
High-Ca Px	0 ± 0	14 ± 1	0 ± 0	0 ± 0	0 ± 0	3 -2/+1
Olivine	7 ± 2	17 ± 2	5 -2/+1	1 -1/+0	3 -1/+0	11 -1/+0
Sheet-Silicates	50 -2/+3	34 -2/+0	51 -5/+3	57 ± 1	23 ± 1	40 -5/+3
Mica	8 ± 0	3 ± 0	8 ± 1	8 -0/+1	2 ± 0	4 ± 0
Serpentine	0 ± 0	2 -1/+0	0 ± 0	0 ± 0	2 ± 0	0 ± 0
Glass	0 ± 0	12 ± 2	0 ± 0	0 ± 0	5 ± 0	14 ± 2
Amphibole	7 ± 1	0 ± 0	0 ± 0	2 ± 1	0 ± 0	0 ± 0
Hematite	20 ± 0	4 ± 0	28 -4/+5	25 -1/+2	2 ± 1	14 -1/+2
Sulfate	0 ± 0	0 ± 1	0 ± 0	0 ± 0	4 ± 0	2 ± 0
Carbonate	8 ± 0	7	8 ± 1	7 -0/+1	5 ± 0	8 ± 1

	03-A-2-S2	04-B-3-int	04-B-3-S1	04-B-3-S2		
Quartz	0 ± 0	0 ± 0	0 ± 0	2 ± 0		
K-Feldspar	0 ± 0	4 ± 0	6 ± 0	8 -2/+3		
Plagioclase	2 ± 0	32 -2/+3	6 -3/+2	10 -5/+2		
OPX	0 ± 0	10 -4/+2	1 ± 1	11 -6/+5		
High-Ca Px	0 ± 0	10 ± 1	0 ± 0	3 ± 3		
Olivine	2 -1/+2	15 ± 1	4 ± 1	13 ± 2		
Sheet-Silicates	67 ± 0	10 ± 4	57 ± 2	25 -2/+0		
Mica	4 ± 0	0 ± 0	5 -0/+1	4 ± 1		
Serpentine	0 ± 0	0 ± 0	1 ± 1	0 ± 0		
Glass	0 ± 0	3 ± 0	0 ± 0	0 ± 0		
Amphibole	3 -1/+0	0 ± 0	1 -1/+0	0 ± 0		
Hematite	17 -1/+2	9 -1/+2	15 -2/+3	15 -3/+5		
Sulfate	0 ± 0	1 ± 0	2 ± 0	5 -0/+1		
Carbonate	5 ± 0	5 ± 1	4 -0/+1	4 ± 1		

Derived Chemistry, wt.%	01-A-int	01-A-S1	01-A-S2	01-B-int	01-B-S1	01-B-S2
SiO_2	46 ± 1	52 ± 0	42 -3/+2	49 -1/+0	45 ± 1	40 ± 2
Al_2O_3	15 ± 1	20 ± 0	13 ± 1	17 ± 0	21 ± 0	21 ± 1
FeO_T	23 -2/+4	14 ± 0	31 -2/+4	15 ± 1	22 -1/+2	29 ± 1
MgO	7 -2/+1	5 ± 0	5 ± 0	7 ± 0	5 ± 0	6 ± 0
CaO	6 ± 0	3 ± 0	4 -0/+1	7 -0/+1	2 ± 0	2 ± 0
Na_2O	2 ± 0	0 ± 0	0 ± 0	2 ± 0	0 ± 0	0 ± 0
MnO	0 ± 0	0 ± 0	0 ± 0	0 ± 0	0 ± 0	0 ± 0
K_2O	1 ± 0	5 ± 0	3 ± 0	2 ± 0	4 ± 0	2 ± 0
TiO_2	0 ± 0	0 ± 0	0 ± 0	0 ± 0	0 ± 0	0 ± 0
SO_3	0 ± 0	1 ± 0	0 ± 0	0 ± 0	0 ± 0	0 ± 0
CO_2 (unnormalized)	3 ± 1	2 ± 0	4 ± 1	3 ± 1	3 ± 0	3 ± 0

	01-B-S3	01-C-int	01-C-S1	01-C-S2	02-A-1-int	02-A-1-S1
SiO_2	54 -0/+1	49 ± 0	46 -1/+1	46 ± 1	52 ± 1	35 -4/+3
Al_2O_3	22 ± 1	17 ± 1	19 ± 0	17 ± 1	25 -3/+4	15 ± 0

FeO_T	10 ± 0	17 -1/+2	20 ± 1	22 ± 2	13 -2/+1	40 -3/+4
MgO	5 ± 1	7 ± 0	4 ± 0	5 ± 1	6 -2/+1	5 ± 0
CaO	1 ± 0	6 ± 0	4 ± 0	3 ± 0	3 ± 1	3 ± 0
Na_2O	0 ± 0	2 ± 0	0 ± 0	1 ± 0	0 ± 0	0 ± 0
MnO	0 ± 0	0 ± 0	0 ± 0	0 ± 0	0 ± 0	0 ± 0
K_2O	4 ± 0	2 ± 0	5 ± 0	4 ± 0	0 ± 0	2 ± 0
TiO_2	0 ± 0	0 ± 0	0 ± 0	0 ± 0	0 ± 0	0 ± 0
SO_3	2 -1/+0	0 ± 0	2 ± 0	3 -1/+0	0 ± 0	0 ± 0
CO_2 (unnormalized)	1 ± 0	3 -0/+1	3 ± 0	2 ± 0	2 ± 0	4 -0/+1

	02-A-1-S2	02-B-int	02-B-S1	02-B-S2	03-A-2-int	03-A-2-S1
SiO_2	38 -0/+1	49 ± 1	38 -3/+2	41 -2/+1	49 ± 0	46 -2/+1
Al_2O_3	25 ± 2	15 -1/+0	15 ± 0	20 ± 0	19 ± 0	13 -1/+0
FeO_T	26 ± 1	19 ± 0	35 -2/+4	27 -1/+2	12 -1/+0	26 -1/+2
MgO	6 ± 1	9 ± 0	5 ± 0	5 ± 0	4 ± 0	4 ± 0
CaO	3 ± 0	6 -0/+1	3 ± 0	2 ± 0	9 ± 0	5 ± 0
Na_2O	0 ± 0	1 ± 0	0 ± 0	0 ± 0	1 ± 0	1 ± 0
MnO	0 ± 0	0 ± 0	0 ± 0	0 ± 0	0 ± 0	0 ± 0
K_2O	1 ± 0	1 ± 0	3 ± 0	3 ± 0	3 ± 0	3 ± 0
TiO_2	0 ± 0	0 ± 0	0 ± 0	0 ± 0	0 ± 0	0 ± 0
SO_3	0 ± 0	0 ± 0	0 ± 0	0 ± 0	2 ± 0	1 ± 0
CO_2 (unnormalized)	4 ± 0	3 ± 1	4 -0/+1	4 ± 0	2 ± 0	4 -0/+1

	03-A-2-S2	04-B-3-int	04-B-3-S1	04-B-3-S2
SiO_2	47 ± 1	47 ± 1	45 ± 2	41 -4/+2
Al_2O_3	20 ± 1	11 ± 1	16 ± 0	15 -0/+1
FeO_T	23 ± 0	20 -1/+2	24 ± 2	24 -1/+3
MgO	4 ± 0	10 ± 0	5 ± 1	8 ± 1
CaO	2 ± 0	6 ± 0	3 ± 0	6 ± 0
Na_2O	0 ± 0	1 ± 0	1 ± 0	1 ± 0
MnO	0 ± 0	0 ± 0	0 ± 0	0 ± 0
K_2O	3 ± 0	3 ± 0	4 ± 0	2 ± 0
TiO_2	0 ± 0	0 ± 0	0 ± 0	0 ± 0
SO_3	0 ± 0	1 ± 0	1 ± 0	3 ± 0
CO_2 (unnormalized)	3 ± 0	2 -0/+1	2 ± 0	2 -0/+1

The dependence of derived chemistry on spectral library composition illustrates the importance of having accurate spectral libraries. Currently, there is a lack of poorly-crystalline weathering product spectra, even though these phases are common in terrestrial alteration environments [*Colman*, 1981; 1982] and are common in the weathering rinds presented here, based on XRD data. In this study, phyllosilicates, particularly illite, were identified in significant abundances in spectral models of weathered basalt surfaces because of spectral similarities between weathered surface spectra and illite (Figure 2.9). *Hamilton et al.* [2008] proposed that spectral similarities between poorly-crystalline aluminosilicates and phyllosilicates caused the inaccurate identification of phyllosilicates in TIR spectra of altered, phyllosilicate-poor Hawaiian tephra. The incorporation of poorly-crystalline aluminosilicates in spectral libraries for weathered Baynton basalts could improve spectral models and model-derived chemistry.

2.5.4 Implications for Studying Mars

The results presented here have important implications for studying the geochemistry of the Martian surface via TIR spectroscopy. The Baynton basalts are not direct Martian analogs, and the style of weathering experienced by these rocks is not directly analogous to Martian weathering. Chemical weathering trends derived from TIR models of Baynton basalts are generally similar to the measured trends and could be identified as weathering trends if they were derived from remotely-sensed data. However, chemical weathering and the precipitation of small amounts of secondary phases in a coating geometry strongly influence TIR-interpreted chemistry, and the associated errors can be significant, particularly in terms of derived alkali abundance. This study shows that an inaccurate spectral library can affect derived alkalis, due to the underestimation of igneous minerals and the overestimation of phyllosilicates, particularly illite. TES-derived SiO_2 vs. Na_2O+K_2O abundances were initially used by *McSween et al.* [2003] to interpret rock types and the petrologic evolution of the

Table 2.5. TIR-model-derived mineralogical and chemical compositions, Library 2

Derived Abundances, vol.%	01-A-int	01-A-S1	01-A-S2	01-B-int	01-B-S1	01-B-S2
Quartz	0 ± 0	3 ± 0	0 ± 0	0 ± 0	1 ± 0	0 ± 0
K-Feldspar	1 ± 1	0 ± 0	0 ± 0	3 ± 1	0 ± 0	3 ± 1
Plagioclase	39 ± 3	0 ± 0	0 ± 0	31 ± 2	0 ± 2	3 ± 2
OPX	2 ± 1	0 ± 0	0 ± 0	2 ± 1	0 ± 0	0 ± 0
Pigeonite	7 ± 2	0 ± 0	0 ± 0	8 ± 2	0 ± 0	0 ± 0
High-Ca Px	12 ± 2	0 ± 0	3 ± 3	15 ± 2	2 ± 2	4 ± 1
Olivine	10 ± 1	0 ± 1	6 ± 2	11 ± 1	0 ± 0	1 ± 1
Sheet-Silicates	2 ± 2	74 ± 3	52 ± 7	0 ± 0	71 ± 4	64 ± 1
Mica	0 ± 1	1 ± 1	1 ± 2	0 ± 0	0 ± 0	0 ± 0
Serpentine	0 ± 0	0 ± 0	0 ± 0	0 ± 0	0 ± 0	0 ± 0
Zeolite	13 ± 1	2 ± 1	5 ± 4	12 ± 2	2 ± 2	0 ± 0
Glass	0 ± 0	0 ± 0	0 ± 0	5 ± 3	0 ± 0	0 ± 0
Opal	2 ± 0	0 ± 0	4 ± 7	1 ± 5	0 ± 0	0 ± 0
Amphibole	1 ± 1	0 ± 0	1 ± 3	1 ± 1	0 ± 0	0 ± 0
Hematite	6 ± 1	10 ± 1	15 ± 2	5 ± 1	17 ± 1	21 ± 1
Sulfate	0 ± 1	3 ± 1	2 ± 1	0 ± 0	2 ± 1	0 ± 0
Carbonate	6 ± 0	6 ± 0	11 ± 1	6 ± 0	5 ± 0	3 ± 0

	01-B-S3	01-C-int	01-C-S1	01-C-S2	02-A-1-int	02-A-1-S1
Quartz	0 ± 1	0 ± 0	4 ± 1	3 ± 0	0 ± 0	0 ± 0
K-Feldspar	0 ± 0	1 ± 1	0 ± 0	8 ± 2	0 ± 0	0 ± 0
Plagioclase	1 ± 1	38 ± 4	0 ± 0	3 ± 2	18 ± 2	0 ± 0
OPX	0 ± 0	6 ± 1	0 ± 0	0 ± 0	1 ± 1	0 ± 0
Pigeonite	0 ± 0	1 ± 2	0 ± 0	0 ± 0	0 ± 0	0 ± 0
High-Ca Px	0 ± 0	14 ± 2	1 ± 2	7 ± 1	24 ± 2	5 ± 2
Olivine	0 ± 0	8 ± 1	1 ± 1	0 ± 0	9 ± 2	3 ± 1
Sheet-Silicates	71 ± 2	0 ± 0	61 ± 4	31 ± 1	12 ± 4	58 ± 3
Mica	0 ± 0	1 ± 0	0 ± 1	0 ± 0	4 ± 1	2 ± 1
Serpentine	0 ± 0	0 ± 0	0 ± 0	0 ± 0	0 ± 0	0 ± 0
Zeolite	0 ± 0	10 ± 2	4 ± 2	17 ± 3	15 ± 2	0 ± 0
Glass	7 ± 1	7 ± 2	0 ± 0	1 ± 1	0 ± 0	0 ± 0
Opal	0 ± 0	2 ± 1	3 ± 5	7 ± 4	0 ± 1	0 ± 0
Amphibole	0 ± 0	0 ± 0	0 ± 0	0 ± 0	0 ± 0	0 ± 0
Hematite	13 ± 1	5 ± 1	14 ± 1	16 ± 1	10 ± 1	23 ± 1
Sulfate	3 ± 1	0 ± 0	5 ± 1	4 ± 0	0 ± 0	1 ± 0
Carbonate	4 ± 0	7 ± 0	7 ± 0	4 ± 0	7 ± 0	8 ± 0

	02-A-1-S2	02-B-int	02-B-S1	02-B-S2	03-A-2-int	03-A-2-S1
Quartz	0 ± 0	0 ± 0	0 ± 0	0 ± 0	0 ± 0	1 ± 1
K-Feldspar	1 ± 1	0 ± 3	0 ± 0	0 ± 0	35 ± 2	0 ± 0
Plagioclase	0 ± 0	7 ± 3	0 ± 0	0 ± 0	33 ± 4	8 ± 1
OPX	0 ± 0	1 ± 1	0 ± 0	0 ± 0	1 ± 1	0 ± 0
Pigeonite	0 ± 0	0 ± 4	0 ± 0	0 ± 0	0 ± 0	0 ± 0
High-Ca Px	0 ± 0	28 ± 2	0 ± 0	3 ± 1	9 ± 2	8 ± 2
Olivine	1 ± 1	14 ± 2	5 ± 1	0 ± 0	2 ± 1	6 ± 1
Sheet-Silicates	74 ± 2	9 ± 3	60 ± 3	67 ± 3	0 ± 2	26 ± 3

Mica	0 ± 0	3 ± 2	1 ± 1	0 ± 0	2 ± 1	1 ± 1
Serpentine	0 ± 0	0 ± 0	0 ± 0	0 ± 0	2 ± 1	0 ± 0
Zeolite	0 ± 0	18 ± 2	1 ± 1	4 ± 2	0 ± 0	8 ± 2
Glass	0 ± 0	0 ± 0	0 ± 0	0 ± 0	1 ± 1	1 ± 1
Opal	0 ± 0	6 ± 3	0 ± 0	0 ± 0	0 ± 0	21 ± 4
Amphibole	0 ± 0	0 ± 0	0 ± 0	0 ± 0	3 ± 1	0 ± 0
Hematite	23 ± 1	5 ± 1	20 ± 1	19 ± 1	4 ± 1	9 ± 1
Sulfate	1 ± 0	0 ± 0	2 ± 0	1 ± 0	1 ± 1	3 ± 1
Carbonate	3 ± 0	9 ± 0	9 ± 0	6 ± 0	6 ± 0	8 ± 0
	03-A-2-S2	04-B-3-int	04-B-3-S1	04-B-3-S2		
Quartz	0 ± 0	0 ± 0	0 ± 0	0 ± 0		
K-Feldspar	3 ± 1	15 ± 4	13 ± 2	22 ± 3		
Plagioclase	0 ± 0	25 ± 4	2 ± 2	7 ± 2		
OPX	0 ± 0	3 ± 1	0 ± 0	3 ± 2		
Pigeonite	0 ± 0	11 ± 3	0 ± 0	7 ± 3		
High-Ca Px	4 ± 1	9 ± 2	4 ± 1	11 ± 2		
Olivine	1 ± 1	15 ± 1	6 ± 1	8 ± 1		
Sheet-Silicates	66 ± 3	1 ± 2	41 ± 3	11 ± 2		
Mica	0 ± 0	0 ± 1	2 ± 1	2 ± 0		
Serpentine	0 ± 0	0 ± 0	0 ± 0	0 ± 0		
Zeolite	4 ± 2	3 ± 2	3 ± 2	4 ± 1		
Glass	0 ± 0	0 ± 0	0 ± 0	0 ± 0		
Opal	0 ± 0	1 ± 1	0 ± 0	0 ± 0		
Amphibole	0 ± 0	3 ± 1	3 ± 1	0 ± 0		
Hematite	16 ± 1	6 ± 1	14 ± 1	15 ± 1		
Sulfate	1 ± 0	2 ± 1	6 ± 1	5 ± 1		
Carbonate	5 ± 0	6 ± 0	6 ± 0	4 ± 0		
Derived Abundances, wt.%	01-A-int	01-A-S1	01-A-S2	01-B-int	01-B-S1	01-B-S2
Quartz	0 ± 0	3 ± 0	0 ± 0	0 ± 0	1 ± 0	0 ± 0
K-Feldspar	1 -1/+0	0 ± 0	0 ± 0	2 ± 0	0 ± 0	2 ± 1
Plagioclase	37 ± 2	0 ± 0	0 ± 0	28 -4/+3	0 -0/+1	2 ± 1
OPX	3 -1/+2	0 ± 0	0 ± 0	2 -2/+3	0 ± 0	0 ± 0
Pigeonite	8 ± 0	0 ± 0	0 ± 0	8 -1/+0	0 ± 0	0 ± 0
High-Ca Px	12 -3/+2	0 ± 0	3 -3/+1	17 ± 3	2 -2/+1	5 ± 1
Olivine	12 -4/+2	0 -0/+1	8 -2/+1	14 -3/+2	0 ± 0	1 ± 1
Sheet-Silicates	1 ± 1	66 -3/+2	44 -5/+2	0 ± 0	61 -3/+2	53 -2/+3
Mica	0 ± 0	1 ± 1	1 ± 1	0 ± 0	0 ± 0	0 ± 0
Serpentine	0 ± 0	0 ± 0	0 ± 0	0 ± 0	0 ± 0	0 ± 0
Zeolite	9 -2/+3	1 ± 1	4 -2/+1	9 -2/+1	1 ± 1	0 ± 0
Glass	0 ± 0	0 ± 0	0 ± 0	4 -2/+1	0 ± 0	0 ± 0
Opal	1 ± 0	0 ± 0	3 -3/+5	1 -1/+3	0 ± 0	0 ± 0
Amphibole	1 ± 0	1 ± 0	1 -1/+2	1 -1/+2	0 ± 0	0 ± 0
Hematite	10 -2/+4	18 ± 1	25 -5/+6	9 ± 1	29 ± 2	34 ± 1
Sulfate	0 ± 0	3 -0/+3	2 -0/+1	0 ± 0	2 -1/+2	0 ± 0
Carbonate	5 -1/+2	6 ± 0	10 -2/+3	5 ± 1	5 ± 0	3 ± 0
	01-B-S3	01-C-int	01-C-S1	01-C-S2	02-A-1-int	02-A-1-S1

Quartz	0 ± 0	0 ± 0	3 ± 0	3 ± 0	0 ± 0	0 ± 0
K-Feldspar	0 ± 0	1 -1/+0	0 ± 0	6 -3/+2	0 ± 0	0 ± 0
Plagioclase	1 ± 1	35 -0/+1	0 ± 0	3 ± 1	23 -2/+1	0 ± 0
OPX	0 ± 0	6 -4/+2	0 ± 0	0 ± 0	1 ± 1	0 ± 0
Pigeonite	0 ± 0	1 ± 1	0 ± 0	0 ± 0	0 ± 0	0 ± 0
High-Ca Px	0 ± 0	15 -5/+2	1 -1/+2	8 ± 1	23 -0/+1	5 ± 1
Olivine	0 ± 0	11 -1/+2	2 ± 2	0 ± 0	11 -1/+2	3 -2/+1
Sheet-Silicates	64 -3/+1	0 ± 0	54 -7/+4	28 ± 4	9 -2/+1	47 ± 1
Mica	0 ± 0	1 ± 0	0 -0/+1	0 ± 0	3 ± 0	2 ± 0
Serpentine	0 ± 0	0 ± 0	0 ± 0	0 ± 0	0 ± 0	0 ± 0
Zeolite	0 ± 0	7 -1/+2	3 ± 1	12 -3/+1	10 ± 1	0 ± 0
Glass	5 ± 0	5 ± 0	0 ± 0	1 ± 1	0 ± 0	0 ± 0
Opal	0 ± 0	1 ± 0	2 ± 2	5 -2/+1	0 ± 0	0 ± 0
Amphibole	0 ± 0	0 ± 0	0 ± 0	0 ± 0	0 ± 0	0 ± 0
Hematite	23 ± 1	9 -2/+3	24 -3/+2	28 ± 4	16 ± 2	35 -2/+3
Sulfate	3 -0/+3	0 -0/+1	5 -0/+3	4 -0/+2	0 ± 0	1 -0/+1
Carbonate	4 ± 0	6 -1/+3	6 -1/+0	4 ± 0	6 ± 1	7 ± 0

	02-A-1-S2	02-B-int	02-B-S1	02-B-S2	03-A-2-int	03-A-2-S1
Quartz	0 ± 0	0 ± 0	0 ± 0	0 ± 0	0 ± 0	1 -1/+0
K-Feldspar	1 ± 1	0 -0/+2	0 ± 0	0 ± 0	30 -7/+11	0 ± 0
Plagioclase	0 ± 0	7 -7/+5	0 ± 0	0 ± 0	35 -10/+6	7 ± 0
OPX	0 ± 0	1 ± 1	0 ± 0	0 ± 0	1 ± 1	0 ± 0
Pigeonite	0 ± 0	0 -0/+3	0 ± 0	0 ± 0	0 ± 0	0 ± 0
High-Ca Px	0 ± 0	30 -1/+0	0 ± 0	3 ± 1	10 ± 1	9 ± 0
Olivine	1 ± 1	18 ± 3	7 -1/+2	0 ± 0	2 -2/+3	9 ± 0
Sheet-Silicates	63 ± 2	8 -1/+0	49 -1/+0	57 ± 1	0 -0/+1	24 ± 0
Mica	0 ± 0	2 ± 1	1 ± 1	0 ± 0	2 -1/+0	1 ± 0
Serpentine	0 ± 0	0 ± 0	0 ± 0	0 ± 0	1 -1/+0	0 ± 0
Zeolite	0 ± 0	13 -3/+4	1 ± 1	3 ± 1	0 ± 0	6 ± 0
Glass	0 ± 0	0 ± 0	0 ± 0	0 ± 0	1 ± 0	1 ± 1
Opal	0 ± 0	4 -1/+0	0 ± 0	0 ± 0	0 ± 0	15 ± 0
Amphibole	0 ± 0	0 ± 0	0 ± 0	0 ± 0	4 ± 0	0 ± 0
Hematite	32 ± 0	9 ± 2	32 ± 3	31 ± 1	7 -1/+2	17 ± 2
Sulfate	0 ± 0	0 ± 0	2 -0/+1	1 -0/+1	1 -1/+0	3 -0/+2
Carbonate	3 ± 0	8 -2/+3	8 -0/+1	5 ± 0	5 -1/+2	8 ± 1

	03-A-2-S2	04-B-3-int	04-B-3-S1	04-B-3-S2
Quartz	0 ± 0	0 ± 0	0 ± 0	0 ± 0
K-Feldspar	3 ± 1	12 -1/+0	10 ± 0	17 -1/+2
Plagioclase	0 ± 0	22 -2/+8	1 ± 1	6 ± 0
OPX	0 ± 0	4 -1/+0	0 ± 0	4 ± 1
Pigeonite	0 ± 0	11 -2/+1	0 ± 0	7 ± 1
High-Ca Px	4 ± 1	10 -6/+1	4 ± 1	12 -2/+1
Olivine	1 ± 1	18 ± 4	6 ± 0	9 ± 3
Sheet-Silicates	57 ± 2	1 ± 1	36 -2/+3	10 -0/+1
Mica	0 ± 0	0 ± 0	2 ± 1	2 ± 0
Serpentine	0 ± 0	0 ± 0	0 ± 0	0 ± 0
Zeolite	3 ± 1	2 ± 2	2 ± 1	2 ± 0
Glass	0 ± 0	0 ± 0	0 ± 0	0 ± 0
Opal	0 ± 0	1 ± 0	0 ± 0	0 ± 0

Amphibole	0 ± 0	3 -1/+0	3 ± 1	0 ± 0		
Hematite	27 ± 2	10 -3/+4	23 -2/+3	23 -3/+5		
Sulfate	1 -0/+1	2 -1/+0	5 ± 1	4 -2/+0		
Carbonate	4 ± 0	5 ± 2	6 -0/+1	3 -0/+1		
Derived Chemistry, wt.%	01-A-int	01-A-S1	01-A-S2	01-B-int	01-B-S1	01-B-S2
SiO_2	46 ± 1	49 -1/+0	40 -6/+4	48 -1/+2	41 ± 1	38 ± 1
Al_2O_3	14 -0/+1	15 -1/+0	11 -0/+1	12 ± 1	15 ± 0	14 ± 0
FeO_T	20 -1/+2	21 -1/+0	32 -2/+4	19 -1/+0	32 ± 2	37 ± 1
MgO	7 -2/+1	4 -0/+1	7 ± 1	8 ± 1	3 ± 0	3 ± 0
CaO	10 ± 0	4 -0/+1	6 ± 0	10 ± 1	3 ± 1	2 ± 0
Na_2O	2 ± 0	0 ± 0	0 ± 0	2 ± 0	0 ± 0	0 ± 0
MnO	0 ± 0	0 ± 0	0 ± 0	0 ± 0	0 ± 0	0 ± 0
K_2O	0 ± 0	4 ± 0	3 -0/+1	1 ± 0	5 ± 0	5 ± 0
TiO_2	0 ± 0	0 ± 0	0 ± 0	0 ± 0	0 ± 0	0 ± 0
SO_3	0 ± 0	2 -0/+1	1 -0/+1	0 ± 0	1 ± 1	0 ± 0
CO_2 (unnormalized)	3 ± 1	3 ± 0	5 ± 1	3 ± 1	2 ± 0	2 ± 0
	01-B-S3	01-C-int	01-C-S1	01-C-S2	02-A-1-int	02-A-1-S1
SiO_2	47 -1/+0	47 -2/+1	43 -2/+0	43 -4/+2	43 ± 1	35 ± 1
Al_2O_3	15 -1/+0	13 -0/+1	14 -1/+0	12 -1/+0	12 -1/+0	12 ± 0
FeO_T	26 ± 1	18 -1/+3	28 -2/+1	30 -4/+5	25 ± 1	41 -2/+1
MgO	3 ± 0	7 -1/+3	3 ± 0	2 ± 0	7 -0/+1	4 ± 0
CaO	3 -0/+1	11 ± 0	5 -0/+1	6 -0/+1	12 ± 0	4 -0/+1
Na_2O	0 ± 0	2 ± 0	0 ± 0	1 ± 0	1 ± 0	0 ± 0
MnO	0 ± 0	0 ± 0	0 ± 0	0 ± 0	0 ± 0	0 ± 0
K_2O	4 ± 0	1 ± 0	4 ± 1	3 ± 0	0 ± 0	4 ± 0
TiO_2	0 ± 0	0 ± 0	0 ± 0	0 ± 0	0 ± 0	0 ± 0
SO_3	2 -0/+2	0 ± 0	3 -0/+2	2 -0/+1	0 ± 0	0 -0/+1
CO_2 (unnormalized)	2 ± 0	3 ± 1	3 ± 0	2 ± 0	3 ± 0	3 ± 0
	02-A-1-S2	02-B-int	02-B-S1	02-B-S2	03-A-2-int	03-A-2-S1
SiO_2	39 ± 0	46 -3/+2	35 -2/+1	40 ± 1	49 ± 0	49 -2/+1
Al_2O_3	15 ± 0	8 -2/+1	11 ± 0	14 ± 0	17 -1/+0	10 ± 0
FeO_T	34 ± 0	22 -2/+3	39 ± 3	34 ± 1	12 -0/+1	25 ± 2
MgO	3 -1/+0	11 ± 1	5 ± 1	3 ± 0	5 ± 1	4 ± 0
CaO	1 ± 0	12 ± 1	4 -0/+1	3 -0/+1	10 -1/+0	7 -0/+1
Na_2O	0 ± 0	1 ± 0	0 ± 0	0 ± 0	2 ± 0	1 ± 0
MnO	0 ± 0	0 ± 0	0 ± 0	0 ± 0	0 ± 0	0 ± 0
K_2O	6 ± 0	0 ± 0	4 ± 0	5 ± 0	4 ± 1	2 ± 0
TiO_2	0 ± 0	0 ± 0	0 ± 0	0 ± 0	0 ± 0	0 ± 0
SO_3	0 ± 0	0 ± 0	1 -0/+1	0 -0/+1	2 ± 0	2 -0/+1
CO_2 (unnormalized)	2 ± 0	4 ± 1	4 ± 0	3 ± 0	3 ± 1	4 -0/+1
	03-A-2-S2	04-B-3-int	04-B-3-S1	04-B-3-S2		
SiO_2	42 -1/+0	46 ± 3	39 ± 1	39 ± 2		

Al_2O_3	15 ± 0	9 -2/+3	12 ± 0	8 ± 0
FeO_T	30 ± 2	22 ± 5	26 ± 2	33 -1/+3
MgO	3 ± 0	11 ± 2	8 ± 0	6 ± 1
CaO	3 -0/+1	7 -2/+1	6 -1/+0	6 ± 0
Na_2O	0 ± 0	2 ± 0	1 ± 0	1 ± 0
MnO	0 ± 0	0 ± 0	0 ± 0	0 ± 0
K_2O	5 ± 0	2 ± 0	5 ± 0	3 ± 0
TiO_2	0 ± 0	0 ± 0	0 ± 0	0 ± 0
SO_3	1 -0/+1	1 -1/+0	3 ± 0	2 -1/+0
CO_2	2 ± 0	3 ± 1	3 ± 0	2 ± 0
(unnormalized)				

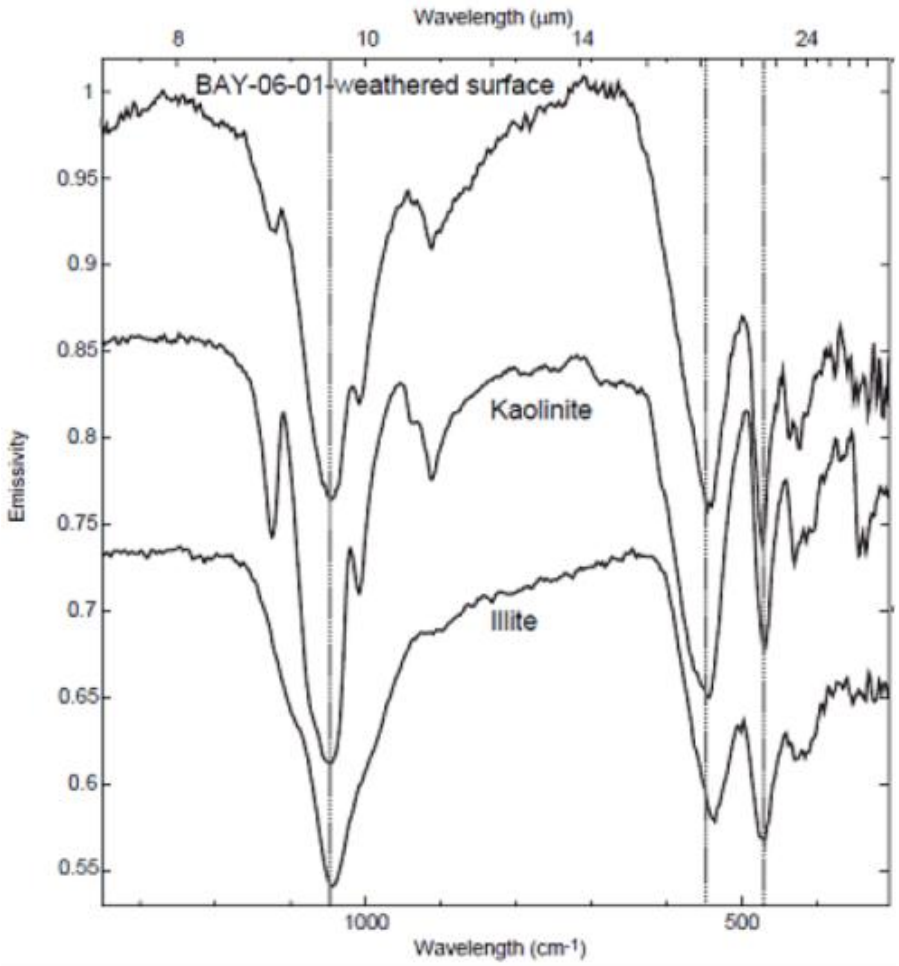

Figure 2.9. TIR spectra of a weathered Baynton surface, kaolinite, and illite. Dashed lines show similarities between absorption positions of the weathered Baynton surface, kaolinite, and illite. Note that absorption positions of the weathered Baynton surface in the Si-O stretching region are most similar to kaolinite, but the overall shape of the Si-O stretching absorption of the weathered Baynton surface is broad like that of illite. Additionally, relative strengths of the absorptions in the doublet in the Baynton surface from 600-450 cm^{-1} are more similar to illite than kaolinite. Spectra are offset in emissivity for clarity.

Martian surface, but it was later suggested by *McSween et al.* [2009] that chemical weathering may inhibit correct igneous classifications from TES-derived chemistry. Spectral models of weathered Baynton surfaces show that relatively minor amounts of poorly-crystalline weathering products have a large effect on derived SiO_2 and alkali abundances, thus obscuring igneous parent composition. Chemical weathering in the Baynton rocks results in loss of SiO_2 and Na_2O+K_2O with weathering. Chemical trends derived from spectral models with the library commonly used to model TES data (Library 2) show a similar loss of SiO_2 but an apparent increase in Na_2O+K_2O because of the overestimation of illite. Illite and K-rich volcanic glass are commonly identified in TES data [*Bandfield et al.*, 2000; *McSween et al.*, 2003; *Minitti and Hamilton*, 2010], which affect model-derived alkali abundances and inferred chemical weathering trends. The identities of secondary silicates in TES models are debated and this study shows that it is critical to accurately identify secondary silicates on Mars to best interpret surface chemistries. The addition of poorly-crystalline aluminosilicate spectra to libraries could improve derived chemistry of weathered surfaces because these mineraloids do not contain alkalis and therefore would not erroneously augment the modeled alkali abundances. It is essential that spectral libraries contain a full suite of appropriate secondary minerals and mineraloids to more accurately derive Martian surface chemistry from TES models.

2.6 Conclusions

The results of this study have important implications for analyzing mineralogical and chemical trends from TIR spectral models of weathered basalt surfaces. Basalt weathering rinds contain small amounts of poorly-crystalline aluminosilicates and Fe-oxides and oxyhydroxides, but are dominated by basaltic igneous minerals. The modeled mineralogy of weathering rinds is dominated by crystalline clays and hematite but is inaccurate because: 1) weathering products are present as coatings on igneous minerals in

weathering rinds, causing non-linear spectral mixing of weathering products and igneous minerals, and 2) the spectral library is incomplete and lacks a full set of secondary phases, particularly poorly-crystalline materials. Estimates of total FeO and alkali abundances from TIR spectral models are inaccurate because of the overestimation of hematite and phyllosilicates, particularly illite. Hematite is likely overestimated because Fe-oxides are present as coatings and because of a graybody effect that Fe-oxides have in spectral models. Illite is likely overestimated because poorly-crystalline aluminosilicates are present in the weathering rind as a coating and they are spectrally similar to illite. Despite inaccurate modeled mineral abundances, model-derived bulk chemical weathering trends are similar to the measured trends when plotted on a $[Al_2O_3]$-$[CaO+Na_2O+K_2O]$-$[FeO_T+MgO]$ ternary diagram, showing a loss in alkalis and an enrichment in total FeO. There are differences in the measured trends between different samples because weathering rind composition varies between samples. Differences between measured and modeled trends may be attributable, in part, to mineralogical heterogeneities on the scale of laboratory TIR measurements. Sampling an average weathered surface, as is done in planetary remote sensing, would remove the effects of small-scale variations in weathering rind composition and would improve model-derived chemistry and trends. A more accurate library of secondary phases improves the model-derived chemistry. Therefore, the use of a more complete spectral library to model Martian spectral data, which must include secondary minerals and mineraloids would improve the model-derived chemistry, particularly the derived alkali content. The ability to derive more accurate surface chemistries could improve interpretations of weathering processes on Mars.

3 Effects of High-Silica Weathering Products on Thermal-Infrared Spectra and Models of Basaltic Igneous Mineral Mixtures

3.1 Introduction

Thermal-infrared (TIR) spectroscopy and linear unmixing models are primary methods by which the mineralogy of the Martian surface is determined. Knowing the surface mineralogy allows us to interpret past and present petrologic and aqueous alteration processes to decipher the geologic history of the planet. These interpretations are a function of the accuracy of TIR spectral models. In-situ and orbital data show that the Martian surface has experienced chemical weathering and aqueous alteration at local to regional scales [*Christensen et al.*, 2004; *Bibring et al.*, 2006; *Ming et al.*, 2006; *Rogers and Christensen*, 2007]. Previous studies of terrestrial weathered basalts reveal that chemical weathering results in non-linear mixing in TIR spectra so that the mineralogy of weathered surfaces cannot be accurately determined [*Kraft et al.*, 2003; *Michalski et al.*, 2006a; *Kraft*, 2009]; however, the precise effects of chemical weathering on spectral models are not well quantified. Recognizing the limitations of TIR spectral models and correcting for these effects is essential for accurately interpreting Martian geologic history.

Basalt weathering rinds are mineralogically and texturally complex and mostly comprised of unaltered igneous minerals with minor amounts of poorly-crystalline Si-Al-Fe-rich phases [*Colman*, 1982; *Michalski et al.*, 2006a]. These complexities make it difficult to quantify how weathering product composition, abundance, and surface texture affect spectral models. To eliminate the complexities within weathering rinds, physical mineral mixtures of basaltic igneous minerals with spectrally distinct, amorphous and crystalline high-silica weathering products were created. TIR emission spectra of the mixtures in loose particulate and compressed pellet configurations were measured and the mineral abundances were modeled with a linear least-squares fitting routine. The goals

of these experiments are 1) determine the effects that small to moderate amounts of different high-silica weathering products have on TIR spectra and models of basaltic igneous minerals; 2) determine the detection limits of amorphous and crystalline silicate weathering products; 3) examine the effects of surface texture on TIR spectra and spectral models; 4) determine how library composition and spectral resolution affect modeled mineralogy; and 5) apply the effects learned from the mixture experiments to spectral models of the Martian surface to further interpret igneous mineralogy and potential weathering processes.

3.2 Background

3.2.1 Interpreting chemical weathering environments on Mars

Understanding past and present weathering environments on the Martian surface are important for determining the history of liquid water on the planet and, thus, assessing habitability. Chemical weathering environments are generally inferred from in-situ chemical data and from the types of weathering products present. Chemical data measured by the Alpha Particle X-ray Spectrometers (APXS) on the Mars Exploration Rovers (MER) in Gusev and Meridiani indicate that soluble cations have been mobilized in some rocks and soils. At Gusev crater, Clovis class rocks are enriched in Br and Cl and the Paso Robles soil is highly enriched in S and P. At Meridiani, S and Br abundances are highly variable over short distances in the Eagle crater outcrops. These specific trends suggest acidic chemical weathering is a localized aqueous process [*Rieder et al.*, 2004; *Squyres et al.*, 2004b; *Gellert et al.*, 2006; *Ming et al.*, 2006]. Chemical data from rocks and soils at the MER, Pathfinder, and Viking landing sites show variation in Fe+Mg concentrations, which may imply that acidic chemical weathering and the preferential dissolution of olivine is a prominent, global alteration process [*Hurowitz and McLennan*, 2007].

Near-infrared (NIR) and thermal-IR (TIR) spectroscopy are principal methods for identifying chemical weathering products on the Martian surface. NIR spectroscopy, which is sensitive to absorptions from H_2O, hydroxyl, and metal-OH bond vibrations, is used to identify hydrated weathering products, such as clays. NIR data from the Observatoire pour la Mineralogie, l'Eau, les Glaces, et l'Activitie (OMEGA) and the Compact Reconnaissance Imaging Spectrometer on Mars (CRISM) show evidence for a wide variety of clay minerals, including smectites, kaolinite, and chlorite, in Noachian-aged terrains, particularly Mawrth Vallis, Nili Fossae, and portions of Terra Meridiani. The presence of clay minerals suggests that these regions experienced aqueous alteration at moderate to alkaline pH and high water-to-rock ratios [*Poulet et al.*, 2005; *Loizeau et al.*, 2007; *Mangold et al.*, 2007; *Bishop et al.*, 2008; *Mustard et al.*, 2008; *Noe Dobrea et al.*, 2008; *Wiseman et al.*, 2010]. Additionally, OMEGA and CRISM spectra have been used to identify hydrated sulfates and amorphous silica in Hesperian-aged terrains, such as Valles Marineris, Aram Chaos, portions of Terra Meridiani, and the north polar dunes, suggesting alteration at low pH and moderate water-to-rock ratios [*Bibring et al.*, 2005; *Gendrin et al.*, 2005; *Langevin et al.*, 2005; *Bibring et al.*, 2006; *Milliken et al.*, 2008; *Roach et al.*, 2008; *Horgan*, 2010; *Wiseman et al.*, 2010].

The thermal-IR spectral range displays absorptions from vibrational modes in a variety of mineral groups, and each mineral has a unique spectrum. TIR spectroscopy and spectral models are fundamental for the identification and quantification of igneous minerals on the Martian surface and, thus, understanding the petrologic evolution of the planet. These data show that the planet is dominantly basalt that has not experienced extensive aqueous alteration [*Christensen et al.*, 2000b]. However, there is evidence for aqueous alteration on localized scales and limited chemical weathering on regional scales. Data from the Thermal Emission Spectrometer (TES) and Mini-TES in Meridiani identify gray crystalline hematite, suggesting deposition in a body of water [*Christensen*

et al., 2004]. Mini-TES in Gusev identified amorphous silica-enriched rocks and soils at Home Plate, suggesting hydrothermal alteration [*Squyres et al.*, 2008; *Ruff et al.*, 2011]. The detection of salts in localized Noachian terrains by the Thermal Emission Imaging Spectrometer (THEMIS) provides further evidence for widespread aqueous alteration and cation mobility [*Osterloo et al.*, 2008]. High-silica weathering products, including phyllosilicates, amorphous silica, and zeolites, are commonly identified in TES models of regional, low-albedo surfaces [*Wyatt and McSween*, 2002; *Rogers and Christensen*, 2007; *Minitti and Hamilton*, 2010]; however, they are usually at or below the detection limit of linear deconvolution and their identities remain debated.

3.2.2 Linear Deconvolution and the Effects of Chemical Weathering on Thermal-Infrared Spectral Models

Linear deconvolution is a linear least squares fitting routine that assumes that the energy emitted from a surface is a linear combination of the energy emitted from each component of the surface, proportional to areal abundances [*Ramsey and Christensen*, 1998]. The technique fits a measured TIR spectrum with a library of end-member mineral spectra. Linear mixing works for certain geologic conditions in the TIR wavelength range (~5-50 microns) because minerals have high absorption coefficients in this spectral range and photons generally only interact with one mineral [*Thomson and Salisbury*, 1993; *Ramsey and Christensen*, 1998]. Linear deconvolution is a valid technique for modeling the mineralogy of unaltered igneous and metamorphic rocks and coarse-grained mineral mixtures. For such samples, it accurately returns mineral abundances within 5-10 vol.% [*Ramsey and Christensen*, 1998; *Feely and Christensen*, 1999; *Hamilton and Christensen*, 2000; *Wyatt et al.*, 2001].

Linear mixing does not occur when fine-grained particles or coatings are present because photons interact with multiple surfaces, significantly changing measured spectra. When fine-grained materials are present, the primary absorption bands (i.e. Reststrahlen

bands), where the absorption coefficient (k) is large, experience a decrease in spectral contrast. This occurs because photons interact with multiple surfaces, instead of a single surface, so that the energy measured by the detector is greater because it is a combination of emitted and reflected energy [*Lyon*, 1964; *Vincent and Hunt*, 1968; *Salisbury and Wald*, 1992; *Moersch and Christensen*, 1995; *Ramsey and Christensen*, 1998]. The regions between the Reststrahlen bands, where k is small, show an increase in spectral contrast because volume transmission occurs at these wavelengths and photons are absorbed as they pass through multiple particles [*Vincent and Hunt*, 1968; *Salisbury and Wald*, 1992; *Moersch and Christensen*, 1995; *Ramsey and Christensen*, 1998]. These particle-size effects make it difficult to apply linear deconvolution to surfaces with small grains because end members in the spectral library are generally coarse grained and do not have transmission or volume scattering features [*Ramsey and Christensen*, 1998]. For coated rocks, the emissivity spectrum can be described as a combination of the energy emitted from the coating and the energy emitted from the underlying rock that is transmitted through the coating [*Christensen and Harrison*, 1993]. The wavelength positions of k and refractive index (n) for silica coatings are offset in the Si-O stretching region [*Kraft*, 2009], where the peak n value occurs at 1050 cm^{-1} and the peak k value occurs at 1115 cm^{-1}. This offset creates a shoulder on the Si-O stretching absorption near 1050 cm^{-1} because the high n value at this wavelength causes more energy from the underlying rock to be refracted away from the detector [*Kraft*, 2009]. The refraction of the emitted energy from the underlying rock causes non-linear spectral mixing between the coating and underlying rock, making the models inaccurate.

Chemical weathering results in the precipitation of fine-grained secondary phases and thin coatings, so non-linear spectral mixing of primary and secondary minerals occurs in TIR spectra of weathered surfaces. TIR studies of natural and laboratory-generated weathered basalt surfaces show that minor amounts of high-silica weathering

products have large effects on TIR spectra. Natural silica coatings <3 microns thick on Hawaiian basalts completely mask the underlying basalt TIR spectrum [*Minitti et al.*, 2007], and synthetic silica coatings <6 microns thick on basalt slabs mask the underlying basalt spectrum [*Kraft et al.*, 2003]. TIR studies of desert varnish, a clay and manganese-iron-oxide-rich coating up to 100 microns thick [*Potter and Rossman*, 1977], show that varnish coatings >50 microns mask the absorptions from the underlying rock [*Christensen and Harrison*, 1993; *Rivard et al.*, 1993].

Spectral models of weathered basalt surfaces commonly overestimate or falsely identify high-silica phases because volumetrically small amounts of high-silica weathering products coat primary igneous minerals [*Michalski et al.*, 2006b; *Kraft*, 2009]. TIR models of palagonitized tephras from Hawaii that lack crystalline weathering products falsely identify phyllosilicates [*Hamilton et al.*, 2008], and TIR models of weathered basalts from Baynton, Australia severely overestimate phyllosilicate abundances even though the weathering products are generally poorly-crystalline and present in small abundances (Chapter 2). Spectral models of weathered Columbia River Basalts (CRBs) incorrectly identify aluminous phyllosilicates and volcanic glass, indicating that these materials may be interchangeable in spectral models [*Michalski et al.*, 2006b]. Poorly-crystalline weathering products may be falsely identified as phyllosilicates if spectral libraries lack appropriate non-crystalline materials, such as allophane [*Michalski et al.*, 2006a; *Hamilton et al.*, 2008; *McDowell and Hamilton*, 2009]. Alternatively, false detections of minerals in weathered surfaces may be the result of non-linear mixing effects from the presence of fine-grained secondary phases or secondary coatings [*Michalski et al.*, 2006b].

Non-linear mixing in weathered surfaces can impede the characterization of igneous mineralogy and the differentiation between primary and secondary high-silica phases. The modeled plagioclase-to-pyroxene (plag/px) ratios of weathered CRB

surfaces are significantly lower than the actual plag/px ratios [*Kraft et al.*, 2009], implying that igneous rock compositions modeled from TIR spectra of weathered rocks may be inaccurate. Furthermore, primary volcanic glasses and high-silica weathering products may replace one another in spectral models [*Wyatt and McSween*, 2002; *Michalski et al.*, 2006b]. Weathered basalt is spectrally similar to unaltered andesite in the TIR region because of spectral similarities between K-rich volcanic glass present in andesite and phyllosilicates and high-silica mineraloids present in weathered basalts [*Wyatt and McSween*, 2002; *Wyatt et al.*, 2004; *Michalski et al.*, 2006a]. These similarities spurred the debate over the origin of the compositional dichotomy on Mars and whether the high-silica phase identified in spectral models of mid-to-high-latitude surfaces is volcanic glass or a product of chemical alteration [*Bandfield et al.*, 2000; *Hamilton et al.*, 2001; *Wyatt and McSween*, 2002; *Hamilton and Minitti*, 2003; *Kraft et al.*, 2003; *Morris et al.*, 2003; *Ruff*, 2004; *Wyatt et al.*, 2004; *Michalski et al.*, 2005, 2006a, 2006b, *Kraft et al.*, 2009]. Mini-TES spectral models of Clovis and Watchtower class rocks in Gusev crater identify basaltic glass [*Ruff et al.*, 2006], which implies a lack of chemical weathering because glass is readily altered by aqueous fluids. Conversely, the chemistry derived from APXS measurements suggests that these surfaces have been moderately to extensively altered [*Ming et al.*, 2006].

3.2.3 Unresolved Issues with Interpreting Martian TIR Data

Thermal-infrared data have been instrumental in our understanding of the geologic history of Mars; however, a series of unresolved issues remain that must be addressed to further constrain petrologic and aqueous alteration processes. A crucial issue is the identity of the high-silica phases in spectral models. High-silica phases are detected in TES models globally, and these include phyllosilicates, zeolites, volcanic glasses, and amorphous silica [*Bandfield et al.*, 2000; *Bandfield*, 2002; *Wyatt and McSween*, 2002; *Ruff*, 2004; *Rogers and Christensen*, 2007; *Minitti and Hamilton*, 2010].

Individually, these phases are generally identified at or below the detection limit of linear deconvolution (~10 vol.%); however, they are grouped together when reporting modeled mineralogy because they are spectrally similar [*Wyatt and McSween*, 2002; *Michalski et al.*, 2006b]. A positive detection of any one of these phases individually would be indicative of very different aqueous alteration environments. For example, the presence of volcanic glass on the Martian surface would indicate very limited chemical weathering because glass is highly susceptible to aqueous alteration [*Ruff et al.*, 2006; *Rogers and Christensen*, 2007], while the presence of phyllosilicates would indicate aqueous alteration at high water-to-rock ratios and a wide range of potential pH depending on the type of phyllosilicate, and the presence of zeolites would indicate hydrothermal alkaline aqueous alteration. The identification of mixed high-silica phases in Martian spectral models could be a result of 1) the presence of various high-silica phases below the detection limit of deconvolution; 2) the presence of poorly-crystalline aluminosilicates that are spectrally similar to modeled high-silica phases, but absent from spectral libraries [*Michalski et al.*, 2005; *Hamilton et al.*, 2008; *McDowell and Hamilton*, 2009]; or 3) non-linear spectral mixing between rocks and secondary coatings/weathering rinds causing the false identification or overestimation of these phases [*Michalski et al.*, 2006b]. A better understanding of how different chemical weathering products affect TIR spectral models is necessary to characterize and quantify the high-silica phases on Mars.

NIR spectral data from OMEGA and CRISM indicate localized concentrations of phyllosilicates in Noachian terrains, while TES models generally do not identify phyllosilicates over the detection limit. The question remains, why don't TES models detect phyllosilicates in these areas? It has been speculated that 1) the detection limits of OMEGA and CRISM are lower than that of TES, and phyllosilicates are present in abundances below the TES detection limit; 2) phyllosilicates on Mars are loose, fine-grained materials so they are better detected by NIR spectroscopy; and 3) the lower

spatial sampling of TES compared to OMEGA and CRISM impedes the detection of phyllosilicates by TES [*Michalski and Fergason*, 2009]. Constraining phyllosilicate detection limits in TIR models will help determine the amounts of clay minerals that could be present in Martian surfaces that show NIR spectral evidence for clay.

It has been suggested that Martian mid-to-high latitude surfaces have experienced chemical weathering [*Wyatt and McSween*, 2002; *Wyatt et al.*, 2004; *Michalski et al.*, 2006a; *Kraft*, 2009]. Spectral models of the northern plains show that they are mineralogically distinct from the rest of the planet, with elevated plag/px ratios and large amounts of high-silica phases [*Bandfield et al.*, 2000; *Rogers and Christensen*, 2007]. Spectral models of terrestrial weathered basalts also identify large amounts of high-silica phases and suggest that chemical weathering compromises modeled igneous mineral abundances [*Michalski et al.*, 2006b; *Hamilton et al.*, 2008; *Kraft*, 2009]. To determine if the modeled mineralogy of the northern plains can be explained by chemical weathering and to constrain the extent of weathering, it is important to ascertain how different styles of weathering and the presence of different weathering products affect modeled mineralogy.

The effects of dust on TIR spectra of basalts have been well-characterized [*Johnson et al.*, 2002a; *Graff*, 2003]. Dust coatings cause non-linear spectral mixing between the dust and basalt substrate [*Graff*, 2003]. Areal dust abundances can be estimated with linear unmixing models, while dust coating thickness cannot and correlates in a quadratic manner. Because of these nonlinearities, TIR spectral models from dust-covered regions on Mars are assumed to be invalid [*Rogers and Christensen*, 2007]. Dusty terrains can be identified from TIR spectra using a dust cover index [*Ruff and Christensen*, 2002]. What remains unknown is how small amounts of very fine-grained silicate weathering products affect the modeled mineralogy.

To address these issues and to better understand the effects of chemical weathering on TIR spectra and spectral models, TIR spectra of loose and compressed particulate mixtures of basaltic igneous minerals and high-silica weathering products were measured and modeled. The goals of this study are: 1) determine how the type of silicate weathering product and surface texture affect modeled high-silica phases and if any cases cause the false detection of volcanic glass; 2) constrain the detection limits of different silicate weathering products and determine how surface texture affects detection limits; 3) characterize the effects of different weathering products and surface textures on modeled igneous mineral abundances; and 4) determine how spectral library composition and spectral resolution affect modeled high-silica phases and igneous minerals.

3.3 Methods

3.3.1 Sample Preparation

Mixtures of sand-sized igneous minerals, commonly found in basalt, and clay-sized secondary silicates were prepared for TIR emission spectroscopy. The igneous minerals included augite (clinopyroxene, WAR-6474), andesine (plagioclase feldspar, BUR-240), and olivine (Fo91, from San Carlos, Arizona), and the secondary silicates were smectite (Na-montmorillonite, SWy-1) and amorphous silica. The igneous minerals and secondary phases are spectrally distinct from one another to best understand the effects of different types of weathering products on spectral models of basaltic minerals (Figure 3.1, Table 3.1). The igneous starting minerals and montmorillonite are well-characterized mineral standards [*Christensen et al.*, 2000a], and the amorphous silica was obtained through evaporation of a colloidal silica solution [*Kraft et al.*, 2003]. The igneous minerals were crushed with an agate mortar and pestle, sieved, and washed with ethanol to obtain 76-105 micron-sized particles. The secondary silicates were crushed with an agate mortar and pestle and centrifuged to obtain the <2 micron size fraction.

Two-component mixtures were composed of one igneous mineral and one secondary silicate, (Table 3.2) and three-component mixtures were composed of two igneous minerals in 1:1 abundances by weight and one secondary silicate (Table 3.3). Secondary silicates comprised 2.5, 5, 10, and 20 wt.% of the mineral mixtures. Approximately 5 mL of distilled water were added to ~0.5 g of each mixture to suspend the secondary phase. The solution was evaporated overnight in a Pyrex watch glass to coat the primary mineral particles with the secondary silicate. Mixtures of igneous minerals in 1:1 abundances by weight without a secondary silicate were prepared as a control for investigating deconvolution results of the three-component mineral mixtures.

Naturally weathered surfaces have a variety of textures, from loose, unconsolidated soil to dense rock coatings. In the TIR spectral range, unconsolidated particles can cause volume scattering and transmission features, causing significant changes to measured spectra, as discussed above. TIR spectra of loose particulate samples and compressed pellets were measured to investigate the effect of particle coherence on spectral morphology and deconvolution results. Pellets were created by compressing ~0.2 g of sample mixtures to ~70 MPa (uncorrected for friction) in a hydraulic press for three minutes [*Michalski et al.*, 2005]. Pellets were 1 cm in diameter and a few mm thick.

3.3.2 Instrumentation, Spectroscopy, and Deconvolution

TIR spectra were collected at the Mars Space Flight Facility at Arizona State University using a Nicolet Nexus 670 spectrometer configured to measure emitted energy [*Christensen and Harrison*, 1993; *Ruff et al.*, 1997]. Samples were placed in copper

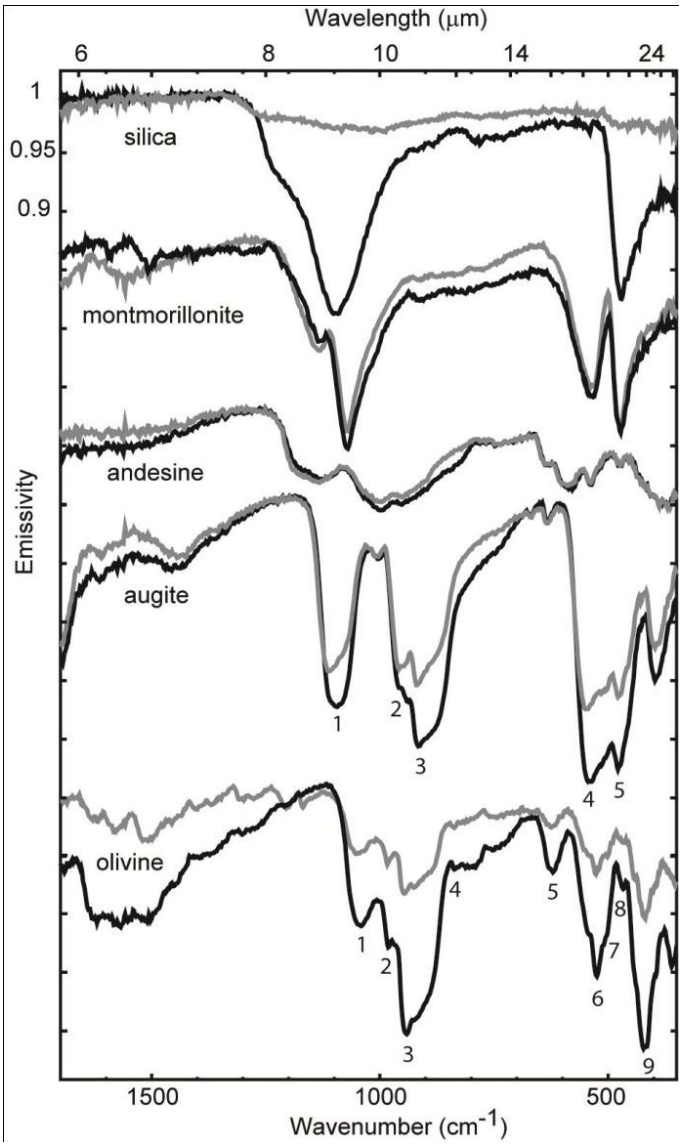

Figure 3.1. TIR emissivity spectra of starting materials in the mixtures. Particulate spectra are in gray and compressed pellet spectra are in black. Critical absorptions (CAs) in augite from *Hamilton* [2000] and bands in olivine from *Hamilton* [2010] are numbered. Spectra are offset in emissivity for clarity.

Table 3.1. Band assignments for phases in mineral mixtures

Mixture End-Member	Absorption Position (cm^{-1})	Bond Vibration
Plagioclase feldspar (Andesine)	900-1200	Si-O antisymmetric stretch in silica tetrahedra[1]
	750-850	SiO_6 octahedral stretch[1]
	450-700	Si-O-Si octahedral bend[1]
	400-550	Bending vibrations in Si-Al-O planar ring[1]
Clinopyroxene (Augite)	1050-1150	Si-O_{br} (bridging oxygen) stretch[2]
	1000-1050, 950-1000, 850-950	Si-O_{nb} (non-bridging oxygen) stretch[2]
	<600	O-Si-O bond deformations[2]
Olivine (Fo_{91})	900-1100	Asymmetric stretch in silica tetrahedron[3]
	750-850	Symmetric stretch in silica tetrahedron[3]
	500-650	Asymmetric bend in silica tetrahedron[3]
	400-475	Symmetric bend in silica tetrahedron[3]
	325-400	Rotation of silica tetrahedron[3]
Amorphous silica	1000-1250	Si-O symmetric stretch[4]
	400-500	O-Si-O bending vibration[5]
Montmorillonite	1100-1200	Si-O stretch, longitudinal mode[6]
	1000-1100	Si-O stretch[6]
	500-600	Al-O-Si deformations[6]
	425-500	Si-O-Si deformation[6]

[1] *Johnson et al.* [2002b]
[2] *Tomisaka and Iishi* [1980]
[3] *Fabian et al.* [2001]
[4] *Thompson and Salisbury* [1993]
[5] *Michalski et al.* [2003]
[6] *Madejova and Komadel* [2001]

Table 3.2. Primary and secondary phases and abundances of secondary phases present in the two-component mixtures

	Montmorillonite (wt%)	Amorphous Silica (wt%)
Augite	2.5, 5, 10, 20[a]	2.5, 5, 10, 20[d]
Andesine	2.5, 5, 10, 20[b]	2.5, 5, 10, 20[e]
Olivine	2.5, 5, 10, 20[c]	2.5, 5, 10, 20[f]

[a] Mixtures were made according to weight percent secondary silicate, but spectral models report abundances in volume percent. Montmorillonite abundances in mixtures with augite are 3.3, 6.6, 13, and 25.2 vol.% for 2.5, 5, 10, and 20 wt%, respectively.
[b] Montmorillonite abundances in mixtures with andesine are 2.6, 5.2, 10.3, and 20.6 vol.% for 2.5, 5, 10, and 20 wt%, respectively.
[c] Montmorillonite abundances in mixtures with olivine are 3.2, 6.3, 12.4, and 24.1 vol.% for 2.5, 5, 10, and 20 wt%, respectively.
[d] Silica abundances in mixtures with augite are 4.1, 8.1, 15.6, and 29.4 vol.% for 2.5, 5, 10, and 20 wt%, respectively.
[e] Silica abundances in mixtures with andesine are 3.2, 6.3, 12.5, and 24.3 vol.% for 2.5, 5, 10, and 20 wt%, respectively.
[f] Silica abundances in mixtures with olivine are 3.9, 7.6, 14.9, and 28.2 vol.% for 2.5, 5, 10, and 20 wt%, respectively.

Table 3.3. Primary and secondary phases and abundances of secondary phases present in the three-component mixtures

	Montmorillonite (wt%)	Amorphous Silica (wt%)
1:1 Augite: Andesine	0, 2.5, 5, 10, 20[a]	0, 2.5, 5, 10, 20[d]
1:1 Olivine: Augite	0, 2.5, 5, 10, 20[b]	0, 2.5, 5, 10, 20[e]
1:1 Olivine: Andesine	0, 2.5, 5, 10, 20[c]	0, 2.5, 5, 10, 20[f]

[a] Montmorillonite abundances in mixtures with augite-andesine are 2.9, 5.8, 11.5, and 22.7 vol.% for 2.5, 5, 10, and 20 wt.%, respectively.
[b] Montmorillonite abundances in mixtures with olivine-augite are 3.2, 6.4, 12.7, and 24.6 vol.% for 2.5, 5, 10, and 20 wt.%, respectively.
[c] Montmorillonite abundances in mixtures with olivine-andesine are 2.8, 5.7, 11.3, and 22.2 vol.% for 2.5, 5, 10, and 20 wt.%, respectively.
[d] Silica abundances in mixtures with augite-andesine are 3.6, 7.1, 13.9, and 26.6 vol.% for 2.5, 5, 10, and 20 wt.%, respectively.
[e] Silica abundances in mixtures with olivine-augite are 4.0, 7.8, 15.2, and 28.8 vol.% for 2.5, 5, 10, and 20 wt.%, respectively.
[f] Silica abundances in mixtures with olivine-andesine are 3.5, 6.9, 13.6, and 26.1 vol.% for 2.5, 5, 10, and 20 wt.%, respectively.

sample cups painted black so that they behave as a spectral blackbody, and heated to 80° C before and during the experiments to increase the signal-to-noise ratio. Spectra were scanned 240 times over the course of ~4 minutes, from 200-2000 cm^{-1} with 2 cm^{-1} spectral resolution. Two blackbodies at 70 °C and 100 °C were measured to calibrate raw data to radiance [*Christensen and Harrison*, 1993]. Radiance spectra were transformed to emissivity spectra by normalizing to the Planck curve corresponding to the sample temperature [*Ruff et al.*, 1997].

Two distinct spectral libraries were created to examine the effects of library composition on modeled mineral abundances. Library 1 contained spectra of minerals commonly found in basalts and weathered basalts, including plagioclase solid solutions, orthopyroxenes, clinopyroxenes, olivine, phyllosilicates, primary and secondary amorphous silica (silica-rich and basaltic glasses and opal-A), and accessory minerals (Table 3.4). Spectra of the phases in the mixtures were included to test whether non-linear mixing occurred; in the absence of non-linear mixing, the model should retrieve the phases present in the mixtures in the correct abundances. The spectrum of particulate silica was omitted because it is spectrally neutral (i.e. lacks absorptions). Spectrally neutral phases may be used in spectral models as a blackbody to uniformly reduce the spectral contrast of the model to fit that of the measured spectrum [*Wyatt et al.*, 2001]. Library 1 also contained two lines with negative slopes to account for emissivity spectra with negatively sloped continua (with increasing wavelength). Negative slopes are imparted on samples when the radiance spectrum of a sample is calibrated with a Planck curve corresponding to a temperature lower than that of the sample. A Planck curve corresponding to a lower temperature may be selected if the sample is not thermally equilibrated or if the spectrum has an emissivity less than 1.0 at the Christiansen feature (where the refractive index is 1, which is ~1300 cm^{-1} for silicates) [*Ruff et al.*, 2006]. The slopes of the lines were normalized to an emissivity of 1.0 at 1300 cm^{-1}. Library 2 is

similar to that used by *Rogers and Christensen* [2007] to model TES data and includes minerals commonly found in basalts and weathered basalts. Library 1 differs from Library 2 in that Library 1 contains basaltic glass, while Library 2 does not, and Library 2 contains quartz, zeolites, sulfates, carbonates, and more olivine solid solutions, while Library 1 does not (Table 3.4). A blackbody spectrum was added to each library to account for differences in spectral contrast between the library and mixture spectra. Modeled phase abundances were normalized after excluding blackbody and slope end members.

Spectra were modeled using a non-negative least squares fitting routine [*Lawson and Hanson*, 1974], as modified by *Rogers and Aharonson* [2008]. Linear deconvolution was performed over the wavelength range 1360-305 cm^{-1} for spectra with 2 cm^{-1} and 10 cm^{-1} spectral sampling, which are the sampling resolutions of the lab spectrometer and TES, respectively. Modeled abundances are reported in volume percent (vol.%), but the mixtures were prepared according to abundance by weight. Areal abundances of secondary silicates in the physical mixtures are reported in Tables 3.2 and 3.3 in terms of vol.% because modeled abundances for a surface are assumed to be similar throughout the material. Detection limits for secondary silicates were quantified by determining how much must be present in the mixtures to consistently cause a positive detection in spectral models.

3.4 Results

3.4.1 Effects of High-Silica Weathering Products on Igneous Mineral Spectra

The spectral effects of adding a high-silica weathering product to igneous mineral(s) are dependent on the composition of the weathering product and igneous mineral(s) present and the mixture's surface texture. The specific spectral effects observed in each mixture are described in detail in Tables 3.5 and 3.6. A universal effect

observed for mixtures without andesine is a shift in the primary Christiansen frequency (CF) to shorter wavelengths with the addition of amorphous silica or montmorillonite. The addition of silica to particulate mixtures causes the dampening of all igneous mineral absorptions, except for the two-component mixture with andesine (Figures 3.2, 3.3). The addition of silica to pellet mixtures causes a sharpening of the augite and olivine absorptions that overlap those of silica, while the other igneous mineral absorptions dampen (Figures 3.4, 3.5). Conversely, when silica is added to pellet mixtures with andesine, the andesine absorptions dampen and the spectral signature from silica is not apparent (Figure 3.4). The addition of montmorillonite to particulate mixtures causes a reduction in the emissivity of the secondary Christiansen frequency (~1250 cm^{-1}), imparting an overall negative slope to the spectra (Figure 3.2). The addition of montmorillonite to particulate mixtures causes the augite and olivine absorptions that overlap those of montmorillonite to sharpen and retain high spectral contrast, while the other igneous mineral absorptions dampen (Figures 3.2, 3.3). A short wavelength shoulder at ~1120 cm^{-1} from montmorillonite appears in augite and olivine mixtures with $\geq$10 wt.% clay, and absorptions from montmorillonite are apparent in andesine mixtures with $\geq$5 wt.% clay. The addition of montmorillonite to pellet mixtures results in a much greater spectral contrast than particulate mixtures with montmorillonite (Figures 3.4, 3.5). Augite and olivine absorptions behave similarly to the particulate mixture spectra with montmorillonite, and montmorillonite absorptions are visible in pelletized andesine mixtures with $\geq$10 wt.% clay.

3.4.2 Effects of High-Silica Weathering Products on Modeled Mineral Abundances

Modeled mineral abundances from spectral models of the mineral mixtures display trends that are dependent on the weathering product composition, the type(s) of igneous mineral(s) present, and the mixture's surface texture. The specific model results using Library 1 for each mixture are described in detail in Tables 3.7 and 3.8. Here, the

Table 3.4. TIR spectral libraries

Mineral Group	Spectral End Member	Composition
Quartz	Quartz BUR-4120†	SiO_2 [a]
Feldspar	Albite WAR-0235 174*	$Na_{0.97}(Al_{1.02}Si_{2.96})O_8$ [b]
	Albite WAR-0244†	$(K_{0.04}Na_{0.87}\ Ca_{0.02})(Al_{0.95}Si_{3.05})O_8$ [b]
	Andesine WAR-0024 175*	$K_{0.04}(Na_{0.4}Ca_{0.45})(Mg_{0.17})(Al_{1.29}Si_{2.51})O_8$ [b]
	Andesine BUR-240†	$K_{0.04}(Na_{0.4}Ca_{0.45})(Mg_{0.17})(Al_{1.29}Si_{2.51})O_8$ [b]
	Andesine BUR-240 1: 75-106 μm pellet*	$K_{0.04}(Na_{0.4}Ca_{0.45})(Mg_{0.17})(Al_{1.29}Si_{2.51})O_8$ [b]
	Anorthite BUR-340†	$(Na_{0.08}Ca_{0.89})(Fe_{0.02}Mg_{0.03})(Al_{1.98}Si_{2.03})O_8$ [b]
	Anorthite WAR-5759 221*	$CaAl_2Si_2O_8$ [a]
	Bytownite WAR-1384 177*†	$K_{0.02}(Na_{0.32}Ca_{0.57})(Fe_{0.01}Mg_{0.03})(Al_{1.63}Si_{2.30})O_8$ [b]
	Labradorite WAR-RGAND01 222*	Ab50An50-Ab30An70 [a]
	Labradorite BUR-3080A 176*	$K_{0.07}(Na_{0.44}Ca_{0.48})(Fe_{0.06}Mg_{0.04}Ti_{0.03})(Al_{1.44}Si_{2.47})O_8$ [b]
	Labradorite WAR-4524†	$K_{0.01}(Na_{0.53}Ca_{0.49})(Al_{1.58}Si_{2.44})O_8$ [b]
	Microcline BUR-3460†	$(K_{0.76}Na_{0.28})(Al_{1.04}\ Si_{2.96})O_8$ [b]
	Oligoclase BUR-060D 69*	$(K_{0.05}Na_{0.82}Ca_{0.16})Fe_{0.14}(Al_{1.17}Si_{2.72})O_8$ [b]
	Oligoclase WAR-0234 22*	$K_{0.05}(Na_{0.58}Ca_{0.26})(Al_{1.16}Si_{2.73})O_8$ [b]
	Oligoclase WAR-5804†	$(K_{0.03}Na_{0.78}Ca_{0.23})(Al_{1.26}Si_{2.75})O_8$ [b]
	Orthoclase WAR-RGSAN01 219*†	$KAlSi_3O_8$ [a]
	Shocked An 22.6 GPa	$CaAl_2Si_2O_8$ [a]
	Shocked An 56.3 GPa	$CaAl_2Si_2O_8$ [a]
Orthopyroxene	Bronzite BUR-1920†	$(Ca_{0.03}Mg_{1.51}Fe_{0.42})(Al_{0.02}Si_{1.98})O_6$ [b]
	Bronzite NMNH-93527†	$(Ca_{0.06}Mg_{1.43}Fe^{2+}_{0.36}Fe^{3+}_{0.05}Al_{0.08})(Al_{0.14}Si_{1.86})O_6$ [b]
	Bronzite NMNH-166555 148*	$(Ca_{0.01}Mg_{1.51}Fe^{2+}_{0.39}Fe^{3+}_{0.04}Al_{0.05})(Al_{0.10}Si_{1.90})O_6$ [b]
	Enstatite HS-94.B†	$(Ca_{0.02}Mg_{1.77}Fe_{0.20})Si_2O_6$ [b]
	Enstatite NMNH-38833 144*	$(Ca_{0.01}Mg1.76Fe^{2+}_{0.19}Fe^{3+}_{0.03})(Al_{0.04}Si_{1.96})O_6$ [b]
Clinopyroxene	Augite DSM-AUG01 164*	$(Ca_{0.85}Mg_{0.83}Fe_{0.27}Na_{0.03}Ti_{0.02})(Al_{0.13}Si_{1.87})O_6$ [b]
	Augite NMNH-9780†	$(Ca,Mg,Fe^{2+},Fe^{3+},Ti,Al)_2(Si,Al)_2O_6$ [a]
	Augite NMNH-119197 147*	$(Ca_{0.94}Mg_{0.80}Fe_{0.19}Na_{0.03}Al_{0.03})Si_2O_6$ [b]
	Augite NMHN-122302†	$(Ca,Mg,Fe^{2+},Fe^{3+},Ti,Al)_2(Si,Al)_2O_6$ [a]
	Augite WAR 6474: 75-106 μm sand*	$(Ca_{0.86}Mg_{0.56}Fe^{2+}_{0.20}Fe^{3+}_{0.20}Na_{0.15}Al_{0.02})(Al_{0.08}Si_{1.92})O_6$ [b]
	Augite WAR 6474: 75-106	$(Ca_{0.86}Mg_{0.56}Fe^{2+}_{0.20}Fe^{3+}_{0.20}Na_{0.15}Al_{0.}$

	μm pellet*	$_{02})(Al_{0.08}Si_{1.92})O_6$ [b]
	Diopside NMNH-107497 146*	$(Ca_{0.99}Mg_{0.98}Fe_{0.03})Si_2O_6$ [b]
	Diopside WAR-6474†	$(Ca_{0.86}Mg_{0.56}Fe^{2+}_{0.20}Fe^{3+}_{0.20}Na_{0.15}Al_{0.02})(Al_{0.08}Si_{1.92})O_6$ [b]
	Hedenbergite, manganoan DSM-HED01 145*†	$(Ca_{0.98}Mg_{0.26}Fe_{0.47}Mn_{0.27})Si_2O_6$ [b]
	Pigeonite†	$(Mg,Fe^{2+},Ca)(Mg,Fe^{2+})Si_2O_6$ [a]
Olivine	Fayalite WAR-RGFAY01 167*†	Fe_2SiO_4 [a]
	Forsterite BUR-3720A 8*†	$(Mg_{1.84}Fe_{0.16})SiO_4$ [b]
	KI 3115 Fo68†	Fo68[c]
	KI 3662 Fo60†	Fo60[c]
	KI 3373 Fo35†	Fo35[c]
	KI 3008 Fo10†	Fo10[c]
Zeolite	Crystalline heulandite†	$(Ca,Na)_{2-3}Al_3(Al,Si)_2Si_{13}O_{36}\cdot 12(H_2O)$ [a]
	Crystalline stilbite†	$NaCa_4[Al_8Si_{28}O_{72}]\cdot 28\text{-}32(H_2O)$ [a]
Sheet Silicates	Antigorite NMNH-47108†	$Mg_3Si_2O_5(OH)_4$ [a]
	Biotite BUR-840†	$K_{1.75}Mg_{3.25}Fe_{2.32}Al_{2.07}Ti_{0.51}Si_{6.09}(OH,F)_{0.72}$ [b]
	Illite IMt-1 <0.2 μm†	$(K_{1.35},Na_{0.02})Al_{3.41}[Si_{7.26}(Fe_{0.67},Mg_{0.55})O_{20}](OH)_4$ [b]
	Illite IMt-2 <0.2μm pellet*	$K_{1.5\text{-}1.0}Al_4[Si_{6.5\text{-}7.0}Al_{1.5\text{-}1.0}O_{20}](OH)_4$ [a]
	Swy-1 montmorillonite < 0.2 μm pellet*	$M_{0.33}(Al_{1.54}Fe_{0.2}Mg_{0.23})(Si_{3.97}OAl_{0.03})O_{10}(OH)_2$ [d]
	Ca-montmorillonite STx-1 <0.2 microns†	$(Ca_{0.1},Na_{0.03})(Al_{1.13}Mg_{0.33})Si_{4.18}O_{10}(OH)_2$ [b]
	Muscovite WAR-5474†	$K_2Al_4[Si_6Al_2O_{20}](OH,F)_4$ [a]
	NAu-2 nontronite < 0.2 μm pellet*	$R_{0.33}Fe_2(Si_{3.67}Al_{0.33})O_{10}(OH)_2$ [a]
	Saponite <0.2 μm pellet*†	$R_{0.33}(Mg_{2.67}R_{0.33})(Si_{3.34}Al_{0.66})O_{10}(OH)_2$ [a]
	Serpentine HS-8.4B†	$Mg_{2.36}[Si_{1.72}O_5](OH)_4$ [b]
	Serpentine 1690 ASU 710-1000 μm particulate*	$(Mg_{2.76}Fe_{0.32})Al_{0.06}Si_{1.83}O_5OH_4$ [b]
Amorphous Silicates	Al-opal†	78.7 wt.% SiO_2, 8.2% Al_2O_3, 1.5 wt.% FeO[e]
	K-rich glass*†	77.9 wt% SiO_2, 5.67 wt% K_2O [f]
	LC m8_1201b basalt glass*	50.6 wt% SiO_2[g]
	Quenched basaltic glass*	50.2 wt% SiO_2[f]
	Opal-A*†	$SiO_2\bullet nH_2O$ [a]
	Silica Glass*	SiO_2 [a]
	Synthetic amorphous silica: <20 μm pellet*	SiO_2 [a, h]
Amphibole	Actinolite HS-116.4B†	$(Ca_{1.82}Na_{0.13})(Mg_{4.39}Fe_{0.55})(Si_{7.60}Al_{0.04})O_{22}(OH)_2$ [b]
	Magnesiohastingsite HS-115.4B†	$(Na_{0.45}K_{0.15})(Ca_{1.85}Na_{0.15})(Mg_{3.60}Fe_{0.84}Al_{0.13}Ti_{0.03})(Al_{1.71}Si_{6.29})O_{22}(OH)_2$ [b]

	Magnesiohornblende WAR-0354†	$(Ca_{1.71}Na_{0.09})(Mg_{4.20}Fe_{0.64})(Si_{7.31}Al_{0.21})O_{22}(OH)_2$ [b]
Carbonate	Calcite C40†	$CaCO_3$ [b]
	Dolomite C20†	$Ca_{104}Mg_{96}(CO_3)_2$ [b]
Sulfate	Anhydrite ML-S9†	$Ca_{104}Mg_{96}(CO_3)_2$ [b]
	Gypsum ML-S6†	$CaSO_4 \cdot 2H_2O$ [a]
Accessory	Apatite ML-P2 96*	$Ca_5(PO_4)_3(F,Cl,OH)$ [a]
Mins.	Ilmenite WAR-4119 35*	$FeTiO_3$ [a]
	Hematite BUR-2600 50*†	Fe_2O_3 [a]
Sloped lines	-1E-5 slope*	
	-5E-5 slope*	
Blackbody	Blackbody*†	

* End members in Library 1
† End members in Library 2
[a] Stoichiometric compositions
[b] Composition from microprobe data from *Christensen et al.* [2000a]
[c] *Koeppen and Hamilton* [2008]
[d] *Madejová et al.* [1998]
[e] *Gallup* [1997]
[f] *Wyatt et al.* [2001]
[g] *Cherednik* [2001]
[h] *Kraft et al.* [2003]

general trends from models using Library 1 are described. Models of particulate mixtures with silica overestimate plagioclase abundances for mixtures that contain andesine and falsely identify significant (>10 vol.%) plagioclase abundances for mixtures without andesine. Models of particulate silica-augite mixtures falsely identify more plagioclase than models of particulate silica-olivine mixtures (Figure 3.6). The overestimation of plagioclase causes an increase in modeled plag/px ratios with the addition of silica to andesine-augite mixtures (Figure 3.7). Models of pellet mixtures with silica overestimate high-silica phase abundances and falsely detect significant abundances of volcanic glass when $\geq$10 wt.% silica is present (Figure 3.8). Models of particulate mixtures with montmorillonite generally overestimate phyllosilicate abundances and underestimate igneous mineral abundances in mixtures with $\geq$10 wt.% clay, while the same is true for models of pellet mixtures with $\geq$5 wt.% clay (Figure 3.9). However, the presence of olivine reduces phyllosilicate detections because olivine absorptions obscure those of montmorillonite, and models of montmorillonite-olivine particulates and pellets and montmorillonite-plagioclase pellets do not identify any high-silica phases in mixtures with 2.5 and 5 wt.% clay.

3.4.3 Effect of Spectral Library Composition on Modeled Mineralogy

The general modeled trends described above are similar for models using Library 2 with a few notable exceptions. Two major differences between Libraries 1 and 2 are that 1) Library 1 lacks zeolite, while Library 2 contains two zeolites, and 2) Library 1 contains two basaltic glasses, while Library 2 does not contain any. Models with Library 2 falsely identify zeolite (both heulandite and stilbite) in mixtures with montmorillonite but do not identify zeolite in mixtures with silica. Models of mixtures with $\geq$10 wt.% montmorillonite can identify significant zeolite abundances, and models of mixtures with 5 and 10 wt.% montmorillonite can report greater amounts of zeolites than phyllosilicates (Figure 3.10). Models of mixtures with 20 wt.% montmorillonite identify more

Table 3.5. Spectral trends with the addition of secondary silicates to mixtures with one basaltic igneous mineral. CA = critical absorption, CF = Christiansen Frequency

	Silica		Montmorillonite	
	particulates	Pellets	Particulates	Pellets
Augite	-Primary CF shifts to shorter wavelengths -Secondary CF emissivity reduced -Augite absorptions dampen -Spectral contrast CA4 = CA5	-Primary CF shifts to shorter wavelengths -CA 1 sharpens and spectral contrast increases -CAs 2, 3, 4 dampen -Spectral contrast CA4 << CA5	-Primary CF shifts to shorter wavelengths -Secondary CF emissivity reduced -CA 1 sharpens -CAs 2, 3 dampen -Spectral contrast CA4 = CA5	-Primary CF shifts to shorter wavelengths -Secondary CF emissivity shifts to shorter wavelengths -CAs 1, 4, 5 sharpen and spectral contrast increases -CAs 2, 3 dampen -Spectral contrast CA4 = CA5
Andesine	No change	All andesine absorptions dampen	-Primary CF shifts to shorter wavelengths -Secondary CF emissivity reduced -New absorption ~1070 cm^{-1} with 5 wt.% clay	Absorptions ~1120, 1070, 550, 470 cm^{-1} from montmorillonite visible with 10 wt.% clay
Olivine	-Primary CF shifts to shorter wavelengths -Olivine absorptions dampen	-Primary CF shifts to shorter wavelengths -Band 8 spectral contrast increases -Bands 2-6, 9 dampen -New absorption near 1110 cm^{-1} with 20 wt.% silica	-Primary CF shifts to shorter wavelengths -Secondary CF emissivity reduced -Bands 1, 8 sharpen and spectral contrast increases -Bands 3, 5, 9 dampen -New absorption near 1120 cm^{-1} with 10 wt.% clay	-Primary CF shifts to shorter wavelengths -Bands 1, 6, 8 sharpen and spectral contrast increases -Bands 3, 5 dampen -New absorption near 1120 cm^{-1} with 10 wt.% clay

Table 3.6. Spectral trends with the addition of secondary silicates to mixtures with two basaltic igneous minerals. CA = critical absorption, CF = Christiansen Frequency

	Silica		Montmorillonite	
	particulates	pellets	Particulates	Pellets
Plag-Px	-Primary CF shifts to shorter wavelengths -Augite and andesine absorptions dampen	-Primary CF shifts to shorter wavelengths -Augite CAs 1, 5 sharpen -Augite CAs 2, 3, 4 dampen -Spectral contrast augite CA4 << CA 5	-Augite CAs 1, 4, 5 sharpen and spectral contrast increases -Augite CAs 2, 3 dampen	-Augite CAs 1, 4, 5 sharpen and spectral contrast increases -Augite CAs 2, 3 dampen
Oliv-Plag	-Primary CF shifts to shorter wavelengths -Olivine and andesine absorptions dampen	-Primary CF shifts to shorter wavelengths -Olivine bands 2, 5, 6 dampen -Olivine band 8 sharpens and spectral contrast increases	-Olivine bands 1, 6, 8 sharpen and spectral contrast increases -Olivine bands 3, 5 dampen	-Olivine bands 1, 6, 8, 9 sharpen and spectral contrast increases -Emissivity of secondary CF reduces -Absorptions ~1120, 1070 cm^{-1} with 5 wt.% clay
Oliv-Px	Olivine and augite absorptions dampen	-Primary CF shifts to shorter wavelengths -Olivine bands 3-9 dampen -Augite CAs 2-5 dampen -New absorption near 1110 cm^{-1} with 10 wt.% silica	-Primary CF shifts to shorter wavelengths -Olivine bands 1, 6, 8 sharpen and spectral contrast increases -Olivine band 3 dampens -Augite CA 1 sharpens -Augite CAs 2, 3 dampen	-Primary CF shifts to shorter wavelengths -Olivine bands 1, 6, 8 sharpen and spectral contrast increases -Olivine band 3 dampens -Augite CAs 1, 4, 5 sharpen and spectral contrast increases -Augite CAs 2, 3 dampen

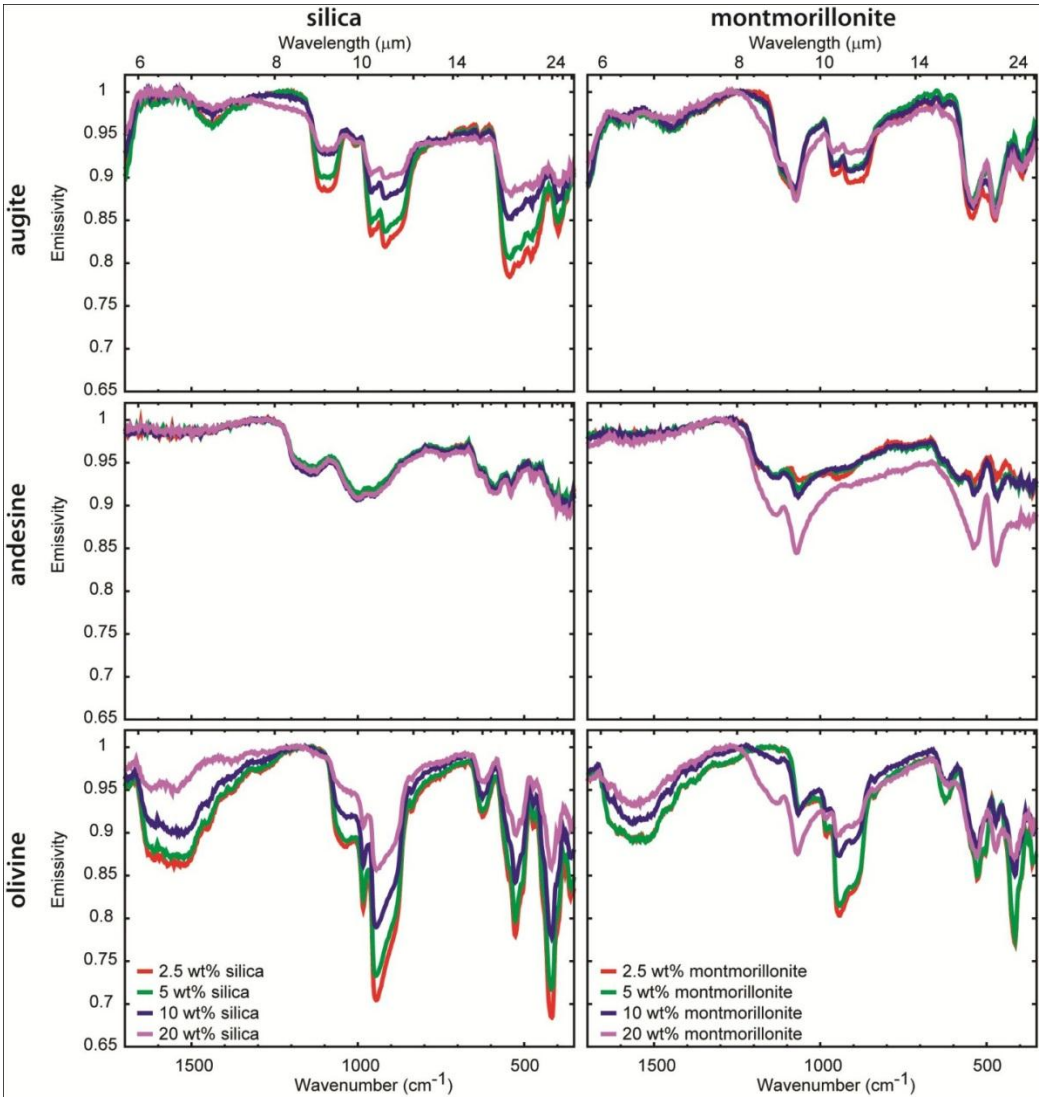

Figure 3.2. TIR emissivity spectra of particulate mixtures with one igneous mineral. See Table 3.5 for a description of spectral effects from adding particulate silica or montmorillonite to basaltic igneous minerals.

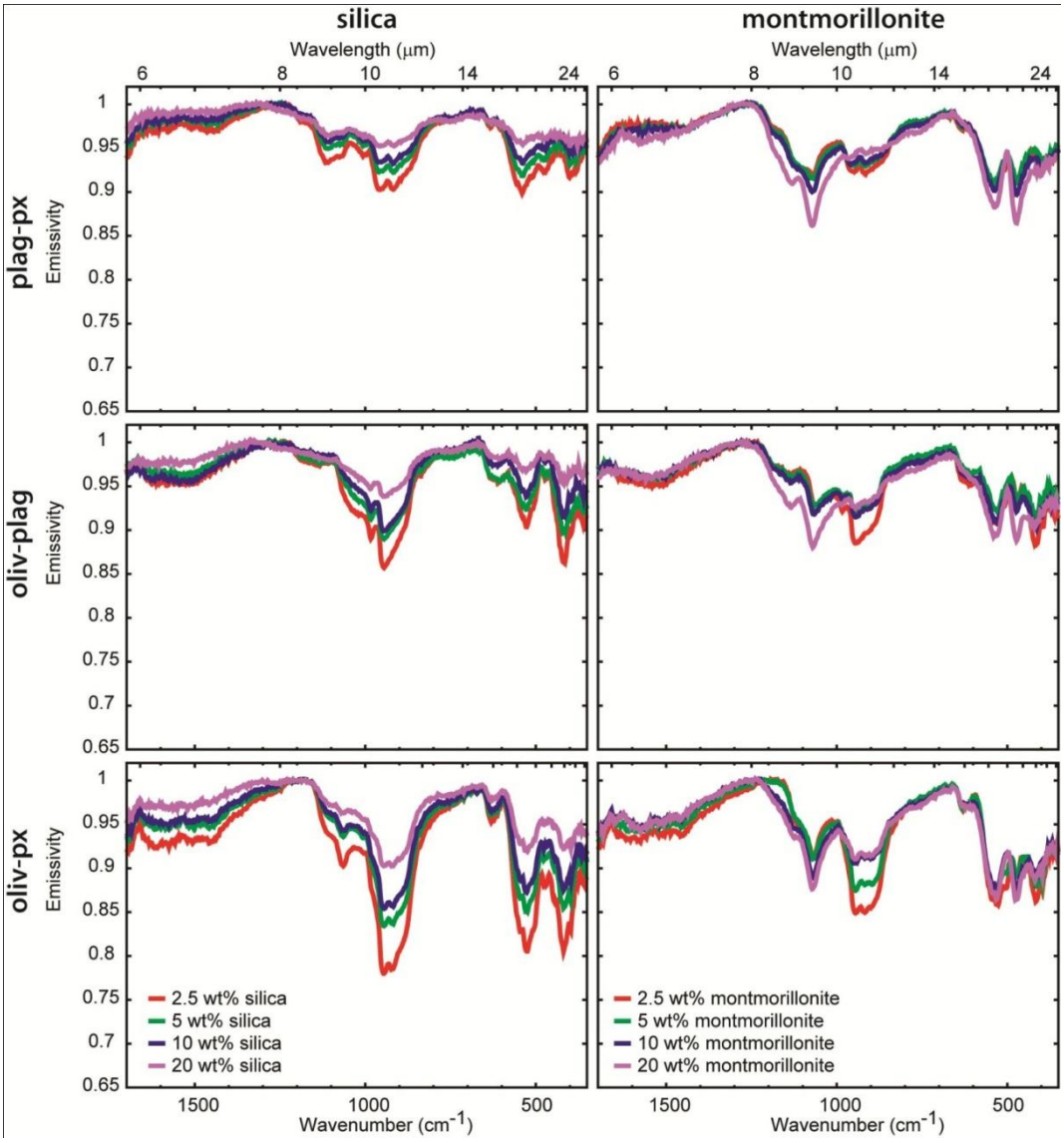

Figure 3.3. TIR emissivity spectra of particulate mixtures with two igneous minerals. See Table 3.6 for a description of spectral effects from adding particulate silica or montmorillonite to two basaltic igneous minerals.

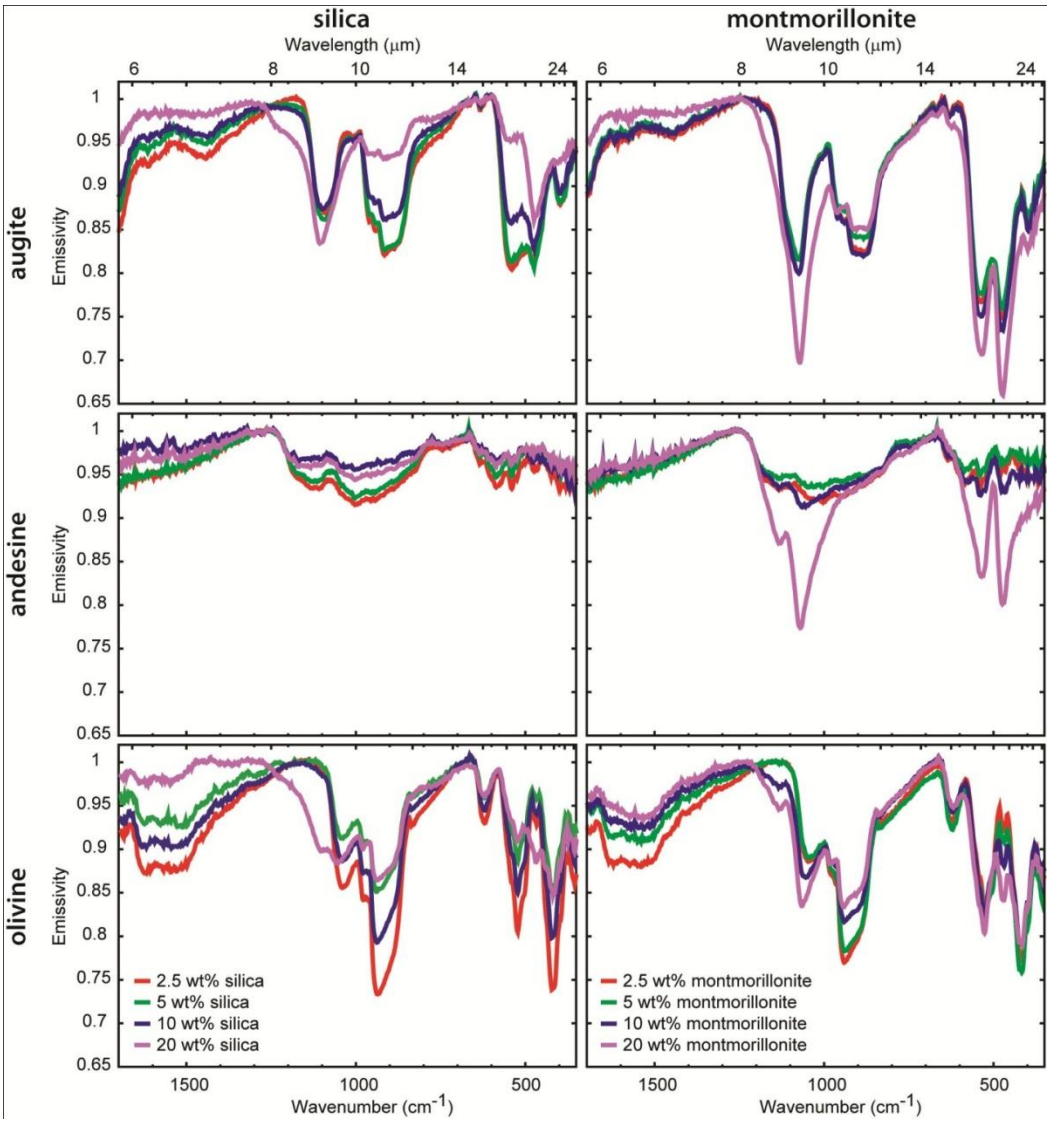

Figure 3.4. TIR emissivity spectra of compressed pellet mixtures with one igneous mineral. See Table 3.5 for a description of spectral effects from adding particulate silica or montmorillonite to basaltic igneous minerals.

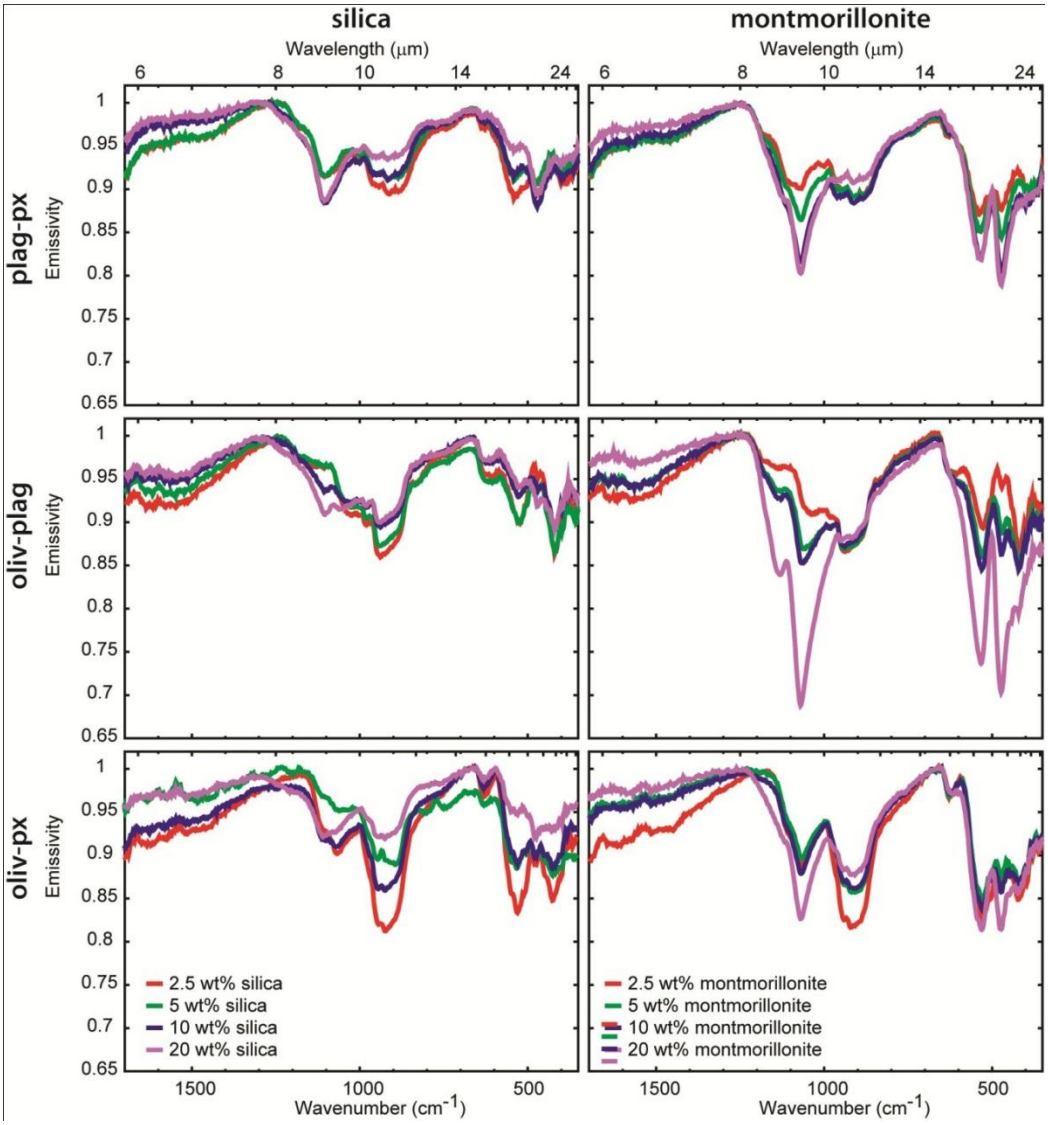

Figure 3.5. TIR emissivity spectra of compressed pellet mixtures with two igneous minerals. See Table 3.6 for a description of spectral effects from adding particulate silica or montmorillonite to two basaltic igneous minerals.

phyllosilicates than zeolite and overestimate clay abundances. Models using Library 1 more severely overestimate phyllosilicate abundances than models using Library 2 because phyllosilicates are modeled rather than zeolites. Basaltic glass is commonly identified in models of silica mixtures with Library 1, the only library with basaltic glass. High-silica phase abundances are greater in Library 2 models because basaltic glass replaces high-silica phases in models using Library 1.

3.4.4 Effect of Spectral Resolution on Modeled Mineralogy

The general trends in modeled mineralogy described above are similar for models of lab resolution and TES resolution spectra, and the differences between the grouped mineral abundances are usually <5 vol.%. However, lab resolution models with Library 1 report significant basaltic glass abundances in some particulate and pelletized mixtures with $\geq$10 wt.% silica and report lesser amounts (<10 vol.%) of basaltic glass in all pelletized silica mixtures. TES resolution models with Library 1 do not identify significant basaltic glass abundances in any mixtures and usually do not identify any basaltic glass, suggesting that models of lower resolution spectra are more accurate. In the cases where there is a significant difference in basaltic glass abundance between lab and TES resolution models, the TES resolution models identify significantly more plagioclase than the lab resolution models.

3.5 Discussion

3.5.1 Coupling Modeled Mineral Trends with Measured Spectral Trends

The trends displayed in the spectral models can be explained by the trends observed in the measured TIR spectra. Models of particulate mixtures with silica falsely identify plagioclase. Plagioclase has a CF at shorter wavelengths than augite and olivine. Its false detection is likely a result of the shift in the primary CF to shorter wavelengths from the addition of silica. Dampening of olivine and especially augite absorptions with the addition of silica (Figure 3.2) makes these spectra more similar to the spectrum of

Table 3.7. General spectral model results from mixtures with one igneous mineral using Library 1.

	Silica		Montmorillonite	
	Particulates	pellets	Particulates	Pellets
Augite	-Plagioclase falsely identified in all mixtures -No high-silica phases identified -Significant BG in 20 wt.% silica mixture	-Significant high-silica abundances in 10, 20 wt.% silica mixtures -Significant K-glass in 20 wt.% silica mixture	-Phyllosilicates overestimated in all mixtures -Significant phyllosilicate abundances in all mixtures -Px underestimated in all mixtures	-Phyllosilicates overestimated in all mixtures -Px underestimated in all mixtures
Andesine	No high-silica phases identified	-High-silica materials not identified in significant abundances -K-spar falsely identified in 5 wt.% mixture	-Phyllosilicates overestimated in all mixtures -Significant phyllosilicate abundances in 5, 10, 20 wt.% clay mixtures -Plag underestimated in all mixtures	-Significant phyllosilicates in 10, 20 wt.% clay mixtures -Phyllosilicates overestimated in 20 wt.% clay mixture -Plag underestimated in all mixtures -K-spar falsely identified in all mixtures
Olivine	-Plagioclase falsely identified in all mixtures -No high-silica phases identified	-Significant BG abundances in 5, 10, 20 wt.% silica mixtures -Significant K-glass in 20 wt.% silica mixture	-Phyllosilicates overestimated in 20 wt.% clay mixture -Significant phyllosilicate abundances in 20 wt.% clay mixture -Olivine underestimated in 20 wt.% clay mixture	-Significant phyllosilicates in 10, 20 wt.% clay mixtures -Phyllosilicates overestimated in 20 wt.% clay mixture -Olivine underestimated in 10, 20 wt.% mixtures

Table 3.8. General spectral model results from mixtures with two igneous minerals using Library 1.

	Silica		Montmorillonite	
	particulates	pellets	Particulates	Pellets
Plag-Px	-Plagioclase overestimated in 5, 10, 20 wt.% silica mixtures -No high-silica phases identified -Olivine falsely identified in all mixtures -Modeled plag/px ratio increases with silica abundance	-Significant high-silica abundances in 10, 20 wt.% silica mixtures Significant K-glass in 10, 20 wt.% silica mixture -High-silica abundances overestimated in 10, 20 wt.% silica mixtures -Px abundances underestimated for all mixtures -Plag abundances underestimated for 10, 20 wt.% silica mixtures	-Significant phyllosilicate abundances in all mixtures -Phyllosilicates overestimated in all mixtures -Plag and px underestimated in all mixtures -Modeled plag/px ratio generally less than actual ratio	-Significant phyllosilicate abundances in all mixtures -Phyllosilicates overestimated in all mixtures -Px underestimated in all mixtures -Plag underestimated in 5, 10, 20 wt.% clay mixtures -Modeled plag/px ratio decreases with increasing clay content
Oliv-Plag	-Plagioclase overestimated in 5, 10, 20 wt.% silica mixtures -No high-silica phases identified -Modeled oliv/plag ratio greater than actual ratio -BG falsely identified in 20 wt.% silica mixture	-Significant high-silica abundances in 10, 20 wt.% silica mixtures -Significant K-glass in 20 wt.% silica mixture -High-silica abundances overestimated in 20 wt.% silica mixture -Significant BG abundances 10, 20 wt.% silica mixtures -Olivine and plag abundances underestimated in 10, 20 wt.% silica mixtures	-Significant phyllosilicate abundances in 5, 10, 20 wt.% clay mixtures -Phyllosilicates overestimated 5, 10, 20 wt.% clay mixtures -Olivine and plag underestimated in 5, 10, 20 wt.% clay mixtures -Modeled oliv/plag ratio greater than actual	-Significant phyllosilicates in 5, 10, 20 wt.% clay mixtures -Phyllosilicates overestimated in 5, 10, 20 wt.% clay mixture -Plag underestimated in all mixtures -Olivine underestimated in 5, 10, 20 wt.% clay mixtures -K-spar falsely identified in 2.5, 5, 10 wt.% clay mixtures -Modeled oliv/plag ratio greater than actual
Oliv-Px	-Plagioclase falsely	-Significant high-silica	-Significant phyllosilicate	-Significant phyllosilicates in

identified 5, 10, 20 wt.% silica mixtures -No high-silica phases identified -Px underestimated in all mixtures -Olivine overestimated in all mixtures -Modeled oliv/px ratio greater than actual ratio	abundances in 10, 20 wt.% silica mixtures -Significant K-glass in 20 wt.% silica mixture -High-silica abundances overestimated in 20 wt.% silica mixture -Significant BG abundances 10, 20 wt.% silica mixtures -Olivine abundances underestimated in 10, 20 wt.% silica mixtures -Px abundances underestimated in all mixtures -Modeled oliv/px ratio greater than actual ratio	abundances in 5, 10, 20 wt.% clay mixture -Phyllosilicates overestimated in 5, 10, 20 wt.% clay mixture -Olivine and px underestimated in 5, 10, 20 wt.% clay mixtures -Modeled oliv/px ratio near actual ratio	5, 10, 20 wt.% clay mixtures -Phyllosilicates overestimated in 5, 10, 20 wt.% clay mixture -Olivine and px underestimated in 5, 10, 20 wt.% clay mixtures -Modeled oliv/px ratio near actual ratio

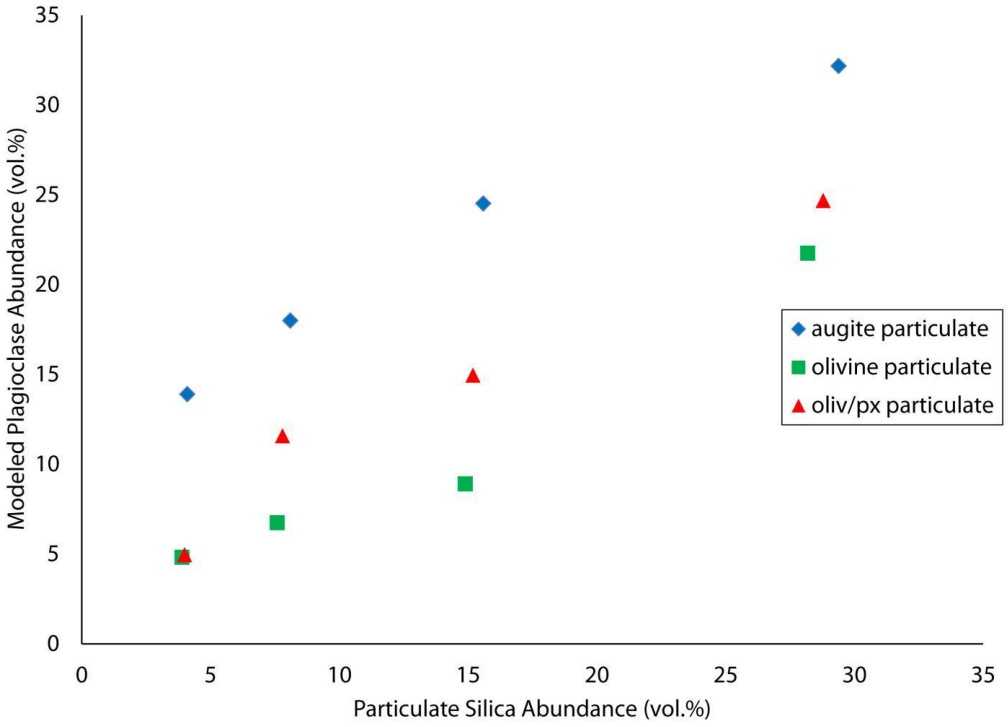

Figure 3.6. False plagioclase detections in particulate mixtures with silica and no plagioclase using Library 1. Models of mixtures with augite falsely detect greater amounts of plagioclase than mixtures with olivine.

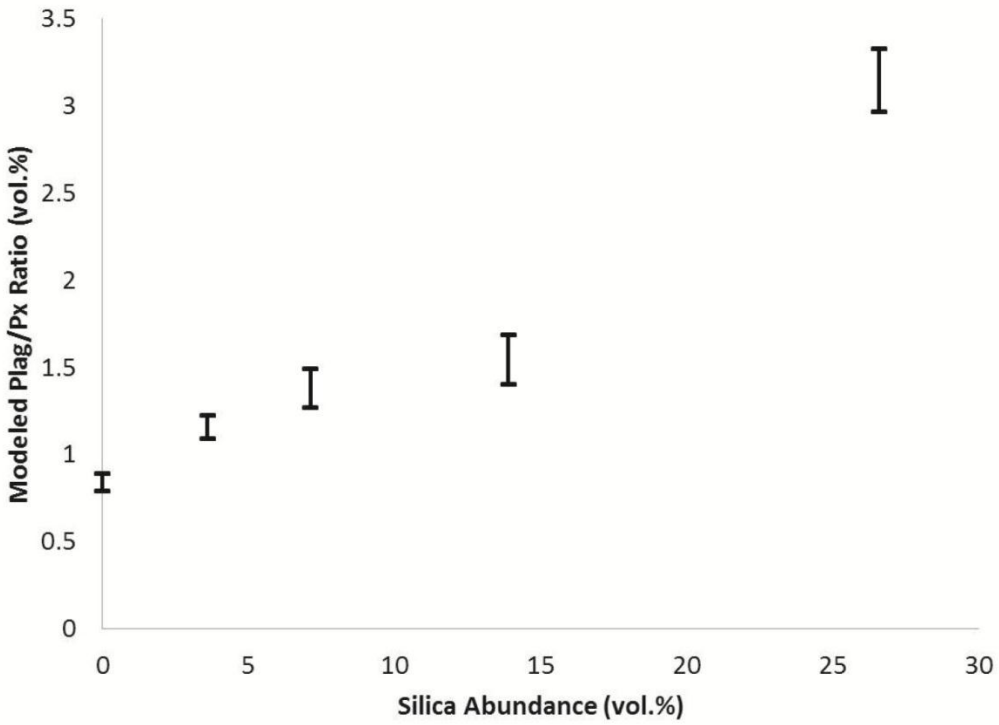

Figure 3.7. Modeled plag/px ratios for particulate silica-plag-px mixtures using Library 1 and 1 sigma error bars. The modeled plag/px ratio increases with particulate silica abundances.

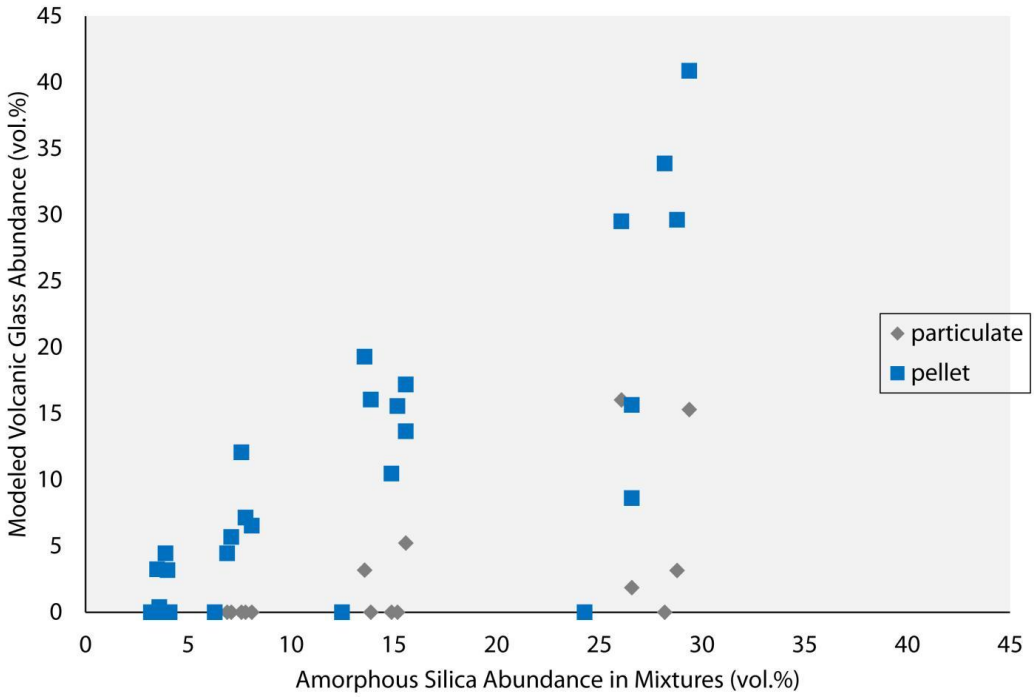

Figure 3.8. Volcanic glass (basaltic glass + K-rich glass) abundances identified in models of particulate (gray diamonds) and compressed pellet (blue squares) mixtures with silica using Library 1. Pellets differ from one another in primary minerals present. Models of silica-plagioclase compressed pellets do not falsely identify volcanic glass (blue squares along the x-axis >5 vol.% silica) because the addition of amorphous silica does not affect the spectrum (Figure 3.2). Note that models of pellets falsely identify more volcanic glass and that significant glass abundances (>10 vol.%) are identified in pellet mixtures with >10 vol.% amorphous silica.

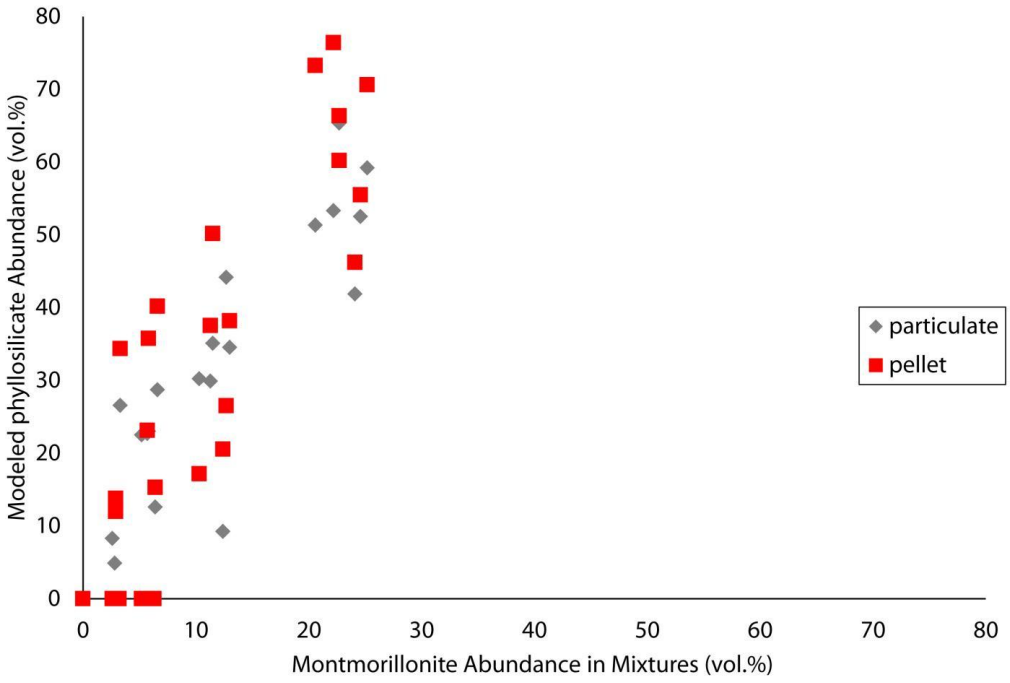

Figure 3.9. Modeled phyllosilicate abundances in all mixtures with montmorillonite using Library 1. Pellet mixture models of 2.5 and 5 wt.% montmorillonite mixed with olivine or andesine do not identify phyllosilicates. Phyllosilicate abundances are generally overestimated by spectral models and models of pellets overestimate phyllosilicates abundances more than particulate models.

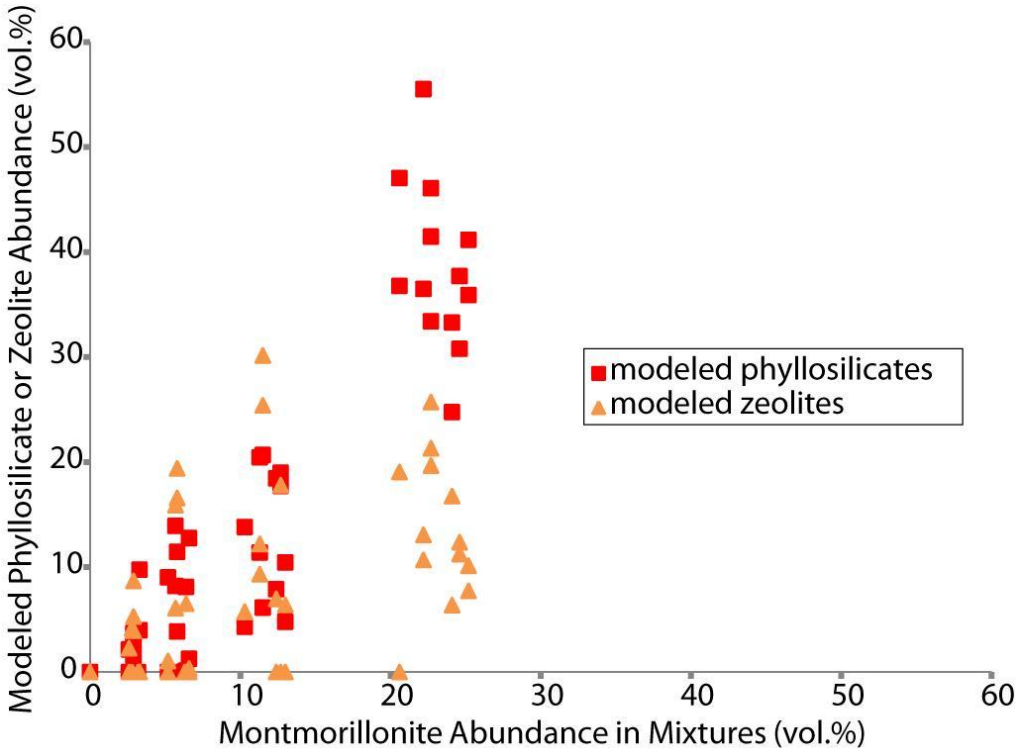

Figure 3.10. Modeled phyllosilicate and zeolite abundances for mixtures with montmorillonite using Library 2. Zeolites can be falsely identified in greater abundances than phyllosilicates in mixtures with 5 and 10 wt% montmorillonite.

andesine (Figure 3.1). The overestimation of plagioclase abundances causes modeled plag/px ratios to increase with the addition of silica to plag-px mixtures and modeled oliv/plag ratios to decrease with the addition of silica to oliv-plag mixtures. This effect on plag/px and oliv/plag ratios result from 1) underestimating pyroxene and olivine abundances because of spectral dampening and 2) overestimating plagioclase abundances because silica does not change or dampen the particulate andesine spectrum (Figure 3.2).

Models of compressed pellet mixtures with 20 wt.% silica falsely identify K-rich volcanic glass (>10 vol.%), rather than the synthetic amorphous silica that is present in the mixtures. The identification of K-rich glass is the result of non-linear mixing, creating spectral features that are more similar to K-rich glass than synthetic amorphous silica. K-rich glass and synthetic amorphous silica spectra have similar shapes and their Si-O stretching absorption minima occur at similar wavelengths, but their primary CFs occur at different wavelengths, where the CF for K-glass is at 1285 cm^{-1} and the CF for the synthetic silica is at 1340 cm^{-1} (Figure 3.11). The CFs of measured spectra whose models identify significant K-rich glass are closer to the CF of K-rich glass than that of synthetic silica. Non-linear spectral mixing between the synthetic amorphous silica coating and the basaltic igneous minerals causes primary CFs to shift to shorter wavelengths so that they do not match those of the synthetic silica, resulting in the false identification of K-rich glass. This suggests that the presence of an amorphous high-silica coating can cause non-linear spectral mixing so that modeling with an accurate spectral library (i.e one that has all end members that are present in the measured surface) will not identify the correct high-silica phase. It is important to note that spectral absorptions from K-O vibrations cannot be used to distinguish between the presence of secondary silica and K-rich glass because these absorptions occur at longer wavelengths and are outside the detection of TIR spectrometers.

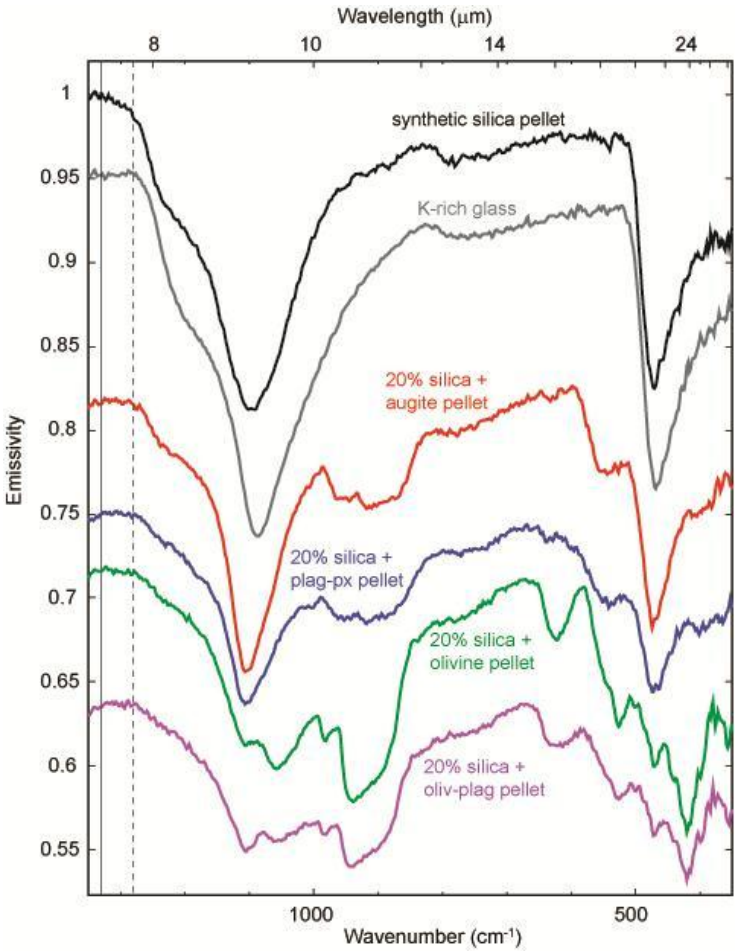

Figure 3.11. TIR spectra of synthetic silica pellet, K-rich glass, and measured spectra of silica pellet mixtures whose models identify significant K-rich glass. Vertical solid line denotes the Christiansen frequency (CF) of the synthetic silica pellet and the vertical dashed line denotes the CF of K-rich glass. Note that the CFs of the mineral mixture spectra match the CF of the K-rich glass, rather than that of synthetic silica, explaining why models identify K-rich glass instead of synthetic silica. Spectra are offset in emissivity for clarity.

The false identification of significant basaltic glass abundances in lab resolution spectral models of silica mixtures but not TES resolution models suggests that there is some characteristic specific to lab-resolution spectra causing the identification of basaltic glass. Lab-resolution spectra have more small-scale spectral variations than TES resolution spectra since the spectral resolution is higher. To account for these small-scale variations, the model will use the smoothest, blandest spectrum to try to minimize the misfits between the measured and modeled spectra. Basaltic glass is the best spectrum to accomplish this because it is smooth and bland but also lacks sharp, prominent absorptions. Thus, its incorporation in spectral models will not create additional misfits elsewhere in the model because those would worsen the fit.

The overestimation of phyllosilicates in models of montmorillonite-bearing mixtures is a result of the physical properties of the montmorillonite particles. Montmorillonite is a smectite clay and smectites naturally adsorb water, causing particles to flocculate. The mixtures were prepared in water in order to coat the igneous minerals with the weathering products, so even though the individual montmorillonite particles were <2 microns, when the mixtures were immersed in water, the clay particles flocculated to create larger effective particle sizes that were macroscopic. The larger effective particle size results in a greater spectral contrast and a greater effect on the particulate TIR spectra. When the montmorillonite-bearing particulates were compressed into pellets, the montmorillonite filled voids between igneous minerals to create a coating geometry. This similarly occurred when silica-bearing particulate mixtures were compressed into pellets. It is important to note, however, that the presence of olivine adversely affects the detection of phyllosilicates. Models of particulate and pellet mixtures with 2.5 and 5 wt.% montmorillonite and olivine do not identify phyllosilicates. Strong olivine absorptions overlap those of montmorillonite so that montmorillonite is masked and has a higher detection limit when mixed with olivine than with another

igneous mineral, such as augite. Thus, phyllosilicate abundances may not be overestimated when olivine is present.

The identification of phyllosilicates in models of montmorillonite-bearing mixtures and the absence of phyllosilicates in models of silica-bearing mixtures shows that amorphous silica cannot cause the false identification of phyllosilicates in spectral models. Previous TIR studies of weathered terrestrial basalts show that models identify significant phyllosilicate abundances [*Michalski et al.*, 2006a; *Hamilton et al.*, 2008; Chapter 2]. Conversely, weathering rinds generally lack crystalline clays but instead contain small amounts of poorly-crystalline aluminosilicates. These poorly-crystalline aluminosilicates are clay precursors, meaning they are structurally and, thus, spectrally more similar to clay minerals than amorphous silicates. This causes the false identification of phyllosilicates, rather than the identification of amorphous silica, in TIR models of weathering rinds.

Zeolite is falsely detected in models of montmorillonite mixtures with Library 2 because zeolite spectra closely resemble the spectrum of the montmorillonite in the mixtures (Figure 3.12). The mixtures contain Na-rich montmorillonite (SWy-1), while Library 2 contains Ca-rich montmorillonite (STx-1). The spectra are broadly similar, but the montmorillonite in the mixtures has a shoulder on the short wavelength side of the Si-O stretching absorption and the montmorillonite in Library 2 does not. The spectra of both zeolites in Library 2 have shoulder features similar to that in SWy-1, so the zeolite spectra are selected by the algorithm to fit that feature. To test this, montmorillonite-bearing mixture spectra were modeled using Library 2 without the zeolite end members. The modeled spectra with zeolite in the library fit the shoulder feature well, while the modeled spectra without zeolite in the library have a poor fit near the shoulder feature (Figure 3.12). When SWy-1 is added to Library 2, modeled zeolite abundances are

below 10 vol.%. This demonstrates that it is crucial to have a complete set of high-silica phases in the spectral library to prevent the false detection of spectrally similar phases.

3.5.2 Implications for Interpreting Martian Spectral Data

3.5.2.1 Characterizing High-Silica Phases in TES Models

The results of these mineral mixture models show that phyllosilicates should be identified in significant abundances (>10 vol.%) in TES models if surfaces are made up of ~5-10 wt.% clay. While the texture of the mixture affects modeled abundances, it does not affect the detection limit of phyllosilicates; however, the types of igneous minerals present affect the detection limit. The presence of olivine, in particular, impedes the detection of phyllosilicates, where phyllosilicates are not detected in particulate and pellet mixtures with 2.5 and 5 wt.% montmorillonite + olivine. The detection limit of phyllosilicates is 2.5 wt.% when olivine is not present, but is 10 wt.% when olivine is present. In spectral models of Mars, phyllosilicates are detected globally in small amounts (<10 vol.%). These may be false detections because clays are not detected by OMEGA and CRISM data in low-albedo surfaces globally and TES spectral indices do not suggest the presence of clays [*Michalski et al.*, 2006a; *Ruff and Christensen*, 2007]. It has been suggested that Martian surface textures may affect the detection of clays by NIR vs. TIR spectroscopy. Fine-grained textures improve detections by NIR spectroscopy because of increased particle scattering, but impede detections by TIR spectroscopy for the same reason [*Michalski and Noe Dobrea*, 2007]. However, the results presented here show that small amounts of phyllosilicates are detectable in TIR spectral models of fine-grained and coarse-grained surfaces, suggesting that the identifications of small amounts of phyllosilicates (<10 vol.%) on the Martian surface represent positive detections.

Models using Library 2 suggest that if the spectral library does not contain the correct phyllosilicate, then zeolites can be falsely detected in significant abundances. In

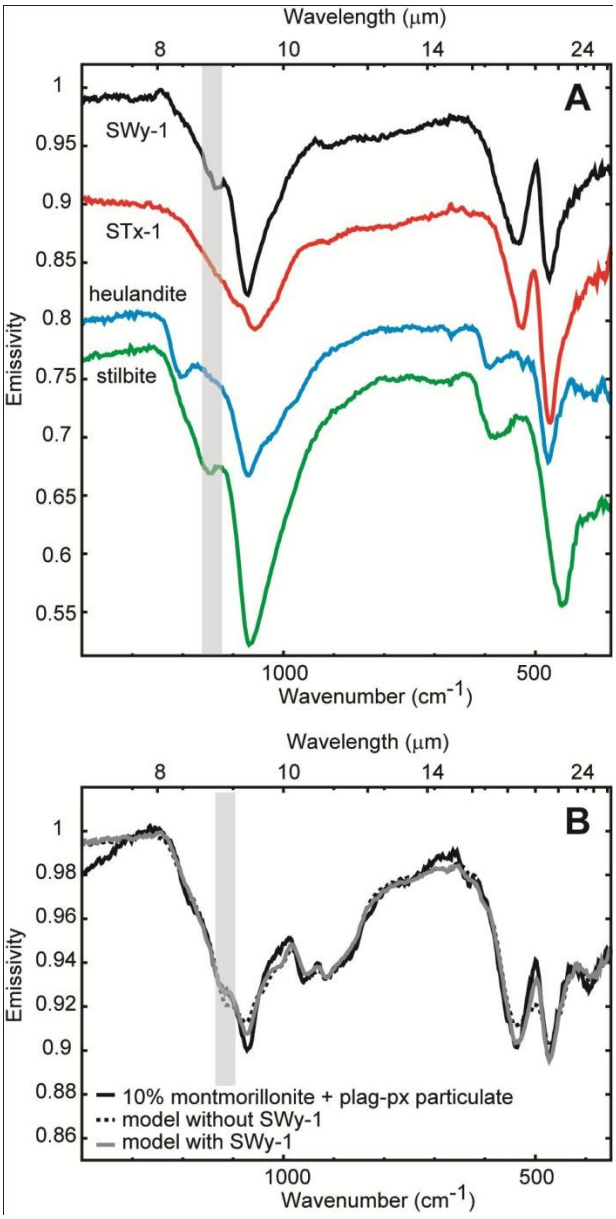

Figure 3.12. A) Montmorillonite and zeolite spectra. SWy-1 is in the mineral mixtures and Library 1 and STx-1 is in Library 2. Note that SWy-1 has a shoulder ~1120 cm^{-1} (highlighted in gray) and STx-1 does not. Zeolite spectra have shoulders in similar regions, but the feature in stilbite best matches that of SWy-1. B) Measured spectrum of 10% montmorillonite + plag-px particulate mixture (solid black line) with modeled spectra using Library 2 without SWy-1 (black, dashed line) and with SWy-1 (solid gray line). Note that the modeled spectrum with SWy-1 in the library fits the shoulder feature highlighted in gray better than the model without SWy-1.

this case, significant zeolite abundances would not be detected unless phyllosilicates comprise ≥10 wt.% of the surface. OMEGA and CRISM spectra of Mawrth show evidence for Al- and Fe/Mg-bearing clay minerals and do not show evidence for zeolites, while TES models report clay and zeolite abundances at 10-20 vol.%, individually [*Michalski and Fergason*, 2009]. Models of regionally averaged TES spectra of Northern Acidalia and Solis Planum identify significant abundances of phyllosilicates (particularly illite) and zeolites [*Minitti and Hamilton*, 2010]. The identification of zeolites and phyllosilicates in TES models of Mawrth Vallis, Northern Acidalia, and Solis Planum may result from an incomplete library [*Michalski and Fergason*, 2009; *Minitti and Hamilton*, 2010]. The results from the experiments presented here suggest that these surfaces could be composed of ~10 wt.% montmorillonite falsely modeled as zeolite.

Models of mixtures with amorphous silica show that the detection limit of amorphous silica is dependent on surface texture and igneous mineralogy. The detection limit of compressed amorphous silica, as would be expected for silica coatings, is 5 wt.%; however, if olivine is present, the detection limit is 10 wt.%. The fine-grained particulate silica spectrum was not included in the original spectral models because it is spectrally bland and may be used instead of a blackbody. The inclusion of the fine-grained silica spectrum to the library did not result in its detection in spectral models, suggesting that the detection limit of fine-grained silica is >20 wt.%. Therefore, if the Martian surface contains fine-grained amorphous silica, it may go undetected in TES spectral models.

3.5.2.2 False Detection of Glass and Implications for Extent of Weathering

Volcanic glass (mostly K-rich) has been identified in significant abundances in TES spectral models of Surface Type 2, and its presence led to the interpretation that mid-to-high latitude surfaces on Mars were basaltic andesite [*Bandfield et al.*, 2000; *Bandfield*, 2002]. Models of silica pellet mixtures show that the presence of ~20 wt.% compressed amorphous silica can cause the false detection of volcanic glass. Very thin

secondary silica coatings can dominate TIR spectra and cause the overestimation of high-silica materials in spectral models [*Kraft et al.*, 2003; *Minitti et al.*, 2007; *Kraft*, 2009]. Volcanic glass may be falsely detected in models of mid-to-high latitude Martian surfaces because of the occurrence of thin silica-rich coatings that formed over millions of years during the Amazonian by aqueous alteration at very low temperatures and very low water-to-rock ratios [*Kraft*, 2009]. The presence of silica coatings at mid-to-high Martian latitudes is consistent with orbital data from multiple instruments. Gamma Ray Spectrometer data show hydrogen enrichment in these regions, suggesting the presence of subsurface water ice [*Boynton et al.*, 2002]. HiRISE imagery and climate models suggest that periglacial soil processes and seasonal melting of subsurface ice have been active during the Amazonian and most recently 5 Ma [*Kreslavsky et al.*, 2008], demonstrating that chemical weathering at very low temperatures and water-to-rock ratios has likely occurred in recent Martian history. NIR data from the region lack features from silica (i.e. absorptions from Si-OH bonds); however, *Kraft* [2009] showed that thin silica coatings may be invisible to NIR spectroscopy. The presence of silica-rich coatings at mid-to-high latitudes, rather than volcanic glass, would indicate that the Martian surface has experienced widespread aqueous alteration at very low rates and water-to-rock ratios. High-silica coatings can form in arid environments on Earth from periodic wetting and drying of thin films of water (fog or dew) causing the dissolution of silicate dust grains [*Curtiss et al.*, 1985]. It has been postulated that silica coatings could form at Martian mid-to-high latitudes in a similar way, from the formation of thin films of water in ice-rich sediments, aqueous attack of dust particles and dissolution of silica, and the deposition of silica coatings with the evaporation of silica-rich fluids [*Kraft et al.*, 2008].

3.5.2.3 Modeled Plagioclase Abundances in Dusty Martian Terrains

TES spectral models of mid-to-high-latitude surfaces have elevated plag/px ratios relative to models of low latitude surfaces [*Bandfield et al.*, 2000; *Rogers and*

Christensen, 2007]. Models of particulate mixtures with silica show that the presence of fine-grained silica causes the overestimation of plagioclase. The presence of amorphous silica in Martian dust could cause an overestimation of plagioclase, creating an apparent elevated plag/px ratio in these regions. It is well-known that the presence of fine-grained materials causes non-linear spectral mixing because they create volume scattering and transmission features [*Ramsey and Christensen*, 1998]. As a result, TES spectra from dusty regions on Mars are generally not modeled by linear deconvolution [*Rogers and Christensen*, 2007]. The dust cover index (DCI) can be measured from TIR spectra of the Martian surface to evaluate whether or not they are too dusty to model with linear deconvolution [*Ruff and Christensen*, 2002]. The DCI is the average emissivity value from 1350-1400 cm^{-1} because dust-sized particles cause transparency features in this wavelength range; dusty surfaces have DCIs <0.96 and non-dusty surfaces have DCIs >0.96. The dust indices of particulate silica-bearing mixtures determined that the spectra were not dusty, indicating that spectra measured from Martian surfaces with similar amounts of fine-grained materials would be appropriate candidates for deconvolution. Thus, if small amounts of silica-bearing dust are present on a Martian surface, the modeled plagioclase abundances and plag/px ratios may not be accurate.

3.6 Conclusions

Thermal-infrared spectroscopy and spectral modeling of physical mineral mixtures of basaltic minerals and high-silica weathering products has led to the following conclusions:

1 The detection limit of phyllosilicates for linear deconvolution is not dependent on surface texture. For both compressed and particulate clay, the detection limit ranges from 2.5 to 10 wt.% and is dependent on the igneous mineralogy. The detection of <10 vol.% phyllosilicates on a Martian surface suggests their presence because phyllosilicates are not falsely identified in mixtures with amorphous silica or without a secondary silicate.

2 The detection limit of amorphous silica for linear deconvolution is dependent on surface texture. The detection limit of amorphous silica in a dense coating is 5 to 10 wt.%. The detection limit of fine particulate amorphous silica is >20 wt.% because it has a neutral spectrum from particle scattering.

3 Detection limits of high-silica weathering products are dependent on the type of igneous minerals present. Olivine, especially, impedes the detection of montmorillonite and amorphous silica, so that if olivine is not present, the detection limit of montmorillonite is 2.5 wt.% and the detection limit of amorphous silica is 5 wt.%. If olivine is present, the detection limits of montmorillonite and amorphous silica are 10 and 20 wt.%, respectively. Thus, the lack of detection of phyllosilicates in Martian spectral models does not mean phyllosilicates are absent from that surface.

4 The presence of montmorillonite can cause the false detection of zeolites in spectral models if the correct montmorillonite spectrum is not in the library. The detection of zeolites and phyllosilicates in spectral models of Mawrth Vallis, Northern Acidalia, and Solis Planum may indicate the presence of ~10 wt.% phyllosilicate that is not represented in the spectral library.

5 Moderate amounts of compressed amorphous silica can cause the false detection of K-rich volcanic glass in spectral models. The precipitation of secondary amorphous silica coatings from low-temperature chemical weathering processes on mid-to-high latitude Martian surfaces could cause the false identification of volcanic glass.

6 Fine-grained amorphous silica causes the overestimation or false detection of plagioclase in spectral models. The presence of small amounts of amorphous silica-bearing dust on the Martian surface could adversely affect modeled plagioclase abundances and plag/px ratios.

4 Thermal-Infrared and Near-Infrared Spectroscopy of Poorly-Crystalline Aluminosilicates

4.1 Introduction

Infrared spectroscopy is an important tool for identifying weathering products on the Martian surface. Near-infrared (NIR) data from the Observatoire pour la Minéralogie, l'Eau, les Glaces et l'Activité (OMEGA) and the Compact Reconnaissance Imaging Spectrometer for Mars (CRISM) indicate the presence of a variety of alteration products across the planet, including phyllosilicates, zeolites, opaline silica, and hydrated sulfates [*Bibring et al.*, 2005; 2006; *Ehlmann et al.*, 2008; 2009; *Milliken et al.*, 2008; *Mustard et al.*, 2008]. Thermal-infrared (TIR) data measured by the Thermal Emission Spectrometer (TES) and Mini-TES indicate the surface is primarily basaltic with regional and local concentrations of high-silica phases, which have been interpreted as volcanic glass [*Bandfield et al.*, 2000; *Bandfield*, 2002; *Rogers and Christensen*, 2007] and/or alteration phases, such as phyllosilicates and amorphous silica [*Wyatt and McSween*, 2002; *Kraft et al.*, 2003; *Rogers and Christensen*, 2007; *Squyres et al.*, 2008]. The types of alteration phases identified from Martian IR spectra can tell us about the chemical weathering environments in which they formed and, thus, elucidate the aqueous alteration history of the planet. Weathering products are identified from Martian NIR and TIR spectra using a library of reference mineral spectra measured in laboratories [*Christensen et al.*, 2000; *R. N. Clark et al.*, 2007]. It is important to have a complete spectral library in order to identify alteration products on Mars. Allophane is a poorly-crystalline, hydrous aluminosilicate that is a common terrestrial alteration product of volcanic glass and is a clay mineral precursor [*Wada*, 1989]; however, allophane reference spectra are not present in NIR and TIR spectral libraries. Previous studies have suggested that allophane is present in Martian mid-to-high latitude surfaces, based on absorption positions of TES spectra measured from those regions [*Michalski et al.*, 2005].

Additionally, it has been suggested that the lack of allophane in spectral libraries causes the detection of phyllosilicates in TIR spectral models of the Martian surface and of altered Hawaiian tephra [*Hamilton et al.*, 2008; *McDowell and Hamilton*, 2009]. Allophanes and other poorly-crystalline aluminosilicates have been synthesized to use as TIR and NIR spectral end members and test for their presence on Mars. The chemistry and structures of these mineraloids are characterized and their synthesis procedures are described.

4.2 Background

4.2.1 Composition, Structure, and Formation of Allophane

Allophane is a hydrated aluminosilicate with molar Si/Al ratios of ~0.5 to 1 [*Wada*, 1989]. Three types of allophane have been proposed, based on composition and structure: Al-rich soil allophanes (Si/Al ~0.5), Si-rich soil allophanes (Si/Al ~1), and stream deposit allophanes (Si/Al ~0.5-1.1) [*Parfitt*, 1990]. Allophane is poorly-crystalline, rather than amorphous, meaning that it only has short-range atomic order. It is composed of irregular aggregates of hollow, roughly spherical particles that are ~3.5-5 nm in diameter [*Henmi and Wada*, 1976]. Incipient weathering of volcanic glass leads to the formation of allophane, so allophane is an important constituent of many soils derived from volcanic ash and tephra [*Wada*, 1989] and of basalt and andesite weathering rinds [*Colman*, 1982]. Allophane forms under near-neutral to mildly acidic conditions (pH ~5-7) because the dominant dissolved aluminum species are in 4- and 6-fold coordination in this pH range [*Childs*, 1990]. It precipitates from fluids with dissolved Al and Si concentrations of 0.1-4 mM [*Wada*, 1989]. Drier conditions favor Si-rich over Al-rich allophane formation because less silica is leached and removed from the system [*Harsh et al.*, 2002]. Environments with large amounts of precipitation favor Al-rich allophane, but less allophane accumulates in the soil [*Harsh et al.*, 2002]. Allophane can form from a range of volcanic glass compositions (i.e. basaltic to rhyolitic) [*Harsh et al.*, 2002]. It

is typically found in young ash deposits (a few thousand to a few tens of thousands of years old) and transforms to halloysite with resilication or gibbsite with desilication [*Wada*, 1989]; however, it persists in 1 Myr old soils on Maui, where soil moisture is limited [*Wada*, 1989].

Allophane is structurally similar to dioctahedral phyllosilicates and is made up of roughly spherical Al^{3+} dioctahedral and silica tetrahedral layers. Variations on two structural end members have been proposed: one where a continuous tetrahedral layer is bonded to a discontinuous dioctahedral sheet. *Parfitt and Henmi* [1980] determined that Al-rich soil allophanes have a structure similar to imogolite, a para-crystalline, hydrous aluminosilicate that forms in similar environments as allophane, but at lower pH. Al-rich soil allophanes are made up of a curved, continuous alumina dioctahedral layer on the outer surface and unpolymerized O_3SiOH groups on the interior of the dioctahedral sheets (Figure 4.1a). The dioctahedral sheets make allophane structurally similar to dioctahedral clays. The O_3SiOH tetrahedra are bonded to the dioctahedral sheets at the vacant octahedral sites to avoid having Si^{4+} and Al^{3+} sharing polyhedral faces [*Cradwick et al.*, 1972]. *Parfitt* [1990] suggested that the Al^{3+} dioctahedral sheet is on the outer surface for both Al- and Si-rich soil allophanes, but the interior Si groups are associated with silica polymers in Si-rich soil allophanes. *Childs et al.* [1990] described the stream deposit allophane structure as an outer, continuous silica tetrahedral sheet, with Al substituting for Si, and an inner, discontinuous alumina octahedral sheet (Figure 4.1b). *Parfitt et al.* [1980] suggested that allophanes with intermediate Si/Al ratios are mixtures of the two different structural end members, rather than structural intermediates, because transmission mid-IR spectra of these materials show distinct absorptions from the two structural end members.

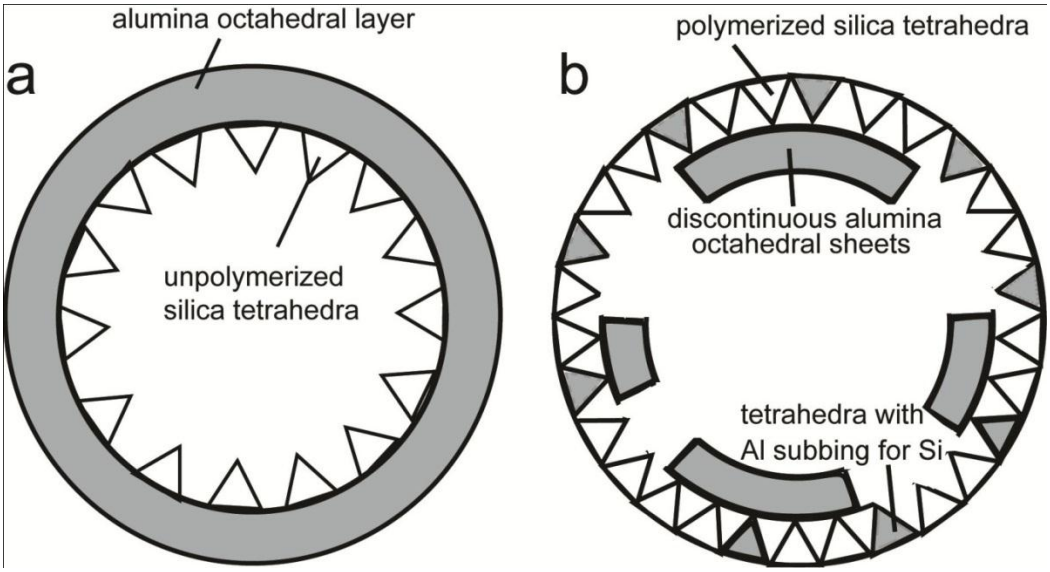

Figure 4.1. Simplified illustrations of allophane structures. a) imogolite-like allophane structure, with continuous alumina dioctahedral layer composing the outer curved layer and unpolymerized O_3SiOH tetrahedra on the interior surface. b) Stream deposit allophane structure, with polymerized tetrahedral sheet composing the outer surface and a discontinuous alumina octahedral layer on the interior surface, adapted from *Childs et al.* [1990]. Al^{3+} substitutes for Si^{4+} in stream deposit allophanes.

Allophane has been synthesized in previous studies to analyze its structure, formation conditions, and its chemical and physical properties. It is generally synthesized by combining dilute orthosilicate and aluminum solutions at pH ~5 and temperatures 95-100 °C [*Wada et al.*, 1979; *Su et al.*, 1992; *Ohashi et al.*, 2002]. The goal of this study is to use previously published methods to synthesize and characterize allophanes with a range of Si/Al ratios and measure their TIR emission and NIR reflectance spectra. These spectra will be made available to the Martian science community to remotely test for the presence allophane on the surface of Mars, and are used in TES spectral models in Chapter 5.

4.3 Methods

4.3.1 Aluminosilicate Syntheses

A series of aluminosilicates were synthesized to achieve a range of Si/Al ratios using methods from *Ohashi et al.* [2002] and methods adapted from *Wada et al.* [1979] (Table 4.1). Two syntheses were performed using the *Ohashi et al.* [2002] methods: 30 and 100 mmol Na-orthosilicate and $AlCl_3$ solutions were prepared and mixed with Si/Al ratios of 0.75 to achieve a final volume of ~2 L. The $AlCl_3$ solution was added to the Na-orthosilicate solution in a Nalgene bottle drop-wise while stirring and was allowed to mix for one hour. Solutions were loosely capped and placed in a ~100 °C oven for 48 hours. The 30 mmol synthesis was performed three separate times because the 30 mmol synthesis produced less precipitate than the 100 mmol synthesis. Four syntheses were performed using the *Wada et al.* [1979] methods: 100 mmol $AlCl_3$ solutions and tetraethyl orthosilicate (TOS) solutions were prepared and mixed with Si/Al ratios of 0.5, 1, 2, and 4 to achieve a final solution volume ~2 L. The $AlCl_3$ solution was added to the TOS solution in a Nalgene bottle at a rate of 1.5 mL/sec while stirring. After the $AlCl_3$ solution was added, the pH was ~3 and 1 M NaOH solution was titrated into the solution at a rate of 0.22 mL/sec to bring the pH to ~4.5 and was allowed to mix for one hour.

Solutions were loosely capped and placed in a ~100° C oven for 96 hours. The syntheses presented here differed from *Wada et al.* [1979] in that *Wada et al.* heated solutions for 113 hours, while solutions in this work were heated for 96 hours, and *Wada et al.* added NaOH to achieve a particular molar NaOH/Al ratio in the parent solution, while NaOH was added until pH 4.5 was attained in these experiments. At the end of each Ohashi-type and Wada-type synthesis, a cloudy precipitate was present at the bottom of the bottle and the clear supernatant was poured off. Precipitates were centrifuged and washed four times with distilled water to remove NaCl and were freeze-dried to obtain the final products. XRD patterns show that NaCl was completely removed. The final precipitates were white, fluffy powders.

4.3.2 Thermal-Infrared Emission Spectroscopy

Synthetic aluminosilicate samples were compressed into pellets for thermal-IR emission spectroscopy. Spectra of loose particulates have very low spectral contrast because of volume scattering effects and are not shown. Pellets 1 cm in diameter and a few mm thick were created by compressing ~0.2 g of particulate material to ~1000 psi in a hydraulic press for three minutes [*Michalski et al.*, 2005]. Emission spectra were collected at the Mars Space Flight Facility at Arizona State University using a Nicolet Nexus 670 spectrometer configured to measure emitted energy [*Christensen and Harrison*, 1993; *Ruff et al.*, 1997]. Samples were placed in copper sample cups painted black to behave as a spectral blackbody, and heated to 80° C before and during the experiments to increase the signal-to-noise ratio. Spectra were scanned 240 times over the course of ~4 minutes, from 200-2000 cm^{-1} with 2 cm^{-1} spectral resolution. Blackbodies at 70 °C and 100 °C were measured to calibrate raw data to radiance [*Christensen and Harrison*, 1993]. Radiance spectra were transformed to emissivity spectra by normalizing to the Planck curve corresponding to the sample temperature [*Ruff et al.*, 1997].

Table 4.1. Synthesis conditions for each aluminosilicate sample.

Sample	Method	Solution Si/Al	Solution pH	Orthosilicate
Ohashi_2009_100 mmol	*Ohashi et al.* [2002]	0.75	3.4	Na-orthosilicate
Ohashi_2010_30 mmol A, B, C	*Ohashi et al.* [2002]	0.75	4.6-4.7	Na-orthosilicate
Ohashi_2010_100 mmol	*Ohashi et al.* [2002]	0.75	4.5	Na-orthosilicate
Wada_2010_Si/Al = 0.5	*Wada et al.* [1979]	0.5	4.6	TOS
Wada_2010_Si/Al = 1	*Wada et al.* [1979]	1	4.2	TOS
Wada_2010_Si/Al = 2, pH 3.7	*Wada et al.* [1979]	2	3.7	TOS
Wada_2010_Si/Al = 2, pH 4.4	*Wada et al.* [1979]	2	4.4	TOS
Wada_2010_Si/Al = 2, pH>10	*Wada et al.* [1979]	2	10	TOS
Wada_Si/Al = 4, pH 3.6	*Wada et al.* [1979]	4	3.6	TOS
Wada_Si/Al = 4, pH 4.4	*Wada et al.* [1979]	4	4.4	TOS

4.3.3 Near-Infrared Reflectance Spectroscopy

Near-infrared (NIR) reflectance spectra of loose powders and compressed pellets were collected on a Nicolet 6700 FTIR spectrometer using a CaF_2 beam splitter, and uncooled InGaAs detector, and a white light source at SUNY Stony Brook. Spectra were measured from 12500-4000 cm^{-1}. The spectrometer was purged of CO_2 and H_2O, and 1024 scans were averaged (~12 minutes total scan time) to create the final spectra. All of the spectra are referenced to a gold mirror standard.

4.3.4 Allophane Characterization Techniques

FTIR transmission spectroscopy, X-ray diffraction, atomic absorption spectroscopy, and transmission electron microscopy was performed on each synthetic sample to determine whether each sample is pure allophane. FTIR transmission spectra were collected at Arizona State University using a Bruker IFS 66 spectrometer. Aluminosilicate powders (0.005 g of sample) were compressed into KBr (0.150 g of KBr) pellets using the same pressing methods as above. Spectra were measured over the wavelength range 6000-400 cm^{-1} with 2 cm^{-1} spectral resolution.

Bright field transmission electron microscope images and diffraction patterns were collected using a Philips CM200-FEG high-resolution TEM/STEM with a 200 kV accelerating voltage in the LeRoy Eyring Center for Solid State Sciences at Arizona State University.

X-ray diffraction patterns were measured at Johnson Space Center with a Panalytical Xpert-pro instrument in Transmission spinner PW3064/60 configuration using Cu K-α radiation with generator settings at 45kV and 40 mA. The runs were performed from 5.00-80.00° 2θ with sample spinner on.

Atomic absorption spectroscopy was performed at Johnson Space Center to determine molar Si/Al ratios. Cations were detected and measured, in triplicate, by AA-Graphite furnace using a Perkin Elmer AAnalyst 800 outfitted with element specific

Hollow Cathode lamps. Concentrations of the cations were determined from calibration curves which were produced from the analysis of four standards prior to each analysis. A modifier (0.3% $MgNO_3$ solution) was added to all standard and sample solutions to ensure complete ionization. Solutions were diluted as needed.

4.4 Results

4.4.1 Atomic Absorption Spectroscopy

Allophane has a specific range of molar Si/Al ratios of ~0.5-1 [*Wada*, 1989], although allophanes with molar Si/Al ratios as low as 0.4 have been reported [*Wada and Wada*, 1977]. Chemistry calculated from atomic absorption spectroscopy shows that seven of the synthetic samples fall within the allophane compositional range (Table 4.2). Synthetic samples with Si/Al ratios greater than 1 are referred to as "aluminosilicate gels," since there are no named allophanes with Si/Al ratios > 1.

4.4.2 Infrared Spectroscopy

4.4.2.1 Emission spectroscopy

Emission spectra of the pelletized samples show broad absorptions over the wavelength ranges 1200-800 cm^{-1} and 650-300 cm^{-1} from Si-O-Si(Al) stretching and deformation vibrations, respectively (Figure 4.2) [*Farmer*, 1968; *Parfitt and Henmi*, 1980; *Parfitt et al.*, 1980; *Wada*, 1989]. Samples can be divided into three broad compositional categories based on emission spectra: 1) Si-rich, 2) Al-rich, and 3) intermediate composition. The Si-rich samples have a V-shaped absorption from Si^{IV}-O (tetrahedrally-coordinated Si) stretching vibrations near 1080 cm^{-1} with a prominent shoulder on the high frequency side and a smaller shoulder on the low frequency side. Si-rich samples have a strong absorption near 430 cm^{-1} from Si^{IV}-O bending vibrations. Al-rich samples have a V-shaped absorption from Si^{IV}-O stretching vibrations near 950 cm^{-1} with a shoulder at lower frequencies. The Si-O stretching absorption occurs at shorter wavelengths for Si-rich samples, suggesting that the tetrahedral sheet is more

polymerized than in Al-rich samples. The shoulder at longer frequencies in Al-rich samples is likely due to Al-OH deformation vibrations [*Wada and Kubo*, 1975; *Madejová et al.*, 2001]. Al-rich samples have three absorptions <700 cm^{-1} centered at 540, 420, and 340 cm^{-1} from Si^{IV}-O-Al^{VI} deformations, Si^{IV}-O bending vibrations, and Al^{VI}-O (octahedrally-coordinated Al) deformations, respectively [*Michalski et al.*, 2006a]. Emission spectra of samples with intermediate compositions are spectral combinations of the Si- and Al-rich samples. Samples with intermediate compositions have Si^{IV}-O stretching absorptions near 1080 cm^{-1} with shoulders at longer wavelengths. Spectra display absorptions from Si^{IV}-O-Al^{VI} deformations and Si^{IV}-O bending vibrations within tetrahedral layers at 540 and 420 cm^{-1}, respectively. This combination of spectral features indicates that there are two distinct aluminosilicate compositions with distinct structures (Si-rich and Al-rich). Samples with intermediate Si/Al ratios are physical mixtures of the Si- and Al-rich phases.

4.4.2.2 Transmission Infrared Spectroscopy

As in the emission TIR spectra, transmission spectra show that there are two distinct aluminosilicate end-members (Si-rich and Al-rich) and samples with intermediate compositions are physical mixtures of the two end members (Figure 4.3). Transmission IR spectra of all synthetic products have absorptions at 3500 cm^{-1} from O-H stretching vibrations in hydroxyl groups and adsorbed H_2O and at 1650 cm^{-1} from H-O-H deformation vibrations in adsorbed H_2O (Figure 4.3) [*van der Marel and Beutelspacher*, 1976; *Wada*, 1989]. The Al-rich sample spectrum has a sharp, strong absorption near 980 cm^{-1} from Si^{IV}-O stretching vibrations. The strong, broad absorption centered near 600 cm^{-1} and the shoulder near 690 cm^{-1} have been ascribed to Al^{VI}-OH and Si^{IV}-OH vibrations, respectively [*Parfitt et al.*, 1980; *Childs et al.*, 1990]. The shoulder on the long wavelength side of this feature (at ~500 cm^{-1}) is likely from Si^{IV}-O-Al^{VI} deformation vibrations, while the absorption at 440 cm^{-1} is from Si^{IV}-O bending vibrations [*Michalski*

et al., 2006a]. Absorptions at 430, 500, 570, and 690 cm^{-1} are characteristic of imogolite [*Parfitt and Henmi*, 1980]. Absorptions in these regions for Al-rich samples suggest that they are imogolite-like allophanes.

The spectrum of the Si-rich sample has a sharp, strong absorption ~1060 cm^{-1} and a shoulder at ~1200 cm^{-1} from Si^{IV}-O stretching vibrations (Figure 4.3). The absorption at 1200 cm^{-1} is indicative of a more polymerized silica species, either from discrete amorphous silica or possibly from silica polymers associated with the allophane tetrahedral layer. The absorption at 810 cm^{-1} is from Si^{IV}-O stretching vibrations and is indicative of polymerized silica [*Madejová and Komadel*, 2001; *Michalski et al.*, 2006a]. The shoulder near 980 cm^{-1} is from Si^{IV}-O stretching vibrations and indicates a small amount of Al-rich material may be present. The weak absorption near 600 cm^{-1} is from Al^{VI}-OH vibrations, and the sharp absorption near 460 cm^{-1} is from Si^{IV}-O bending vibrations [*Parfitt et al.*, 1980; *Michalski et al.*, 2006a].

Transmission spectra of synthetic allophanes with an intermediate Si/Al ratio contain features found in both Si-rich and Al-rich sample spectra (Figure 4.3). For example, there are three distinct minima in the Si^{IV}-O stretching vibration absorption near 1200 and 1060 cm^{-1} (from the presence of the Si-rich phase) and 980 cm^{-1} (from the presence of the Al-rich phase). A broad absorption centered near 600 cm^{-1} is from overlapping Al^{VI}-OH and Si^{IV}-OH vibrations. A sharp, weak absorption at 440 cm^{-1} is from Si^{IV}-O bending, also observed in the Al-rich sample spectrum. The sample "Wada Si/Al 2 pH >10" was synthesized at a higher pH than required for allophane precipitation, so its TIR spectrum should not be used to deconvolve Martian TIR spectra.

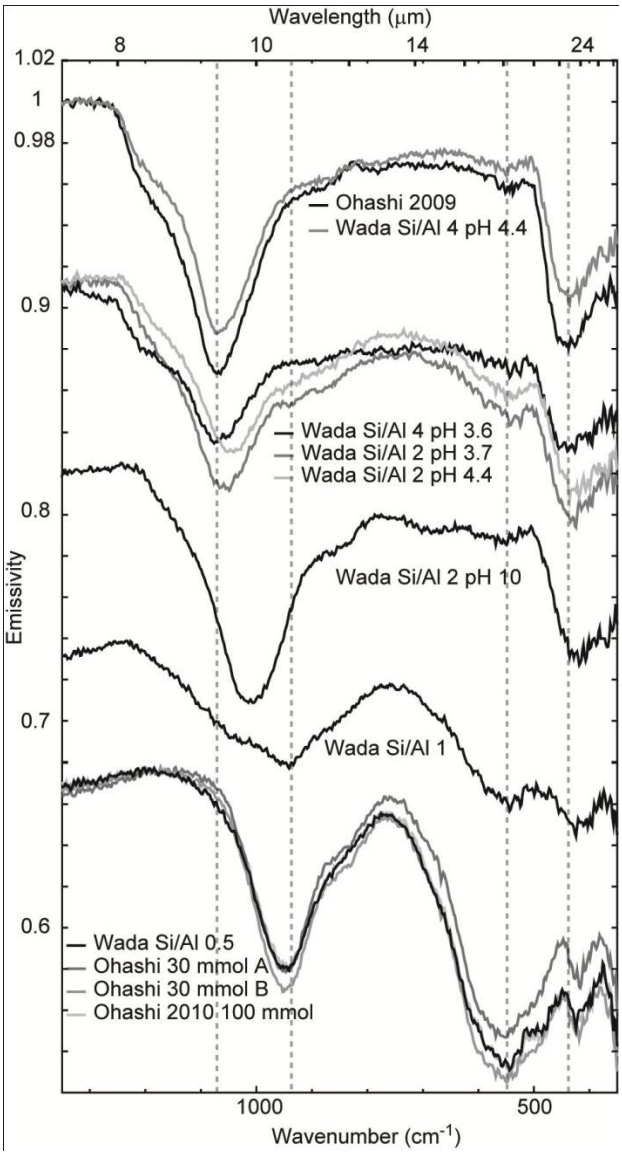

Figure 4.2. TIR emission spectra of pellets of synthetic aluminosilicates. Vertical lines denote major absorption positions. Moving from left to right, absorptions are from Si-O stretching (where Si is more polymerized), Si-O stretching (where Si is less polymerized), Si-O-Al deformations, and Si-O bending. Spectra are offset in emissivity for clarity.

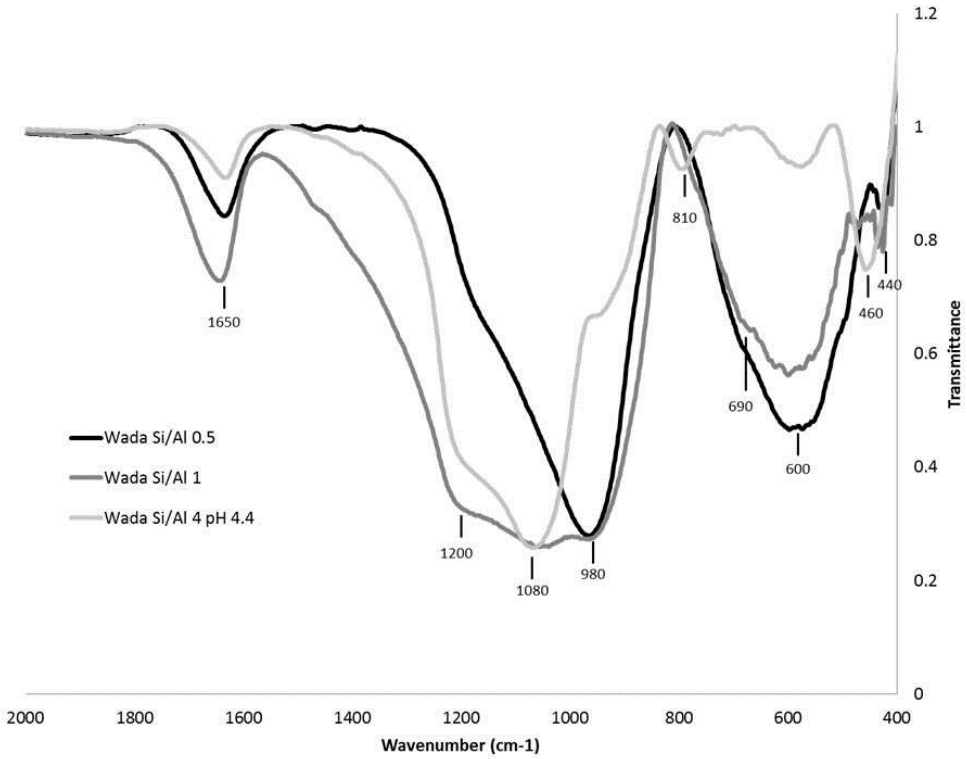

Figure 4.3. Transmission IR spectra of Si-rich, Al-rich, and intermediate synthetic aluminosilicates. Note that the high-silica sample (Wada Si/Al 4 pH 4) has an absorption at 810 cm^{-1}, suggesting the presence of discrete opaline silica.

4.4.2.3 Near-Infrared Spectroscopy

Near-IR spectra of all samples show absorptions at 1.4 microns from O-H vibrations, 1.9 microns from O-H and H-O-H vibrations, and 2.2 microns from Al-OH and Si-OH vibrations (Figure 4.4). With increasing Si content, absorptions at 1.4 and 1.9 microns become sharper. The absorption at 2.2 microns broadens and the minimum shifts to longer wavelengths with increasing Si-content, suggesting that the high-Si products are less ordered.

4.4.3 Transmission Electron Microscopy

TEM images from previous studies of natural and synthetic allophanes show allophane is made up of clusters of 3-5 nm spherical particles [*Wada*, 1989; *Ohashi et al.*, 2002]. Bright field TEM images of aluminosilicate products synthesized in this study show two different end-member morphologies which are dependent on chemical composition. Si-rich products are made up of the characteristic fluffy aggregates of ~5 nm particles (Figure 4.5a,b). High-resolution images lack lattice fringes that are expected for discrete tetrahedral and octahedral layers. This lack of fringes could indicate structural disorder of the layers within the particles. However, this lack of local order may be a result of irradiation-induced beam damage caused by the higher electron fluxes used in high-resolution imaging. Diffraction patterns are similar to those of allophanes from previous studies and have one diffuse ring at ~0.35 nm [*Wada*, 1989; *Farmer et al.*, 1991], further demonstrating a lack of long-range order (Figure 4.5c). Al-rich products are composed of dense gel-like fragments that lack porosity (Figure 4.5d). Diffraction patterns of these Al-rich products are similar to diffraction patterns of allophanes from previous studies, showing a diffuse ring at 0.35 nm (Figure 4.5e) [*Wada*, 1989; *Farmer et al.*, 1991]. Bright field images of allophanes with intermediate Si content show a morphology that is between the Si- and Al-rich allophanes, in which the products are composed of dense, closely packed, roughly spherical particles (Figure 4.5f,g).

4.4.4 XRD

X-ray diffraction patterns of the synthetic products indicate all samples are X-ray amorphous with broad diffuse peaks (Figure 4.6). XRD patterns of all materials have a strong, broad reflection centered near 0.35 nm, from reflections within the silica tetrahedral layer [*Ohashi et al.*, 2002]. This reflection is shifted to ~0.37 nm for Si-rich products, which indicates these products are similar to silica gels and opaline silica, which have reflections at 0.39 nm [*Ohashi et al.*, 2002]. Patterns of Al-rich and intermediate products have a strong, broad reflection at 0.22 nm from reflections within the alumina octahedral layer [*Iyoda et al.*, 2011] and a weak, broad reflection at 0.14 nm. These reflections diminish in strength with increasing Si/Al ratio. Patterns are characteristic of natural and synthetic allophanes from previous studies and other X-ray amorphous aluminosilicates [*Wada*, 1989; *Ohashi et al.*, 2002].

4.5 Discussion

4.5.1 Comparisons of Synthetic Aluminosilicates to Natural Allophanes

Analyses of the synthetic aluminosilicates suggest that some products are true allophanes. Based on Si/Al ratios calculated from atomic absorption spectroscopy, the Ohashi 30 mmol, Ohashi 100 mmol, Wada Si/Al = 0.5, and Wada Si/Al = 1 samples have allophanic compositions (Table 4.2). XRD patterns of these samples show three broad reflections that are similar to those of natural allophanes and indicate that these materials lack long-range order.

TEM images of the synthetic samples with Si/Al ratios within the allophane range show that they are gel-like or are composed of fused nano-particles (Figure 4.5), rather than aggregates of roughly spherical particles that have been reported for natural allophanes [*Wada*, 1989]. However, allophane can precipitate as a gel [*Farmer et al.*, 1985], so the gel morphology for Al-rich samples is consistent with allophane. FTIR

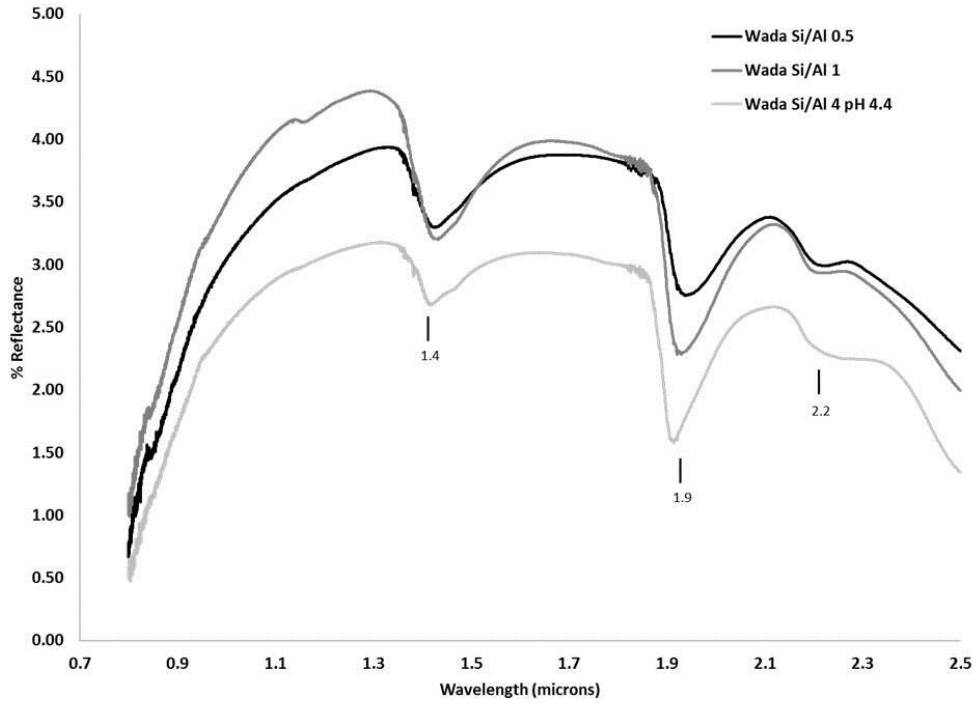

Figure 4.4. Near-infrared spectra of Al-rich, intermediate, and Si-rich synthetic aluminosilicate samples. Note that all samples have absorptions at 1.4, 1.9, and 2.2 microns. With increasing Si content, absorptions at 1.4 and 1.9 microns become narrower and the absorption at 2.2 microns broadens and shifts to longer wavelengths.

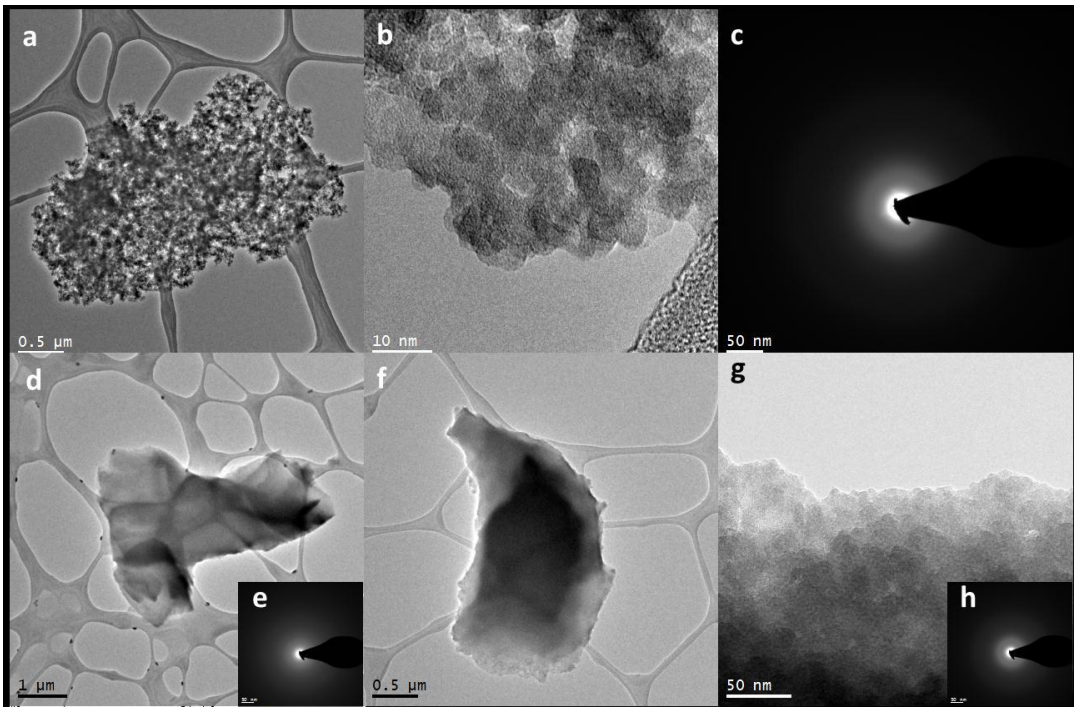

Figure 4.5. TEM bright field images of synthetic aluminosilicates. A, b. High-Si product is composed of aggregates of spherical particles ~5 nm in diameter. d. Al-rich product is composed of irregularly shaped gel-like particles. F. Products with intermediate Si/Al ratios are composed of irregularly shaped gel-like particles as in Al-rich products, but on closer inspection, show some spherical particulate morphology is present (g), as in Si-rich products. Electron diffraction patterns of all products show they are amorphous (c,e,h).

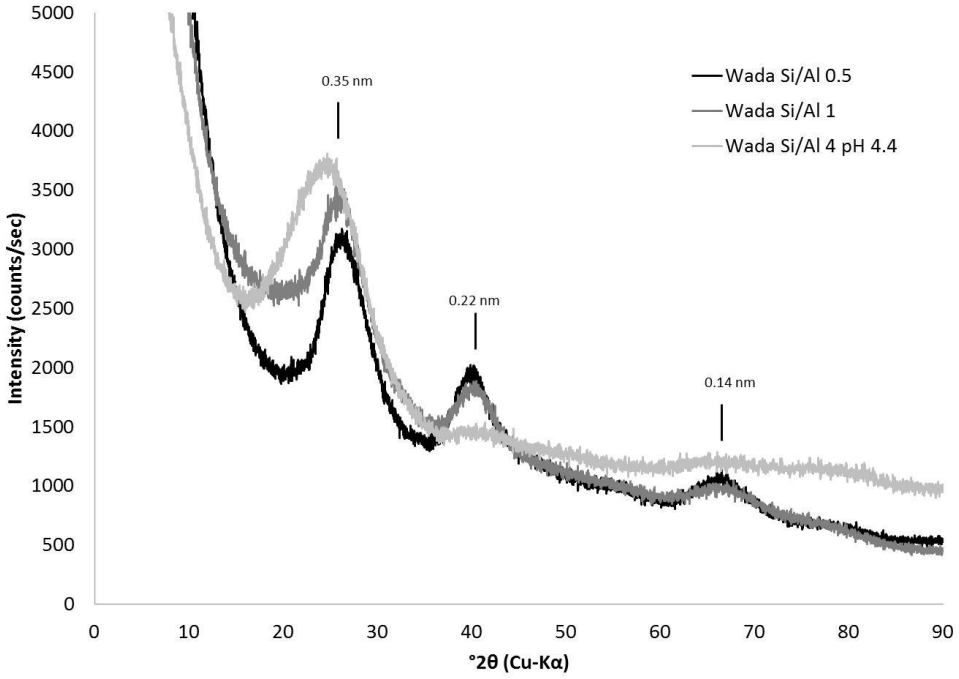

Figure 4.6. XRD patterns of synthetic aluminosilicates with Al-rich, intermediate, and Si-rich compositions. Each sample displays broad absorptions, indicating they are poorly-crystalline. Note that the peaks with d-spacings at 0.22 nm and 0.14 nm for the Si-rich sample are diminished and the peak at 0.35 is shifted to slightly larger d-spacings, suggesting this sample contains discrete amorphous silica.

Table 4.2. Molar Si/Al ratios for synthetic aluminosilicates do determine if compositions are consistent with allophane or gel.

Sample	Molar Si/Al ratios from AA	Allophane or Gel
Ohashi_2009_100 mmol	4.4	Gel
Ohashi_2010_30 mmol A	0.77	Intermediate allophane
Ohashi_2010_30 mmol B	0.48	Al-rich allophane
Ohashi_2010_30 mmol C	0.58	Al-rich allophane
Ohashi_2010_100 mmol	0.43	Al-rich allophane
Wada_2010_Si/Al = 0.5	0.44	Al-rich allophane
Wada_2010_Si/Al = 1	0.92	Si-rich allophane
Wada_2010_Si/Al = 2, pH 3.7	1.88	Gel
Wada_2010_Si/Al = 2, pH 4.4	2.19	Gel
Wada_2010_Si/Al = 2, pH>10	0.94	Si-rich allophane
Wada_Si/Al = 4, pH 3.6	3.71	Gel
Wada_Si/Al = 4, pH 4.4	5.61	Gel

transmission spectra of Al-rich products with molar Si/Al ratios ~0.5 are similar to spectra of imogolite-like allophanes reported previously [*Parfitt and Henmi*, 1980], suggesting that these materials are pure allophanes. Transmission spectra of materials with molar Si/Al ratios ~1 show evidence for imogolite-like allophanes, but also show evidence for polymerized silica. It is unknown whether polymerized silica is present as discrete amorphous silica or polymerized units associated with the silica tetrahedral layers in allophane, as suggested by *Parfitt* [1990] for Si-rich soil allophanes. The lack of absorptions near 810 cm^{-1} in these materials suggests that discrete amorphous silica is not present. Furthermore, the lack of absorptions near 880 cm^{-1} in transmission spectra of products with Si/Al ratios ~0.5-1 indicates that tetrahedrally coordinated Al is not present in significant amounts. This demonstrates that the synthetic samples are structurally similar to soil allophanes, where continuous Al-OH octahedral sheets make up the exterior surface and tetrahedral SiO_3OH groups make up the interior surface. SiO_3OH groups are more polymerized with increasing Si content, as evidenced from the presence of absorptions ~1060 cm^{-1}. Ohashi 30 mmol, Ohashi 100 mmol, Wada Si/Al = 0.5, and Wada Si/Al = 1 samples are true allophanes, based on the characterization techniques in this study.

Synthetic products with molar Si/Al ratios >1 are likely a combination of allophanic material and discrete amorphous silica. Transmission FTIR spectra of high-Si products have absorptions at 810 cm^{-1}, indicating the presence of discrete amorphous silica, and XRD patterns are dominated by reflections from the silica tetrahedral layer. Furthermore, molar Si/Al ratios are significantly higher than the allophane range. These high-silica aluminosilicates are not pure allophanes and they are referred to as "aluminosilicate gels."

TIR emission spectra from all samples can be added to Martian spectral libraries, except for Wada Si/Al 2 pH>10 because this sample was synthesized outside of the pH

range required for precipitating allophane. When deconvolving Martian TIR spectra, it is essential to add spectrally distinct phases so that they do not replace one another in spectral models. Thus, adding Al-rich allophane, Si-rich allophane, and one or two distinct gel spectra with different Si/Al ratios to individual spectral libraries is recommended. The identification of allophane on the Martian surface would suggest aqueous alteration of volcanic glass under neutral to mildly acidic conditions and would point towards specific Si and Al concentrations present in the fluids from which allophane precipitated. It is important to note that the synthetic aluminosilicate gels are not true allophanes. Therefore, the identification of this material in TIR models of the Martian surface would not indicate the same weathering conditions as those that lead to the precipitation of allophane. High-Si aluminosilicate gels and opaline silica would precipitate from solutions with higher silica concentrations than solutions from which allophane precipitate. Higher silica concentrations could result from the aqueous alteration of Al-poor materials, such as high-Si volcanic glass or olivine. Low pH, water-limited aqueous alteration conditions favor the alteration of olivine over other igneous minerals [*Hurowitz and McLennan*, 2007] and the precipitation of opaline silica [*Tosca et al.*, 2004]. Therefore, the identification of high-Si aluminosilicate gels on Mars from TIR spectral models could be consistent with acidic weathering conditions.

4.5.2 Comparing Spectra of Synthetic Allophanes and Gels to Other High-Silica Phases

TIR emission spectra of high-silica phases, including phyllosilicates, volcanic glasses, zeolites, and opaline silica, are broadly similar. It has been suggested that these materials may replace one another in TIR models because of their spectral similarities [*Wyatt and McSween*, 2002; *Michalski et al.*, 2006b]. However, TIR emission spectra of Al-rich and Si-rich allophanes are spectrally distinct from other high-silica phases (Figure 4.7). Al-rich allophane has a Si^{IV}-O stretching absorption at much longer wavelengths

compared to other high-silica phases (950 vs. ~1050 cm^{-1}, respectively). Additionally, the absorption from Si^{IV}-O-Al^{VI} deformation vibrations at 550 cm^{-1} is stronger relative to the Si^{IV}-O bending absorption and it is broader than the same absorptions in other high-silica phases.

The TIR emission spectrum of Si-rich allophane has a very broad absorption ~1200-900 cm^{-1} from Si^{IV}-O stretching vibrations and multiple absorptions at longer wavelengths from Si^{IV}-O-Al^{VI} deformation and Si^{IV}-O bending vibrations. The spectrum of Si-rich allophane is unique compared to other high-silica phases. The basaltic glass spectrum has broad absorptions in the Si^{IV}-O stretching and bending regions because it is amorphous and there are variations in bond strengths from the presence of various network modifying cations (ex: K^+, Na^+, Ca^{2+}, Al^{3+}). However, Si-rich allophane has short-range atomic order while basaltic glass is amorphous, so the spectrum of Si-rich allophane displays distinct absorption minima within the Si^{IV}-O stretching and bending regions. Additionally, the Si-rich allophane spectrum has an absorption from Si^{IV}-O-Al^{VI} deformation vibrations, while the basaltic glass spectrum does not.

The high-Si aluminosilicate gel spectrum is most similar to other high-silica phases. The Si^{IV}-O stretching absorption position is similar to that of K-rich volcanic glass, zeolite (heulandite), and phyllosilicates (montmorillonite). The aluminosilicate gel spectrum is most similar to K-rich glass because both have single absorptions from Si^{IV}-O stretching and Si^{IV}-O bending vibrations. However, the aluminosilicate gel spectrum is distinct from K-rich glass because its Si^{IV}-O bending absorption occurs at longer wavelengths.

NIR reflectance spectra of Al-rich and Si-rich allophanes and aluminosilicate gels are similar to those of Al-phyllosilicates (montmorillonite) and opaline silica because all have absorptions at 1.4, 1.9, and 2.2 microns (Figure 4.8). Absorptions at 1.4 and 1.9 microns are present in all hydrated phases because they are from vibrations

within OH and H_2O. Thus, they are generally not used to characterize hydrated phases on the Martian surface, except in the case of hydroxylated but not hydrated phases, such as kaolinite, which has a feature at 1.4 microns but not at 1.9 microns [*Mustard et al.*, 2008]. The absorptions from metal cation-OH vibrations in the 2.1-2.5 microns wavelength range are principally used to identify specific phases [*Ehlmann et al.*, 2008; 2009; *Milliken et al.*, 2008; *Mustard et al.*, 2008]. Absorptions from Al-OH and Si-OH vibrations occur near 2.2 microns. The absorption at 2.2 microns in montmorillonite is sharper than those in allophane, gel, and opaline silica spectra, suggesting that allophane and gel could be distinguished from montmorillonite on Mars. The opaline silica spectrum shows a broad 2.2 micron feature, similar to features in allophanes and gel, but the opaline silica spectrum has a distinct minimum, while allophane and gel spectra do not. Based on the different morphologies of the 2.2 micron features, allophane and gel should be distinguishable from montmorillonite and opaline silica in NIR data from the Martian surface.

4.6 Conclusions

It has been suggested, based on absorption positions of Martian TIR spectra, that allophane is present on Mars [*Michalski et al.*, 2006a]. However, TIR and NIR spectral libraries previously lacked allophane so their presence on Mars could not be tested by spectroscopy. This study synthesized allophanes and other poorly-crystalline aluminosilicates to measure their TIR and NIR spectra and add them to spectral libraries. Transmission FTIR spectroscopy suggests that Al-rich allophanes have imogolite-like structures, where the alumina dioctahedral layer makes up the external surface and unpolymerized silica tetrahedral layers are on the interior of particles. It is likely that Si-rich allophanes also have an imogolite-like structure with silica polymers associated with the tetrahedral silica layer. High-Si aluminosilicate gels have small amounts of discrete opaline silica, based on a small absorption at 810 cm^{-1} in transmission FTIR spectra.

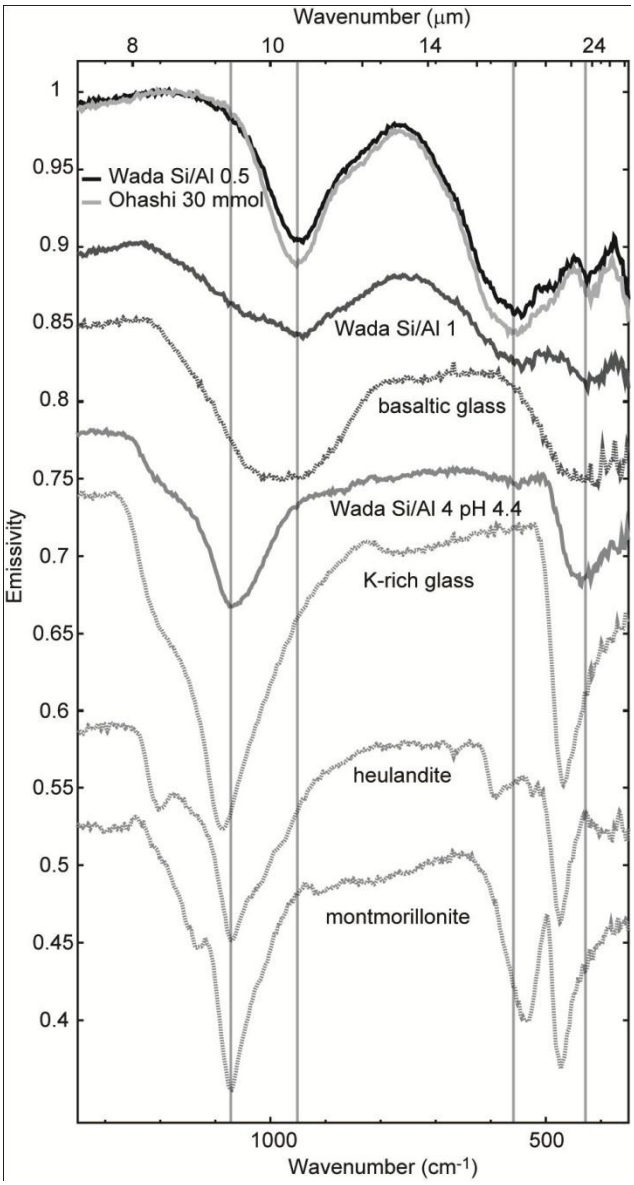

Figure 4.7. TIR emission spectra of synthetic Al-rich and Si-rich allophanes and aluminosilicate gel from this study compared to volcanic glass, phyllosilicate, and zeolite spectra. Vertical lines denote allophane and gel absorption minima positions. Note that the Al-rich allophanes (at the top of the figure) are spectrally distinct from other phases. The Si-rich allophane spectrum (Si/Al 1) is similar to the basaltic glass spectrum, but has distinct minima in the Si-O stretching region and has an absorption from Si-O-Al deformation vibrations, which the basaltic glass spectrum lacks. The aluminosilicate gel spectrum (Si/ Al 4) is most similar to other high-silica phase spectra, where the Si-O stretching minimum is similar to that of K-rich glass, heulandite (zeolite), and montmorillonite (Al-smectite). However, the Si-O bending vibration is at longer wavelengths compared to other high-Si phases, showing that the aluminosilicate gel is spectrally distinct.

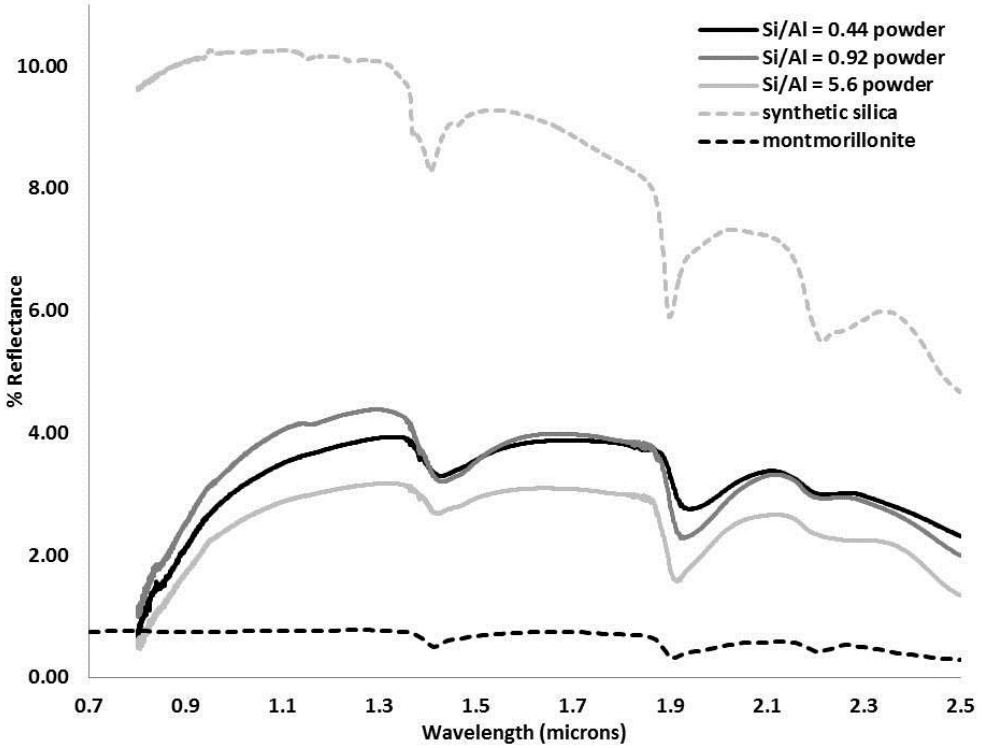

Figure 4.8. NIR reflectance spectra of Al-rich and Si-rich allophanes and aluminosilicate gel compared to NIR spectra of montmorillonite and synthetic opaline silica, precipitated from orthosilicate solution. Note that all spectra have absorptions at 1.4, 1.9, and 2.2 microns. Allophane, gel, and synthetic silica spectra have broad 2.2 micron absorptions, while that of montmorillonite is sharper.

NIR reflectance spectra of allophanes have absorptions at 1.4 and 1.9 microns from O-H and H-O-H vibrations and broad absorptions at 2.2 microns from Si-OH and Al-OH vibrations that broaden to longer wavelengths with increasing Si/Al ratios. NIR spectra of the synthetic samples are most similar to opaline silica and montmorillonite but are spectrally distinct, so it is suggested that allophanes and gels are distinguishable from other high-silica phases in Martian NIR spectra. TIR emission spectra of allophanes show absorptions from Si^{IV}-O stretching, Si^{IV}-O-Al^{VI} deformation, and Si^{IV}-O bending vibrations. Al-rich and Si-rich allophanes are spectrally distinct from other high-silica phases. TIR emission spectra of high-Si aluminosilicate gels are most similar to K-rich volcanic glass, but the Si^{IV}-O bending vibration for gels is at longer wavelengths, showing that gel is distinct from K-rich glass. Al-rich, Si-rich, and gel spectra should be added to libraries used to model TIR spectra of the Martian surface because they are spectrally distinct from other high-silica phases.

5 The Identification of Allophane on Mars through Thermal Emission Spectrometer Models

5.1 Introduction

One primary model of the aqueous alteration history of Mars defines a sequence of three distinctive eras, each characterized by a different, global alteration process [*Bibring et al.*, 2006]. During the Noachian Period (~4.5-3.7 Ga), the Martian surface experienced alteration under high water-to-rock ratios and alkaline pH. During the Hesperian Period (~3.7-3 Ga), acid sulfate alteration occurred under low water-to-rock ratios and low pH. During the Amazonian Period (~3 Ga-present), acidic aqueous alteration under low water-to-rock ratios was limited and anhydrous oxidation was and remains the dominant surface alteration process [*Bibring et al.*, 2006; *Hurowitz and McLennan*, 2007]. The presence of poorly-crystalline aluminosilicates, such as allophane, on the Martian surface has been predicted from thermal-infrared (TIR) data from the Thermal Emission Spectrometer (TES) [*Michalski et al.*, 2006a] and from in-situ chemical analyses at Gusev crater and Meridiani by the Alpha Particle X-ray Spectrometer (APXS) [*Clark et al.*, 2005; 2007; *Ming et al.*, 2006]. Allophane is a poorly-crystalline, hydrous aluminosilicate that commonly forms from low-temperature chemical weathering of volcanic glass or feldspar under near-neutral to mildly acidic pH [*Wada*, 1989]. The presence of allophane on the Martian surface has not been accounted for in the current model of Mars' global aqueous alteration history described above. Linear least squares modeling of Martian TIR data is a primary tool for understanding mineral distributions across the surface [*Ramsey and Christensen*, 1998]. Up until now, TIR spectral libraries lacked allophane so the presence of allophane on Mars could not be tested through TIR spectral modeling. Allophanes and aluminosilicate gels with a range of Si/Al ratios were synthesized and their TIR spectra were measured (Chapter 4). The goal of this study is to test for the presence of allophane on Mars on regional and local

scales by 1) modeling regional TES spectra identified by *Rogers et al.* [2007], 2) modeling TES spectra from the four potential landing sites for the Mars Science Laboratory (MSL) mission, and 3) modeling Mini-TES spectra of chemically weathered rocks from Gusev crater. The identification of allophane and its distribution across the surface could constrain past regional and local chemical weathering environments and help develop a new view of Mars' aqueous alteration history.

5.2 Background

5.2.1 Aqueous Alteration History of Mars

The aqueous alteration history of Mars has been inferred from orbital and in-situ mineralogical and chemical data. Near-infrared (NIR) spectroscopy is an important tool for identifying aqueous alteration products on the Martian surface, including phyllosilicates, zeolites, opaline silica, sulfates, and carbonates. NIR data measured by the Observatoire pour la Minéralogie, l'Eau, les Glaces et l'Activité (OMEGA) and the Compact Reconnaissance Imaging Spectrometer for Mars (CRISM) suggest that there are a variety of phyllosilicates in localized Noachian terrains [*Bibring et al.*, 2005; 2006; *Ehlmann et al.*, 2008; 2009; *Mustard et al.*, 2008]. This indicates that these areas once had long-lasting reservoirs of liquid water with alkaline pH, implying that these paleoenvironments may have been habitable [*Bibring et al.*, 2006]. A primary NASA goal is to explore potentially habitable environments in the solar system to investigate whether life evolved on a planetary surface other than Earth. The Mars Science Laboratory (MSL) mission will visit an area of Mars that shows evidence for phyllosilicates from NIR spectroscopy in order to study a potentially habitable region [*Mahaffy*, 2007]. The Mars science community has narrowed the landing site selection to four potential sites: 1) Eberswalde Crater, 2) Gale Crater, 3) Holden Crater, and 4) Mawrth Vallis (Figure 5.1). Eberswalde and Holden Craters have fluvial deltaic deposits with Fe/Mg-smectites and/or mixed-layer chlorite/smectite [*Milliken*, 2010]. Gale Crater

contains a several km thick mound of sediments that has Fe/Mg smectites and a variety of sulfates [*Bell*, 2010]. Mawrth Vallis is an ancient outflow channel and has a wide diversity of secondary silicates. The stratigraphy of Mawrth shows a basal 150-200 m thick layer containing Fe/Mg-rich smectite (i.e. nontronite or saponite), an intermediate ~10 m thick layer with a Fe^{2+}-rich hydrated silicate that has not been characterized, and an upper ~20 m thick layer enriched in Al-phyllosilicates (montmorillonite, beidellite, and kaolinite) and hydrated silica [*Bishop et al.*, 2010].

Alteration products in Hesperian-aged terrains are dominated by sulfates and Fe-oxides [*Bibring et al.*, 2006; *Hurowitz and McLennan*, 2007]. This drastic change in secondary mineralogy between the Noachian and Hesperian Periods has led to the hypothesis that there was a global change in aqueous environments from alkaline environments with high water-to-rock ratios in the Noachian to acidic, water-limited environments in the Hesperian [*Bibring et al.*, 2006]. Furthermore, APXS chemistry from all landing sites displays depletion in Fe+Mg in soils compared to rocks, indicating that acidic chemical weathering caused preferential dissolution of olivine [*Hurowitz et al.*, 2006; *Hurowitz and McLennan*, 2007]. The presence of this chemical trend at all landing sites suggests that acid sulfate weathering was a global process during the Hesperian [*Hurowitz et al.*, 2006; *Hurowitz and McLennan*, 2007]. Alteration products on Amazonian-aged surfaces are dominated by anhydrous Fe-oxides, suggesting that oxidative alteration processes in the absence of liquid water occurred during the most recent Martian time period [*Bibring et al.*, 2006].

5.2.2 High-Silica Phases Identified in Previous TES and Mini-TES Models

TES models of low-albedo surfaces show that the Martian surface is primarily composed of basalt [*Bandfield et al.*, 2000; *Christensen et al.*, 2000a; *Rogers and Christensen*, 2007]. Regional spectral variability within TES data (on the order of ~10^4-10^6 km^2) signifies regional mineralogical variations. *Bandfield et al.* [2000] identified

two distinct spectral types in Martian low-albedo surfaces, Surface Type 1 (ST1), present at low latitudes, and Surface Type 2 (ST2), present at mid-to-high latitudes. Models of ST1 were dominated by plagioclase and clinopyroxene, while models of ST2 were dominated by plagioclase and volcanic glass, suggesting that igneous processes caused the compositional variations. Models of each region identified phyllosilicates near the detection limit of linear deconvolution (~10-15 vol.%), so it was speculated that phyllosilicates may be present in very low (<<1 vol.%) abundances [*Bandfield*, 2002]. Subsequent studies found that ST2 was spectrally similar to weathered basalts and that clays can replace volcanic glass in spectral models of ST2 [*Wyatt and McSween*, 2002]. Further studies have suggested that amorphous silica or poorly-crystalline clay-like materials are also consistent with ST2 models [*Kraft et al.*, 2003; *Michalski et al.*, 2006a]. *Rogers et al.* [2007] further examined variability within TES data and identified 11 distinct regional spectra in low-albedo surfaces. Models of the nine non-dusty units identified significant abundances (>10 vol.%) of high-silica phases (volcanic glass, phyllosilicates, and opal), and models of the Solis Planum and Northern Acidalia surface types (Figure 5.1) identified the most (>30 vol.%) [*Rogers and Christensen*, 2007]. It was suggested that the origin of the high-silica phases is dependent on latitude, where high-silica phases at low latitudes were likely igneous in origin, while high-silica phases at mid-to-high latitudes (i.e. in Northern Acidalia) were weathering products. *Minitti and Hamilton* [2010] modeled the nine non-dusty units from *Rogers et al.* [2007] with five additional mafic to intermediate volcanic glass spectra to examine whether the high-silica phases identified in previous models could be replaced by volcanic glass. The mafic to intermediate glass spectra were not used by the models, and secondary silicates, including amorphous silica, clays, and zeolites, were identified. The authors suggest that glasses may have been altered to form amorphous secondary silicates or clay-like alteration products [*Minitti and Hamilton*, 2010].

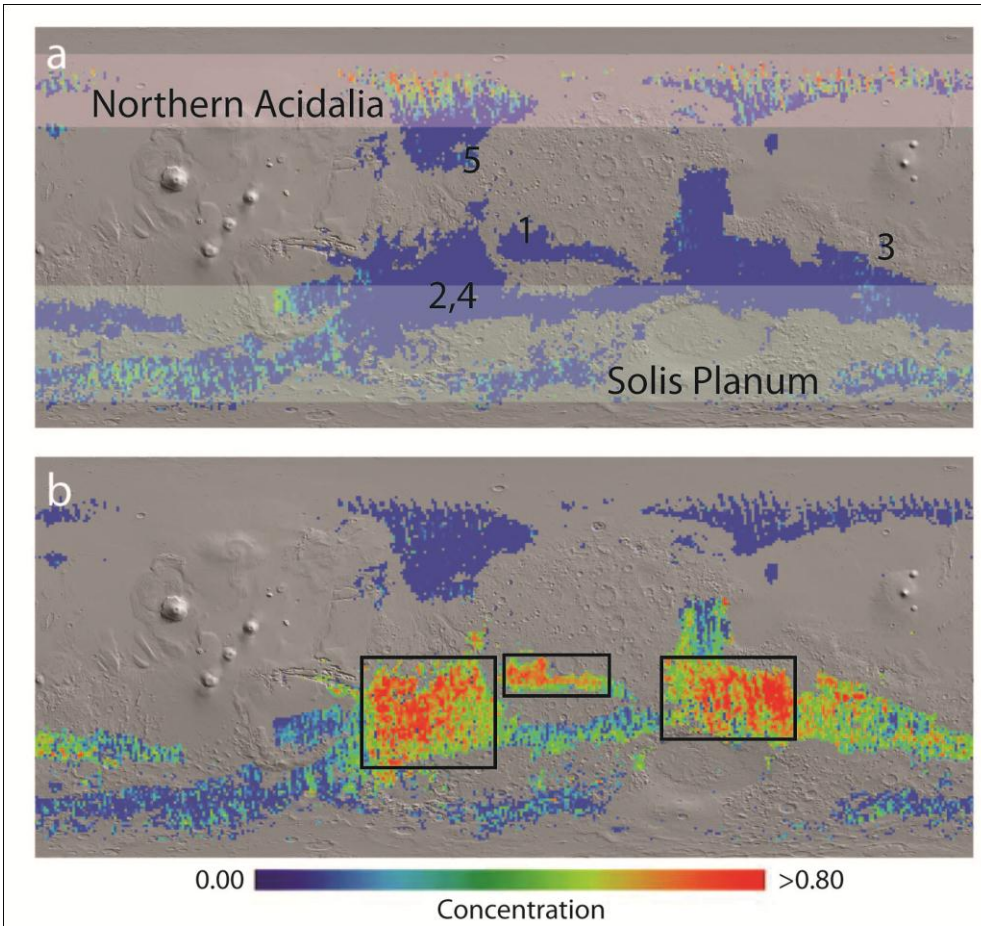

Figure 5.1. Maps of TES regional surface types and MSL landing sites. Maps are 360° longitude centered at 0°, and 77° S to 77° N latitude. The background image is MOLA shaded relief. a) Northern Acidalia and Solis Planum surface type concentration maps in shaded pink and gray, respectively, adapted from *Rogers et al.* [2007]. Numbers denote areas where localized TES data are from: 1) hematite-bearing Meridiani surfaces, 2) Eberswalde crater, 3) Gale crater, 4) Holden crater, and 5) Mawrth Vallis. b) Group 3 TES regional surface type concentration map, adapted from *Rogers et al.* [2007]. Group 3 includes Cimmeria, Tyrrhena, Hesperia, and Sinus Meridiani surface types. Black boxes outline the locations of the greatest concentrations of the Sinus Meridiani surface type.

Although NIR spectroscopy has been used to identify a variety of phyllosilicates within localized Noachian terrains, TES models generally do not identify significant phyllosilicate abundances in these areas. It has been suggested that TES cannot detect clays in the regions that OMEGA and CRISM do because 1) OMEGA and CRISM have higher spatial resolution and the phyllosilicates may be in areas too small to be detected by TES; 2) NIR spectroscopy is more sensitive to the detection of phyllosilicates than TIR spectral models are, with detection limits of 1-2 wt.% and ~10 vol.%, respectively [*Ramsey and Christensen*, 1998; *Bibring et al.*, 2005]; and 3) surface textures that are favorable for NIR spectroscopy are different for those that are favorable for TIR spectroscopy, where rough surfaces improve mineral detection using NIR spectroscopy because multiple surface scattering is enhanced and coarse-grained surfaces are ideal for TIR spectroscopy because multiple surfaces scattering is diminished [*Michalski and Fergason*, 2009]. Additionally, phyllosilicates may not be detected in TES models of clay-rich regions if these clays are poorly- or para-crystalline, like allophane or imogolite, because these materials are not represented in spectral libraries.

Mini-TES models of Meridiani and Gusev rocks show evidence for high-silica phases. Mini-TES models of the light-toned outcrop at Meridiani identify ~25 vol.% aluminous opaline silica and ~10 vol.% nontronite, in addition to Mg-, Ca-, and Fe-rich sulfates, plagioclase, and hematite [*Glotch et al.*, 2006]. *Glotch et al.* [2006] suggested that both Al-rich amorphous silica and phyllosilicates are likely present in this outcrop because removing either of them from the spectral library results in a poorer fit to the measured spectrum. High-silica rocks and soils have been identified near the Home Plate feature in Gusev crater and likely formed from hydrothermal processes [*Squyres et al.*, 2008; *Ruff et al.*, 2011]. Conversely, Mini-TES models of Clovis- and Watchtower-class rocks at Gusev crater, which show chemical evidence for aqueous alteration [*Ming et al.*, 2006], generally do not identify significant abundances of high-silica phases [*Ruff et al.*,

2006]. Instead, basaltic glass was identified in significant abundances in models of Clovis and Watchtower (40-45 vol.% and 35-50 vol.%, respectively) [*Ruff et al.*, 2006]. Removing the basaltic glass end members from the spectral library resulted in a poor fit and crystalline secondary silicates did not replace basaltic glass in the models. However, the authors noted that a poorly-crystalline aluminosilicate, such as allophane, might replace basaltic glass if it is spectrally similar [*Ruff et al.*, 2006].

5.2.3 Allophane and its Formation on Earth

Allophane is a hydrated aluminosilicate mineraloid with molar Si/Al ratios ranging from ~0.4 to 1 [*Wada and Wada*, 1977; *Wada*, 1989]. It forms as aggregates of roughly spherical, hollow particles ~3-5 nm in diameter or as gel films [*Farmer et al.*, 1985; *Wada*, 1989]. Allophane is a clay mineral precursor and is structurally similar to phyllosilicates. It is composed of curved Al^{3+} dioctahedral layers and Si^{4+} tetrahedral layers, where the silica tetrahedra become more polymerized as the Si/Al ratio increases [*Childs et al.*, 1990]. Allophane most commonly forms from the alteration of volcanic glass at low temperatures and neutral to mildly acidic pH (~5-7), but can also form from the alteration of plagioclase under a very specific pH range of 4.8-5 [*Harsh et al.*, 2002]. Allophane can form from the alteration of all compositions of volcanic parent material (i.e. basalt to rhyolite) [*Harsh et al.*, 2002]. It is generally found in soils that are a few thousand to a few tens of thousands of years old, and alters to form halloysite (under resilicating conditions) or gibbsite (under desilicating conditions); however, it has been shown to persist in volcanic soils that are >1 million years old [*Wada*, 1989].

5.2.4 Evidence for Allophane on Mars

In-situ chemical analyses from APXS on both Mars Exploration Rovers suggest that allophane is present in specific outcrops and soils [*Clark et al.*, 2005; 2007; *Ming et al.*, 2006]. Mineral models calculated from APXS data of the siliciclastic sediments from the Karatepe outcrop in Meridiani identify ~10 wt.% allophane [*Clark et al.*, 2005].

APXS chemistry and Mossbauer data of Wishstone-, Watchtower-, and Clovis-class rocks and the Paso Robles soil at Gusev suggest that these materials have been chemically altered because of the mobility of volatile elements and the high Fe^{3+}/Fe_{total} ratios [*Ming et al.*, 2006]. Mineral models derived from APXS data of these outcrops and soil show that they could be composed of up to ~70 wt.% allophane + amorphous silica [*Ming et al.*, 2006]. APXS chemistry of Independence-class rocks from Gusev show elevated Al_2O_3/SiO_2 ratios and low iron abundances, suggesting the presence of montmorillonite; however, Mini-TES spectral models of Independence-class rocks do not identify montmorillonite and instead identify aluminous opal [*Clark et al.*, 2007]. The combination of APXS and Mini-TES data may indicate the presence of allophane and amorphous silica instead of a crystalline clay [*Clark et al.*, 2007].

Qualitative assessments of TES absorption positions suggest that a clay-like material may be present on a global scale [*Michalski et al.*, 2006a]. TES models generally identify <15 vol.% phyllosilicates on regional to global scales [*Bandfield et al.*, 2000; *Rogers and Christensen*, 2007; *Minitti and Hamilton*, 2010]; however, NIR spectroscopy does not show evidence for phyllosilicates in these surfaces. Poorly-crystalline clay, such as allophane, could account for the detection of phyllosilicates in TES models and the absence of phyllosilicate absorptions in NIR spectra because NIR spectra of poorly-crystalline materials may display muted absorption features if the materials are less hydrated than clays [*Michalski et al.*, 2006b]. The purpose of this study is to further test for the presence of poorly-crystalline aluminosilicates on Mars by modeling TES and Mini-TES spectra using a library containing allophane and high-Si aluminosilicate gel. The specific goals of this investigation are to: 1) test for the presence of allophane on a regional scale by modeling regional TES spectra determined by *Rogers et al.* [2007] to see if allophane may replace phyllosilicates in previous TES models and thus explain the lack of evidence for phyllosilicates in NIR spectra of these regions; 2)

test for the presence of allophane in outcrops where it has been predicted from APXS measurements by modeling Mini-TES data from Clovis-, Wishstone-, and Watchtower-class rocks; and 3) examine whether allophane is detected in TES models of locations with positive phyllosilicate detections from NIR spectroscopy, specifically the proposed MSL landing sites, to investigate whether these phyllosilicates may be poorly crystalline.

5.3 Methods

TIR emission spectra of three synthetic allophanes and one synthetic high-Si aluminosilicate gel were added to spectral libraries used to model TES and Mini-TES spectra (Figure 5.2). The synthetic allophanes have molar Si/Al ratios of 0.44, 0.58, and 0.92 and the aluminosilicate gel has a molar Si/Al ratio of 5.6 (characterized in Chapter 4). *Rogers et al.* [2007] identified 11 distinct regional TES spectra from low-albedo Martian surfaces. We modeled nine of these regional spectra using the spectral library in *Rogers and Christensen* [2007] with the four poorly-crystalline aluminosilicate spectra (Table 5.1). The Southern Acidalia and Pandorae Fretum surface types were not modeled because dust coatings may affect the Southern Acidalia spectrum, making the models unreliable, and the Pandorae Fretum spectral shape was derived at a lower confidence level than other regional spectra [*Rogers and Christensen*, 2007]. TES spectra from the low-albedo hematite-bearing surfaces in Meridiani were excluded from the derivation of regional spectra by *Rogers et al.* [2007]; however, the averaged spectrum of the low-albedo hematite-bearing Meridiani unit was reported in *Rogers and Aharonson* [2008] and it is modeled in this study with the library used to model other TES spectra (Table 5.1). The spectra were modeled over the wavelength range from 307 to 1301 cm^{-1} using a linear least squares algorithm, specifically the iterative library reduction (ILR) method, as was done by *Rogers and Christensen* [2007]. In the ILR method, end member spectra that are identified in negative concentrations are iteratively removed from the final solution until all end members are positive. It is possible that end members that are

present on the surface in low abundances may be prematurely removed using ILR [*Bandfield et al.*, 2000; *Rogers and Christensen*, 2007]. To find the best model, a modeling routine that was similar to that used by *Rogers and Christensen* [2007] was followed, where different end members that are generally identified in <5 vol.% abundances (quartz, orthoclase, hematite, and amphiboles) were selectively removed. Pigeonite was also removed because pigeonite had a large effect on spectral models in *Rogers and Christensen* [2007]. Finally, the allophane and gel spectra were removed to test their influence on spectral models. The model with the lowest root mean square (RMS) error is reported, after removing the modeled blackbody component and renormalizing mineral abundances to 100%.

TES spectra of the four potential MSL landing sites were obtained using the TES Data Tool online. We averaged low- to intermediate-albedo spectra (with albedo ranges of 0-0.17) from each landing site that met constraints listed in Table 5.2. TES spectra of more localized, bright-toned surfaces from Mawrth Vallis were targeted because these surfaces show evidence for widespread clay minerals in OMEGA and CRISM data [*Michalski and Noe Dobrea*, 2007]. The TES Data Tool was searched using the same criteria as for the four landing sites, but the albedo range was increased to 0.13-0.23 (Table 5.2). It is important to note that while these surfaces are bright, they also have high thermal inertias so they are considered to be bedrock and not dusty [*Michalski and Noe Dobrea*, 2007]. The spectra from surfaces near the four proposed landing ellipses were averaged (Table 5.3). These spectra were modeled using the same library and modeling techniques as for the regional TES spectra, described above; however, kaolinite, halloysite, and an additional montmorillonite spectrum were added to the library used to model Mawrth data because NIR data suggests that these phases are present [*Bishop et al.*, 2010].

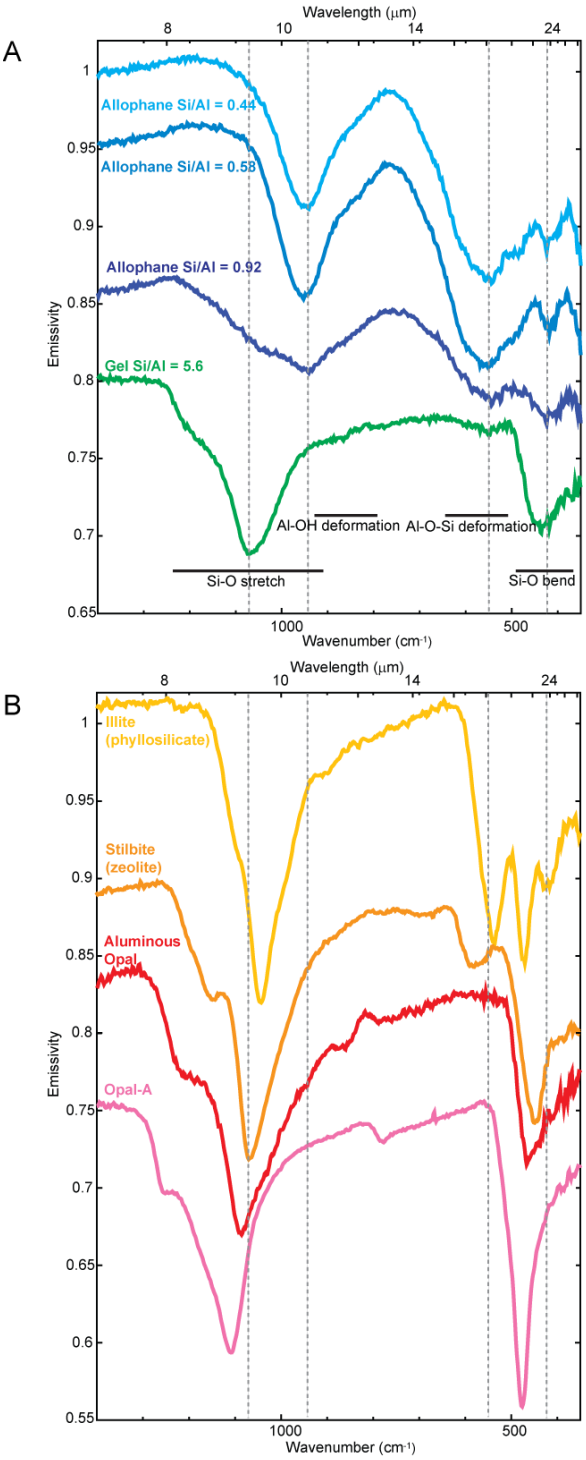

Figure 5.2. A) TIR emission spectra of synthetic allophanes and high-silica gel in the spectral library. Vertical lines denote absorption positions for Al-rich allophane and high-silica gel. B) TIR emission spectra of high-silica phases identified in significant abundances in models without allophane by *Rogers and Christensen* [2007]. Vertical lines denote absorption minima for Al-rich allophane and high-silica gel. Note that absorption positions for allophanes/gel differ from those of other high-silica phases and absorptions are broader for allophanes and gel. Spectra are offset in emissivity for clarity.

Table 5.1. Spectral library for TES models[1]

Mineral Group	Spectral End-Member
Quartz	Quartz BUR-4120
Feldspar	Albite WAR-0244
	Andesine BUR-240
	Anorthite BUR-340
	Bytownite WAR-1384
	Labradorite WAR-4524
	Microcline BUR-3460
	Oligoclase WAR-5804
	Orthoclase WAR-RGSAN01
	Shocked An 22.6 GPa
	Shocked An 56.3 GPa
Orthopyroxene	Bronzite BUR-1920
	Bronzite NMNH-93527
	Enstatite HS-9.4B
Clinopyroxene	Augite NMNH-9780
	Augite NMNH-122302
	Diopside WAR-6474
	Hedenbergite (Manganoan) DSM-HED01
Pigeonite	Pigeonite
Olivine	Fayalite WAR-FAY01
	Forsterite BUR-3720A
	KI3115 Fo68
	KI3362 Fo60
	KI3373 Fo35
	KI3008 Fo10
Zeolite	Crystalline heulandite
	Crystalline stilbite
Sheet silicates	Antigorite NMNH-47108
	Biotite BUR-840
	Halloysite WAR-5102
	Illite IMt-1 <0.2 microns
	Kaolinite KGa-1b
	Ca-montmorillonite STx-1
	Na-montmorillonite SWy-1 <0.2 microns
	Muscovite WAR-5474
	Saponite <0.2 microns
	Serpentine HS-8.4B
Am. Silica	Al-opal
	K-rich glass
	Opal-A (02-011)
	SiO_2 Glass
Amphibole	Magnesiohastingsite HS-115.4B
	Actinolite HS-116.4B
	Magnesiohornblende WAR-0354
Sulfates	Anhydrite S9
	Gypsum ML-S6
Carbonates	Calcite C40
	Dolomite C20
	Hematite BUR-2600 50

Allophane	Si/Al ratio = 0.44
	Si/Al ratio = 0.58
	Si/Al ratio = 0.92
Aluminosilicate gel	Si/Al ratio = 5.61
Blackbody	Blackbody

[1] The dust end member from *Rogers and Christensen* [2007] was not included because it did not affect spectral models.

End members in bold were added to the spectral library for modeling light-toned Mawrth surface spectra.

Table 5.2. TES data constraints[1]

	MSL low-albedo surfaces	Mawrth bright-toned surfaces
Target temperature (K)	255-350	255-350
Emission angle	0-30	0-30
Orbit range (ock)	1583-7000	1583-7000
Total ice extinction	0-0.04	0-0.04
Total dust extinction	0-0.15	0-0.15
Lambert albedo	0-0.17	0.13-0.23
Scan length (cm^{-1})	10	10
Observation type	Warm surface	Warm surface
Time of day	Day	Day

[1] Spectra that were returned were adjusted for atmosphere.

Table 5.3. Latitudinal and longitudinal constraints for selecting TES data from MSL landing sites

	Latitude[1] (° N)	Longitude[1] (° E)	Number of spectra returned
Eberswalde[2]	-24.5 to -22.5	325.5-327.5	27
Gale	-6.3 to -4.4	136.7 to 138.4	3
Holden	-27.1 to -25.9	324.2 to 326	38
Mawrth	22.8 to 25.3	338.6 to 342.4	306
Mawrth Ellipse 1	24.2 to 25.2	339.6 to 340.6	47
Mawrth Ellipse 2	23.7 to 24.3	340.7 to 341.3	8
Mawrth Ellipse 3	22.9 to 23.5	342.1 to 342.7	12
Mawrth Ellipse 4	24.55 to 25.15	339.1 to 340.6	9

[1] Latitudinal and longitudinal constraints (Table 3) were based off of the positions of landing site images listed on NASA's landing site webpage [http://marsoweb.nas.nasa.gov/landingsites/msl/topsites/].

[2] The latitudinal and longitudinal constraints for Eberswalde were expanded past the rim of the crater because no TES spectra met the initial criteria.

Mini-TES spectra of four rock classes from Gusev crater were modeled with the spectral libraries that were used in the original models by *Ruff et al.* [2006], plus the same allophane and aluminosilicate gel spectra that were added to TES libraries (Table 5.4). The Mini-TES library contains a negative slope end member that was calculated by dividing the Planck curve of a blackbody at 250 K by the Planck curve of a blackbody at 247 K and normalizing emissivity to 1.0 at 1300 cm^{-1} [*Ruff et al.*, 2006]. Slopes can be imparted on emissivity spectra of geologic surfaces if radiance spectra are calibrated with a blackbody that corresponds to a temperature that differs from the surface temperature [*Ruff et al.*, 2006]. The identification of slope in the spectral models is similar to the identification of blackbody. A spectrum of the dust in Gusev crater is in the library to account for dusty rock surfaces, and a sky end member is present because thermal radiation from the atmosphere can reflect off of rock surfaces into the detector and affect rock emissivity spectra [*Ruff et al.*, 2006]. The four rock classes modeled in this study include Clovis, Watchtower, and Wishstone, which may contain allophane [*Ming et al.*, 2006], and Adirondack, an unaltered basalt. The potential replacement of basaltic glass in the original models [*Ruff et al.*, 2006] by allophane was tested by selectively removing basaltic glass, allophane, and gel end members to find the best fit. Models were run using the ILR method of linear deconvolution over the wavelength range of 1350-390 cm^{-1}, as was done by *Ruff et al.* [2006]. Models with the lowest RMS errors are reported, once corrected for blackbody, slope, dust, and sky components.

5.4 Results

5.4.1 TES Regional Models

Significant abundances (>10 vol.%) of poorly-crystalline aluminosilicates were identified in regional spectral models of Northern Acidalia, Solis Planum, Sinus Meridiani, and the hematite-bearing unit in Meridiani, and the compositions of the modeled aluminosilicates differ for each region. High-Si aluminosilicate gel is identified

Table 5.4. Spectral Library for Mini-TES Models

Mineral Group	Spectral End-Member
Quartz	Quartz BUR-4120 55[1]
Feldspar	Albite WAR-0612 26[2,3]
	Albite WAR-0235 174[1,3]
	Oligoclase WAR-0234 22[2,3]
	Oligoclase BUR-3680 48[1,3]
	Andesine BUR-240[1,2,3]
	Andesine WAR-0024 175[1,3]
	Labradorite WAR-4524 63[1,2,3]
	Labradorite BUR-3080A 176[1,3]
	Labradorite WAR-RGAND01 222[1,3]
	Bytownite WAR-1384 177[1,2,3]
	Anorthite BUR-340 178[1,2,3]
	Anorthite WAR-5759 221[3]
	Shocked An 22.6 GPa[1,2,3,4]
	Shocked An 37.5 GPa[1,2,3,4]
Clinopyroxene	Augite HS-119.4B 56[3]
	Augite BUR-620 71[2,3]
	Augite DSM-AUG01 164[1,3]
	Augite NMNH-119197 147[3]
	Augite NMNH-9780 157[3]
	Augite NMNH-122302 170[3]
	Average augite[1]
	Diopside WAR-6474 54[2,3]
	Diopside NMNH-80819 150[3]
	Diopside HS-15.4B 16[1,3]
	Diopside HS-317.4B 32[3]
	Diopside DSM-DIO01 212[3]
	Diopside WAR6454 213[3]
Pigeonite	Pigeonite[1,2,3]
Orthopyroxene	Hedenbergite (Manganoan) DSM-HED01 145[1,3]
	Hedenbergite (Manganoan) NMNH-R11524 151[2,3]
	Hedenbergite NMNH-16158 215[3]
	Enstatite NMNH-38833 144[3]
	Enstatite NMNH-R14440 154[2,3]
	Enstatite WAR-2889 217[3]
	Average enstatite[1]
	Bronzite BUR-1920 6[2,3]
	Bronzite NMNH-166555 148[3]
	Bronzite NMNH-119793 149[3]
	Bronzite NMNH-C2368 159[3]
	Average bronzite[1]
	Hypersthene NMNH-B18247 12[1,2,3]
	Pyroxmangite HS-325.4B 33[3]
Olivine	Forsterite BUR-3720A 8[1,2,3]
	Forsterite AZ-01 38[2,3]
	KI3115 Fo68[1,2,3]
	KI3362 Fo60[1,2,3]
	KI3373 Fo35[1,2,3]
	KI3008 Fo10[1,2,3]

	Fayalite WAR-FAY01 167[1,2,3]
Glass	K-rich glass[1,2,3]
	Silica glass[2,3]
	Quenched basalt[1,2,3]
	Obsidian[2,3]
	Mars glass[2,3]
	Basaltic glass HWMK 124D, Rind, Spot B[1,2,3]
	Basaltic glass HWKV340A, matte uneven surface[2,3]
	Basaltic glass HWKV340A,glassy black flat surface[1,2,3]
	Maskelynite (chunk) ASU-7591[1,2,3]
Zeolite	Crystalline heulandite[1,2,3]
	Crystalline stilbite[1,2,3]
	Analcime tuff[3]
Sheet silicates	Serpentine HS-8.4B 14[1,2,3]
	Serpentine BUR-1690 51[1,2,3]
	Kaolinite KGa-1b granular 185[1,2]
	Halloysite WAR-5102 solid 189[1,2]
	Saponite ASU-SAP01 granular 194[1,2,3]
	Saponite <0.2 microns[2]
	Ca-montmorillonite STx-1 solid 197[1,2,3]
	Na-montmorillonite SWy-2 granular 200[1,2]
	Nontronite WAR-5108 granular 203[1,2,3]
	Fe-smectite SWa-1 solid 207[1,2,3]
	Illite IMt-2 granular 211[1,2,3]
	Beidellite Sbdl-1 <0.2 microns[1,2]
	Nontronite Nau-1 0.2 microns[2]
	Nontronite Nau-2 <0.2 microns[2]
	Hectorite Shca-1 <0.2 microns[2]
	Montmorillonite SWy-1 <0.2 microns[2]
Amphibole	Wollastonite BUR-5080 60[3]
Sulfates	Gypsum var. Alabaster ML-S11[1,2]
	Anhydrite ML-S9[1,2]
	Celestite ML-S13[1,2]
	Kieserite KIEDE1 < 1 mm[1,2]
.	Glauberite GBYAZ-R1[1,2]
	Epsomite 2[1,2]
Fe-oxides	Black hematite coating (Swansea AZ)[1,2,3]
	Ilmenite WAR-4119 35[1]
	Synthetic packed magnetite powder MTS5[1,2,3]
	Synthetic packed goethite powder GTS2[2]
Phosphates	Wavellite ML-P7 73[1]
	Meta-variscite ML-P4 95[1]
	Pyromorphite ML-P3 77[1]
	Apatite ML-P1 86[1]
Allophane	Si/Al ratio = 0.44[1,2,3]
	Si/Al ratio = 0.58[1,2,3]
	Si/Al ratio = 0.92[1,2,3]
Aluminosilicate gel	Si/Al ratio = 5.61[1,2,3]
Blackbody	Blackbody[1,2,3]
Dust	Gusev surface dust[1,2,3]
Slope	Slope 250/247[1,2]

Sky	Average sky[1,2] Sky sol056[3]

[1] End members used to model Wishstone and Watchtower
[2] End members used to model Clovis
[3] End members used to model Adirondack
[4] *Ruff et al.* [2006] categorized shocked plagioclase as "glassy phases" and, here, it is categorized as "feldspar" to be consistent with *Rogers and Christensen* [2007].

in Northern Acidalia, gel and Al-rich allophane are identified in Solis, and Si-rich allophane is identified in Sinus Meridiani and in the hematite-bearing Meridiani unit (Table 5.5). The addition of poorly-crystalline aluminosilicates to spectral models of all regions reduces RMS errors, a measure of the model's goodness of fit (Table 5.5). Furthermore, visual inspections of the modeled spectra confirm a very close match to the measured spectra (Figure 5.3). The best models of the other six regional spectra generally did not identify allophane/gel, suggesting that poorly-crystalline aluminosilicates are below detection limit for most of the regions.

The identification of poorly-crystalline aluminosilicates in Northern Acidalia, Solis, and Sinus Meridiani does not affect the overall modeled high-silica abundances (Figure 5.4); allophane and/or gel replace specific high-silica phases in each region. Gel replaces phyllosilicates in models of Northern Acidalia; gel and Al-rich allophane replace phyllosilicates and volcanic glass in Solis; and Si-rich allophane replaces aluminous opal in Meridiani (Table 5.5). Conversely, the model of the hematite-bearing Meridiani unit with allophane identifies greater amounts of high-silica phases and lower amounts of igneous minerals (feldspar, olivine, and pyroxene) than the model without allophane by *Rogers and Aharonson* [2008] (Figure 5.4).

The identification of allophane in TES spectral models affects the modeled pyroxene mineralogy. Models without allophane in the spectral library by *Rogers and Christensen* [2007] identify primarily orthopyroxene (OPX) and high-calcium pyroxene (HCP) in Solis and Sinus Meridiani, respectively. With the addition of allophanes and gel to the library, pigeonite becomes the most abundant pyroxene in models of Solis, and a combination of pigeonite and HCP are identified in models of Sinus Meridiani (Figure 5.4). Models of the hematite-bearing Meridiani surfaces by *Rogers and Aharonson* [2008] identify pigeonite as the dominant pyroxene, while models with allophane identify

Table 5.5. Modeled high-silica phase abundances from this study and *Rogers and Christensen* [2007]. Abundances of specific high-silica phases from the *Rogers and Christensen* [2007] study are listed in [*Minitti and Hamilton*, 2010]. Values in bold represent phase abundance + uncertainty values > 10 vol.%. PCA = poorly-crystalline aluminosilicates.

	N. Acidalia		**Solis Planum**		**Meridiani**		**Meridiani (hematite)**	
	This Study	R&C	This Study	R&C	This Study	R&C	With PCA	Without PCA[1]
Biotite	3	1	1					
Muscovite			3					
Illite		**7**		**15**				
Saponite		4						
Antigorite			1					
K-rich glass				7		2		
SiO_2 glass		1						
Opal-A	8	**8**	2	1	2		2	
Al-opal						**9**	**4**	
Stilbite	**9**	**13**	**10**	8	**11**	**11**	4	3
Allophane Si/Al 0.5			**10**					
Allophane Si/Al 0.9					**10**		**32**	
Gel Si/Al 5.6	**17**		**10**		3			
Total	37	34	37	31	26	22	42	3
RMS	0.128	0.136	0.081	0.110	0.096	0.127	0.245	0.256

[1] This model is from excluding allophane and gel from the spectral library in Table 1 and is not what was reported by *Rogers and Aharonson* [2008].

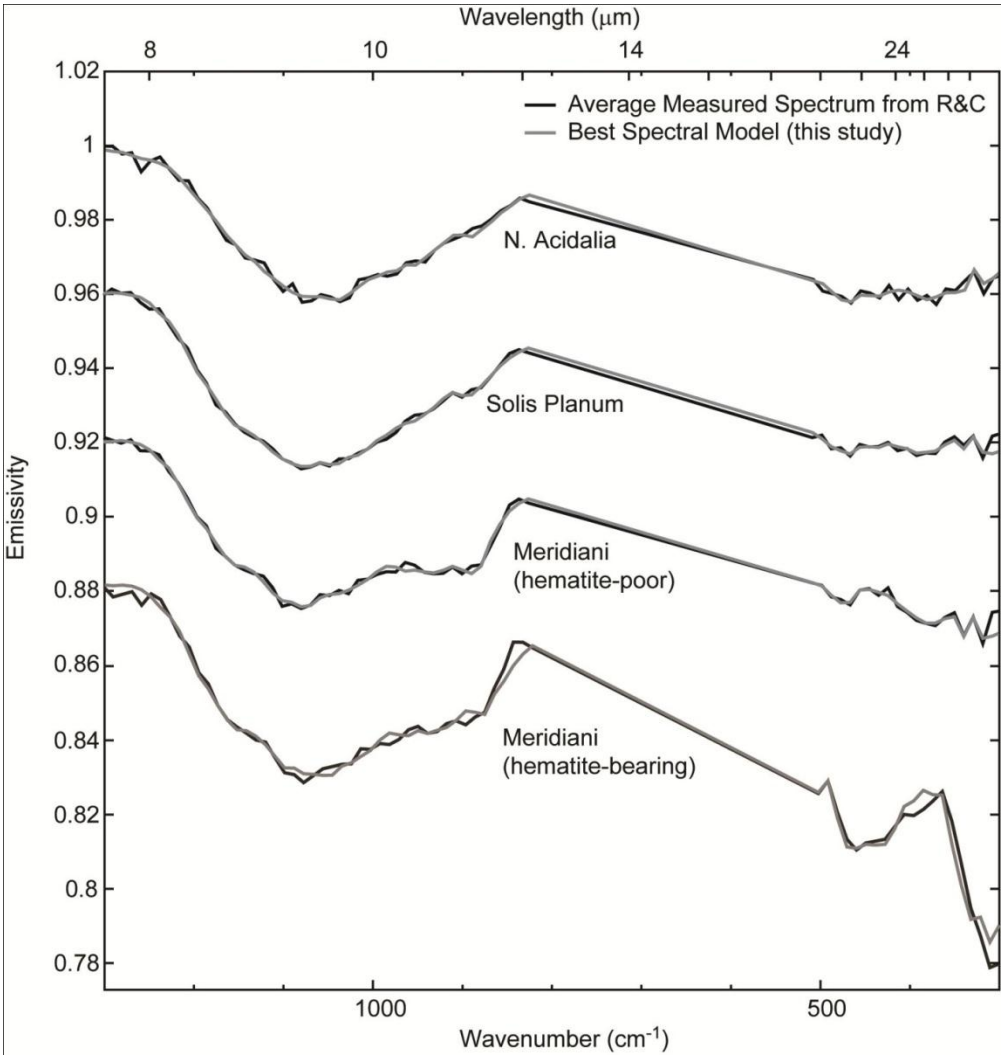

Figure 5.3. Averaged measured TES spectra determined by (18) for regions on Mars whose models identify significant abundances of allophane (in black) and the best spectral models from this study (in grey).

HCP. Additionally, K-feldspar is the dominant feldspar in models with allophane, while plagioclase is the dominant feldspar in models without allophane (Figure 5.3).

5.4.2 TES Models of Potential MSL Landing Sites

Significant abundances of poorly-crystalline aluminosilicates were identified in models of low-to-intermediate albedo surfaces of Mawrth Vallis, but not in models of Eberswalde, Gale, or Holden Craters (Table 5.6). The best model of Mawrth identified 30 vol.% Si-rich allophane. RMS errors of models without allophane and gel in the library were higher than those with allophane and gel (0.171 vs. 0.162, respectively), and visual inspection of the modeled spectrum shows a good fit to the measured spectrum (Figure 5.5). Models of Mawrth identified other high-silica phases, including stilbite, muscovite, and opal, but only stilbite was identified in significant abundances (Table 5.6). The best models of Gale and Holden identified significant abundances of high-silica phases, including stilbite at both landing sites and K-rich glass at Gale (Table 5.6). Models of Eberswalde crater identified the least amount of high-silica phases of all landing sites and did not identify any high-silica phases in significant abundances (Table 5.6).

Models of bright-toned surfaces in Mawrth identify different high-silica phases than models of darker-toned surfaces. The modeled mineralogy of landing ellipses 1, 2, and 4 is predominantly composed of high-silica phases, while the model of landing ellipse 3 identifies the least amount of high-silica phases (16 vol.%). The types of secondary silicates identified in models vary between the landing ellipses within Mawrth (Table 5.7). Significant abundances of poorly-crystalline aluminosilicates are identified in landing ellipses 1, 2, and 4. Significant abundances of montmorillonite (SWy-1, a Na-montmorillonite) are -identified in landing ellipses 1 and 3; however, when the SWy-1 montmorillonite end member was excluded from the library, the other montmorillonite

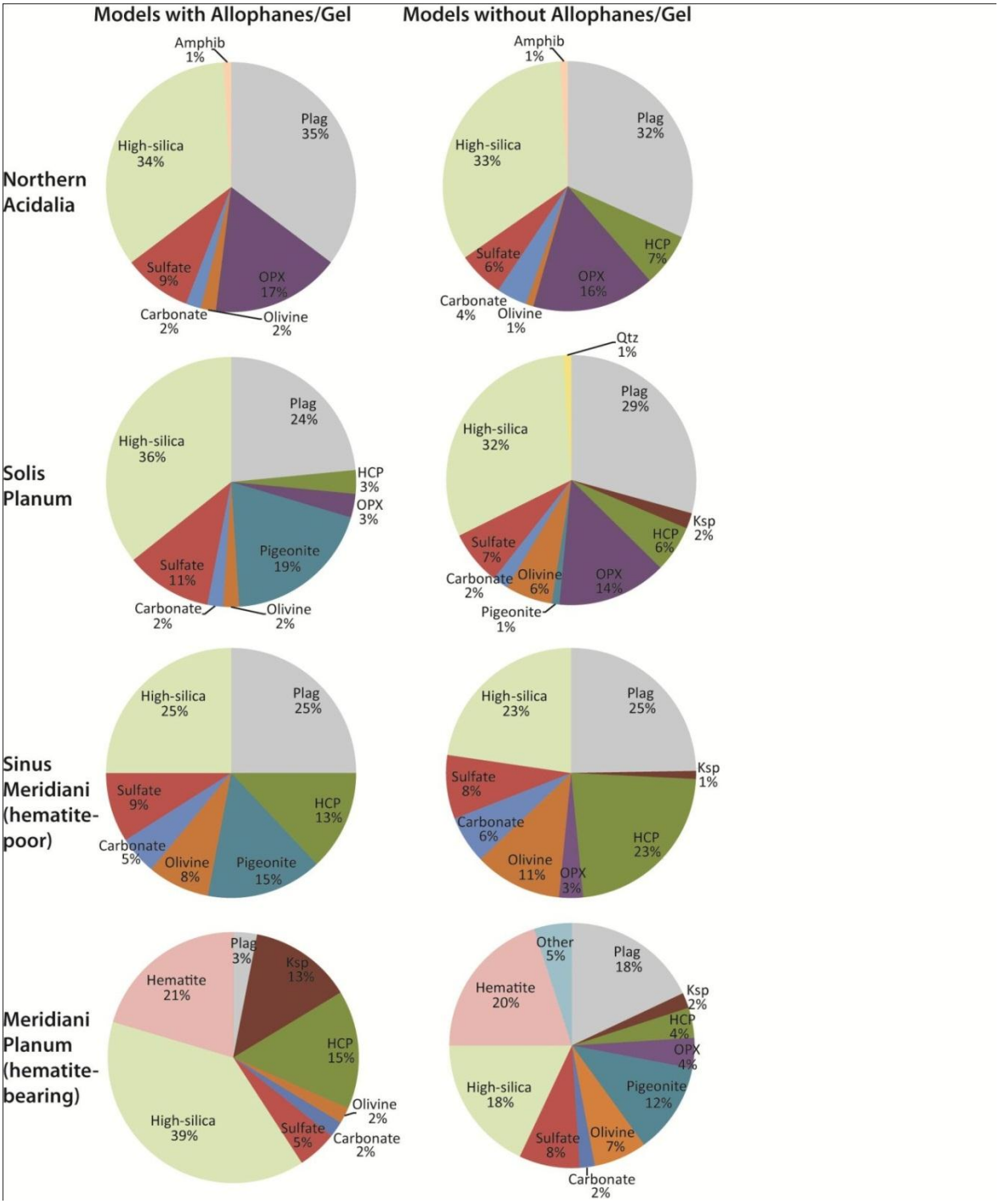

Figure 5.4. Modeled mineral abundances by group for TES spectral models from this study and without allophane from *Rogers and Christensen* [2007] (N. Acidalia, Solis, and Sinus Meridiani) and from *Rogers and Aharonson* [2008] (hematite-bearing Meridiani Planum). The high-silica group includes modeled allophanes and gel. The addition of allophane to the spectral library causes the identification of significant pigeonite abundances in Solis and Sinus Meridiani. Conversely, the identification of allophane in models of the hematite-bearing Meridiani unit causes the identification of less pigeonite and plagioclase but more HCP and K-feldspar.

Table 5.6. Modeled high-silica phase abundances of averaged TES spectra from low-albedo surfaces of MSL landing sites. Values in bold represent phase abundance + uncertainty values > 10 vol.%.

	Eberswalde	Gale	Holden	Mawrth
Muscovite				7
Illite			3	
Serpentine	3			
K-rich glass	4	**19**		
SiO_2 glass			2	
Opal-A				5
Stilbite		**9**	**11**	**14**
Allophane Si/Al 0.44			6	
Allophane Si /Al 0.92				**30**
Total	7	28	22	56
RMS	0.166	0.274	0.183	0.159

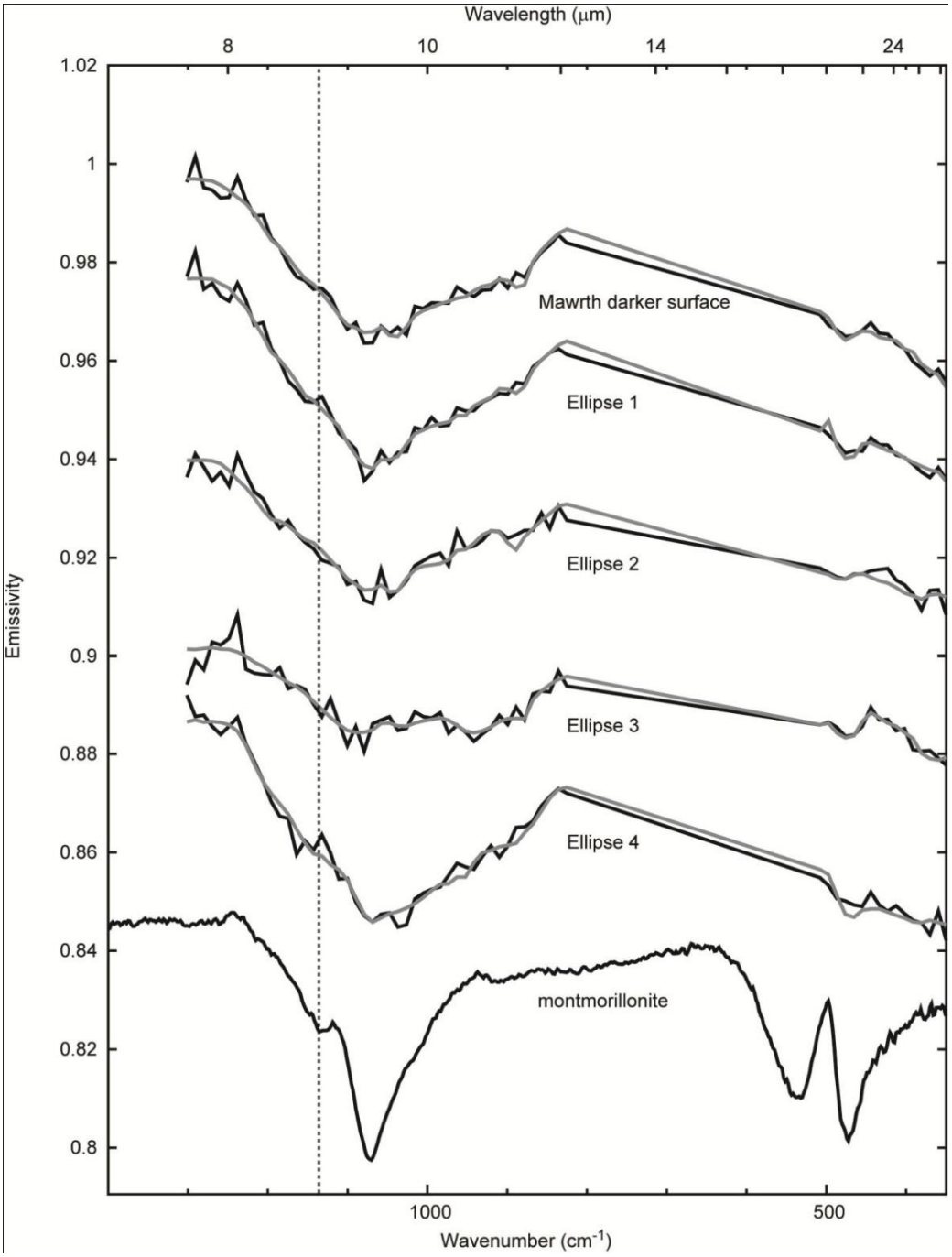

Figure 5.5. Averaged measured spectra of dark-to-intermediate-toned Mawrth surfaces and bright-toned Mawrth surfaces near the four proposed landing ellipses (in black) and their models in gray. Models of ellipses 1 and 3 identify SWy-1 montmorillonite, shown below Mawrth spectra. Vertical dashed line denotes shoulder feature in SWy-1. Note that this shoulder appears in measured spectra of ellipses 1 and 3. Also note the presence of a shoulder in ellipse 4 at shorter wavenumbers compared to montmorillonite (~1160 cm^{-1} vs. 1120 cm^{-1}). This suggests the presence of a more polymerized high-silica phase in ellipse 4.

end member (STx-1, a Ca-montmorillonite) was not identified in the models. Measured spectra of ellipses 1 and 3 have absorptions at ~1120 cm^{-1} that are characteristic of the SWy-1 montmorillonite spectrum, further indicating the presence of montmorillonite in these surfaces (Figure 5.5). Zeolite is identified in significant abundances for landing ellipses 2, 3, and 4.

RMS errors of bright-toned Mawrth surface models without poorly-crystalline aluminosilicates in the library show that the addition of allophane and gel to libraries either improves the model fit or results in a similarly good fit as the models without allophane and gel. The RMS error from the model of landing ellipse 4 with allophane (Table 5.7) is smaller than the model without allophane and gel in the library (Table 5.8), demonstrating that the addition of poorly-crystalline aluminosilicates to the spectral library improves the model fit. The RMS errors from models of landing ellipses 1 and 2 are similar to the errors from the models without allophane in the library. The model of ellipse 1 without allophane and gel in the library identifies significant abundances of halloysite, stilbite, and montmorillonite, and the model of ellipse 2 without allophane and gel in the library identifies significant abundances of stilbite and muscovite (Table 5.8). Models without allophane and gel in the library identify slightly greater abundances of igneous minerals, including plagioclase, OPX, CPX, and olivine. The difference in modeled igneous mineral abundances between models with and without poorly-crystalline aluminosilicates is generally $\leq$5 vol.%, except in the case of landing ellipse 4, where the model with allophane/gel identifies 8 vol.% plagioclase and the model without identifies 30 vol.% plagioclase. Models of ellipses 1 and 4 with and without poorly-crystalline aluminosilicates show that allophane/gel replaces phyllosilicates in spectral models, particularly halloysite and montmorillonite.

Table 5.7. Modeled high-silica phase abundances of averaged TES spectra from bright-toned surfaces near the four proposed landing ellipses in Mawrth Vallis. Values in bold represent phase abundance + uncertainty values > 10 vol.%.

	Ellipse 1	Ellipse 2	Ellipse 3	Ellipse 4
Muscovite	4	**14**		
Montmorillonite SWy-1	**23**		**9**	
Opal-A	2			
Heulandite		**8**	**7**	**24**
Stilbite	3	**17**		
Allophane Si/Al 0.44		**9**		
Allophane Si/Al 0.58	**9**			**12**
Gel Si/Al 5.6	**13**			**32**
Total	54	48	16	68
Total allophane + gel	22	9	0	44
RMS	0.162	0.204	0.181	0.217

Table 5.8. Modeled high-silica phase abundances of bright-toned Mawrth surfaces without allophane or gel in the library. Values in bold represent phase abundance + uncertainty values > 10 vol.%,

	Ellipse 1	Ellipse 2	Ellipse 3	Ellipse 4
Muscovite	2	**12**		
Montmorillonite SWy-1	**14**		**9**	**10**
Halloysite	**19**			**21**
Opal-A	3	2		4
Heulandite		**8**	**7**	
Stilbite	**8**	**19**		**10**
Total	46	41	16	45
RMS	0.165	0.206	0.181	0.233

5.4.3 Mini-TES Models of Gusev Rocks

Models of the four Gusev rock classes generally do not identify poorly-crystalline aluminosilicates. High-Si aluminosilicate gel is only identified in the model of Wishstone-class rocks, at 25 vol.% abundance. However, the RMS error from the model that identifies gel is similar to the error from the model without poorly-crystalline aluminosilicates in the spectral library, showing that the model with gel is just as good as the model without gel. Comparing the mineralogy from these two models shows that gel replaces a combination of basaltic glass and plagioclase. Models of Adirondack, Clovis, and Watchtower are consistent with those by *Ruff et al.* [2006]. Clovis and Watchtower models identify 38 and 42 vol.% glass, respectively, and the primary end member used is a Hawaiian basaltic glass from Kilauea (HWKV340A, glassy black flat surface).

5 Discussion

5.5.1 Effects of Poorly-Crystalline Aluminosilicates on Modeled High-Silica Phases and Igneous Minerals

Poorly-crystalline aluminosilicates replace other high-silica phases, particularly phyllosilicates and amorphous silica, in spectral models of Northern Acidalia, Solis, and Sinus Meridiani (Table 5.5). This supports the hypothesis that the presence of allophane on Mars has caused the false identification of other high-silica phases in previous TES models [*Hamilton et al.*, 2008; *Kraft*, 2009; *McDowell and Hamilton*, 2009]. The replacement of phyllosilicates by poorly-crystalline aluminosilicates in TES models explains why NIR spectra of these regions lack absorptions from crystalline clays, since poorly-crystalline aluminosilicates have muted absorptions compared to clay minerals [*Michalski et al.*, 2006b]. A previous study on amorphous silica-coated basalts showed that when amorphous silica is present as a thin coating on the order of a few microns thick, NIR spectra lack absorptions near 2.2 microns from Si-OH vibrations [*Kraft*, 2009]. This suggests that if poorly-crystalline aluminosilicates are present as thin

coatings on the Martian surface, they may not be detected by orbital NIR spectroscopy. Modeled zeolite abundances are not affected, suggesting that zeolites are present in these regions or there are additional poorly-crystalline silicates in these regions that are spectrally similar to zeolites but are not present in the spectral library.

The identification of poorly-crystalline aluminosilicates in TES spectral models affects the types of pyroxenes identified in models of Solis, Sinus Meridiani, and hematite-bearing Meridiani surfaces. When allophane is present in the library, pigeonite is detected in models of Sinus Meridiani, while HCP is detected in models of hematite-bearing Meridiani surfaces. Pigeonite has been identified in Meridiani from orbit in NIR data measured by OMEGA [*Poulet et al.*, 2008] and by the Opportunity rover in Mini-TES models of the unweathered basaltic sand component [*Glotch et al.*, 2006]. It is important to note that the type of secondary silicates identified can affect the modeled pyroxene compositions, making it necessary to consider additional datasets when determining the types of pyroxenes on the Martian surface.

The identification of allophanes in TES spectral models does not affect the interpretations of grouped mineral abundances in Northern Acidalia, Solis, and Sinus Meridiani. Models of each region with and without poorly-crystalline aluminosilicates in the library could be interpreted as weakly altered basaltic terrains with certain plagioclase-to-pyroxene ratios and olivine content. Spectral models with allophane and gel in the library further improve an already good model to help better understand the alteration environments and igneous petrology. Models of hematite-bearing Meridiani surfaces with allophane in the library identify more high-silica phases than models without allophane (Figure 5.4). Poorly-crystalline aluminosilicate abundances may be overestimated because the spectral contrast of allophane and gel is lower than that of other high-silica phases (Figure 5.2).

It is important to note that the TES model of the hematite-bearing Meridiani unit identifies significant K-feldspar abundances. K-feldspar has been falsely identified in TIR models of terrestrial weathered basalts [*Michalski et al.*, 2006b; *Kraft*, 2009] and it was identified in significant abundances in Surface Type 2 models [*Wyatt and McSween*, 2002]. It is likely that K-feldspar is not present in Meridiani and is falsely identified because the surface is chemically weathered. K-feldspar abundances in models with allophane are similar to plagioclase abundances in models by *Rogers and Aharonson* [2008], suggesting that K-feldspar and plagioclase can be interchangeable in spectral models.

5.5.2 High-Silica Mineralogy at MSL Landing Sites

TES models of low-to-intermediate-albedo surfaces from the four potential landing sites show that poorly-crystalline aluminosilicates are only present in Mawrth Vallis. Furthermore, the model of Mawrth identifies the greatest abundances of high-silica phases, suggesting that this surface may have the greatest spatial extent of weathering products and that aqueous alteration at the other landing sites is more localized. The identification of allophane in Mawrth and the lack of significant abundances of phyllosilicates indicate that crystalline clays may not be present in dark-to-intermediate-toned surfaces. Models by *Michalski and Fergason* [2009] of surfaces in Mawrth with similar albedos identified ~20 vol.% clay minerals. This suggests that allophane replaces crystalline clays in spectral models of low-to-intermediate albedo surfaces in Mawrth. Models presented here also identify greater abundances of high-silica phases compared to the models by *Michalski and Fergason* [2009], on the order of 10-20 vol.%, which may be a result of the lower spectral contrast of allophanes and gel compared to other high-silica phases. It is important to note, however, that allophane commonly forms as coatings on igneous phases or is present within weathering rinds [*Colman*, 1982; *Farmer et al.*, 1985]. This coating geometry makes it difficult to

determine the areal abundances of weathering products because of non-linear spectral mixing between the coating and underlying rock [*Kraft et al.*, 2003; *Kraft*, 2009].

TES models of bright-toned surfaces from Mawrth show that the high-silica mineralogy is variable between the four proposed landing ellipses. The variability in modeled secondary aluminosilicate phases is consistent with NIR data from OMEGA and CRISM of the region. Interpretations of CRISM data within the Mawrth Vallis landing ellipse have identified montmorillonite, beidellite, and kaolinite clays and hydrated silica [*Bishop et al.*, 2010]. Some CRISM spectra from the Al-phyllosilicate unit are similar to the NIR spectra of allophane and aluminosilicate gel (Chapter 4), showing broad 2.2 micron absorptions [*Bishop et al.*, 2010]. The agreement between NIR data and TES models strengthens the argument for allophane at Mawrth. The identification of kaolinite with hydrated silica from CRISM spectra [*McKeown et al.*, 2011] is consistent with the identification of halloysite in TES models of ellipse 1 (Table 5.8). Halloysite is a hydrated kaolinite, and the NIR spectra of kaolinite and halloysite are similar, except that halloysite shows a prominent hydration feature at 1.9 microns that is lacking in the kaolinite spectrum [*R. Clark et al.*, 2007]. Hydrated silica has hydration features at 1.4 and 1.9 microns, so the NIR spectrum of a surface with kaolinite and hydrated silica would be similar to that of a surface with halloysite. Zeolite is identified in significant abundances in TES models of all landing ellipses within Mawrth; however, zeolites have not been identified from NIR data. Zeolites can be difficult to positively identify through NIR spectroscopy because they only have features at 1.4 and 1.9 microns. Thus, zeolites could be present on Mawrth and hydrated phyllosilicates and poorly-crystalline aluminosilicates could obscure their detection by NIR spectroscopy.

The absence of montmorillonite in models of ellipse 1 and 3 when the SWy-1 montmorillonite end member is excluded demonstrates the importance of having a complete set of secondary silicates in the spectral library. This was also demonstrated in

models of mineral mixtures in Chapter 3, where the lack of the appropriate clay mineral in the spectral library caused the false identification of zeolite. The identification of zeolite in Mawrth, Gale, Holden, Northern Acidalia, Solis, and the hematite-bearing and hematite-poor Meridiani surfaces may represent the lack of a secondary aluminosilicate(s) in the spectral library that is present in these surfaces. Therefore, one reason that TES models do not identify clay minerals in clay-bearing regions may be the lack of the correct clay mineral in the spectral library.

The difference in modeled secondary mineralogy between dark-to-intermediate-toned and bright-toned surfaces in Mawrth suggests that surfaces with different albedos have experienced different aqueous alteration histories. Models of darker surfaces contain allophane, implying water-limited aqueous alteration at neutral to mildly acidic pH, while models of brighter surfaces generally contain more phyllosilicates, implying alteration at high water-to-rock ratios and alkaline pH. TES spectra with higher albedos are usually excluded from spectral models because a higher albedo can indicate a higher dust content [*Rogers and Christensen*, 2007]. However, bright surfaces from Mawrth have high thermal inertias, showing that they are bedrock [*Michalski and Noe Dobrea*, 2007], and models of these surfaces identify significant clay abundances [*Michalski and Fergason*, 2009]. Thus, an additional reason that TES models don't identify phyllosilicates in surfaces where clays have been identified by NIR spectroscopy may be that bright surfaces contain more clays and these surfaces are generally not included in TES models.

The Mars Science Laboratory will land on a surface that shows evidence for liquid water to study an environment that may have been habitable. Clay minerals form in environments with greater water-to-rock ratios than poorly-crystalline aluminosilicates, so surfaces with clays, rather than poorly-crystalline aluminosilicates, should be targeted for MSL. Based on TES models of bright-toned surfaces from the

four proposed landing ellipses in Mawrth, landing ellipse 1 likely has the greatest amount of clay minerals, suggesting the most water was present at this site. However, models of mineral mixtures with clays (Chapter 3) show that the identification of 20-30 vol.% clay is consistent with the presence of 5-20 wt.% clay in these rocks. This indicates that either 1) these rocks have been weakly altered and are not clay-rich, or 2) surfaces are dominated by unaltered rocks with small outcrops of clay-rich rocks. Analyses of MOC images show that the light-toned, clay-bearing unit is ~0.6 to $\geq$1 km thick and is layered on decimeter to meter scales [*Michalski and Noe Dobrea*, 2007]. The light-toned unit is likely sedimentary or pyroclastic in origin, based on the low dips of the layers and the presence of buried impact structures [*Michalski and Noe Dobrea*, 2007]. If the clays were transported and the composition of the source materials varied in clay content, clay-rich and clay-poor layers could have formed and could account for the low modeled clay abundances. The lack of clays in models of bright-toned surfaces in ellipses 2 and 4 suggest that not all bright-toned units contain clay minerals.

5.5.3 Absence of Allophane from Mini-TES Models of Gusev Rocks

The presence of allophane in Clovis-, Watchtower-, and Wishstone-class rocks was suggested from APXS data [*Ming et al.*, 2006]. However, only the Mini-TES model of Wishstone identified high-Si aluminosilicate gel, and that model had a similar RMS error to the model without gel, indicating gel does not improve the model. Mini-TES models of Clovis and Watchtower identify basaltic glass, which may suggest that these rocks have not been extensively altered because basaltic glass is highly susceptible to chemical weathering [*Ruff et al.*, 2006]. A closer look at the TIR emission spectrum of the basaltic glass end member that is identified in the models (HWKV340A, glassy black flat surface) shows that it has experienced aqueous alteration (Figure 5.6). The most intense Si-O stretching absorption occurs at 930 cm^{-1}, similar to a basaltic glass spectrum provided by *Wyatt et al.* [2001], but there is an additional absorption at shorter

wavelengths at 1090 cm^{-1}. The position of this absorption is consistent with the Si-O stretching absorption of aluminosilicate gel and indicates the presence of a polymerized secondary silicate, like a gel coating. Glassy surfaces of young basalt flows in Hawaii are readily altered by acid sulfate and leaching processes to form silica-rich coatings and leached layers up to a few tens of microns thick in ~20-30 years [*Minitti et al.*, 2007; *Chemtob et al.*, 2010]. The TIR spectrum of HWKV340A suggests that it has a thin silica-rich coating or leached layer. This, combined with the evidence for allophane from APXS data, suggests that Clovis and Watchtower rocks have experienced limited aqueous alteration.

5.5.4 Effect of Allophane on TIR-Model-Derived Chemistry

Chemistry of the Martian surface has been inferred from orbital measurements by the Gamma Ray Spectrometer (GRS), from in-situ measurements by APXS instruments, and from Martian meteorite samples. Surface chemistry has also been derived from TES models, which has been used to infer petrologic processes [*McSween et al.*, 2003; 2009]. Chemistries derived from TES models show enrichment in alkali and SiO_2 content compared to other datasets. It was suggested that chemical weathering could cause the discrepancy between datasets [*McSween et al.*, 2009]. Phases enriched in potassium are commonly identified in models of weathered surfaces. TIR models of weathered basalts identify K-rich glass, K-feldspar, and illite [*Michalski et al.*, 2006b; *Kraft*, 2009; Chapter 2]. The addition of poorly-crystalline aluminosilicates to spectral libraries could improve modeled alkali abundances if they replace alkali-bearing phases in spectral models because poorly-crystalline aluminosilicates do not contain alkalis. The chemistry for Northern Acidalia, Solis, and Sinus Meridiani was derived from models with and without poorly-crystalline aluminosilicates in the library to test how the identification of allophane/gel affects modeled alkali abundances. The K-bearing phases identified in models without allophane and gel in the library include significant amounts of orthoclase

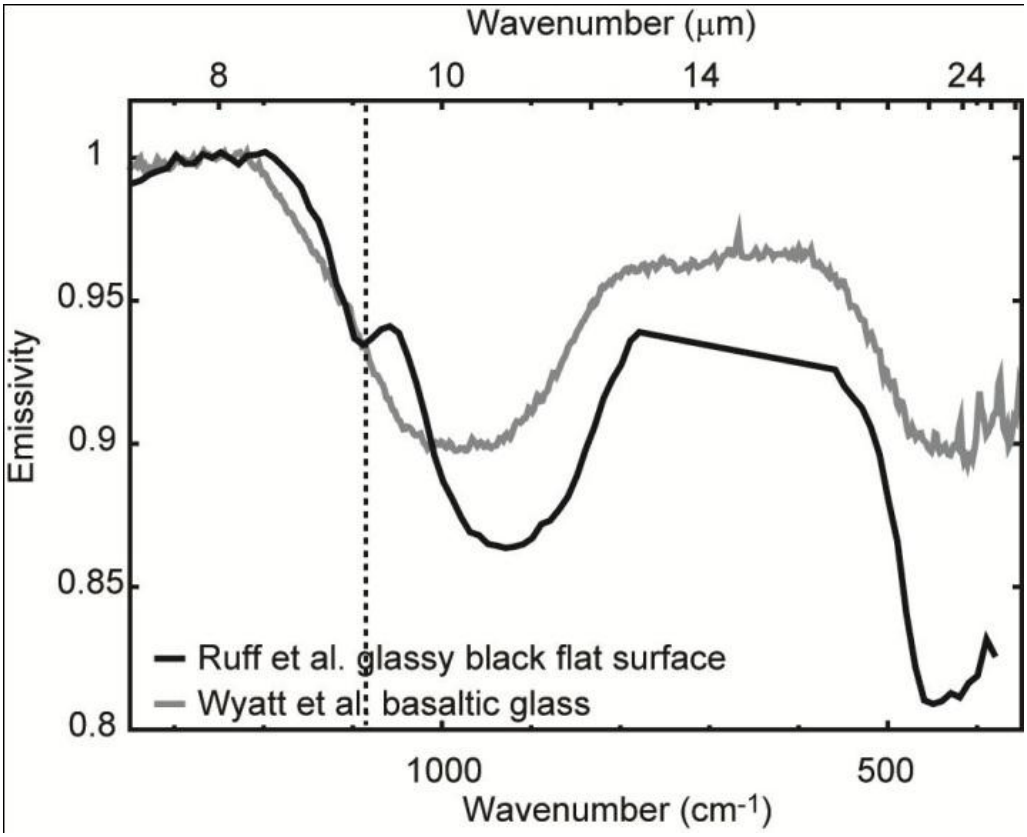

Figure 5.6. TIR emission spectra of the basaltic glass identified in Mini-TES models of Clovis and Watchtower in our models and the models by *Ruff et al.* [2006] and the basaltic glass synthesized by *Wyatt et al.* [2001]. Note that the basaltic glass end member identified in models has an absorption at 1090 cm^{-1}, indicating a more polymerized, high-silica phase is present. The position of this absorption is consistent with the synthetic gel spectrum (Figure 5.2), which suggests that this basaltic glass end member has a secondary silicate coating or leached layer and is weakly altered.

in Northern Acidalia and Solis (10 and 15 vol.%, respectively), minor amounts of K-rich glass in Solis (~5 vol.%), and minor amounts of muscovite in Meridiani (~5 vol.%). Models with allophane and gel in the library do not identify these phases. Thus, the derived alkali abundances for models with allophane and gel are lower than those for models without allophane and gel (Figure 5.7). This indicates that the inclusion of allophane and gel in TES libraries can improve model-derived alkali abundances. The identification of poorly-crystalline aluminosilicates generally does not reduce model-derived SiO_2 values because the SiO_2 values of allophane/gel are similar to the values of the end members they replace. It is important to note that if a surface is weathered, the chemistry derived from spectral models would reflect that of the weathered surface, not the parent rock.

5.5.5 Implications for Regional and Local Martian Weathering Environments

The identification of allophane in regional and local Martian surfaces suggests that low-T, water-limited chemical weathering under near-neutral to mildly acidic pH has been a widespread surface process. Allophane and/or gel are regionally significant weathering products at northern and southern mid-to-high latitudes, based on their occurrence in models of Northern Acidalia and Solis Planum surface types. The identification of two different poorly-crystalline aluminosilicate compositions in Northern Acidalia and Solis Planum may signify two different formation mechanisms. Northern Acidalia models identify aluminosilicate gel with a high Si/Al ratio. A Si-rich aluminosilicate gel may precipitate from a solution with a lower pH than that required for allophane because Al becomes increasingly soluble as solutions become more acidic and could be removed so that a high-Si gel forms [*Minitti et al.*, 2007]. The identification of aluminosilicate gel in Northern Acidalia could also be consistent with the presence of leached volcanic glass, where acid sulfate solutions cause dissolution and removal of low valence cations (i.e. Na^+, K^+, Ca^{2+}, Mg^{2+}) while the silica network remains intact [*Minitti*

et al., 2007]. Aluminum is generally not removed from leached layers because it substitutes for Si in the silica network [*Minitti et al.*, 2007]. Leached glass layers have been hypothesized for Southern Acidalia based on OMEGA spectra [*Horgan*, 2010]. Conversely, the identification of Al-rich allophane and aluminosilicate gel in Solis may suggest the precipitation of a poorly-crystalline aluminosilicate, rather than the presence of leached glass. Poorly-crystalline aluminosilicates and leached glass could have formed at mid-to-high latitudes as a result of volatile transport away from the poles under periods of higher obliquity during the Amazonian [*Kreslavsky et al.*, 2008].

The identification of allophane at low latitudes in hematite-poor and hematite-bearing Meridiani surfaces indicates that near-neutral, water-limited aqueous alteration was an important weathering process during the Hesperian Period. Interpretations of TIR data and APXS data suggest that acid sulfate weathering was a global process during the Hesperian. THEMIS data of low-latitude dark surfaces show that soils derived from olivine-rich bedrock lack olivine, which may indicate that acid sulfate weathering preferentially dissolved olivine from the bedrock [*Bandfield et al.*, 2011]. APXS data show depletions in Fe+Mg abundances in soils across the planet, suggesting that acid-sulfate weathering preferentially dissolved olivine and removed Fe+Mg [*Hurowtiz and McLennan*, 2007]. The presence of jarosite in light-toned surfaces in Meridiani shows that acid sulfate weathering occurred during the Hesperian [*Morris et al.*, 2006]; however, the indication of regionally extensive allophane in low-albedo surfaces from TES models of Sinus Meridiani suggests that near-neutral aqueous alteration was a regionally important process during the Hesperian and that acid sulfate weathering was not a global process. The preferential dissolution of olivine by acid sulfate weathering cannot account for the presence of poorly-crystalline aluminosilicates because Al-bearing phases (such as volcanic glass or feldspar) must alter to release Al into solution and allow for the precipitation of secondary aluminosilicates.

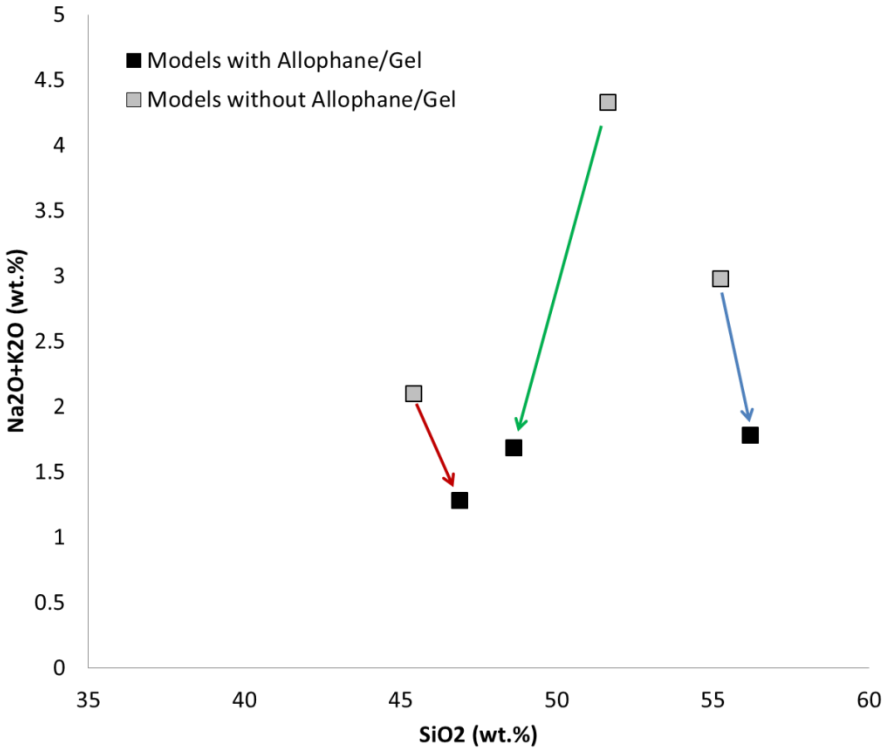

Figure 5.7. SiO_2 vs. alkali abundances derived from TES models of Northern Acidalia, Solis, and hematite-poor Meridiani regional spectra. Black squares represent chemistry derived from models with allophane and gel in the library and grey squares represent chemistry derived from models without allophane and gel in the library. Note that the identification of allophane/gel reduces modeled alkali abundances. Blue arrow represents the Northern Acidalia models, the green arrow represents the Solis models, and the red arrow represents the Sinus Meridiani model.

The variability in modeled high-silica phases throughout Mawrth indicates a wide range of aqueous alteration environments, particularly within the previously identified Al-phyllosilicate-bearing unit [*Bishop et al.*, 2008; *Wray et al.*, 2008]. The presence of allophane suggests low-temperature alteration of volcanic glass under near-neutral to mildly acidic, water-limited conditions. Evidence for halloysite from NIR spectroscopy and TES models suggests allophane was altered under resilicating weathering regimes in select areas [*Wada*, 1989]. Allophane and halloysite are common weathering products of soils derived from volcanic ash [*Wada*, 1989]. Analyses of MOC and HiRISE images show that the Al-phyllosilicate-bearing unit drapes topography [*Michalski and Noe Dobrea*, 2007; *Wray et al.*, 2008]. This geomorphology and the presence of allophane and halloysite in TES models suggest that the Al-phyllosilicate unit is an altered volcanic ash layer.

6 Conclusions

Modeling TES data from regional surfaces and from potential MSL landing sites and Mini-TES data from altered rocks in Gusev crater using a spectral library that includes poorly-crystalline aluminosilicates (allophanes and gel) has led to the following conclusions:

1 Poorly-crystalline aluminosilicates are identified in TES models of three regional surface types: Northern Acidalia, Solis Planum, and Sinus Meridiani. Poorly-crystalline aluminosilicates are identified on a local scale in TES models of hematite-bearing Meridiani surfaces and models of dark-to-intermediate-toned and some bright-toned surfaces in Mawrth Vallis.

2 Poorly-crystalline aluminosilicates replace specific high-silica phases in TES spectral models of regional surfaces and in Mawrth Vallis. High-Si aluminosilicate gel replaces phyllosilicates in models of Northern Acidalia; gel and Al-rich allophane replace

phyllosilicates and K-rich glass in models of Solis; Si-rich allophane replaces Al-opal in models of Sinus Meridiani; and allophane and gel replace phyllosilicates in models of dark-, intermediate-, and bright-toned surfaces in Mawrth. The replacement of phyllosilicates by poorly-crystalline aluminosilicates explains why NIR data do not detect phyllosilicates on these surfaces.

3 The identification of allophane and gel in Solis, Sinus Meridiani, and hematite-bearing units in Meridiani affects the type of pyroxene identified in spectral models.

4 The identification of poorly-crystalline aluminosilicates in TIR models in Northern Acidalia, Solis, and Sinus Meridiani surface types reduces model-derived alkali abundances. The addition of poorly-crystalline aluminosilicates to TES libraries may improve model-derived alkali abundances.

5 Poorly-crystalline aluminosilicates may not be present in altered rocks from Gusev. High-Si aluminosilicate gel was identified in Mini-TES models of Wishstone, but basaltic glass was identified in models of Clovis and Watchtower. However, the TIR emission spectrum of the basaltic glass in the spectral models shows that it is altered, so the identification of this end member in spectral models of Clovis and Watchtower is consistent with the APXS data that demonstrates that these rocks are altered.

6 The identification of allophane in regional TES models of Sinus Meridiani and Solis Planum indicates these surfaces experienced low-temperature, water-limited aqueous alteration at near-neutral to mildly acidic pH. The presence of allophane in Meridiani suggests that acid sulfate weathering was not a global process during the Hesperian and that near-neutral chemical weathering was a regionally important surface process on Mars. The identification of high-Si aluminosilicate gel in models of Northern Acidalia may indicate the deposition of a Si-rich aluminosilicate gel, but is also consistent with the presence of leached volcanic glass from acid sulfate weathering. Poorly-crystalline aluminosilicates and leached glass could have formed in Solis and Northern Acidalia

surface types during the Amazonian, as a result of volatile movement away from the poles during periods of high obliquity.

7 TES models of bright-toned surfaces in Mawrth Vallis show that the high-silica mineralogy is variable across the landing ellipse. The identification of allophane, high-Si aluminosilicate gel, montmorillonite, and halloysite in TES models is consistent with NIR data of the region. Models of bright-toned surfaces within proposed landing ellipse 1 identify the most clay, suggesting that this area experienced the greatest amount of aqueous alteration. However, modeled clay abundances indicate this surface is only made up of 5-20 wt.% clay. The presence of allophane and halloysite in spectral models of bright-toned surfaces may indicate that the Al-phyllosilicate unit in Mawrth is an altered volcanic ash layer.

8 Models of bright- and dark-toned surfaces in Mawrth show that bright-toned surfaces contain more clay minerals. The exclusion TES data of bright-toned, high thermal inertia surfaces from spectral models may explain why TES models do not identify clay minerals in locations where NIR spectroscopy indicates the presence of clay minerals. The absence of the appropriate clay mineral spectrum in the spectral library may also explain the lack of clay minerals in TES models.

6 Understanding Chemical Weathering Processes on Mars from Laboratory Studies and TES Models with Poorly-Crystalline Aluminosilicates

6.1 Determining High-Silica Phase Abundances on Mars

The types of weathering products present on the Martian surface can tell us about the aqueous environments in which they formed, including solution pH, water-to-rock ratio, and temperature. The types of high-silica materials on the Martian surface have been a subject of debate. High-silica phases are most abundant in TIR models of mid-to-high latitude surfaces, and have been identified as primary phases (i.e. volcanic glass) [*Bandfield et al.*, 2000; *Rogers and Christensen*, 2007] or secondary minerals and/or mineraloids, including clay minerals, opaline silica, and poorly-crystalline aluminosilicates [*Wyatt and McSween*, 2002; *Kraft et al.*, 2003; *Michalski et al.*, 2006a; *Rogers and Christensen*, 2007; *Kraft*, 2009]. These high-silica phases are individually identified at or below the detection limit of linear deconvolution (~10 vol.%) [*Ramsey and Christensen*, 1998], although high-silica phases as a group have been reported in abundances >30 vol.% in Solis Planum and Northern Acidalia surface types [*Rogers and Christensen*, 2007]. The detection of individual high-silica phases, such as phyllosilicates, at or near the detection limit globally has prompted the suggestion that these phases are not volumetrically important on the Martian surface and may represent <<1 vol.% of the total surface mineralogy [*Bandfield et al.*, 2000; *Bandfield*, 2002]. However, TIR models of mineral mixtures with montmorillonite clay and amorphous silica presented in Chapter 3 show that minor detections of high-silica phases are real and that detection limits of these materials are generally less than the previously reported value of 10 vol.%.

6.1.1 Previous TES Models

Initial models of TES Surface Types 1 and 2 identified 15 vol.% phyllosilicates in ST1 and 15 vol.% phyllosilicates + 25 vol.% K-rich volcanic glass in ST2 [*Bandfield*

et al., 2000]. A subsequent study by *Wyatt and McSween* [2002] that excluded volcanic glass from the spectral library identified 15 vol.% and 30 vol.% phyllosilicates in models of ST1 and ST2, respectively. Models of the nine regional spectra that were characterized by *Rogers et al.* [2007] show that high-silica abundances vary by region [*Rogers and Christensen*, 2007; *Minitti and Hamilton*, 2010] (Table 6.1). Models of Northern Acidalia and Solis Planum surface types identified the greatest abundances of phyllosilicates and models of all surface types identified ~10 vol.% zeolite. Studies of regional TES spectra suggested that high-silica phases identified in surfaces polewards of 45° were likely secondary in origin, while those at lower latitudes were likely primary volcanic glasses [*Rogers and Christensen*, 2007]. However, models with additional volcanic glass end members in the spectral library did not identify more volcanic glass, suggesting that volcanic glass is not a volumetrically important phase on the Martian surface [*Minitti and Hamilton*, 2010].

6.1.2 Regional High-Silica Abundances on Mars

TIR models of mineral mixtures of basaltic igneous minerals with small to moderate amounts of secondary high-silica phases (Chapter 3) have helped refine detection limits for crystalline clay minerals and amorphous silica. The detection limits of linear deconvolution for clay minerals and amorphous silica are 2.5 wt.% and 5 wt.%, respectively, meaning that only 2.5 wt.% clay and 5 wt.% silica must be on a surface to be identified in spectral models; however, when olivine is present, these values may be as high as 10 wt.%. Taking these detection limits into account, it is possible to constrain clay and amorphous silica abundances on the Martian surface from previous models (Table 6.1). For example, models of Aonium identify 5 vol.% phyllosilicates, 3 vol.% glass, and 10 vol.% zeolites [*Rogers and Christensen*, 2007]. Based off of TIR models of mineral mixtures, this implies the presence of 2.5-5 wt.% phyllosilicates and 2.5-5 wt.% amorphous silica (Table 6.1). This assumes that the identification of both phyllosilicates

Table 6.1. Modeled high-silica phases from previous studies of regional TES surface types and implications for high-silica phase abundances from mineral mixture models in Chapter 3.

R&C[1]	Phyllosilicates	Glass[2]	Opal[3]	Zeolite	Total	Implications for high-silica mineralogy[4]
N. Acidalia	12	1	8	13	34	10 wt.% clay, 2.5-5 wt.% silica (gel[5])
Cimmeria	1	4	0	10	15	?
Aonium	5	3	0	10	18	2.5-5 wt.% clay, 2.5 wt.% silica
Sirenum	4	3	1	14	22	5 wt.% clay, 2.5 wt.% silica
Meridiani	0	2	9	11	22	5 wt.% silica (allophane[5])
Syrtis	4	1	0	7	12	2.5-5 wt.% clay
Hesperia	3	11	0	7	21	2.5-5 wt.% clay, 5-10 wt.% silica
Tyrrhena	1	4	0	8	13	2.5-5 wt.% silica
Solis	15	8	0	8	31	10 wt.% clay, 5 wt.% silica (allophane and gel[5])
M&H[6]						
N. Acidalia	12	0	5	12	29	10 wt.% clay, 2.5-5 wt.% silica (gel[5])
Cimmeria	0	3	0	10	13	?
Aonium	5	1	1	10	17	2.5-5 wt.% clay, 2.5 wt.% silica
Sirenum	3	0	3	16	22	5 wt.% clay, 2.5 wt.% silica
Meridiani	0	3	3	11	17	5 wt.% silica (allophane[5])
Syrtis	5	0	0	8	13	2.5-5 wt.% clay
Hesperia	3	3	1	10	17	2.5-5 wt.% clay, 5-10 wt.% silica
Tyrrhena	1	3	0	8	12	2.5-5 wt.% silica
Solis	9	1	3	11	24	10 wt.% clay, 5 wt.% silica (allophane and gel[5])

[1] Models by *Rogers and Christensen* [2007], reported in *Minitti and Hamilton* [2010]
[2] Glass includes K-rich glass and SiO_2 glass
[3] Opal includes opal-A and aluminous opal
[4] Implications are derived assuming olivine does not affect the detection of high-silica phases. Olivine is present in >10 vol.% abundances in Tyrrhena, Hesperia, Cimmeria, and Meridiani [*Rogers and Christensen*, 2007; *Minitti and Hamilton*, 2010]. The presence of olivine in these regions may increase the detection limit of amorphous silica to 10 wt.%, meaning that these surfaces are likely composed of at least 10 wt.% silica.
[5] Models from Chapter 5 identify allophane and/or high-Si aluminosilicate gel in these regions, suggesting that poorly-crystalline aluminosilicates are present in these regions instead of clay and/or amorphous silica.
[6] Models by *Minitti and Hamilton* [2010]

and zeolites is indicative of the presence of a phyllosilicate end member that is not represented in the spectral library. The amorphous silica identified by spectral models could be primary or secondary in origin. It is important to note that allophane and/or high-Si aluminosilicate gel replaces phyllosilicates, glass, and opal in models of Northern Acidalia, Solis Planum, and Meridiani (Chapter 5). Thus, it is likely that poorly-crystalline aluminosilicates are present in these regions instead of clay and/or amorphous silica. Models of Cimmeria identify glass and zeolite and do not identify phyllosilicates (Table 6.1). None of the models from the mineral mixtures in Chapter 3 identified a combination of glass and zeolites without phyllosilicates. Therefore, phyllosilicates are probably not present in Cimmeria but amorphous silica could be present. Future experiments should test the detection limits of zeolites and understand what mineralogical combinations lead to the detection of glass and zeolites in TIR spectral models.

6.2 Deriving Chemistry from TIR Models of Weathered Surfaces on Mars

6.2.1 Effects of Chemical Weathering on TIR-Derived Chemistry

Surface chemistry derived from TES models shows that derived SiO_2 and alkali abundances are higher in TES-derived data than in other datasets, including GRS and APXS measurements and values for Martian meteorites [*McSween et al.*, 2003; 2009]. It was suggested that chemical weathering causes these differences, but the specific causes and ways to correct the TES-derived data were not elaborated upon. TIR-derived chemistry of weathered basalts from Baynton, Australia reported in Chapter 2 shows that terrestrial weathering at near-neutral pH generally causes the overestimation of alkalis and FeO_T and the underestimation of SiO_2. The false identification and/or overestimation of K-bearing phases, including illite and K-feldspar, results in the overestimation of alkali abundances. The identification of significant amounts of hematite causes an overestimation of FeO_T and underestimation of SiO_2. Despite these inaccuracies,

modeled weathering trends are similar to measured weathering trends. This indicates that TIR-derived chemistry cannot be used to infer exact surface chemistry or to classify igneous rock types but it can be used to identify weathered surfaces and broadly interpret weathering processes.

6.2.2 Chemistry Derived from TES Surfaces

The addition of poorly-crystalline aluminosilicates to TES libraries resulted in the identification of these materials in Northern Acidalia, Solis, and Meridiani (Chapter 5). Poorly-crystalline aluminosilicates lack alkalis, so their identification in models reduced derived alkali abundances. This shows that the identification of poorly-crystalline aluminosilicates can improve modeled alkali abundances, but not modeled SiO_2 abundances. TIR spectroscopy samples the upper 10s of microns of a surface, and if a surface is weathered, TIR data would reflect the composition of the weathering rind or coating, rather than the unweathered parent material. Thus, it is reasonable to expect that we cannot derive the parent rock chemistry from TIR models of weathered surfaces.

Surface chemistry derived previously from TES models shows variation in Fe+Mg abundances, suggesting that acid sulfate alteration during the Hesperian Period caused dissolution of olivine globally [*Hurowitz et al.*, 2007]. Terrestrial chemical weathering at near-neutral pH results in the removal of alkali and alkaline earth elements and enrichment in aluminum and iron with the precipitation of secondary aluminosilicates and Fe-oxides and oxyhydroxides [*Eggleton et al.*, 1987; *Nesbitt and Wilson,* 1992]. The identification of poorly-crystalline aluminosilicates in models of Northern Acidalia, Solis, and Meridiani (Chapter 5) suggests that chemical weathering may have proceeded under terrestrial-like, near-neutral pH conditions, rather than under acid sulfate conditions. Plotting the derived Al_2O_3, $Ca_2O+Na_2O+K_2O$, and FeO_T+MgO abundances from Northern Acidalia, Solis, and Meridiani on ternary diagrams and comparing these values to a relatively unaltered surface (Syrtis) illustrates a terrestrial-

style weathering trend with depletion in $Ca_2O+Na_2O+K_2O$ and enrichment in Al_2O_3 and FeO_T+MgO (Figure 6.1). This indicates that acid sulfate weathering is not a global process and that weathering under near-neutral pH occurred on regional scales.

6.3 New Views of Regional and Local Weathering Environments from TES Models

6.3.1 Previous Views of Martian Chemical Weathering Environments

The identification of weathering products by NIR spectroscopy has been instrumental in our understanding of weathering processes on Mars. OMEGA data show that the types of weathering products are constrained to specific surface ages [*Bibring et al.*, 2006]. *Bibring et al.* [2006] defined three Martian eras based on the types of weathering products present during those time periods: 1) the Phyllosian (phyllosilicates are the dominant weathering products, indicating near-neutral to alkaline alteration under high water-to-rock ratios, 2) the Theiikian (sulfates are the dominant weathering products, indicating acid sulfate weathering under low water-to-rock ratios), and 3) the Siderikian (Fe-oxides are the dominant weathering products, indicating anhydrous, oxidative weathering). Each of these eras broadly correlates to the Noachian, Hesperian, and Amazonian Periods, respectively.

The identification of weathering products on more localized scales illustrates a greater diversity of aqueous alteration processes. The presence of gray crystalline hematite and sulfates in Meridiani and the sedimentary stratigraphy suggests a complex aqueous alteration history, possibly one similar to a sabkha environment, with alternating wet and dry periods [*Squyres et al.*, 2004; *Grotzinger et al.*, 2006]. The identification of jarosite at Meridiani further constrains alteration environments and demonstrates acid sulfate weathering occurred at a pH <4 [*Morris et al.*, 2006]. Sulfates have also been identified in Gusev, suggesting alteration by acidic fluids [*Wang et al.*, 2006]. The presence of amorphous silica-rich soils and outcrops near Home Plate and carbonate-rich

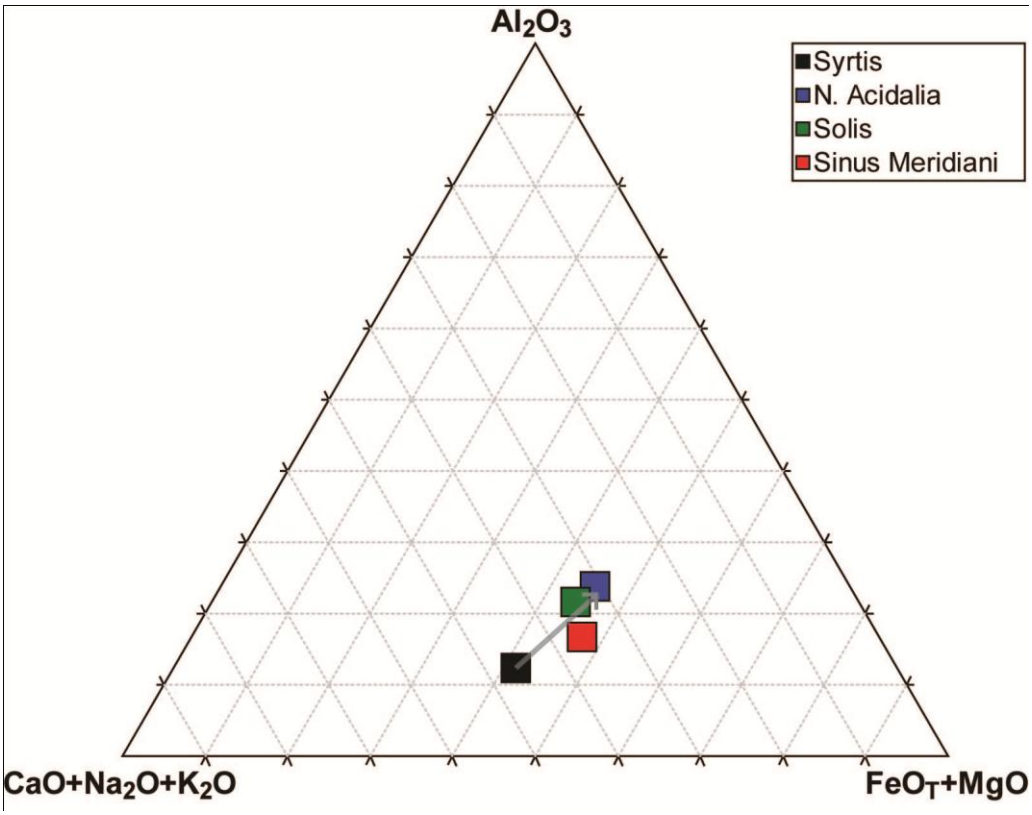

Figure 6.1. Regional surface chemistry (in mol.%) derived from TES models with allophanes and aluminosilicate gel in the library for Syrtis Major, Northern Acidalia, Solis Planum, and Sinus Meridiani. Gray arrow shows the general chemical weathering trend from the least altered surface (Syrtis) to the most weathered surfaces, based on the identification of allophane and/or gel in TES models. This trend is similar to the trend derived for terrestrial weathered basalts by *Nesbitt and Wilson* [1992], suggesting that near-neutral alteration occurred in Northern Acidalia, Solis, and Sinus Meridiani and that acid sulfate weathering was not the dominant regional surface process.

rocks in Gusev indicates a variety of alteration process occurred in Gusev in addition to acidic weathering. The mineralogy, texture, and chemistry of the amorphous silica-enriched surfaces suggest aqueous alteration at high water-to-rock ratios and near-neutral pH in a hot spring or geyser environment [*Ruff et al.*, 2011]. Similarly, the identification of Mg-Fe-rich carbonates in olivine-rich outcrops in Gusev suggests hydrothermal alteration at near-neutral pH during the Noachian [*Morris et al.*, 2010]. Mg-rich carbonates were also detected in Noachian terrains in Nili Fossae by NIR spectroscopy [*Ehlmann et al.*, 2008], suggesting that this style of aqueous alteration was not confined to Gusev [*Morris et al.*, 2010]. Calcium carbonates were identified in high-latitude soils at the Phoenix landing site, indicating that aqueous alteration at near-neutral pH occurred during the Amazonian [*Boynton et al.*, 2009].

6.3.2 Lessons from TES Models with Poorly-Crystalline Aluminosilicates

The identification of poorly-crystalline aluminosilicates in TES models of Northern Acidalia, Solis, and Meridiani is not consistent with the hypothesis that acid sulfate weathering was a global surface process for the last 3.5 billion years [*Hurowitz and McLennan*, 2007]. Acid sulfate weathering occurs at low pH and results in the preferential dissolution of olivine and removal of Fe and Mg [*Hurowitz et al.*, 2006]. Poorly-crystalline aluminosilicates, like allophane, form at near-neutral to mildly acidic pH and require the dissolution of Al-bearing phases, such as volcanic glass or feldspar, to precipitate [*Wada*, 1989]. The identification of allophane in Meridiani suggests chemical weathering at near-neutral pH occurred during the Hesperian Period. The presence of allophane in Meridiani, along with the identification of carbonates and silica in Gusev, and carbonates at the Phoenix landing site shows that aqueous alteration at near-neutral pH has been an important surface process across the globe and was not limited to the Noachian Period. However, the identification of poorly-crystalline aluminosilicates is

consistent with the idea that aqueous alteration during the Hesperian and Amazonian Periods was limited and occurred at low water-to-rock ratios.

High-silica aluminosilicate gel was identified at mid-to-high latitudes in Northern Acidalia and Solis surface types, possibly indicating alteration at lower pH than that required for allophane precipitation. The presence of aluminum in the structure, however, still indicates that an Al-bearing phase must be weathering to allow for the precipitation of an aluminosilicate gel. The identification of gel may also be consistent with the presence of volcanic glass leached by acidic solutions. OMEGA data suggests leached glass is present in Southern Acidalia [*Horgan*, 2010]. Leached volcanic glass has an elevated aluminum content compared to silica coatings precipitated from acidic solution [*Minitti et al.*, 2007]; however the Al_2O_3 content of the leached glass is generally <1 wt.%, while the aluminosilicate gel identified in spectral models has 13 wt.% Al_2O_3. It is important to further examine spectral properties of leached volcanic glasses compared to aluminosilicate gels to better understand chemical weathering processes in Acidalia and Solis.

TES models of dark- and light-toned surfaces from Mawrth Vallis show that a variety of alteration processes occurred in this region (Chapter 5). The identification of allophane in dark-toned surfaces indicates water-limited alteration under near-neutral pH, while the identification of allophane, halloysite, and montmorillonite in bright-toned surfaces indicates near-neutral to alkaline alteration at low to high water-to-rock ratios. The dark-toned units are younger than the bright-toned units and generally have higher thermal inertias [*Michalski and Noe Dobrea*, 2007], suggesting that allophane could be present in weathering rinds in the dark surfaces and could represent a later stage of alteration after the formation of clay minerals. Allophane commonly alters to form halloysite in soils derived from volcanic ash on Earth [*Wada*, 1989]. The Al-phyllosilicate-bearing unit in Mawrth has been shown to drape topography [*Michalski*

and Noe Dobrea, 2007; *Wray et al.*, 2008]. Previous studies identified kaolinite in this unit, suggesting that it had experienced intense leaching in a warm climate [*Bishop et al.*, 2010]. Conversely, the TES-derived mineralogy and geomorphology of this unit implies it is a weakly to moderately altered volcanic ash layer.

6.3.3 Implications for the MSL Mission

A primary goal for the MSL mission is to assess the habitability of a region that once had liquid water [*Mahaffy*, 2007]. Clay minerals form at high water-to-rock ratios compared to poorly-crystalline aluminosilicates, so it is important to target a surface with evidence for the greatest amount of clays. Models of bright-toned surfaces within the four proposed landing ellipses at Mawrth imply that not all bright-toned surfaces contain crystalline clay minerals and that some contain poorly-crystalline aluminosilicates. Models of proposed ellipses 1 and 3 identify montmorillonite clay and ellipse 1 identifies the greatest amount of phyllosilicates (~30 vol.%). The identification of 30 vol.% phyllosilicates is consistent with the presence of phyllosilicates in 10-20 wt.% abundances (Chapter 3). Thus, these bright-toned, clay-bearing surfaces are probably not clay-rich mudstones and have a patchy distribution of clay minerals. If MSL goes to Mawrth, landing ellipse 1 is the best area to target since it shows evidence for the greatest amount of clay minerals. Fe/Mg-smectites have been identified at Mawrth in a basal layer that is 150-200 m thick from NIR spectroscopy; however, TES spectral models in Chapter 5 do not identify these minerals. The stratigraphy of Mawrth shows that the Al-phyllosilicate layer is above the Fe/Mg-smectite layer, so the Al-phyllosilicate layer may be preferentially sampled by TIR spectroscopy. TIR spectra of Mg-smectites do not have a doublet at 600-400 cm^{-1} because the Si-O bending and Mg-O-Si deformation absorptions overlap [*Michalski et al.*, 2006]. The lack of this diagnostic feature may affect the detection of Mg-smectites compared to Al-smectites, like montmorillonite. It is

important to do further laboratory experiments to understand if detection limits vary for clay minerals with different compositions and structures.

6.4 Resolving Detections of Clay Minerals on Mars by TIR and NIR Spectroscopy

Clay mineral detections on Mars by TIR spectroscopy have been assumed to be inconsistent with detections by NIR spectroscopy. For example, the greatest abundances of clay minerals are modeled in TES spectra from low-albedo regions in Northern Acidalia and Solis Planum but NIR spectra of low-albedo regions globally do not show evidence for clay minerals [*Rogers and Christensen*, 2007]. Additionally, TES models of surfaces that have been shown to have clays from NIR spectroscopy do not identify significant abundances of clays [*Michalski and Fergason*, 2009], further illustrating the inconsistencies between clay detections in the NIR and TIR. The replacement of clay minerals with poorly-crystalline aluminosilicates in TES models of Northern Acidalia and Solis (Chapter 5) resolves this inconsistency between TIR and NIR data because poorly-crystalline aluminosilicates within basalt weathering rinds have muted absorptions in the NIR compared to crystalline clays [*Michalski et al.*, 2006b]. NIR spectroscopy of Mawrth bright-toned surfaces indicate a variety of clay minerals, including montmorillonite, beidellite, kaolinite, and Fe/Mg-smectites [*Bishop et al.*, 2008; *Wray et al.*, 2008; *Bishop et al.*, 2010; *McKeown et al.*, 2011]. While TES models of bright-, intermediate-, and dark-toned surfaces of Mawrth do not identify "significant" clay abundances [*Michalski and Fergason*, 2009], they still identify ~20 vol.% clay. Based on TIR models of mineral mixtures with montmorillonite (Chapter 3), this represents a real detection of clays and indicates that surfaces are made up of ~10 wt.% clay. TES models of bright-toned, high thermal inertia surfaces in Mawrth (Chapter 5) further suggest 10-20 wt.% clay abundances in certain areas, and there are TIR spectral features diagnostic of montmorillonite within these areas. Therefore, TES data should not be discounted

when characterizing clay mineral abundances on the Martian surface and should be used in concert with NIR data to identify and quantify secondary silicates.

6.5 Recommendations for Future Studies

The research presented here helps resolve some unanswered questions about chemical weathering processes on the Martian surface. Chapter 2 illustrates why chemical weathering adversely affects the chemistry derived from TIR models of weathered basalts, particularly alkali abundances. Chapter 3 constrains detection limits of crystalline clay and amorphous silica in TIR models and shows that secondary amorphous silica can cause the false detection of volcanic glass while crystalline clays can cause the false detection of zeolites. Chapter 4 provides previously unavailable TIR emission and NIR reflectance spectra of poorly-crystalline aluminosilicates, including allophanes, so that the Mars science community can examine spectroscopic evidence for these mineraloids on Mars. Regional-scale TES models presented in Chapter 5 show that poorly-crystalline aluminosilicates replace phyllosilicates in spectral models and can account for the lack of NIR evidence for phyllosilicates in low-albedo mid-to-high latitude surfaces. Poorly-crystalline aluminosilicates are regionally significant chemical weathering products and suggest that acid sulfate weathering was not a global process, as was previously hypothesized [*Hurowitz and McLennan*, 2007]. Finally, local-scale TES models of Mawrth show that TES can be used to identify clay-bearing surfaces. Models suggest that the distribution of clay-bearing units is patchy and clay-bearing surfaces may only contain 5-20 wt.% clay.

This research illuminates a new set of issues that should be investigated to better understand chemical weathering on Mars. Zeolites are identified in all regional TES models in ~10 vol.% abundances. It is important to characterize the detection limits of zeolites in TIR models to determine if the identification of zeolites in TES models could represent real detections. Additionally, the detection limits of clay minerals that are

spectrally dissimilar from montmorillonite, such as trioctahedral clays, should be characterized to help understand why Fe/Mg-smectites have not been identified in TES models of Mawrth. The detection limits of poorly-crystalline aluminosilicates should also be constrained. TIR models of mineral mixtures with zeolites, trioctahedral clays, and poorly-crystalline aluminosilicates similar to those in Chapter 3 should be carried out to help estimate the abundances of these materials on the Martian surface. TIR spectral properties of leached volcanic glass and how they compare to spectral properties of poorly-crystalline aluminosilicate coatings should be further studied to understand weathering processes in Acidalia. TES spectra of bright-toned surfaces in regions other than Mawrth that show NIR evidence for clays, such as Nili Fossae, should be modeled to estimate clay mineral abundances in these areas. The research presented here suggests that poorly-crystalline aluminosilicates are important weathering products on the Martian surface. Although this work has provided the Mars science community with TIR and NIR spectra of some allophanes and high-Si aluminosilicate gels, there are a slew of other poorly-crystalline and para-crystalline weathering products that are still absent from the spectral libraries, including other aluminosilicates, like imogolite and hisingerite, and Fe-oxides and oxyhydroxides, like ferrihydrite. It is important to continue synthesizing these materials and add them to spectral libraries to further constrain chemical weathering processes on Mars.

REFERENCES

Bandfield, J. L. (2002), Global mineral distributions on Mars, *J. Geophys. Res.*, *107*, E6(5042), doi:10.1029/2001JE001510.

Bandfield, J. L., V. E. Hamilton, and P. R. Christensen (2000), A global view of Martian surface compositions from MGS-TES, *Science*, *287*, 1626-1630, doi:10.1126/science.287.5458.1626.

Bandfield, J. L., A. D. Rogers, and C. S. Edwards (2011), The role of aqueous alteration in the formation of martian soils, *Icarus*, *211*, 157-171, doi:10.1016/j.icarus.2010.08.028.

Bell, III , J. F., R. Anderson, R. Milliken, and K. Edgett (2010), Mineralogy and physical properties of the proposed Gale crater MSL field site, Fourth MSL Landing Site Workshop, http://marsoweb.nas.nasa.gov/landingsites/msl/workshops/4th_workshop/program.htht.

Bibring, J. -P., 11 colleagues (2005), Mars surface diversity as revealed by the OMEGA/Mars Express observations, *Science*, *307*, 1576-1581, doi:10.1126/science.1108806.

Bibring, J. -P., 10 colleagues (2006), Global mineralogical and aqueous Mars history derived from OMEGA/Mars Express data, *Science*, *312*, 400-404, doi:10.1126/science1122659.

Bishop, J. L., 11 colleagues (2008), Phyllosilicate Diversity and Past Aqueous Activity Revealed at Mawrth Vallis, Mars. *Science*, *321***,** 830-833, doi:10.1126/science.1159699.

Bishop, J. L., 13 colleagues (2010), Mineralogy of the Mawrth Vallis landing site and surrounding terrains, Fourth MSL Landing Site Workshop, http://marsoweb.nas.nasa.gov/landingsites/msl/workshops/4th_workshop/program.html.

Boynton, W. V., 24 colleagues (2002), Distribution of hydrogen in the near surface of Mars: Evidence for subsurface ice deposits, Science, 297, 81-85, doi:10.1126/science.1073722.

Boynton, W. V. 13 colleagues (2009), Evidence for calcium carbonate at the Mars Phoenix landing site, *Science*, *325*, 61-64, doi:10.1126/science.1172768.

Chemtob, S. M., B. L. Joliff, G. R. Rossman, J. M. Eiler, and R. E. Arvidson (2010), Silica coatings in the Ka'u Desert, Hawaii, a Mars analog terrain: A micromorphological, spectral, chemical, and isotopic study, *J. Geophys. Res.*, *115*, E04001, doi:10.1029/2009JE003473.

Cherednik, L. (2001), A thermal emission spectroscopic study of glassy basalts, Ph.D. Thesis, Geology, Arizona State Univ., Tempe, AZ.

Childs, C. W., R. L. Parfitt, R. H. Newman (1990), Structural studies of Silica Springs allophane, *Clay Mins.*, *25*, 329-341.

Christensen, P. R., and S. T. Harrison (1993), Thermal infrared emission spectroscopy of natural surfaces: Application to desert varnish coatings on rocks, *J. Geophys. Res.*, *98*, 19,819-19,834, doi:10.1029/93JB00135.

Christensen, P. R., J. L. Bandfield, M. D. Smith, V. E. Hamilton, and R. N. Clark (2000a), Identification of a basaltic component on the Martian surface from Thermal Emission Spectrometer data, *J. Geophys. Res.*, *105*(E4), 9609-9621, doi:10.1029/99JE001127.

Christensen, P. R., 7 colleagues (2000b), A thermal emission spectral library of rock-forming minerals, *J. Geophys. Res.*, *105*(E4), 9735-9739, doi:10.1029/98JE000624.

Christensen P. R., 21 colleagues (2003), Morphology and composition of the surface of Mars: Mars Odyssey THEMIS results, *Science*, *300*, 2056-2061, doi:10.1126/science.1080885.
Christensen, P. R., 26 colleagues (2004a), Initial results from the Mini-TES experiments in Gusev Crater from the Spirit Rover, *Science*, *305*, 837-842, doi:10.1126/science.1100564.
Christensen, P. R., 26 colleagues (2004b), Mineralogy at Meridiani Planum from the Mini-TES experiment on the Opportunity Rover, *Science*, *306*, 1733-1739, doi:10.1126/science.1104909.
Clark, B. C., A. K. Baird, R. J. Weldon, D. M. Tsusaki, L. Schnabel, and M. P. Candelaria (1982), Chemical composition of Martian fines, *J. Geophys. Res.*, *87*(B12), 10,059-10,067, doi:10.1029/JB087iB12p10059.
Clark, B. C., 23 colleagues (2005), Chemistry and mineralogy of outcrops at Meridiani Planum, *Earth Planet. Sc. Lett.*, *240*, 73-94, doi:10.1016/j.epsl.2005.09.040.
Clark, R. N., 6 colleagues (2007), USGS Digital Spectral Library splib06a, *U.S. Geological Survey*, *Data Series 231*.
Colman, S. M. (1981) Chemical weathering of basalts and andesites: Evidence from weathering rinds: Washington, U.S. Geol. Survey Prof. Paper 1246, p. 51.
Colman, S. M. (1982), Clay mineralogy of weathering rinds and possible implications concerning the sources of clay minerals in soils, *Geology*, *10*, 370-375.
Couture, R. A. (1989), An improved fusion technique for major-element analysis by XRF, *Advances in X-Ray Analysis*, ***32***, 233-238.
Couture, R. A. (1993), Sample transparency effects in tin determination by x-ray fluorescence, *X-Ray Spectrometry*, ***22***, 92-96.
Cradwick, P. D. G., V. C. Farmer, J. D. Russell, C. R. Mason, K. Wada, and N. Yoshinaga (1972), Imogolite, a hydrated aluminum silicate of tubular structure, *Nature*, *240*, 187-189.
Crisp, J. A., A. B. Kahle, and E. A. Abbott (1990), Thermal infrared spectral character of Hawaiian basaltic glasses, *J. Geophys. Res.*, *95*, 21,657-21,669, doi:10.1029/JB095iB13p21657.
Curtiss, B. C., J. B. Adams, and M. S. Ghioroso (1985), Origin, development and chemistry of silica-alumina rock coatings from the semi-arid regions of the island of Hawaii, *Geochim. Cosmochim. Acta*, *49*, 49-56.
Drever, J. I. (1992), The Geochemistry of Natural Waters, Prentice-Hall, Inc., Upper Saddle River, New Jersey, 436 pp.
Eggleton, R. A. (1984), Formation of iddingsite rims on olivine: A transmission electron microscope study, *Clay Clay Min.*, *32*, 1-11, doi:10.1346/CCMN.1984.0320101.
Eggleton, R. A., C. Foudoulis, and D. Varkevisser (1987), Weathering of basalt: Changes in rock chemistry and mineralogy, *Clays Clay Miner.*, *35*, 161-169.
Ehlmann, B. L. 7 colleagues (2008), Clay minerals in delta deposits and organic preservation potential on Mars, *Nature Geosci.*, ***1,*** 355-358, doi:10.1038/ngeo207.
Ehlmann, B.L., 11 colleagues (2009), Identification of hydrated silicate minerals on Mars using MRO-CRISM: Geologic context near Nili Fossae and implications for aqueous alteration, *J. Geophys. Res.*, ***114,*** E00D08, doi:10.1029/2009JE003339.
Fabian, D., T. Henning, C. Jäger, H. Mutschke, J. Dorschner, and O. Wehrlan (2001), Dependence of crystalline olivine IR spectra on iron content and particle shape, *A&A*, *378*, 228-238, doi:10.1051/0004-6361:20011196.
Farmer, V. C. (1968), Infrared spectroscopy in clay mineral studies, *Clay Mins.*, *7*, 373-387.

Farmer, V. C., W. J. McHardy, L. Robertson, A. Walker, and M. J. Wilson (1985), Micromorphology and sub-microscopy of allophane and imogolite in a podzol Bs horizon: Evidence for translocation and origin, *J. Soil Sci.*, *36*, 87-95.

Farmer, V. C., W. J. McHardy, F. Palmieri, A. Violante, P. Violante (1991), Stability of a synthetic proto-phyllosilicate allophane relative to bayerite, based on the equilibrium $Si(OH)_4$ concentration, *Clay Mins.*, *26*, 421-425.

Feely, K. C., and P. R. Christensen (1999), Quantitative compositional analysis using thermal emission spectroscopy: Application to igneous and metamorphic rocks, *J. Geophys. Res.*, *104*(E10), 24,195-24,210, doi:10.1029/99JE001034.

Gallup, D. L. (1997), Aluminum silicate scale formation and inhibition: Scale characterization and laboratory experiments, *Geothermics*, *26*, 483-499.

Gellert, R., 11 colleagues (2006), Alpha Particle X-Ray Spectrometer (APXS): Results from Gusev crater and calibration report, *J. Geophys. Res.*, *111*, E02S05, doi:10.1029/2005JE002555.

Gendrin, A., 10 colleagues (2005), Sulfates in Martian layered terrains: The OMEGA/Mars Express view, *Science*, *307*, 1587-1591, doi:10.1126/science.1109087.

Glotch, T. D., 7 colleagues (2006), Mineralogy of the light-toned outcrop at Meridiani Planum as seen by the Miniature Thermal Emission Spectrometer and implications for its formation, *J. Geophys. Res.*, *111*, E12S03, doi:10.1029/2005JE002672.

Golombek, M. P., 13 colleagues (1997), Overview of the Mars Pathfinder mission and assessment of landing site predictions, *Science*, *278*, 1743-1748, doi:10.1126/science.278.5344.1743.

Graff, T. G. (2003), Effects of dust coatings on visible, near-infrared, thermal emission and Mossbauer spectra: Implications for mineralogical remote sensing of Mars, M.S. Thesis, Geology, Arizona State Univ., Tempe, AZ.

Grotzinger, J., 17 colleagues (2006), Sedimentary textures formed by aqueous processes, Erebus crater, Meridiani Planum, Mars, *Geology*, *34*, 1085-1088, doi:10.1130/G22985A.1.

Hamilton, V. E. (2000), Thermal infrared emission spectroscopy of the pyroxene mineral series, *J. Geophys. Res.*, *105*, E4, 9701-9716.

Hamilton, V. E., and P. R. Christensen (2000), Determining the modal mineralogy of mafic and ultramafic igneous rocks using thermal emission spectroscopy, *J. Geophys. Res.*, *105*(E4), 9717-9733, doi:10.1029/99JE001113.

Hamilton, V. E., and M. E. Minitti (2003), Are oxidized shergottite-like basalts an alternative to "andesite" on Mars?, *Geophys. Res. Let.*, *30*, 18, doi:10.1029/2003GL017839.

Hamilton, V. E. and P. R. Christensen (2005), Evidence for extensive, olivine-rich bedrock on Mars, *Geology*, *33*, 6, 433-436, doi:10.1130/G21258.1.

Hamilton, V. E., R. V. Morris, J. E. Gruener, and S. A. Mertzman (2008), Visible, near-infrared, and middle infrared spectroscopy of altered basaltic tephras: Spectral signatures of phyllosilicates, sulfates, and other aqueous alteration products with application to the mineralogy of the Columbia Hills of Gusev Crater, Mars, *J. Geophys. Res.*, *113*, E12S43, doi:10.1029/2007JE003049.

Harsh, J., J. Chorover, E. Nizeyimana (2002), Allophane and Imogolite in *Soil Mineralogy with Environmental Applications*, Soil Science Society of America, no.7, pp. 291-322.

Haskin, L. A, and P. A. Salpas (1992), Genesis of compositional characteristics of Stillwater AN-I and AN-II thick anorthosite units, *Geochim. Coscmochim. Acta*, *56*, 1187-1212.

Henmi, T., K. Wada (1976), Morphology and composition of allophane, *Am. Min.*, *61*(5-6), 379-390.
Horgan, B. (2010), Wind, water, and the sands of Mars, Ph.D. Thesis, , Cornell Univ., Ithaca, NY.
Hunt, G. R. (1980), Electromagnetic radiation: The communication link in remote sensing. In B. S. Siegel, and A. R. Gillespie (Eds.), *Remote sensing in geology* (pp. 5-45). New York: John Wiley.
Hurowitz, J. A., 7 colleagues (2006), In situ and experimental evidence for acidic weathering of rocks and soils on Mars, *J. Geophys. Res.*, *111*, E02S19, doi:10.1029/2005JE002515.
Hurowitz, J. A., and S. M. McLennan (2007), A ~3.5 Ga record of water-limited, acidic weathering conditions on Mars, *Earth Planet. Sc. Lett.*, *260***,** 432-443.
Hurowitz, J. A., 5 colleagues (2007), A global view of Martian weathering based on lander, GRS, and MGS-TES data, paper presented at 7th Int. Conf. Mars, Abstract 3263.
Iyoda, F., S. Hayashi, S. Arakawa, and M. Okamoto (2011), Nanostructure and adsorption behavior of natural/synthetic allophanes, *27th World Congress of the Polymer Processing Society*, PPS-27.
Johnson, J. R., P. R. Christensen, P. G. Lucey (2002a), Dust coatings on basaltic rocks and implications for thermal infrared spectroscopy of Mars, *J. Geophys. Res.*, *107*, E6, 5035, doi:10.1029/2000JE001405.
Johnson, J. R., F. Hörz, P. G. Lucey, and P. R. Christensen (2002b), Thermal infrared spectroscopy of experimentally shocked anorthosite and pyroxenite: Implications for remote sensing of Mars, *J. Geophys. Res.*, *107*, E10, doi:10.1029/2001JE001517.
Koeppen, W. C., and V. E. Hamilton (2008), Global distribution, composition, and abundance of olivine on the surface of Mars from thermal infrared data, *J. Geophys. Res.*, *113*, E05001, doi:10.1029/2007JE002984.
Kraft, M. D. (2009), Effects of alteration on infrared spectra: Interpreting aqueous redistribution of silica on Mars, Ph.D. Thesis, School of Earth and Space Exploration, Arizona State Univ., Tempe, AZ.
Kraft, M. D., J. R. Michalski, and T. G. Sharp (2003), Effects of pure silica coatings on thermal emission spectra of basaltic rocks: Considerations for Martian surface mineralogy, *Geophys. Res. Lett.*, *30*, 2288, doi:10.1029/ 2003GL018848.
Kraft, M. D., J. R. Michalski, T. G. Sharp, and E. B. Rampe (2008), An aqueous weathering model for middle and high latitude regions of Mars, *LPS XXXIX*, 2539.
Kreslavsky, M. A., J. W. Head, III, and D. R. Marchant (2008), Periods of active permafrost layer formation during the geological history of Mars: Implications for circum-polar and mid-latitude processes, *Planet. Space Sci.*, *56*, 289-302, doi:10.1016/j.pss.2006.02.010.
Lawson, C. L., and R. J. Hanson (1974), *Solving Least-Squares Problems*, 340 pp., Prentice-Hall, Englewood Cliffs, N. J.
Langevin, Y., F. Poulet, J.-P. Bibring, and B. Gondet (2005), Sulfates in the north polar region of Mars detected by OMEGA/Mars Express, *Science*, *307*, 1584-1586, doi:10.1126/science.1109091.
Loizeau, D., 10 colleagues (2007), Phyllosilicates in the Mawrth Vallis region of Mars, *J. Geophys. Res.*, *112*, E08S08, doi:10.1029/2006JE002877.
Lyon, R. J. P. (1964), Evaluation of infrared spectrophotometry for compositional analysis of lunar and planetary soils, II, Rough and powdered surfaces, *NASA Conf. Rep.*, *CR-100*.
Madejová, J., J. Bujdak, M. Janek, and P. Komadel (1998), Comparative FT-IR study of structural modifications during acid treatment of dioctahedral smectites and

hectorite, *Spectrochimica Acta Part A: Molecular and Biomolecular Spectroscopy*, *54*, 10, 1397-1406.
Madejová, J., and P. Komadel (2001), Baseline studies of the Clay Minerals Society source clays: Infrared methods, *Clays and Clay Mins.*, *49*, 5, 410-432.
Mahaffy, P (2007), Exploration of the habitability of Mars: Development of analytical protocols for measurement of organic carbon on the 2009 Mars Science Laboratory, *Space Sci. Rev.*, *135*, doi:10.1007/s11214-007-9223-1.
Mangold, N., 11 colleagues (2007), Mineralogy of the Nili Fossae region with OMEGA/Mars Express data: 2. Aqueous alteration of the crust, *J. Geophys. Res.*, *112*, E08S04, doi:10.1029/2006JE002835.
McDowell, M. L., and V. E. Hamilton (2009), Seeking phyllosilicates in thermal infrared data: A laboratory and Martian data case study, *J. Geophys. Res.*, *114*, E06007, doi:10.1029/2008JE003317.
McKeown, N. K., 7 colleagues (in prep), Interpretation of reflectance spectra of clay mineral-silica mixtures: implications for Martian clay mineralogy at Mawrth Vallis.
McSween, H. Y., T. L. Grove, and M. B. Wyatt (2003), Constraints on the composition and petrogenesis of the Martian crust, *J. Geophys. Res.*, *108*, E12, doi:10.1029/2003JE002175.
McSween, H. Y., G. J. Taylor, and M. B. Wyatt (2009), Elemental composition of the Martian crust, *Science*, *324*, doi:10.1126/science.1165871.
MEPAG (2010), Mars Scientific Goals, Objectives, Investigations, and Priorities: J. R. Johnson, et., 49 p. white paper posted September, 2010 by the Mars Exploration Program Analysis Group (MEPAG) at http://mepag.jpl.nasa.gov/reports/index.html.
Michalski, J. R., and R. L. Fergason (2009), Composition and thermal inertia of the Mawrth Vallis region of Mars from TES and THEMIS data, *Icarus*, *199*, 25-48, doi:10.1016/j.icars.2008.08.016.
Michalski, J. R., and E. Z. Noe Dobrea (2007), Evidence for a sedimentary origin of clay minerals in the Mawrth Vallis region, Mars, *Geology*, *35*(10), 951-954, doi:10.1130/G23845A.1.
Michalski, J. R., M. D. Kraft, T. G. Sharp, L. B. Williams, and P. R. Christensen (2005), Mineralogical constraints on the high-silica Martian surface component observed by TES, *Icarus*, *174*, 161-177.
Michalski, J. R., M. D. Kraft, T. G. Sharp, L. B. Williams, P. R. Christensen (2006a), Emission spectroscopy of clay minerals and evidence for poorly crystalline aluminosilicates on Mars from Thermal Emission Spectrometer data, *J. Geophys. Res.*, *111*, doi:10.1029/2005JE002438.
Michalski, J. R., M. D. Kraft, T. G. Sharp, and P. R. Christensen (2006b), Effects of chemical weathering on infrared spectra of Columbia River Basalt and spectral interpretations of Martian alteration, *Earth Plan. Sc. Lett.*, *248*, 822-829.
Milliken, R. E., 11 colleagues (2008), Opaline silica in young deposits on Mars, *Geology*, *36(11)*, 847–850, doi: 10.1130/G24967A.
Milliken, R. E., W. W. Fischer, and J. A. Hurowitz (2009), Missing salts on early Mars, *Geophys. Res. Lett.*, *36*, L11202, doi:10.1029/2009GL038558.
Milliken, R. (2010), The mineralogy of the four MSL landing sites, Fourth MSL Landing Site Workshop, http://marsoweb.nas.nasa.gov/landingsites/msl/workshops/4th_workshop/program.html.
Ming, D. W., 16 colleagues (2006), Geochemical and mineralogical indicators for aqueous processes in the Columbia Hills of Gusev crater, Mars, *J. Geophys. Res.*, *111*, E02S12, doi:10.1029/2005JE002560.

Ming, D. W., 18 colleagues (2008), Geochemical properties of rocks and soils in Gusev Crater, Mars: Results of the Alpha Particle X-Ray Spectrometer from Cumberland Ridge to Home Plate, *J. Geophys. Res.*, *113*, E12S39, doi:10.1029/2008JE003195.

Minitti, M. E., and V. E. Hamilton (2010), A search for basaltic-to-intermediate glasses on Mars: Assessing Martian crustal mineralogy, *Icarus*, *210*, 135-149, doi:10.1016/j.icarus.2010.06.028.

Minitti, M. E., C. M. Weitz, M. D. Lane, and J. L. Bishop (2007), Morphology, chemistry, and spectral properties of Hawaiian rock coatings and implications for Mars, *J. Geophys. Res.*, *112*, E05015, doi:10.1029/2006JE002839.

Moersh, J. E., and P. R. Christensen (1995), Thermal emission from particulate surfaces: A comparison of scattering models with measured spectra, *J. Geophys. Res.*, *100*, E4, 7456-7477, doi:10.1029/94JE03330.

Moore, D. M. and R. C. Reynolds (1989), *X-Ray Diffraction and the Identification and Analysis of Clay Minerals*, Oxford University Press, Oxford.

Moore, C. L. (1996), Processes of chemical weathering of selected Cainozoic eastern Australian basalts, Ph.D. Thesis, Department of Geology, Australian National University, Canberra, Australia.

Morris, R. V., T. G. Graff, S. A. Mertzman, M. D. Lane, and P. R. Christensen (2003), Palagonitic (not andesitic) Mars: Evidence from thermal emission and VNIR spectra of palagonitic alteration rinds on basaltic rock, 6^{th} *Int'l. Conf. Mars*, 3211.

Morris, R. V., 23 colleagues (2006), Mossbauer mineralogy of rock, soil, and dust at Meridiani Planum, Mars: Opportunity's journey across sulfate-rich outcrop, basaltic sand and dust, and hematite lag deposits, *J. Geophys. Res.*, *111*, E12S15, doi:10.1029/2006JE002791.

Morris, R. V., 12 colleagues (2010), Identification of carbonate-rich outcrops on Mars by the Spirit rover, *Science*, *329*, 421-424, doi:10.1126/science.1189667.

Mustard, J. F., 35 colleagues (2008), Hydrated silicate minerals on Mars observed by the Mars Reconnaissance Orbiter CRISM instrument, *Nature*, 305-309, doi:10.1038/nature07097.

Nesbitt, H. W., and R. E. Wilson (1992) Recent Chemical-Weathering of Basalts, *Am. J. Sci.*, *292*, 740-777.

Nesse, W. D. (2000), *Introduction to Mineralogy*, Oxford University Press, Oxford.

Neuendorf, K. E., J. P. Mehl, and J. A. Jackson (2005), *Glossary of Geology*, American Geological Institute, Alexandria, p. 779.

Noe Dobrea, E. Z., 15 colleagues (2008), Clay bearing units in the region around Mawrth Vallis: Stratigraphy, extent, and possible alteration fronts, *LPSXXXIX*, 1077.

Ohashi, F., S.-I. Wada, M. Suzuki, M. Maeda, S. Tomura (2002), Synthetic allophane from high-concentration solutions: nanoengineering of the porous solid, *Clay Minerals*, *37*, 451-456.

Osterloo, M. M., 7 colleagues (2008), Chloride-bearing materials in the southern highlands of Mars, *Science*, *319*, 1651-1654, doi:10.1126/science.1150690.

Parfitt, R. L. (1990), Allophane in New Zealand – A review, *Australian J. Soil Res.*, *28*(3), 343-360.

Parfitt, R. L., T. Henmi (1980), Structure of some allophanes from New Zealand, *Clays and Clay Mins.*, *28*(4), 285-294.

Parfitt, R. L., R. J. Furkert, T. Henmi (1980), Identification and structure of two types of allophane from volcanic ash soils and tephras, *Clays Clay Mins.*, *28*(5), 328-334.

Pelkey, S. M., 11 colleagues (2007), CRISM multispectral summary products: Parameterizing mineral diversity on Mars from reflectance, *J. Geophys. Res.*, *112*, E08S14, doi:10.1029/2006JE002831.

Potter, R. M., and G. R. Rossman (1977), Desert varnish: The importance of clay minerals, *Science*, *24*, 1446-1448, doi:10.1126/science.196.4297.1446.Murchie, S., 49 colleagues (2007), Compact Reconnaissance Imaging Spectrometer for Mars (CRISM) on Mars Reconnaissance Orbiter (MRO), *J. Geophys. Res.*, *112*, E05S03, doi:10.1029/2006JE002682.

Poulet, F., 9 colleagues (2005), Phyllosilicates on Mars and implications for early Martian climate, *Nature*, *438*, 623-627, doi:10.1038/nature04274.

Poulet, F., 7 colleagues (2008), Mineralogy of Terra Meridiani and western Arabia Terra from OMEGA/MEx and implications for their formation, *Icarus*, *195*, 106-130, doi:10.1016/j.icarus.2007.11.031.

Rampe, E. B., M. D. Kraft, T. G. Sharp, and J. R. Michalski (2007), The influence of chemical alteration on thermal infrared spectroscopy and interpretations of igneous mineralogy of Mars, paper presented at 7th Int. Conf. Mars, Abstract 3242.

Rampe, E.B., M. D. Kraft, and T. G. Sharp (2011), Deriving chemical trends from thermal infrared spectra of weathered basalt: Implications for remotely determining chemical trends on Mars, *J. Geophys. Res.*, submitted Jan. 2011.

Ramsey, M. S., and P. R. Christensen (1998), Mineral abundance determination: Quantitative deconvolution of thermal emission spectra, *J. Geophys. Res.*, *103*(B1), 577-596, doi:10.1029/97JB02784.

Rieder, R., 7 colleagues (1997), The chemical composition of Martian soil and rocks returned by the mobile Alpha Proton X-ray Spectrometer: Preliminary results from the X-ray mode, *Science*, *278*, 1771-1774, doi:10.1126/science.278.5344.1771.

Rieder, R., 13 colleagues (2004), Chemistry of rocks and soils at Meridiani Planum from the Alpha Particle X-ray Spectrometer, *Science*, *306*, 1746-1749, doi:10.1126/science.1104358.

Rivard, B, S. B. Petroy, and J. R. Miller (1993), Measured effects of desert varnish on the mid-infrared spectra of weathered rocks as an aid to TIMS imagery interpretation, *IEEE Trans. Geosci. Rem. Sens.*, *31*, 1, 284-291.

Roach, L. H., 8 colleagues (2008), Constraints on the rate of sulfate phase changes in Valles Marineris interior layered deposits, *LPS XXXIX*, 1823.

Rogers, A. D., and O. Aharonson, (2008), Mineralogical composition of sands in Meridiani Planum determined from Mars Exploration Rover data and comparison to orbital measurements, *J. Geophys. Res.*, *113*, E06S14, doi:10.1029/2007JE002995.

Rogers, A. D., and P. R. Christensen (2007), Surface mineralogy of Martian low-albedo regions from MGS-TES data: Implications for upper crustal evolution and surface alteration, *J. Geophys. Res.*, *112*, E01003, doi:10.1029/2006JE002727.

Rogers, A. D., J. L. Bandfield, and P. R. Christensen (2007), Global spectral classification of Martian low-albedo regions with Mars Global Surveyor Thermal Emission Spectrometer (MGS-TES) data, *J. Geophys. Res.*, *112*, E02004, doi:10.1029/2006JE002726.

Ruff, S. W. (2004), Spectral evidence for zeolite in the dust on Mars, *Icarus*, *168*, 131-143.

Ruff, S. W., and P. R. Christensen (2002), Bright and dark regions on Mars: Particle size and mineralogical characteristics based on Thermal Emission Spectrometer data, *J. Geophys. Res.*, *107*, E12, 5127, doi:10.1029/JE2001JE001580.

Ruff, S. W., and P. R. Christensen (2007), Basaltic andesite, altered basalt, and a TES-based search for smectite clay minerals on Mars, *Geophys. Res. Lett.*, *34*, L10204, doi:10.1029/2007GL029602.

Ruff, S. W., P. R. Christensen, P. W. Barbera, and D. L. Anderson (1997), Quantitative thermal emission spectroscopy of minerals: A laboratory technique for measurement and calibration, *J. Geophys. Res.*, *102*(B7), 14,899-14,913, doi:10.1029/97JB00593.

Ruff, S. W., 8 colleagues (2006), The rocks at Gusev Crater as viewed by the Mini-TES instrument, *J. Geophys. Res.*, *111*, E12S18, doi:10.1029/2005JE002747.

Ruff, S. W., 10 colleagues (2011), Characteristics, distribution, origin, and significance of opaline silica observed by the Spirit rover in Gusev crater, Mars, *J. Geophys. Res.*, *116*, E00F23, doi:10.1029/2010JE003767.

Salisbury, J. W., and A. Wald (1992), The role of volume scattering in reducing spectral contrast of Reststrahlen bands in spectra of powdered minerals, *Icarus*, *96*, 121-128.

Squyres, S. W., 18 colleagues (2004a), In situ evidence for an ancient aqueous environment at Meridiani Planum, Mars, *Science*, *306*, 1709-1714, doi:10.1126/science.1104559.

Squyres, S. W., 49 colleagues (2004b), The Opportunity Rover's Athena Science Investigation at Meridiani Planum, Mars, *Science*, *306*(5702), 1698-1703, doi:10.1126/science1106171.

Squyres, S., W., 17 colleagues (2008), Detection of silica-rich deposits on Mars, *Science*, *320*, 1063-1067, doi:10.1126/science.1155429.

Su, C., J. B. Harsh, and P. M. Bertsch (1992), Sodium and chloride sorption by imogolite and allophanes, *Clay Clay Miner.*, *40*, 3, 280-286.

Taylor, R. and R. A. Eggleton (2001), *Regolith Geology and Geomorphology*, Wiley, Chichester, UK.

Thomson, J. L., and J. W. Salisbury (1993), The mid-infrared reflectance of mineral mixtures (7-14 μm), *Remote Sens. Environ.*, *45*, 1-13.

Tomisaka, T., and K. Iishi (1980), Some aspects of the lattice dynamics of diopside, *Min. Journ.*, *10*, 2, 84-96.

Tosca, N. J., S. M. McLennan, D. H. Lindsley, and M. A. A. Schoonen (2004), Acid-sulfate weathering of synthetic Martian basalt: The acid fog model revisited, *J. Geophys. Res.*, *109***,** E05003, doi:10.1029/2003JE002218.

Van der Marel, H. W., H. Beutelspacher (1976), Atlas of infrared spectroscopy of clay minerals and their admixtures, Amsterdam: Elsevier Scientific Publishing Company, pp. 396.

Vincent, R. K., and G. R. Hunt (1968), Infrared reflectance from mat surfaces, *Appl. Opt.*, *7*, 53-59.

Wada, K. (1989), Allophane and Imogolite in *Minerals in Soil Environments*, Soil Science Society of America, no.1, pp. 1051-1087.

Wada, K., and H. Kubo (1975), Precipitation of amorphous aluminosilicates from solution containing monomeric silica and aluminum ions, *J. Soil Sci.*, *26*, 100-111, do:10.1111/j.1365-2359.1975.tb01935.

Wada, S.-I., K. Wada (1977), Density and structure of allophane, *Clay Minerals*, *12*, 289-298.

Wada, K., T. Henmi, N. Yoshinaga, and S. H. Patterson (1972), Imogolite and allophane formed in saprolite of basalt on Maui, Hawaii, *Clay Clay Min.*, *20*, 375-380.

Wada, S.-I., A. Eto, and K. Wada (1979), Synthetic allophane and imogolite, *J. Soil Sci.*, *30*, 347-355.

Wang, A., 12 colleagues (2006), Evidence of phyllosilicates in Wooly Patch, an altered rock encountered at West Spur, Columbia Hills, by the Spirit rover in Gusev crater, Mars, *J. Geophys. Res.*, *111*, E02S16, doi:10.1029/2005JE002513.

Wiseman, S. M., 9 colleagues (2010), Spectral and stratigraphic mapping of hydrated sulfate and phyllosilicate-bearing deposits in northern Sinus Meridiani, Mars, *J. Geophys. Res.*, *115*, E00D18, doi:10.1029/2009JE003354.

Wray, J. J., B. L. Ehlmann, S. W. Squyres, J. F. Mustard, and R. L. Kirk (2008), Compositional stratigraphy of clay-bearing layered deposits at Mawrth Vallis, Mars, *Geophys. Res. Lett.*, *35*, L12202, doi:10.1029/2008GL034385.

Wyatt, M. B., V. E. Hamilton, H. Y. McSween, Jr., P. R. Christensen, and L. A. Taylor (2001), Analysis of terrestrial and Martian volcanic compositions using thermal emission spectroscopy: 1. Determination of mineralogy, chemistry, and classification strategies, *J. Geophys. Res.*, *106*(E7), 14,711-14,732, doi:10.1029/2000JE001356.

Wyatt, M. B., and H. Y. McSween, Jr. (2002), Spectral evidence for weathered basalt as an alternative to andesite in the northern lowlands of Mars, *Nature*, *417*, 263-266, doi:10.1038/417263a.

Wyatt, M. B., H. Y. McSween, Jr., K. L. Tanaka, and J. W. Head, III (2004), Global geologic context for rock types and surface alteration on Mars, *Geology*, *32*, 8, 645-648, doi:10.1130/G20527.1.

Yen, A. S., 35 colleagues (2005), An integrated view of the chemistry and mineralogy of Martian soils, *Nature*, *436*, doi:10.1038/nature03637.